Development of Correlated and Computational Methods for Predicting Premixed Turbulent Flame Speed

Eoin M. Burke, B.E. (2012)

A thesis submitted to the National University of Ireland as fulfilment of the requirements for the degree of Doctor of Philosophy

Submitted June, 2018

Supervisor: Dr. Rory F. D. Monaghan

Mechanical Engineering
College of Engineering and Informatics
National University of Ireland, Galway

Abstract

Turbulent flame speed (S_T) is an important property within turbulent flames and an invaluable parameter for gas turbine combustor design. A major issue however is the difficulty in accurately predicting S_T due to the complexity of reactive turbulent flow. The aim of this research is to: (1) carry out an extensive study on literature analytical S_T correlation, (2) develop a new empirical correlation, and (3) develop of a one-dimensional (1D) freely propagating turbulent flame speed model implemented in Cantera.

For the correlation study 15 state-of-the-art premixed turbulent flame speed correlations from the literature are examined in three studies to provide insight into each expression. A newly-developed empirical correlation is also introduced and assessed alongside the literature correlations. The assessment is carried out by comparing each expression against experimental data and determining accuracy using a mean absolute percentage error (MAPE). The combined findings of the three studies shows that a minimum of two correlations and two sets of adjustable parameters are required to accurately account for the entire range of data in the study and shows that there is currently no general correlations.

A predictive model is therefore developed based on the existing Cantera solver. To solve for S_T, significant additions are made to Cantera to include: (1) the gradient transport model for the temperature and species transport equations to account for increase transport, (2) a Taylor series expansion of the reaction rate around the mean temperature to model the effects of temperature fluctuation on the Arrhenius rate, and (3) the eddy dissipation concept model with finite rate chemistry to define the influence of the turbulent-chemistry interactions. Validation shows a very small difference between the MAPE of the most accurate correlation of Muppala, (38.1%) and the predictive model (41.3 %). For gas turbine relevant conditions it is found that the solver improved on existing empirical approaches, providing a smaller error. A series of trend studies showed that the model predicted the trends well over a wide range of conditions.

Acknowledgements

Firstly I would like to thank my supervisors Dr. Rory Monaghan and Dr. Henry Curran for their support, expertise and enthusiasm for this research over the past number of years.

Next I would like to acknowledge the Irish Research Council (IRC) for co-funding this project with GE Power under the Enterprise Partnership Scheme. Thanks in particular to my industrial supervisors Dr. Felix Güthe and Dr. Birute Bunkute from GE Power. I would like to thank the guys in C3 for their support with everything chemistry related. Without the help of Kieran, Ultan and John nothing would have burned. I would like to thank Dr. Ray Speth for his help with everything related to Cantera and its source code. Next I would like to thank Dr. Ivar Ertesvåg and Mr. Sandeep Jella for their extensive help in understanding the Eddy Disapation Concept model. I would also like to thank Eimear O'Hara for her extensive proof reading, while it wasn't easy we got there in the end.

I would like to thank my friends and colleagues in the engineering building, including, Brían, Conor, Caoimhe, Donnacha, Ed, Fiona, Heather, Lizanne, Myles, Nicola, Noddy, Orla, Paul, Sarah, Stefaan, Tarek, Ted, and the wider PhD, research group. I would like to thank the O'Connors for all their help and support during my time in Galway, with thanks in particular to Tadhg for keeping me sane with adventures around Ballyforan. To my family, my parents Rose and Ulick and my sister Aoife, thank you so much for your love, support and for everything you have done to get me this far.

Finally, but by no means the least, I would like to acknowledge Sarah Kenny for looking after me, her endless support and most importantly not murdering me throughout my PhD. I would not have been able to do this without you.

Publications

Peer-Reviewed Papers in Print

E.M. Burke, F. Güethe, R.F.D. Monaghan, “A comparison of turbulent flame speed correlations for hydrocarbon fuels at elevated pressures”, ASME Turbo Expo 2016, Seoul, South Korea, June 2016.

E.M. Burke, A. Singlitico, A. Morones , E.L. Petersen, F. Güethe, B. Bunkute, R.L. Speth, R.F.D. Monaghan, “Progress Towards a Validated Cantera-based Turbulent Flame Speed Solver”, European Combustion Meeting, Budapest, Hungary, Mar 2015.

“Multi-Scale Pollutant Emissions Modelling for Gas Turbines”, Ryan Institute Research Day, NUI Galway, Ireland, September 2013.

Papers for submission

E.M. Burke, F. Güethe, R.F.D. Monaghan, “Optimization of Turbulent Flame Speed Correlations for C_1 - C_3 fuels over a range of pressures”, Combustion Science and Technology, 2018.

E.M. Burke, F. Güethe, R.F.D. Monaghan, “Development of Cantera-based 1D Freely Propagating Planar Turbulent Flame Speed Solver”, Combustion Science and Technology, 2018.

Contents

List of Figures

List of Tables

Nomenclature

Abbreviations

BB	Bunsen Burner
BML	Bray Moss Libby
CCGT	Combined Cycle Gas Turbine
CD	Conical Diffuser
CFD	Computational Fluid Dynamics
CFM	Coherent Flame Model
CV	Cylindrical Vessel
DLN	Dry Low NO_x
DNS	Direct Numerical Simulation
DRZ	Distributed Reaction Zone
EBU	Eddy Break Up
EDC	Eddy Dissipation Concept
EV	Explosive Vessel
FSD	Flame Surface Density
GHG	Green House Gases
GW	Gigawatts
IEA	International Energy Agency
ISP	Intermediate Steady Propagation
KPP	Kolomogorov-Petrovski-Piskunov
LBO	Lean Blowout
LES	Large Eddy Simulation
MAPE	Mean Absolute Percentage Error
MW	Megawatts
ODT	One-Dimensional Turbulent
OECD	Organization for Economic Cooperation and Development
PDF	Probability Density Function
PSR	Perfectly Stirred Reactor
RANS	Reynolds-averaged Navier-Stokes
SB	Spherical Bomb
TCI	Turbulent Chemistry Interaction
UHC	Unburned Hydrocarbons

Greek Symbols

α	Thermal Diffusivity
$\bar{\dot{\omega}}$	Mean Reaction Rate

β	Temperature Exponent
χ	Reacting Portion of the Fine Structure
δ_{diff}	Diffusive Laminar Flame Thickness
δ_{ij}	Kronecker Delta
δ_{th}	Thermal Laminar Flame Thickness
δ_t	Mean Flame Brush Thickness
$\dot{\omega}$	Reaction Rate
ε	Turbulent Energy Dissipation
ε_{ij}	Stress Dissipation Rate
η	Kolmogorov Length Scale
γ	Mass Fraction of the Fine Structure Region
γ^3	Mass Fraction of the Fine Structure
Λ	Integral Length Scale
λ	Thermal Conductivity
μ	Kinematic Viscosity
ϕ	Equivalence Ratio
Π_{ij}	Pressure Strain Correlation
ρ	Density
τ	Viscous Stress
τ_c	Chemical Time Scale
τ_{ij}	Subgrid Stress Tensor
τ_k	Kolmogorov Time Scale
υ	Dynamic Viscosity
$\upsilon_{kr}^{'}$	Stoichiometric Coefficients

Roman Symbols

$\bar{S}_{ij}$	Rate of Strain Tensor
$\bar{T}_k$	Equivalent Kinetic Temperature
Λ/δ_{th}	Turbulent Length Scale Ratio
$\overline{c}$	Progress Variable
$\overline{T}$	Time Averaged Fluctuations
$\widetilde{u''_i\phi''}$	Reynolds flux term for ϕ
$\widetilde{u''_i u''_j}$	Reynolds stress term
$a_{k,r}$	Collision Efficiency
AFR	Air Fuel Ratio
c_p	Constant Pressure Specific Heat
Cc	Correction Coefficient
D	Species Diffusion
Da	Damköhler Number
Ea	Activation Energy
$F(\varphi)$	Residual Vector
h	Enthalpy
I_0	Stretch Factor
j_k	Diffusive Mass Flux
J_{ij}	Turbulent Diffusive Transport

k	Turbulent Kinetic Energy
$k_f(T)$	Forward Rate Constant
Ka	Karlovitz Number
L_{ij}	Germano Identity
Le	Lewis Number
m^*	Mass Transfer pre unit of Mass of the Fine Structure
m_k'''	Net Rate of of Mass Production
Ma_{sr}	Markstein Number
P	Pressure
P_r	Reduced Pressure Term
Pr_t	Turbulent Prandtl Number
R	Ideal Gas Constant
r	Radius
Re_t	Turbulent Reynolds Number
S_d	Displacement Speed
S_L	Laminar Flame Speed
S_T	Turbulent Flame Speed
Sc_t	Turbulent Schmidt Number
t	Time
T'/T	Temperature Fluctuation Intensity
T'	Turbulent Temperature Fluctuations
T'^2	Turbulent Temperature Variance
Ta_f	Activation Temperature
u	Axial Velocity
u'	Turbulent Velocity Fluctuations
u'/S_L	Turbulent Velocity Ratio
V	Radial Velocity
v	Diffusive Velocity
W	Molecular Weight
X	Mole Fraction
Y	Mass Fraction
z	Distance
C_2H_4	Ethylene
C_2H_6	Ethane
C_3H_8	Propane
CH_4	Methane
CO	Carbon Monoxide
CO_2	Carbon Dioxide
H_2	Hydrogen
NO_x	Nitrogen Oxides
SO_x	Sulphur Oxides

Superscript

$\prime$	Fluctuating Value
*	Fine Structure Value
o	Surrounding Fluid Value

Subscript

0	Inlet Conditions
b	Burnt Conditions
fu	Fuel
GC	Global Consumption
i	Axial Direction
j	Radial Direction
jk	Binary Diffusion
k	Species k
k,m	Mixture-average Diffusion
L	Laminar
lam	Laminar
LC	Local Consumption
LD	Local Displacement
LE	Leading Edge
ox	Oxidiser
pr	Product
T	Turbulent
u	Unburnt Conditions
z	Grid Point z
0.05	Progress Variable of 0.05
0.5	Progress Variable of 0.5
actual	Actual Conditions
eff	Effective Value
ref	Reference Value
stoich	Stoichiometrc Conditions

Chapter 1

Introduction

1.1 Energy and the Environment

The reliance on fossil fuels, coupled with the effects of anthropogenic climate change, is one of humanity's greatest challenges for the foreseeable future. A transition towards renewable sources of power generation, in an effort to mitigate these problems, is not trivial. The frontrunners of the renewable sources are wind, solar, biomass and hydro, and are set to become the fastest growing sector of energy production in the next 25 years [1, 2]. However, these state-of-the-art technologies are not without their problems, which include intermittency for wind and solar, and environmental sustainability for biomass. Coupling this with the current low price of fossil fuels, combustion based power generation will remain necessary for the foreseeable future [1, 3]. BP's latest energy outlook [2] forecasts that 75% of the world's energy demand will be supplied by fossil fuels in 2035, down from 85% in 2015. The International Energy Agency (IEA) forecast a contribution of 62% from fossil fuels for the worlds electricity generation in 2040 under current policies [1]. A large influencing factor for this is the growing energy demand from developing countries, where fossil fuels play a major role due to the abundance of cheap indigenous resources. The energy consumption for Organization for Economic Cooperation and Development (OECD) countries peaked circa 2008 and only marginally changes over the forecast period, 2016-2040. On the other hand, rapidly developing countries like China and India are estimated to account for over half of the growth in world energy demand over the next two decades, as shown in Figure 1.1.

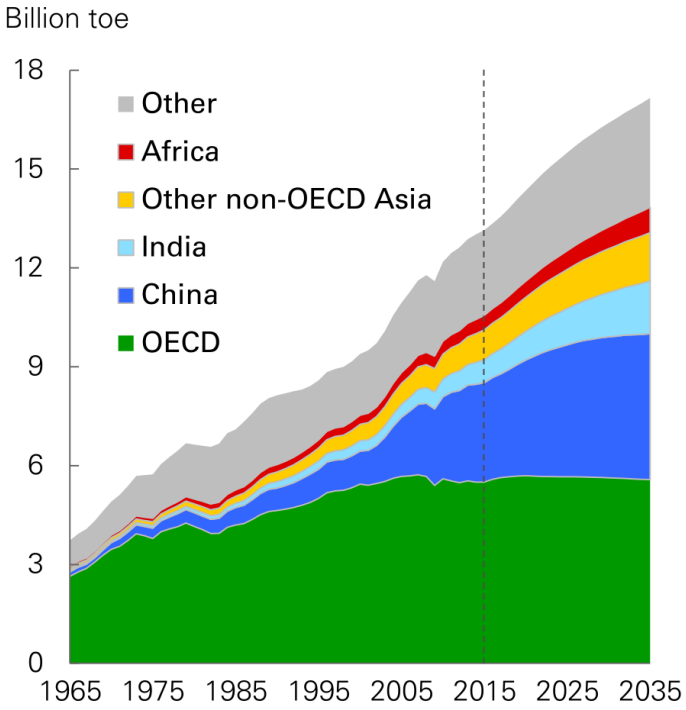

Figure 1.1: History and forecast of energy consumption by region [2]

Anthropogenic climate change as a result of emissions is a well-known issue. An increase in the concentrations of atmospheric greenhouse gases (GHG) such as methane and carbon dioxide (CH_4, CO_2), is the cause of increased mean global atmospheric temperatures, oceanic acidity, rising sea level and a reduction in the volume of ocean and land based ice sheets [4]. Fossil fuel combustion is the major contributing source of these emissions, accounting for 95% of CO_2 released into the atmosphere in 2007 [5]. In addition to these greenhouse gases, combustion pollutants such as nitrogen oxides (NO_x), sulphur oxides (SO_x) and particulate matter/soot pose serious risks to human health and can result in acid rain and urban smog. The 2015 Paris Agreement [6] was a major step in recent years to address these environmental challenges, with one of its major aims to hold the increase in the global average temperature to well below 2 °C above pre-industrial levels. In order to achieve this is has been found that, globally, 33% of oil reserves, 50% of gas reserves and 80% of current coal reserves must remain unused between 2010 and 2050 [7]. The agreement was signed by both developed and developing countries however the USA

withdrew in 2017. The EU has promised to reduce GHG emissions by at least 40% by 2030 compared to 1990 levels. China has proposed to reduce its peak carbon emissions per gross domestic product (GDP) by 60-65% before 2030. To acheive this fossil fuels are set to remain at the forefront of power generation well beyond the target dates of the Paris Agreement, so efficient combustion is key for reducing emission levels and ensuring any further consumption of fossil fuels in future is achieved in the least environmentally damaging manner possible. One approach for achieving this is the replacement of coal with natural gas. Gas is a much cleaner and efficient burning fuel when compared to coal due to the larger carbon contain in coal when compare to gas and highly effiecent nature of modern combine cycle power plantes respectively. This makes natural gas an obvious choice for future fossil fuel power generation sources. It is due to these clean and efficient burning characteristics that BP forecasts gas to become the second largest fuel source by 2035, overtaking coal by 2030 [2].

1.2 Gaseous Fuels: Composition and Sources

One of the earliest uses of gaseous fuels was in the widespread introduction of gas-fired street lamps. Currently most gas fuels are used for power generation. However, they are also employed for heating, cooking and a feedstock for industrial processes. These fuels can be categorised as natural or manufactured gases. Similar to other fossil fuels, natural gas has been formed over millions of years where decomposing biomass matter is exposed to intense heat and pressure under the Earth's surface. Natural gas is a blend of hydrocarbons mainly consisting of methane (CH_4) but commonly including other alkanes such as ethane (C_2H_6) and propane (C_3H_8) [8]. Small quantities of impurities are also commonly found in natural gas and can include carbon dioxide, nitrogen and hydrogen sulphide [9]. Natural gas is the most common form of gaseous fuel on Earth and is obtained by extracting if from reservoirs similar to those used for oil or through hydraulic fracturing to extract shale gas. The exact composition of the mixture depends on the location of the well site as can be seen in Figure 1.2.

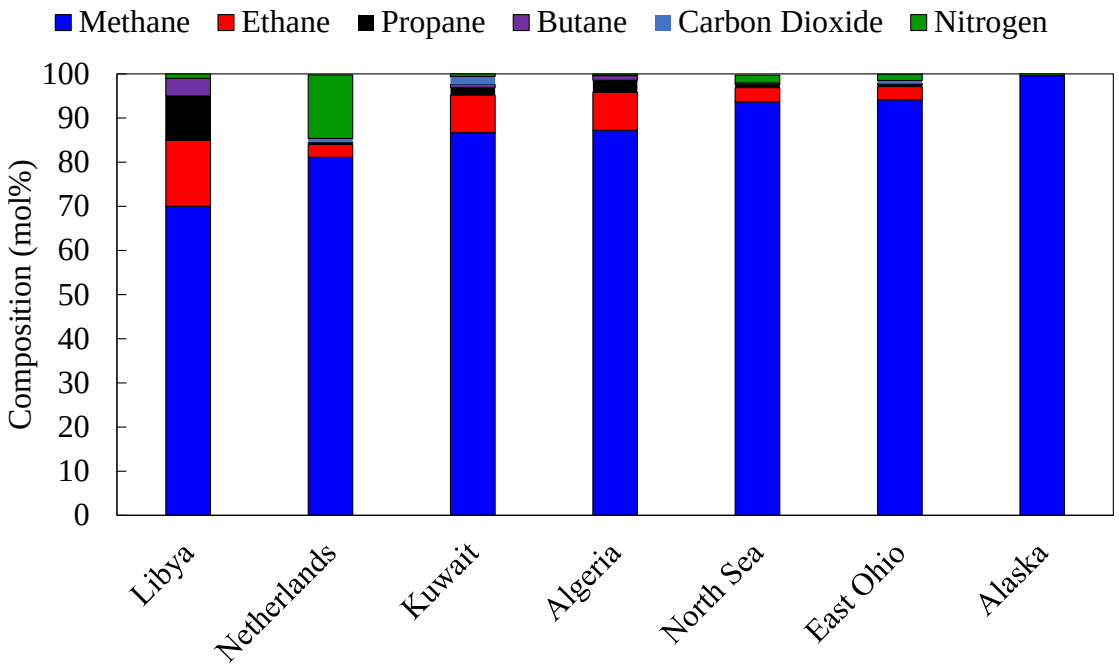

Figure 1.2: Composition of Natural gas from worldwide sources [10]

Many different types of manufactured gases exist, with the main varieties including coal gas, synthetic gas (syngas), hydrogen and biogas. Each of the manufactured gases have different compositions and manufacturing processes as shown in Table 1.1. Similar to natural gas the fractions of species making up the composition of manufactured gases depends on the feedstock. For example syngas primarily comprises of hydrogen (H_2) and carbon monoxide (CO), however these ratios can vary such that mixtures can comprise of 22-55% of CO, 9-62% of H_2 and 1-30% of CO_2 on a volumetric basis [9]. While gas turbines mainly use natural gas as a fuel source, one of the major advantages of gas turbines is their fuel flexibility. As a result, manufactured gaseous fuels are often used for power generation. However, this comes with considerable drawbacks due to the different combustion characteristics resulting from each fuels' composition which will be presented in Section 1.4.1.

Table 1.1: Various compositions, production processes and feedstock for common manufactured gases

Fuel Type	Fuel Components	Production Process	Feedstock	Ref
Syngas	H_2 / CO / CO_2	Gasification	Natural Gas, Coal, Biomass	[8]
Coal Gas	H_2 / CO / CH_4	Destructive Distillation	Coal	[8]
Hydrogen	H_2	Electrolysis	Water	[8]
		Steam-Methane Reforming	Natural Gas	[8]
Biogas	CH_4 CO_2	Anaerobic Digestion	Organic Waste	[11]

1.3 Technologies

Current natural gas fired power plants mostly employ stationary gas turbine combustors for power generation. In the EU alone, the predicted growth between 2010 and 2050 for gas fired power plant output reaches up to 290 Gigawatts (GW), more than doubling the 2010 capacity of 215 GW [12]. The majority of investments are being made in premixed combined cycle gas turbine (CCGT) plants. Both General Electric (GE) and Siemens have recently commissioned high capacity and efficient, $>$600 MW and $>$61% respectively, CCGT plants in Europe [13, 14]. Combined cycle gas turbine plants are a combination of gas fired and steam driven turbines and are capable of producing power in a more efficient manner when compared to the individual use of the turbines. The gas turbine accounts for roughly two-thirds of the total power, with the steam turbine supplying the remainder under full load conditions. The current state-of-the-art combustors for gas turbines is the Dry Low NO_x (DLN) system [15, 16]. The amount of NO_x produced by a gas turbine is highly influenced by the flame temperature. If the temperature within the combustor can be kept low, NO_x emission can be reduced. Unlike wet systems [17] which use water or steam to reduce the combustion temperature, DLN systems operate at relatively low temperature (1360 K firing temperature [15]) due to lean conditions where excess air is present, in the fuel/air ratio, for the combustion process to maintain the low temperature and therefore low NO_x [17]. To ensure lean conditions are uniform throughout the combustor, the air and fuel are premixed before entering the burning zone. If premixing is not achieved, combustion zones with higher fuel concentrations can lead to higher tem-

peratures, resulting in elevated NO_x levels. GE began development of the DLN1 system in the 1970s [15] and introduced the system commercially to industrial gas turbines in 1989 [18]. To accommodate larger capacity power plants and increasing combustor efficiency while ensuring CO and NO_x emission remain low, continuous improvements of combustion systems are required. Figure 1.3 shows the evolution of the Dry Low NO_x combustion system from its first iteration as DLN1 to the current combustor employed in GE gas turbines, DLN2.6+.

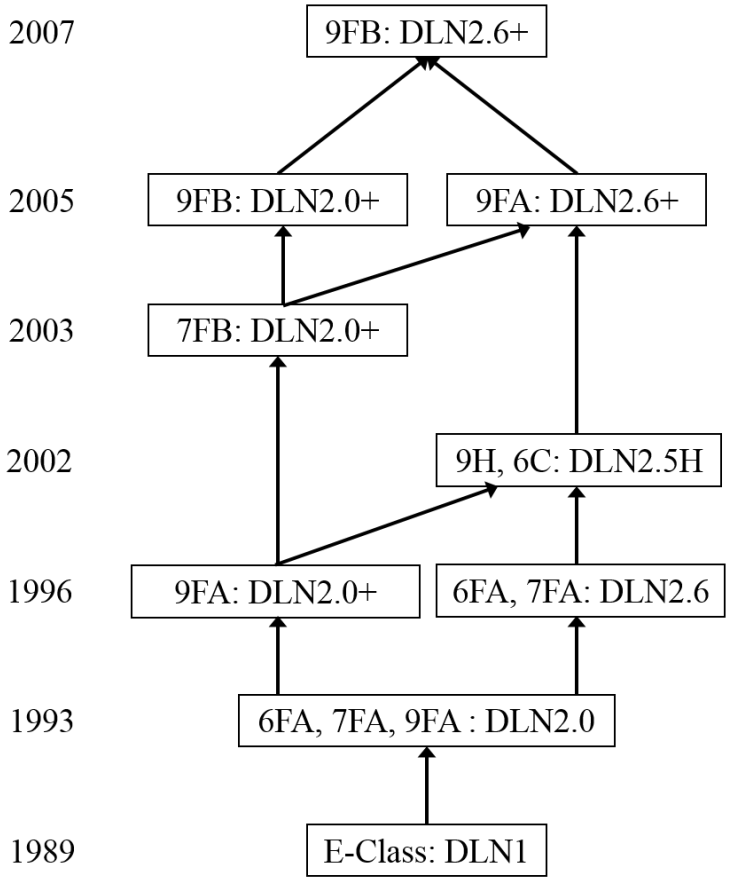

Figure 1.3: Evolution of Dry Low NO_x combustors and the associated class of turbine with each evolution of combustion system. The numbers and letters refer to the gas turbine frame size and class respectively [18]

The DLN2.0 combustion system shown in Figure 1.4, developed in 1993, is the basis for all subsequent combustor designs. The DLN2.0 system is a single-stage (one burning zone) dual mode (capable of operating under premixed or nonpremixed conditions)

combustor that can operate with both gaseous and liquid fuels. Figure 1.4 shows that the burning zone is formed in the space surrounded by the combustion liner and the face of the cap, as indicated by the red box. The fuel and air is thoroughly mixed in the premixer assembly and flows out of the assembly at high velocity before entering the burning zone where lean, low NO_x combustion takes place.

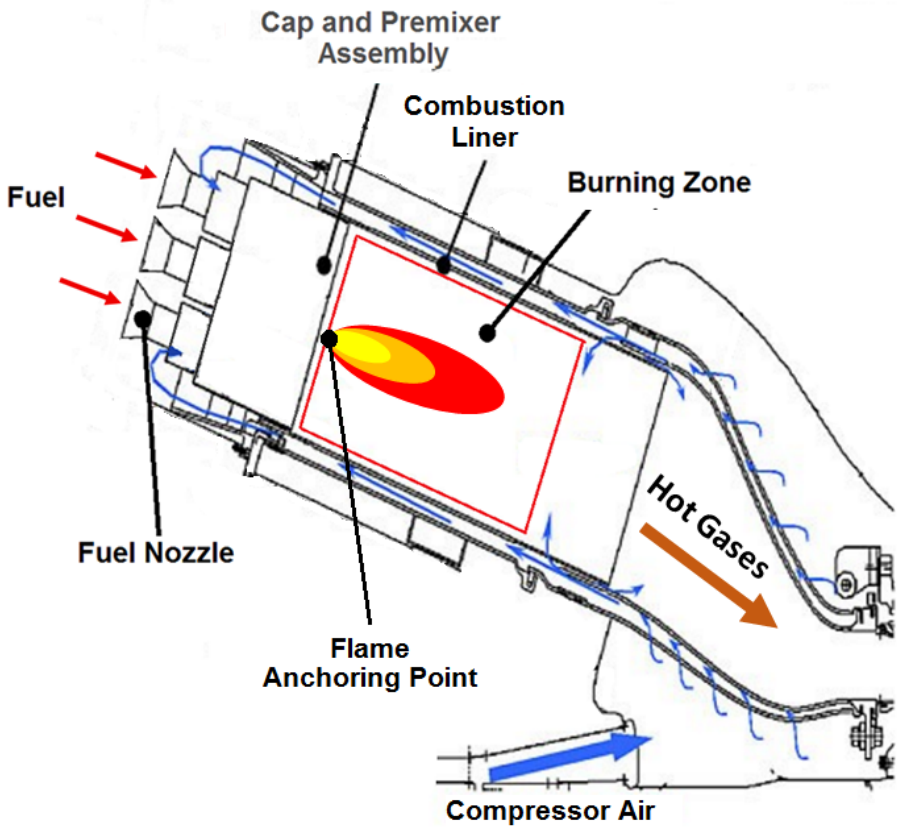

Figure 1.4: Simplified illustration of the DLN2.0 System [15]

Each iteration of the DLN combustion systems has sought to improve on both thermal efficiency and power output while addressing the need for low NO_x concentrations and the ability to operate with a wide variety of fuel compositions. The DLN2.6+ combustor is based on the original DLN2.0 design, with additional contributions from the DLN2.6 and DLN2.0+ systems. The additional centre nozzle, first introduced in the DLN2.6 system, was included to aid in flame stabilization and operational flexibility, while the swirling nozzle design approach for all premixers from the DLN2.0+ system was retained to promote stable ignition and part load operation [18]. Further advancements in gas tur-

bine combustor technology will be essential to meet the ever increasing high performance and low emissions requirements of modern power plants. Although major progress has been made in gas turbine technologies, designers are still faced with significant challenges when trying to further improve combustor design.

1.4 Challenges

The challenges associated with the future of power generation in natural gas power plants include:

1. Fuel Flexibility: The ability to operate over a range of fuel types (H_2, syngas, CH_4, natural gas) and mixture compositions. [19]

2. Part Load: The necessity to operate efficiently, ensuring low emissions, at a percentage of the design load

3. Fast Ramp: The capability of quick ramp up from zero/partial load to full load [9]

4. Low NO_x: The requirement to ensure NO_x emissions remain low to meet stringent regulations while gas turbine thermal efficiencies increase as a result of higher combustor firing temperature.

1.4.1 Fuel Flexibility

Increasing demand for gaseous fuels means that new and alternative fuel sources will be required in the years to come. Although premixed combustion has allowed for significant reductions in emissions, variable fuel composition can cause issues within premixed combustors such as the DLN systems previously discussed [19]. The combustion properties of a fuel mainly depend on its composition. Altering this composition can lead to a flame with vastly different burning characteristics. In addition to fuel composition, the location of the power plant also has an effect on the burning characteristics of the gas turbine combustor. The properties of the air required to oxidise the fuel in the combustor can vary with altitude and temperature, affecting density and humidity, and subsequently

water content, making the issue of fuel flexibility even more complex. If fuel flexibility is not accounted for, gas composition variability can have significant and often negative effects on gas turbine combustors such as:

Blowout, which refers to when the flame is no longer attached to where it should be anchored and is physically blown out. When the flame is blown out, an expensive shut-down and relight procedure is required, resulting in a loss of power generation during the period [20]. This phenomenon occurs when the residence time in the combustion zone is shorter than the time required for combustion to occur (e.g. reaction time). Instabilities can easily occur in the flame in gas turbines operating at extremely lean conditions, to ensure NO_x formation remains low, resulting in lean blowout (LBO). The conditions at which LBO occurs can be affected by a number of parameters relating to the configuration of the combustor and operating conditions [21]. Blowout also becomes an issue when the fuel composition is varied, as fuels with similar heating values at similar conditions can have chemical kinetic time scales up to an order of magnitude different [19].

Flashback is the opposite to blowout, in which the flame travels upstream, away from where it should be anchored and into the premixer assembly which is not designed for high temperatures. As a result, serious damage can be caused to the premixing tubes contained in the premixer assembly. This occurs when the flow velocity is not substantially greater than the turbulent flame speed. Fuels with similar heating values can have flame speeds that vary by a factor of five, making flashback a major issue when considering fuel flexibility. [19]

In addition to these issues, alternative fuels can result in different and often higher pollutant emissions characteristics due to different flame temperatures, shapes and velocities. Considering the fact that new wells and alternative sources may have different composition to current gas mixtures, the ability to burn a wider range of fuel types is essential for the development of future gas turbines.

1.4.2 Gas Turbine Load Conditions

Along with fuel flexibility, load flexibility also has to be considered. Turndown is the ability of an engine to operate over a range of loads while still ensuring sufficiently low emissions and high efficiency levels [9]. Transient response is the ability of the turbine to respond to changing grid demand through an increase/decrease in engine load over a short period of time [9]. For growing penetrations of intermittent and variable output renewable sources, gas turbines are often used to supply the deficit in energy demand, meaning gas turbines capable of effective turndown and transient response are essential. Under certain transient load conditions, similar to fuel flexibility, blowout and flashback can become an issue and lead to the same problems as previously discussed [20, 22].

1.4.3 Emissions

Another major consideration for gas turbine design is ensuring low pollutant emissions while operating with high fuel flexibility. The most advanced GE dry low NO_x system, DLN 2.6+, is capable of emissions as low as 5 parts per million ppm NO_x at optimal conditions [23]. However the largest and most efficient CCGT plant [13], which employ the 9HA.01 turbines, can produce up to 25 ppm of NO_x emissions depending on gas turbine load [15]. These low emissions are achieved by operating at lean conditions, however designers must be careful to avoid combustion instabilities associated with these conditions which can cause pulsations in the combustor leading to LBO. Therefore the engine must operate in a regime between low NO_x formation and combustion instabilities [24]. CO and unburned hydrocarbons (UHC) emissions are less of an issue, in gas turbines, for all but very low loads for steady state combustion. However at startup and ramp up conditions these emissions must be considered as their formation can be significantly higher [25]. With a need for large scale plants and ever more stringent regulatory restrictions of emissions expected, further improvements to the already advanced technologies will be required. This is important as the original equipment manufacturer (OEM) that can produce the lowest emission system may have an edge in the competitive market.

Individually each of these challenges will prove difficult to accomplish, while the necessity of coupling them only adds to the complexity. However, these challenges must be overcome to reduce the impact of anthropogenic climate change and meet the growing energy demand, to achieve this gas turbine technology must improve.

1.5 Goals and Overview of *This Thesis*

The previous sections stated how fossil fuels will likely remain at the forefront of electrical power generation for the foreseeable future. However, with anthropogenic global warming becoming one of humanity's greatest challenges, the need to further refine current gas turbine technologies is essential to avoid further environmental and health damage. In order to achieve this, a greater level of detailed understanding of combustion is required. Turbulent flame speed (S_T) is an important property within turbulent premixed flames, influenced by the chemistry within the flame, flow properties, and turbulent and laminar transport of heat, species and temperature [26]. S_T indicates the level of reactivity within the flame, which has a direct impact on the length and spatial distribution of the flame in the combustor, as well as the flame's tendency to flashback [27]. For this reason, S_T is used as an aid to estimate chemical reactivity within the combustor as a function of key parameters such as inlet temperature, pressure, equivalence ratio and fuel composition. In gas turbine development, results for turbulent flame speed obtained at atmospheric pressure are frequently extrapolated to engine conditions.

Due to the widespread use of premixed combustion, a significant amount of research has been carried out on turbulent flame speed. As shown in Section 2.5, these studies include extensive analytical [28–31], experimental [32–35] and computational [36, 37] studies, as well as literature reviews [38–41]. Current methods of predicting S_T fall into two categories: (1) analytical correlations based on laminar flame properties, turbulent flow properties and dimensionless numbers, and (2) computational approaches that use models to describe the physical phenomena associated with turbulence and combustion. Correlations are generally single line expressions that typically include no turbulent chem-

istry interactions and define a single value for turbulent flame speed. The computational approaches model the entire burning process, the level of complexity in the turbulence and chemistry models employed relate directly to the numerical expense and the user's understanding of the models and phenomena.

In an effort to improve on the drawbacks of current methods which are detailed in the next chapter, two new models for the prediction of premixed turbulent flame speed have been developed in this work: (1) a correlation (empirical model) with adjustable parameters optimized using a large experimental database of S_T values, and (2) a one-dimensional (1D) freely propagating turbulent flame speed model implemented in Cantera [42]. A Nelder-Mead simplex direct search method [43] and ≈ 335 data points, over a wide range of conditions, have been employed to define seven parameters in the new empirical model for defining S_T. Current versions of Cantera focus on laminar combustion. In comparison to laminar flow, turbulent flow is highly complex, characterised by (1) temporal fluctuations in flame properties, (2) increased rates of transport of species, momentum and heat, and (3) spatially non-uniform and locally-enhanced chemical reactivity. Aspects of the widely used k-ε turbulence model have been selected to be used in the Cantera S_T solver for modelling the temporal fluctuations statistically. The interaction between the flow and chemistry within the flame, which causes spatial non-uniformity is handled using the Eddy Dissipation Concept [44]. In addition to these interactions, the turbulence within the flame causes temporal fluctuations (T') in the mean temperature $(\overline{T})$. As a result, the mean chemical reaction rate $(\dot{\omega})$ used to define species consumption and production is modelled using a Taylor series expansion of $\dot{\omega}$ around the mean temperature.

The following treatise is arranged as follows:

Chapter 2 reviews literature relevant to this research. It details: (1) the theoretical basis behind computational methods used to describe non-reactive and reactive flows, (2) the development and background of empirical correlations used to predict S_T, (3) an in-depth review of previous work done on the prediction of premixed turbulent flame speed using experimental and computational approaches, and (4) the research

need for this work.

Chapter 3 describes the comparison of fifteen literature turbulent flame speed correlations against experimental data, in which a mean absolute percentage error (MAPE) is used to assess accuracy over a range of pressures and fuel types. A newly developed empirical correlation is also described in detail and examined alongside the literature correlations. A further comparison between the four most accurate literature correlations from the previous study and the new empirical correlation is then carried out using the original author's adjustable parameters. Finally, the adjustable parameters for each correlation reported in the literature, are optimized to reduce the MAPE over the range of experimental test data. The accuracy of the correlations are tested using a MAPE and by assessing each correlation's ability to match trends in the experimental data.

Chapter 4 presents the development of a 1D predictive model for determining premixed turbulent flame speed. The solver is developed from the laminar flame speed model within the well-known Cantera software. A theoretical background to Cantera is presented followed by detailed descriptions of the modifications that were made to the existing version of Cantera. With the addition of the turbulent modifications the robustness of the original solver has suffered, so the best practice for implementation of the S_T is described. This is followed by a validation of the new predictive model through a comparison of predicted results to a set of experimental data as well as the five correlations from the previous chapter. The chapter closes with a discussion of the results and key findings related to the development of the model.

Chapter 5 summarizes the main outcomes and conclusions from the previous chapters. This leads to recommendations for potential future work.

Chapter 2

Literature Review

2.1 Introduction

Chapter 1 showed how combustion is essential for electrical power generation and is set to continue being so for many decades. Essentially all combustion in practical devices takes place within turbulent flow, from domestic boilers to industrial scale gas turbines. This is due to the increased reactivity associated with turbulent combustion and the resulting increase in power output of the combustion device. As previously discussed, numerical modelling is essential for designing combustion devices. Property distribution for laminar flames can be accurately solved using first principles [45]. Cantera and other solvers are regularly employed to compute the solution of a system of non-linear partial differential equations, effectively modelling various forms of laminar combustion. Although the same first principles approach can be used to describe turbulent reacting flow, the chaotic nature of turbulence makes it too computationally expensive to use them for practical flows. In order to reduce computational expenses, mathematical models are used to simplify the description of the governing equations for reacting flow. CFD for modelling turbulent reactive flows is generally divided into two categories: (1) a turbulence model used to predict the flow of an inert gas, and (2) a combustion model consisting of the necessary additional physics and chemistry to describe the presence of chemical reactions in the flow. Both of which are needed to model turbulent combustion in CFD. The following sections will discuss the theory of chemically non-reactive and reactive models employed

to predict turbulent premixed flames.

2.2 Chemically Non-Reactive Flow

Turbulence is chaotic by nature, occurring when a fluids viscous forces can no longer dampen the instabilities present in the flow, resulting in the fluid velocity exhibiting random temporal fluctuations at each point in the flow. The transition from laminar to turbulent flow is characterised using the Reynolds number ($\mathrm{Re}_L = \frac{uL}{\upsilon}$) where u and L are characteristic velocity and length relating to the flow, and υ is kinematic viscosity of the fluid. The transition occurs when Re_L exceeds a certain geometry dependent value. Once the flow is turbulent, solving the Navier-Stokes equations, shown in Equations 2.1 to 2.3, becomes extremely practically difficult. This is due to the large number of length and time scales present in the flow as well as the coupled nature of the equations.

Continuity:

$$\frac{\partial \rho}{\partial t} + \frac{\partial \rho u_i}{\partial z_i} = 0 \tag{2.1}$$

Momentum:

$$\frac{\partial \rho u_i}{\partial t} + \frac{\partial \rho u_i u_j}{\partial z_j} = \frac{\partial \tau_{ij}}{\partial z_i} - \frac{\partial p}{\partial z_j} \tag{2.2}$$

Energy:

$$\frac{\partial \rho h_s}{\partial t} + \frac{\partial \rho u_i h_s}{\partial z_i} = \frac{Dp}{Dt} + \frac{\partial}{\partial z_i}\left(\lambda \frac{\partial T}{\partial z_i}\right) + \tau_{ij}\frac{\partial u_i}{\partial z_j} \tag{2.3}$$

where ρ is the fluid density, t is time, z is distance, τ is viscous stress, p is pressure, h is the enthalpy, T is temperature, λ is thermal conductivity and subscripts i and j refer to the axial and radial directions within the flow with respect to z. Equations 2.1 to 2.3 are used to define the flow properties in the x-direction, denoted by subscript i. An additional two sets of continuity, momentum and energy equations are solved for the y- and z- directions, denoted by subscripts j and k in order to complete describe a three-dimensional flow. Various mathematical models have been used to solve the Navier-Stokes equations, each with different levels of simplifications and computational expense. These models are known as closure models and can generally be grouped into three categories based on the

size of the spatial frequencies resolved by each approach. The three methods for solving the Navier-Stokes equations are described as:

- Reynolds-averaged Navier-Stokes (RANS): solves the time-averaged equations for all quantities in the flow.
- Large Eddy Simulations (LES): simulates the largest scales of turbulence present within the flow, and uses subgrid closure rules to model the smaller turbulent eddies.
- Direct Numerical Simulations (DNS): resolves the full instantaneous Navier-Stokes equations without any need for closure models.

2.2.1 Reynolds-averaged Navier-Stokes

As only the Reynolds-averaged properties of the flow are solved for, the RANS approach is computationally inexpensive compared to LES and DNS and for this reason is one of the most popular CFD approaches. In 1895 Reynolds [46] proposed a simple statistical approach whereby the fluctuating quantities were divided into mean and fluctuating parts characterised by $\tilde{\phi} = \bar{\phi} + \phi'$, where the overbar $(\bar{\phi})$ denotes the average and the term superscripted with a prime, (ϕ') denotes the fluctuation of the scalar property (ϕ). By applying this decomposition to the Navier-Stokes equations, a set of Reynolds-averaged Navier Stokes equations are produced. When solved, they predict a time-averaged flow field rather than an exact turbulent flow field at a point in time. With time averaging, an unclosed correlation between density, and velocity fluctuation $(\overline{\rho' u_i'})$ appears and requires modelling, which is difficult in CFD codes. For combustion process where an incompressible assumption cannot be made and density fluctuations are non-zero, an alternative approach is therefore needed. The mass-weighted averages or Favre-averaging, where $\widetilde{\phi} = \frac{\overline{\rho\phi}}{\overline{\rho}}$, and any quantity can be decomposed into $\phi = \widetilde{\phi} + \phi''$, where $\widetilde{\phi''} = 0$, is preferred for these conditons. The Favre-average Navier Stokes equations can be seen in Equations 2.4 to 2.6.

Continuity:

$$\frac{\partial \overline{\rho}}{\partial t} + \frac{\partial \overline{\rho}\widetilde{u_i}}{\partial z_i} = 0 \tag{2.4}$$

Momentum:

$$\frac{\partial \overline{\rho}\widetilde{u_i}}{\partial t} + \frac{\partial \overline{\rho}\widetilde{u_i}\widetilde{u_j}}{\partial z_j} = \frac{\partial}{\partial z_i}\left(\tau_{ij} - \overline{\rho}\widetilde{u_i''u_j''}\right) - \frac{\partial \overline{p}}{\partial z_j} \tag{2.5}$$

Energy:

$$\frac{\partial \overline{\rho}\widetilde{h_s}}{\partial t} + \frac{\partial \overline{\rho}\widetilde{u_i}\widetilde{h_s}}{\partial z_i} = \overline{\frac{Dp}{Dt}} + \frac{\partial}{\partial z_i}\left(\overline{\lambda\frac{\partial T}{\partial z_i}} - \overline{\rho u_i'' h_s''}\right) + \overline{\tau_{ij}\frac{\partial u_i}{\partial z_j}} \tag{2.6}$$

By using this approach, new unknowns have been introduced which include six Reynolds stress components ($\overline{\rho}\widetilde{u_i''u_j''}$) and three Reynolds enthalpy flux components ($\overline{\rho u_i'' h_i''}$). The number of unknowns is greater than the number of equations to be solved. This issue is referred to as the Turbulence Closure Problem. To solve the equation set, additional expressions are introduced using turbulence models. For RANS approaches, these can generally be classified as Eddy Viscosity models or Reynolds Stress models. These can also be referred to as first and second order models, respectively.

Eddy Viscosity models include zero- [47], one- [48] or two- [49] equation models and were some of the first closure approaches developed for CFD. In these models, an analogy between laminar and turbulent flow is made, where it is assumed that the average turbulent flow field is similar to the corresponding laminar flow with additional terms for turbulent viscosity and thermal conductivity. The turbulent stresses and fluxes are then expressed as functions of these new terms. The definitions used to describe the new turbulent properties depends on the Eddy Viscosity model employed. The most common approaches are known as the Boussinesq approach [50] which defines the Reynolds stress as shown in Equation 2.7 and the gradient transport model [51] for the Reynolds fluxes as described in Equation 2.8.

$$\overline{\rho u_i'' u_j''} = \overline{\rho}\widetilde{u_i''u_j''} = -\mu_t\left(\frac{\partial \widetilde{u_i}}{\partial z_j} + \frac{\partial \widetilde{u_j}}{\partial z_i} - \frac{2}{3}\delta_{ij}\frac{\partial \widetilde{u_k}}{\partial z_k}\right) + \frac{1}{3}\overline{\rho}\sum_{k=1}^{3}\widetilde{u_k''u_k''} \tag{2.7}$$

$$\overline{\rho u_i'' u_j''} = \overline{\rho} \widetilde{h'' u''} = -\frac{\mu_t}{\mathrm{Pr}_t} \frac{\partial \widetilde{h}}{\partial z_j} \tag{2.8}$$

where the subscript k refers to the z-direction, δ_{ij} is the Kronecker delta, Pr_t is the turbulent Prandtl number and μ_t is the turbulent dynamic viscosity. As the name suggests, the Eddy Viscosity model is used to calculate μ_t, which is assumed to be an isotropic scalar quantity. Since a two-equation model, the turbulent kinetic energy-turbulent energy dissipation $(k\text{-}\varepsilon)$ model, is used in this work further discussion on the model will take place in Section 4.3.3.

In the Reynolds Stress model, the individual components of the Reynolds stresses are computed. Compared to the isotropic approach used by the first order models, the Reynolds Stress model can account for the directional effects of the Reynolds stresses. However, this has the downside of requiring a larger number of partial differential equations. The Reynolds stresses transport expression is shown in Equation 2.9, in which the second order model involves solving the turbulent diffusive transport (J_{ij}), pressure strain correlation (Π_{ij}) and the stress dissipation rate (ε_{ij}).

$$\frac{\partial \overline{\rho u_i'' u_j''}}{\partial t} + \frac{\partial \widetilde{u_k} \overline{\rho u_i'' u_j''}}{\partial z_i} = P_{ij} - \overline{\rho} \varepsilon_{ij} - \frac{\partial J_{ij}}{\partial z_i} + \Pi_{ij} - \overline{u_j''} \frac{\partial \overline{p}}{\partial z_i} - \overline{u_i''} \frac{\partial \overline{p}}{\partial z_j} \tag{2.9}$$

In the Reynolds stress transport equation, the J_{ij}, Π_{ij} and ε_{ij} terms require closure. For the turbulent transport term, this is calculated using the gradient diffusion hypothesis to model the turbulent diffusive transport as:

$$J_{ij} = \frac{\partial \overline{\rho u_i'' u_j'' u_k''}}{\partial z_i} = \frac{\partial}{\partial z_i} \left(C_s \frac{k}{\varepsilon} \widetilde{u_i'' u_m''} \frac{\partial \overline{u_j'' u_k''}}{\partial z_m} \right) \tag{2.10}$$

where C_s is a constant with a value of 0.22 and z_m denotes the Cartesian space co-ordinates with $m = 1, 2, 3$.

The pressure fluctuations act to redistribute the turbulent stresses resulting in more isotropic turbulence. They are described by the redistribution tensor Π_{ij}. These effects can be divided into slow and rapid portions as shown below, along with the pressure-diffusion term. The superscripts H and I denote homogeneous and inhomogeneous terms, with the S and R terms denoting slow and rapid parameters. An expansion of the terms in Equation 2.11 can be found in [52].

$$\Pi_{ij} = \phi_{ij}^{(RH)} + \phi_{ij}^{(RI)} + \phi_{ij}^{(SH)} + \phi_{ij}^{(SI)} + d_{ij}^{(p)} \tag{2.11}$$

Finally the stress dissipation can be described using a simple isotropic model to define ε_{ij} with an additional transport equation for the dissipation rate as shown in Equations 2.12 and 2.13

$$\varepsilon_{ij} = \frac{2}{3}\delta_{ij}\varepsilon \tag{2.12}$$

$$\frac{\partial}{\partial z_i}(\rho\varepsilon u_i) = \frac{\partial}{\partial z_j}\left[\left(\mu + \frac{\mu_t}{\sigma_\varepsilon}\right)\frac{\partial \varepsilon}{\partial z_j}\right] C_{\varepsilon 1}\frac{1}{2}P_{ij}\frac{\varepsilon}{k} - C_{\varepsilon 2}\rho\frac{\varepsilon^2}{k} \tag{2.13}$$

where $C_{\varepsilon 1} = 1.44$, $C_{\varepsilon 1} = 1.92$, $\sigma_\varepsilon = 1.0$ and P_{ij} is the production term.

RANS approaches are some of the most widely used turbulence models in the literature and have shown to provide adequte results for turbulent premixed flames [53–55] however when RANS is unable to describe the turbulent flow in sufficient detail alternative approaches are needed.

2.2.2 Large Eddy Simulation

The objective of Large Eddy Simulation is to compute the largest turbulent structures, typically those larger than the computational mesh, directly within the flow and to model the smaller turbulent eddies. Although computationally more expensive than RANS, LES is better equipped to simulate the physics present in the flow. As large eddies are dependent on the geometry, and the smaller scales are more universal, the large scales can be

accounted for explicitly, and a subgrid-scale model can be used to implicitly solve for the small scale eddies. To differentiate between the large and small scale eddies, LES uses a filtering approach to determine which turbulent scales are simulated and which are modelled. Variables can be filtered in the spectral domain, in which components greater than a given frequency are ignored, or in the physical domain. Equation 2.14 is used to define the filter quantity, using the mass-weighted Favre approach.

$$\overline{\rho}\widetilde{\phi}(z) = \int \rho\phi\left(z'\right)\Phi\left(z-z'\right)dz' \tag{2.14}$$

This results in $\phi = \widetilde{\phi} + \phi''$ where $\widetilde{\phi}$ is the resolvable scale and ϕ'' is the subgrid-scale that requires modelling. Unlike RANS averaging, the averaged filtered quantity ($\overline{\phi''}$) does not equal zero. To determine which terms are filtered the following LES techniques are used:

- Cut-off filter (Spectral Domain)

$$\Phi(k) = \begin{cases} 1 \text{ if } k \leqslant k_c = \pi/\Delta \\ 0 \qquad \text{otherwise} \end{cases} \tag{2.15}$$

  where k is the spatial frequency number. The cut off approach retains scales larger than 2Δ, where Δ is the filter size.

- Box filter (Physical Domain)

$$\Phi(z) = \Phi(z_1, z_2, z_3) = \begin{cases} 1/\Delta^3 \text{ if } |z_m| \leqslant \Delta/2, \text{ m = 1,2,3} \\ 0 \qquad\qquad \text{otherwise} \end{cases} \tag{2.16}$$

  where z_1-z_3 correspond to the spatial coordinates of the location of z. This method of filtering relates to an averaging over a cube side length of Δ. In most practical and commercial implementations of LES, the box filters approach is used.

- Gaussian filter (Physical Domain)

$$\Phi(z) = \Phi(z_1, z_2, z_3) = \left(\frac{6}{\pi\Delta^2}\right)^{\frac{3}{2}} \exp\left[-\frac{6}{\Delta^2}\left(z_1^2 + z_2^2 + z_3^2\right)\right] \tag{2.17}$$

By using one of the above filtering techniques, the instantaneous governing equations can be filtered, which leads to the following LES transport equations:

Continuity:

$$\frac{\partial \overline{\rho}}{\partial t} + \frac{\partial \overline{\rho}\widetilde{u_i}}{\partial z_i} = 0 \tag{2.18}$$

Momentum:

$$\frac{\partial \overline{\rho}\widetilde{u_i}}{\partial t} + \frac{\partial \overline{\rho}\widetilde{u_i}\widetilde{u_j}}{\partial z_j} = \frac{\partial}{\partial z_i}\left(\tau_{ij} - \overline{\rho}(\widetilde{u_i u_j} - \widetilde{u_i}\widetilde{u_j})\right) - \frac{\partial \overline{p}}{\partial z_j} \tag{2.19}$$

Energy:

$$\frac{\partial \overline{\rho}\widetilde{h_s}}{\partial t} + \frac{\partial \overline{\rho}\widetilde{u_i}\widetilde{h_s}}{\partial z_i} = \overline{\frac{Dp}{Dt}} + \frac{\partial}{\partial z_i}\left(\overline{\lambda \frac{\partial T}{\partial z_i}} - \overline{\rho}(\widetilde{u_i h_s} - \widetilde{u_i}\widetilde{h_s})\right) + \overline{\tau_{ij}\frac{\partial u_i}{\partial z_j}} \tag{2.20}$$

In these equations the unresolved Reynolds stresses $\left(\widetilde{u_i u_j} - \tilde{u}_i \tilde{u}_j\right)$ and fluxes $\left(\widetilde{u_i h_s} - \tilde{u}_i \widetilde{h_s}\right)$ require subgrid-scale turbulence models. Similar to the RANS approach, the Reynolds fluxes can be handled using a gradient assumption, with the subgrid viscosity being estimated from the unresolved Reynolds Stress models. These subgrid-scale turbulence models have been derived assuming constant density. This assumption is not appropriate for reactive flows due to the presence of large temperatures and subsequent density variations [56]. Nevertheless constant density subgrid-scale models are regularly employed to describe reactive flows [57]. The most common LES closure models include:

2.2.2.1 Smagorinsky Model

Popular for its simplicity, the Smagorinsky model [58] expresses the unresolved momentum fluxes using the Boussinesq assumption:

$$\tau_{ij} = -\upsilon_t \left(\frac{\partial \overline{u}_i}{\partial z_j} + \frac{\partial \overline{u}_j}{\partial z_i}\right) = -2\upsilon_t \overline{S}_{ij} \tag{2.21}$$

where τ_{ij} is the subgrid stress tensor, $\overline{S}_{ij}$ is the rate of strain tensor and υ_t is the subgrid-

scale viscosity, defined as

$$\upsilon_t = (C_s\Delta)^2\left(\overline{S}_{ij}\overline{S}_{ij}\right)^{1/2} \tag{2.22}$$

The downside of the Smagorinsky model is the geometry dependency of the constant C_s, as well as the fact that it is too dissipative [56].

2.2.2.2 Scale Similarity Model

The Scale Similarity model [59] assumes that the unresolved Reynolds stresses, $\left(\widetilde{u_i u_j} - \tilde{u}_i\tilde{u}_j\right)$, are generally controlled by the largest unresolved structures that can be related to the smallest resolved structures. This leads to the following definition:

$$\tau_{ij} = \overline{\overline{u}_i\overline{u}_j} + \overline{\overline{u}_i}\,\overline{\overline{u}}_j \tag{2.23}$$

2.2.2.3 Germano Dynamic Model

The Germano Dynamic Model [60] is a more general approach for turbulence closure at the subgrid level. The model can be viewed as a modified version of the Smagorinsky Model that allows for C_s to vary in time and space. C_s is calculated locally at each time step using two filters, denoted by superscript r and superscript t, which refer to the grid and test filter, respectively. The Germano identity (L_{ij}) is then used to relate the two subgrid-scale stress terms, allowing for the C_s term to be defined as:

$$C_s^2 = -\frac{1}{2}\frac{L_{ij}^* S_{ij}^r}{M_{ij}S_{ij}^r} \tag{2.24}$$

where L_{ij}^* is the anisotropic part of L_{ij}, and M_{ij} can be defined as:

$$M_{ij} = (\Delta)^2\left|S^{rt}\right|S_{ij}^{rt} - (\Delta^r)^2\left(|S^r|\,S_{ij}^r\right)^t \tag{2.25}$$

The Germano Dynamic Model has been found to be very efficient in a wide range of applications and can be extended to encompass compressible flow. When implemented, to

avoid negative numbers and numerical instabilities, C_s is not calculated locally but rather averaged in a homogeneous direction.

2.2.3 Direct Numerical Simulation

Direct Numerical simulation is the most computationally expensive numerical approach available but it also resolves the entire range of temporal and spatial scales of turbulence in the flow, accurately describing the physics of fluid dynamics. To achieve this, the DNS approach solves the instantaneous Navier-Stokes equations, shown in Equations 2.1 to 2.3, without the need for any turbulence models. For this to be possible, the spatial scales of the turbulent flow must be resolved on the computational mesh from the integral length scale (Λ), associated with the eddies containing the majority of the flow's kinetic energy, to the smallest length scale, the Kolmogorov scale (η). To ensure these scales can be resolved, the mesh in any given direction must have a number of mesh points (N) and increments (h) such that $Nh > \Lambda$, so the integral length scale is within the computational mesh and $h \leqslant \eta$ to satisfy the resolution requirements for the Kolmogorov scales. In addition to the spatial requirements, solution integration is achieved using an explicit method. For this reason, the integration time step (Δt) must be sufficiently small such that a fluid particle can only travel a fraction of h over Δt. Using the definition of turbulent Reynolds number (Re_t), where $Re_t^{3/4} \approx \frac{\Lambda}{\eta}$ [56], it can be seen that the number of time steps grows as a power law of the Re_t and the computational cost is high even for small Reynolds numbers. For the majority of commercial applications, the computational expense is greater than the capacity of the most powerful computer currently available. The additional physics required to describe reactive flow increases this expense therefore making DNS currently impractical for industrial combustor design with complex geomerty but has been used for smaller simplified systems [61, 62].

2.3 Chemically Reactive Flow

For premixed combustion to occur, the fuel and oxidiser must be sufficiently mixed. If the reactants are not fully mixed, partially premixed or non-premixed combustion will take place. Once completely mixed, ignition will occur if the ratio of fuel to oxidiser is within the flammability limits and a sufficiently high local mixture temperature is present. For spark ignition engines the initial heat required for the reaction to occur is supplied via a spark from a spark plug. In gas turbines recirculation of hot burnt gases sufficiently raises the mixture temperature for reaction to occur. For a methane-air mixture, a simplified reaction path from the fuel, CH_4, to the complete combustion product carbon dioxide (CO_2) can be seen in Figure 2.1.

$$CH_4 \rightarrow CH_3 \rightarrow CH_2O \rightarrow HCO \rightarrow CO \rightarrow CO_2$$

Figure 2.1: Simplified reaction path of CH_4 oxidation

A single step chemical reaction can be used to globally describe the complete combustion between methane and air (oxygen (O_2) and nitrogen (N_2)) to produce mainly water vapour (H_2O) and CO_2, as well as aiding in the definition of the air to fuel ratio (AFR) and equivalence ratio (ϕ).

$$CH_4 + 2(O_2 + 3.76N_2) \rightarrow CO_2 + 2H_2O + 7.52N_2$$

AFR is used to define the ratio between the number of moles of air and fuel (CH_4). Equation 2.26 shows that for stioichiometric conditions, where complete burning of the fuel occurs, leaving no excess oxygen, the AFR is approximately 9.52

$$AFR_{stoich} = \frac{\text{moles of air}}{\text{moles of } CH_4} \approx 9.52 \tag{2.26}$$

The equivalence ratio can be defined using Equation 2.27 where $\phi > 1$ is refered to as rich conditons and $\phi < 1$ is refered to as lean condtions.

$$\phi = \frac{AFR_{stoich}}{AFR_{actual}} \tag{2.27}$$

where subscripts *stoich* and *actual* refer to stoichiometric and actual conditions respectively. For combustion reactions in practical flames, a single step chemical reaction is insufficient to describe the complex reactive process present [63]. For a simple methane/air flame, a minimum of tens of species and hundreds of reactions are required to computationally describe the chemistry in the flame. Chemical kinetic mechanisms are used to determine the reactions, transport and thermodynamics of a flame, with mechanisms development being a considerably large area of research in the combustion community. As the size of the fuel molecule or the number of species making up the fuel increases so too does the size and complexity of the chemical kinetics mechanism, with mechanisms as large as 484 species and 19,341 reactions being used to describe the combustion of fuel with up to 12 carbons atoms in the fuel molecule (C_{12} fuel) [64].

2.3.1 Characteristics of Laminar Premixed Combustion

In laminar flames, the burning velocity and thickness of the flame front are controlled by transport processes. On a molecular level concurrent thermal conductivity and species radical diffusion are the main influences on the transport processes. For turbulent flames, the burning velocity and thickness are additionally controlled by a variety of turbulent phenomena. As a prerequisite to turbulent combustion, a discussion of laminar flame speed (S_L) and flame front thickness (δ_L) is necessary for understanding the structure of laminar flames and how these properties are used to characterise properties of turbulent flames.

2.3.1.1 Laminar Flame Speed

In combustion research, burning velocity is one of the most important characteristics of premixed flames, determining both fuel consumption and heat release rates. The laminar flame speed can be defined as the propagation speed of a flame front, normal to the front, as it moves relative to a stationary unburnt gas mixture. Prior to computational methods, S_L was found using either experimental campaigns or simplified thermal theory first proposed by Mallarad and Le Chatelier [65]. With the development of computational

techniques for determining S_L, the dependence of laminar flame speed on pressure, pre-heating temperature and mixture composition can more easily be determined, allowing for a more in-depth understanding of the structure of laminar flames and combustion in general. S_L is valuable to researchers for validating chemical kinetic mechanisms, such as DRM19 [66] and GRI-Mech3.0 [67], which are regularly employed in turbulent models. Validation of these mechanisms is carried out by comparing numerically predicted values of S_L with experimental results. Additionally S_L is frequently used to normalise turbulent flame parameters and calculate dimensionless numbers.

2.3.1.2 Laminar Flame Thickness

Similar to S_L, laminar flame thickness is routinely used to normalize turbulent flame properties. The thickness of a laminar premixed flame can be defined in a number of ways with, the most common approaches being the thermal thickness (δ_{th}) and the diffusive thickness (δ_{diff}). Figure 2.2 shows the temperature profile of a 1D laminar flame for a hypothetical methane/air flame. The figure shows a visual representation of δ_{th}, which is defined using Equation 2.28. The thermal thickness is based on the temperature while the diffusive thickness is defined using the unburnt gas quantities shown in Equation 2.29.

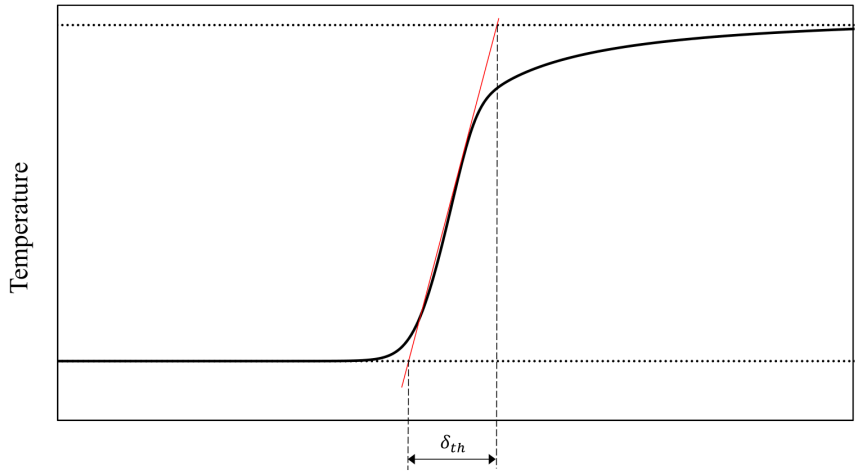

Figure 2.2: Temperature profile for a 1D laminar premixed methane/air flame with thermal thickness indicated

$$\delta_{th} = \frac{T_b - T_u}{\max(dT/dz)} \tag{2.28}$$

$$\delta_{diff} = \frac{\lambda_0}{\rho_0 C_p S_L} = \frac{D_{th}}{S_L} \tag{2.29}$$

Although δ_{diff} and δ_{th} are both equally valid with respect to temperature, pressure and equivalence ratio, δ_{diff} can be smaller by an order of magnitude when compared to δ_{th} [68]. As a result and to ensure consistency, a single definition of laminar flame thickness is selected for this work. For future sections of this thesis the thermal flame thickness, as defined in Equation 2.28, will be used. Although δ_{th} and δ_{diff} are the most common definitions of laminar flame thickness, alternative definitions are available and can be found in [56].

2.3.2 Characteristics of Turbulent Premixed Combustion

One of the major characteristics of turbulent combustion, in comparison to laminar flames, is the interaction between turbulence and chemistry. The complex nature of these turbulent-chemistry interactions (TCI) leads to modifications of both the turbulent flame front and the flow velocity. In addition to these interactions the rapid fluctuations present in the flow influence both the transport and reaction processes of the flame. Due to these complex phenomena, the theoretical concepts used to describe turbulent combustion are not well defined, with the majority of these theories relying on experimental observations and phenomenological reasoning. In his groundbreaking work, Damköhler [69] described how the wrinkling of the flame front is solely due to the influence of the large-scale turbulence in the flame while having no effect on the internal structure, whereas the small eddies present affect the transport processes only. Since Damköhler's first description of the influence of turbulence on flame characteristics, the understanding of TCI has grown immensely. It has been found that the large ranges of turbulent length and time scales have a wide array of effects on the flame, depending on the size ratios of the turbulent

eddies and the reaction zone within the flame. Due to the varying impact, that turbulence has on flames, it is essential to not only consider the time and length scales present in the flame but also the physical impact turbulence has on the flame. A widely implemented approach for characterising this relationship is through the use of dimensionless numbers. The most common ones used are the turbulent Reynolds number (Re_t), the Damköhler number (Da) and the Karlovitz number (Ka) which are defined in Equations 2.30 to 2.32.

$$Re_t = \frac{u'\Lambda}{\upsilon} = \frac{u'}{S_L}\frac{\Lambda}{\delta} \tag{2.30}$$

$$Da = \frac{\tau_t}{\tau_c} = \frac{S_L}{u'}\frac{\Lambda}{\delta} \tag{2.31}$$

$$Ka = \frac{\tau_c}{\tau_k} = \left(\frac{\delta}{\eta_k}\right)^2 = \left(\frac{u'}{S_L}\right)^{3/2}\left(\frac{\Lambda}{\delta}\right)^{-1/2} \tag{2.32}$$

where τ_t is the integral time scales, τ_k is the Kolmogorov time scale and τ_c is a chemical time scale that can be defined as $\tau_c = \delta_{diff}/S_L$. The turbulent Reynolds number is used to define the ratio of the momentum forces, which act to destabilize the flame, to the viscous forces, which have the opposite effect and dampen turbulence. Large values of Re_t are associated with flames characterised by high levels of fluctuation. Da is associated with the largest turbulent eddies and corresponds to the ratio of the integral time scale and the chemical time scale. For large values of Damköhler number ($Da \gg 1$) all of the times scales are large when compared to the chemical time scales, therefore chemistry is fast and mixing is the rate limiting step for the combustion process, this results in the flames forming sheet type structures and the flame front can be clearly distinguished. For the case where $Da < 1$, the turbulent motions have shorter time scales and can be characterised by intense mixing, this form of combustion is described by a well-stirred reactor and the flame propagation is controlled by chemical kinetics.

The Karlovitz number is used to define the relationship between the Kolmogorov time scale and chemical time scale. Ka can also be used to relate the thickness of the reac-

tion zone to the smallest eddies in the flame. When $Ka < 1$ the chemical time scales is the shortest scales present in the flame, and the flame thickness is smaller than the Kolmogorov length, resulting in no flame thickening. If $Ka > 1$ the flame thickens. The level of thickening at these conditions depends on properties of the flow, such as Da and the ratios between the Kolmogorov length scales and the flame reaction zone thickness. It should be noted that the times scales used to define Re_t, Da and Ka are implicitly based on a single-step irreversible reaction. Even though better definitions for the time scales could be employed, using these dimensionless numbers allows for turbulent premixed flames to be classified into various groups or regimes of turbulent combustion. First proposed by Borghi [70] and later extended by Peters [41], an example of the modified Borghi diagram can be seen in Figure 2.3 and allows for a fast and easy assessment of turbulent flame characteristics.

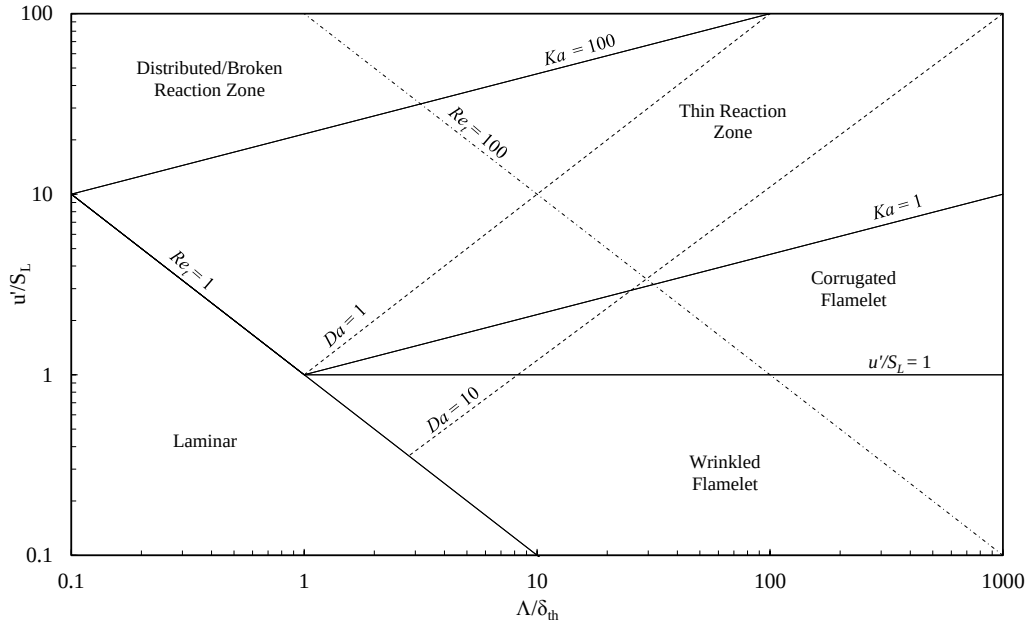

Figure 2.3: Borghi diagram modified by Peters [41] showing the classification of turbulent premixed flames

The x-axis of the diagram represents the size of the flame structure using a turbulent length ratio ($\frac{\Lambda}{\delta_{th}}$). As the value of $\frac{\Lambda}{\delta_{th}}$ increases, the size of the turbulent eddies within the flow grow. The y-axis represents the intensity of turbulence within the flame using the

turbulent speed ratio ($\frac{u'}{S_L}$), comparing the fluctuating velocity to the laminar flame speed. Laminar flames are characterised by $Re_t < 1$, and above this limit turbulent combustion occurs. The wrinkled flamelet regime is located on the Borghi diagram below the constant horizontal line for u'/S_L, as the laminar flame speed is greater than the fluctuating velocity the flame front propagates with a velocity close to that of S_L. As the thickness of the flame front is smaller than the smallest eddy present in the flow $(Ka < 1)$, turbulence does not affect the reaction rates. Therefore the ratio of turbulent to laminar flame speed is due to the competition between the flame front propagation speed and the turbulent flow creating wrinkles in the flame front, which results in increased S_T. The corrugated regime, situated above the $u'/S_L = 1$ line and below the constant $Ka = 1$ line, exhibits similar chemical properties to the wrinkled flamelet, as a result of the Kolmogorov eddies being unable to penetrate the reaction zone ($Ka < 1$ as $\delta_{th} > \eta$). Nevertheless, the level of turbulence present in the flame is larger and therefore the intensity of wrinkling is greater, leading to an increase in S_T values. In some cases, the wrinkling can lead to the formation of "flame pockets", which can physically detach from the continuous flame sheet. For this regime, chemical kinetics can be characterized by the laminar flame properties, allowing the flames to be described as turbulent flow embedded with relatively thin reactions fronts, similar to laminar premixed flames. These reaction fronts are often referred to laminar flamelets This description is used in the classic flamelet concept which is frequently employed in turbulent premixed combustion models.

The thin reaction zone is defined for $Re_t > 1$ and $1 < Ka < 100$. The regime was proposed by Peters [41], where it was postulated that the reaction zone can be separated into a preheat zone and an inner sub-layer. The preheat zone is chemically inert and requires both the laminar and turbulent diffusion to define the thickness, and is large enough to be influenced by the smallest turbulent eddies. The majority of the chemical reactions take place in the inner sub-layers, where the thickness is on the order of 10% of the reaction zone thickness. Although the Kolmogorov eddies can affect the preheat zone, the thickness of the inner sub-layer is too small and therefore the chemical processes are not influenced. For the distributed/broken reaction zone, where $Ka > 100$, the Kolmogorov

eddies are small enough to penetrate the thickness of the inner sub-layer and can lead to local extinctions in the flame front, which can result in complete flame extinction. Peters suggested that when $Ka > 100$ premixed flames extinguish.

2.3.3 Turbulent Premixed Combustion Models

To model reactive flows, additional terms are included in the Favre-averaged energy transport expression (Equation 2.6) to account for the diffusion of enthalpy by species diffusion and the production/consumption of thermal energy by chemical reactions as shown in Equation 2.33. New species transport equations, shown below, must also be included for each of the species (k) present in the reactive flow, where the number of species is defined by the chemical kinetic mechanism being used. Equation 2.34 describes the transport and production/consumption of the species present within the flow

$$\frac{\partial \bar{\rho}\tilde{h}_s}{\partial t} + \frac{\partial \bar{\rho}\tilde{u}_i\tilde{h}_s}{\partial z_i} = \overline{\frac{Dp}{Dt}} + \frac{\partial}{\partial z_i}\left(\overline{\lambda\frac{\partial T}{\partial z_i}} - \overline{\rho u''_i h''_s}\right) + \overline{\tau_{ij}\frac{\partial u_i}{\partial z_j}} + \overline{\dot{\omega}_T} - \frac{\partial}{\partial z_i}\left(\overline{\rho\sum_{k=1}^{N} V_{k,i}Y_k h_{s,k}}\right) \tag{2.33}$$

$$\frac{\partial\left(\bar{\rho}\tilde{Y}_k\right)}{\partial t} + \frac{\partial\left(\bar{\rho}\tilde{u}_i\tilde{Y}_k\right)}{\partial z_i} = -\frac{\partial}{\partial z_i}\left(\overline{V_{k,i}Y_k} + \bar{\rho}\widetilde{u''_i Y''_k}\right) + \overline{\dot{\omega}_k} \tag{2.34}$$

The Reynolds fluxes $(\bar{\rho}\widetilde{u''_i Y''_k})$ in the species equation are computed using the same approach described in Section 2.2 for the non-reactive Reynolds fluxes. In laminar flows the new reaction rate term $(\dot{\omega}_k)$ is typically expressed using the modified Arrhenius rate law, however, the highly non-linearity and exponential nature of the Arrhenius rate law leads to various difficulties for turbulent flows and requires a new closure method. In general, the combustion models can be grouped into two categories; infinitely fast and finite rate chemistry, as shown in Table 2.1.

It should be noted that the Eddy Dissipation Concept is employed in the development of the 1D turbulent flame speed solver and therefore a description of the combustion model will be omitted from this Chapter, and instead, a detailed discussion regarding EDC will

Table 2.1: Overview of infinitely fast and finite rate chemistry closure models

Combustion Model	Chemistry Rate	Model
Eddy Break Up (EBU) [71]	Infinitely Fast Rate	RANS & LES
Bray Moss Libby (BML) [72]	Infinitely Fast Rate	RANS
Level Set Approach (G-equation) [73]	Finite Rate	RANS & LES
Flame Surface Density (FSD) [74]	Finite Rate	RANS & LES
Eddy Dissipation Concept (EDC) [75]	Infinitely Fast & Finite Rate	RANS & LES
Probability Density Function (PDF) [56]	Infinitely Fast & Finite Rate	RANS & LES

take place in Chapter 4.

2.3.3.1 Eddy Break Up (EBU) model

The EBU model was first proposed by Spalding [71] for combustion with high Reynolds and Damköhler numbers ($Re_t \gg 1$ and $Da \gg 1$), where the reactivity within the flame is controlled by the level of mixing rather than the chemistry. Therefore the EBU reactions rate, $\dot{\omega}_{EBU}$, shown in Equation 2.37, is mainly controlled by a characteristic turbulent mixing time (τ_{EBU}) and a fluctuating temperature term.

$$\dot{\omega}_{EBU} = C_{EBU}\overline{\rho}\frac{\sqrt{c''^2}}{\tau_{EBU}} \tag{2.35}$$

where c''^2 is the progress variable variance and C_{EBU} is a model constant on the order of unity. The characteristic time scale is defined as the ratio between the turbulent kinetic energy and the turbulent energy dissipation ($\tau_{EBU} = k/\varepsilon$). Under the assumption of an infinitesimally thin flame, the mean progress variable can be used in place of c''^2:

$$\overline{\rho}\widetilde{c''^2} = \overline{\rho\left(c-\widetilde{c}\right)^2} = \overline{\rho}\left(\widetilde{c^2}-\widetilde{c}^2\right) = \overline{\rho}\widetilde{c}(1-\widetilde{c}) \tag{2.36}$$

when defining the Eddy Break Up model reaction rate because progress variable can only take two values $\widetilde{c}=0$ at unburnt conditions and $\widetilde{c}=1$ at burnt conditions so that $\widetilde{c}^2 = \widetilde{c}$, $\dot{\omega}_{EBU}$ can be defined as:

$$\dot{\omega}_{EBU} = C_{EBU}\overline{\rho}\frac{\varepsilon}{k}\widetilde{c}(1-\widetilde{c}) \tag{2.37}$$

This simplification makes the EBU model very attractive, as the expression for the reaction rate relies solely on known mean quantities and does not require additional transport equations, though the obvious limitation with the EBU model is the lack of detailed chemical kinetics and limited applicability.

2.3.3.2 Bray Moss Libby (BML) model

The BML model was first proposed by it's authors Bray, Moss and Libby [72] and has been further improved on by Bray, Champion and Libby [76]. The model assumes that the turbulent structure in the surrounding fluid does not disturb the structure of the thin turbulent flame. Defining a progress variable, $(\bar{c})$, using Equation 2.38 such that $\bar{c} = 0$ refers to unburnt gas and $\bar{c} = 1$ to burnt gas, a probability density function (PDF) of the progress variable, at a given location z, can be defined as the sum contribution from the unburnt, burnt and reacting mixture as shown in Equation 2.39.

$$\bar{c} = \frac{T - T_u}{T_b - T_u} \tag{2.38}$$

$$p(\bar{c}, z) = \alpha(z)\,\delta(\bar{c}) + \beta(z)\,\delta(1-\bar{c}) + \gamma(z)\,f(\bar{c}, z) \tag{2.39}$$

α, β and γ are used to denote the probability of finding the reactants, products and reacting mixtures $(0 < \bar{c} < 1)$, respectively, at position z. $\delta(\bar{c})$ and $\delta(1-\bar{c})$ are the Dirac delta functions for the unburnt and burnt gas, respectively. Similar to the EBU model, the flame front is assumed to be thin, such that $Re \gg 1$ and $Da \gg 1$. Therefore the probability of finding the reactive gas mixture at the location z is very small $(1 \gg \gamma)$ and so can be neglected, allowing for Equation 2.39 to be written as:

$$p(\bar{c}, x) = \alpha(x)\,\delta(\bar{c}) + \beta(x)\,\delta(1-\bar{c}) \tag{2.40}$$

where α and β can be determined as functions of the progress variable such that the probabilities rely solely on $\bar{c}$ and the heat release parameter (τ):

$$\alpha = \frac{1-\bar{c}}{1+\tau\bar{c}} \qquad \beta = \frac{(1+\tau)\,\bar{c}}{1+\tau\bar{c}} \tag{2.41}$$

From Equation 2.41 it can be seen that the progress variable is required. Starting with the instantaneous transport equation for $\bar{c}$, Bray and Moss derived a balance equation for $\bar{c}(1-\bar{c}) = \bar{c} - \bar{c}^2$. Under the assumptions of the BML model, the progress variable is restricted to values of 0 or 1, therefore reducing the balance equation to the following expression:

$$2\rho D \frac{\partial \bar{c}}{\partial z_i}\frac{\partial \bar{c}}{\partial z_i} = 2\bar{c}\dot{\omega}_{\bar{c}} - \dot{\omega}_{\bar{c}} \tag{2.42}$$

where D is the $\bar{c}$ diffusive term. After averaging Equation 2.42 can be expressed as:

$$\overline{\dot{\omega}_{\bar{c}}} = \frac{\bar{\rho}\,\tilde{\chi}_{\bar{c}}}{2\bar{c}_m - 1} \tag{2.43}$$

where $\tilde{\chi}_{\bar{c}}$ is the scalar dissipation rate of $\bar{c}$ and $\bar{c}_m$ is a constant, typically between 0.7 and 0.8 for hydrocarbon-air flames. As can be seen from the above equations, $\overline{\dot{\omega}_{\bar{c}}}$ has a direct link with the scalar dissipation rate and as a result, an accurate prediction of the scalar dissipation will allow for the calculation of a valid reaction rate. Nevertheless, the closure for the mean scalar dissipation rate still remains a challenge for premixed flames due to the need to close and solve a transport equation for the scalar dissipation rate. Making the definition of $\overline{\dot{\omega}_{\bar{c}}}$ difficult when using Equation 2.43.

2.3.3.3 Level Set Approach (G-equation)

This approach was first introduced by Williams in the original form of G-equations. A level set of a real-valued function f of n real variables is a set of the form:

$$L_c(f) = \{(x_1, \cdots, x_n)\,|\,f(x_1, \cdots, x_n) = c\} \tag{2.44}$$

that is, a set where the function corresponds to a real value c. In this approach, a level set of a non-reacting scalar (G) is used to represent the flame surface rather than using the reactive progress variable scalar. By using a non-reactive term, this approach avoids the

complexity associated with the counter-gradient diffusion and the need for source term closure. Considering an iso-scalar surface (G^*), an equation for G can be derived, where this surface divides the mixture into regimes such that $G > G^*$ refers to burnt gas and $G < G^*$ refers to unburnt gas. The selection of G^* is arbitrary but remains constant for a particular flame. The location of the iso-scalar surface at any time t, is the solution to the equation $G(x,t) = G^*$ and when differentiated leads to the following expression:

$$\frac{\partial G}{\partial t} + u \cdot \nabla G = S_d \left|\nabla G\right| \tag{2.45}$$

The expression for displacement speed (S_d) is then modified, as shown in Equation 2.46, to include the effects of laminar burning velocity and the influence of strain and curvature effects.

$$S_d = S_L - S_L \mathscr{L} \kappa_c - a\mathscr{L} \tag{2.46}$$

where $\mathscr{L}$ is the Markstein length, $a = -n \cdot \nabla u \cdot n$ is the strain rate, $\kappa_c = \nabla \cdot n$ is the curvature and the flame normal vector is given by $n = -\nabla G/|\nabla G|$. Using this decomposition the G-equations become:

$$\frac{\partial G}{\partial t} + u \cdot \nabla G = S_L \left|\nabla G\right| - D_{\mathscr{L}} \kappa_c \left|\nabla G\right| - a\mathscr{L} \left|\nabla G\right| \tag{2.47}$$

where $D_{\mathscr{L}} = S_L \mathscr{L}$ is the Markstein diffusivity. Equation 2.47 is solely for the corrugated flamelets regime. G-equation for the thin reaction zones regime [77] is defined as:

$$\frac{\partial G}{\partial t} + u \cdot \nabla G = (s_r + s_n) \left|\nabla G\right| - D\kappa_c \left|\nabla G\right| \tag{2.48}$$

For RANS modelling the equation is Favre-averaged, using the decomposition such that $G = \widetilde{G} + G''$, and the $\tilde{G}$ transport equation takes the following form:

$$\frac{\partial \tilde{G}}{\partial t} + \tilde{u} \cdot \nabla \tilde{G} = S_T \left|\nabla \tilde{G}\right| - D\kappa_c \left|\nabla \tilde{G}\right| \tag{2.49}$$

To close the turbulent flux term, a gradient transport model can be applied but, to fully close Equation 2.49, additional information is required about the turbulent flame speed

on the R.H.S. of Equation 2.49. S_T is typically supplied using a turbulent flame speed correlation of the form:

$$\frac{S_T}{S_L} = 1 + C\left(\frac{u'}{S_L}\right)^n \tag{2.50}$$

where C and n are model adjustable parameters and generally have values of unity and 0.7 respectively, but due to the complex nature of turbulent combustion tuning can be required. Further discussion on S_T correlations and the necessity of tuning the adjustable parameters will be described in later sections of the work. A key difference between the G-equations and the EBU and BML models is the ability of the G-equations to include detailed chemical kinetics in the form of S_L. The underlining theory, however, restricts the use of G-equations to flows where mixing is the rate limiting step.

2.3.3.4 Flame Surface Density Model

The Flame Surface Density (FSD) model is a widely used flamelet approach based on the work of Marble and Broadwell [74] and the coherent flame model (CFM) [53]. The mean reaction rate is described in terms of the flame surface area, where $\dot{\omega}$ is taken as the product of the flame surface density (Σ) and the local consumption rate per unit of flame area ($\langle S_c \rangle_s$) and can be defined as:

$$\overline{\dot{\omega}} = \rho_u \langle S_c \rangle_s \Sigma \tag{2.51}$$

where the subscript u refers to the unburnt properties. For a flame with a high surface density at a given location, the related turbulent reactivity at this point will also be high. The FSD model is attractive due to the separation of the turbulent-chemistry interactions, which are modelled by the flame surface density, from the complex chemistry features, which are incorporated into $\langle S_c \rangle_s$. Flame stretch, caused by turbulent eddies, influence the propagation velocity and it is useful to write the local consumption rate as $\langle S_c \rangle_s = S_L I_0$, where I_0 accounts for the stretch effects on S_L. The main challenge for the FSD model is defining Σ. The two main closure approaches are (1) simple algebraic expressions, or (2) Σ balance equation. Simple algebraic models have been proposed many times in

the literature, with Equation 2.52 and 2.53 showing algebraic expressions for the flame surface density proposed by Bray et al. [78, 79].

$$\Sigma = \frac{g}{\sigma_y} \frac{\bar{c}(1-\bar{c})}{C_l \Lambda \left(\frac{S_L}{u'}\right)} \tag{2.52}$$

$$\Sigma \delta_L \simeq \frac{2C_{D_c}}{(2C_m - 1)} \frac{\bar{\rho}}{\rho_u} \left(1 + \frac{2}{3} C_{\varepsilon_c} S_L \frac{1}{\sqrt{\tilde{k}}}\right) \left(1 + \frac{C_D \tilde{\varepsilon} \delta_L}{C_{D_c} \tilde{k} S_L}\right) \widetilde{c''^2} \tag{2.53}$$

where C_x, g and σ_y are constants and δ_L is a laminar flame thickness.

Various forms of the FSD model using balance equations can also be found in the literature. According to Pope [80], the surface density of an iso-temperature surface (Θ) can be expressed in the form shown in Equation 2.54. An exact balance equation for Σ can then be derived from this definition and the balance equation for $\bar{c}$ as shown in Equation 2.55.

$$\Sigma = \overline{|\nabla \Theta| \, \delta(\Theta - \Theta^*)} = \left(\overline{|\nabla \Theta| \, | \Theta = \Theta^*}\right) p(\Theta^*) \tag{2.54}$$

$\delta(\Theta)$ is the Dirac δ function, $\overline{|\nabla \Theta| \, | \Theta = \Theta^*}$ is the conditional average of $|\nabla \Theta|$ for $\Theta = \Theta^*$ and $p(\Theta^*)$ is the probability of finding $\Theta = \Theta^*$ at a given location.

$$\frac{\partial \Sigma}{\partial t} + \frac{\partial}{\partial z_i} \left(\langle u_i \rangle_s \Sigma \right) + \frac{\partial}{\partial z_i} \left[\langle s_d n_i \rangle_s \Sigma \right] = \left\langle \left(\delta_{ij} n_i n_j \right) \frac{\partial u_i}{\partial z_i} \right\rangle_s \Sigma + \left\langle s_d \frac{\partial n_i}{\partial z_i} \right\rangle_s \Sigma \tag{2.55}$$

s_d is the displacement speed of the flame relative to unburnt gas, n_i are the component unit vectors $\overrightarrow{n}$ normal to the flame front. The flame surface density balance equation is unclosed and modelling is required to close the propagation speed, turbulent flux of the flame surface, the strain rate and curvature effects. Many studies have focused on such modelling, with a general closed version of the Σ equation being written as:

$$\frac{\partial \Sigma}{\partial t} + \frac{\partial \widetilde{u_i} \Sigma}{\partial z_i} = \frac{\partial}{\partial z_i} \left(\frac{\nu_t}{\sigma_c} \frac{\partial \Sigma}{z_i} \right) + \kappa_m \Sigma + \kappa_t \Sigma + D \tag{2.56}$$

where D is a consumption term and κ_m and κ_t relate to the strain rate acting on the flame surface, created by the mean flow field and turbulent motions. A brief overview of the various closure approaches found in the literature is summarized in Table 2.2.

Table 2.2: Overview of the source and consumption terms in the Σ balance equation (Equation 2.56) where $\alpha_0, \beta_0, \gamma, \lambda, \Theta^*(0 < \Theta^* < 1), C_A, a, c, C, E$ and K are model parameters

Model	$\kappa_m\Delta$	$\kappa_t\Delta$	D
CPB [81]	$A_{ik}\frac{\partial\widetilde{u}_k}{\partial x_i}\Sigma$	$\alpha_0 C_A\sqrt{\frac{\varepsilon}{\upsilon}}\Sigma$	$\beta_0\langle S_c\rangle_s\frac{2+e^{-aR}}{3(1-\widetilde{\Theta})}\Sigma^2$ $R=\frac{(1-\widetilde{\Theta})\varepsilon}{\Sigma\langle S_c\rangle_s k}$
CFM1 [53]	$A_{ik}\frac{\partial\widetilde{u}_k}{\partial x_i}\Sigma$	$\alpha_0\frac{\varepsilon}{k}\Sigma$	$\beta_0\langle S_c\rangle_s\frac{c\sqrt{k}}{1-\widetilde{\Theta})}\Sigma^2$
CFM2-a [53]	$A_{ik}\frac{\partial\widetilde{u}_k}{\partial x_i}\Sigma$	$\alpha_0\Gamma_K\frac{\varepsilon}{k}\Sigma$	$\beta_0\langle S_c\rangle_s\frac{c\sqrt{k}}{1-\widetilde{\Theta})}\Sigma^2$
CFM2-b [53]	$A_{ik}\frac{\partial\widetilde{u}_k}{\partial x_i}\Sigma$	$\alpha_0\Gamma_K\frac{\varepsilon}{k}\Sigma$	$\beta_0\langle S_c\rangle_s\frac{c\sqrt{k}}{1-\widetilde{\Theta})}\Sigma^2$
CFM3 [82]	$A_{ik}\frac{\partial\widetilde{u}_k}{\partial x_i}\Sigma$	$\alpha_0\Gamma_K\frac{\varepsilon}{k}\Sigma$	$\beta_0\langle S_c\rangle_s\frac{\Theta^*-\widetilde{\Theta}}{\widetilde{\Theta}(1-\widetilde{\Theta})}\Sigma^2$
MB [83]	$E\frac{\widetilde{u_i''u_k''}}{k}\frac{\partial\widetilde{u}_k}{\partial x_i}\Sigma$	$\alpha_0\sqrt{Re_t}\frac{\varepsilon}{k}\Sigma$ $+\frac{F}{\langle S_c\rangle_s}\frac{\varepsilon}{k}\widetilde{u_i''\Theta''}\frac{\partial\widetilde{\Theta}}{\partial x_i}$	$\frac{\beta_0\langle S_c\rangle_s\sqrt{Re_t}\Sigma^2}{\widetilde{\Theta}(1-\widetilde{\Theta})\left(1+c\frac{\langle S_c\rangle_s}{\sqrt{k}}\right)^{2\gamma}}$
CD [84]		$\alpha_0\lambda\frac{epsilon}{k}\Sigma$ if $\kappa_t\leqslant\alpha_0 K\frac{\langle S_c\rangle_s}{\delta_L}$	$\beta_0\frac{\langle S_c\rangle_s}{(1-\widetilde{\Theta}}\Sigma^2$
CH1 [55]		$\alpha_0\sqrt{\frac{\varepsilon}{15\upsilon}}\Sigma$	$\beta_0\frac{\langle S_c\rangle_s}{\widetilde{\Theta}(1-\widetilde{\Theta})}\Sigma^2$
CH2 [55]		$\alpha_0\frac{u'}{l_{tc}}\Sigma$	$\beta_0\frac{\langle S_c\rangle_s}{\widetilde{\Theta}(1-\widetilde{\Theta})}\Sigma^2$

Equations 2.51 and 2.56 close the reactive flow transport equation for premixed turbulent combustion and have been shown to accurately predict chemistry effects in turbulent combustion models.

2.3.3.5 Transported Probability Density Function

The transported probability density function (PDF) approach uses the stochastic nature of turbulence to calculate the reaction rates for turbulent combustion. For single step chemistry, the pdf $(p(\bar{c}^*))$ predicts the likelihood of the progress variable having values between $\bar{c}^*$ and $\bar{c}^*+d\bar{c}^*$, with the normalised probability density function taking the form $\int_0^1 p(\bar{c}^*)\,d\bar{c}^*=1$. For an adiabatic flame with a Lewis number (Le) of unity, the mean

reaction rate can be defined as:

$$\overline{\omega}_{\bar{c}} = \int_0^1 \dot{\omega}_{\bar{c}}(\bar{c}^*)\, p(\bar{c}^*) d\bar{c}^* \tag{2.57}$$

For multi-step chemistry, a larger array of species mass fractions and temperature have to be accounted for. To achieve this a joint probability function is implemented with the normalised relationship taking the form:

$$\int_{\psi_1,\psi_2,....,\psi_{N+1}} p(\psi_1,\psi_2,....,\psi_{N+1}) d\psi_1 d\psi_2 ....d\psi_{N+1} = 1 \tag{2.58}$$

where $\psi(Y_1, Y_2, ..., Y_N, T)$ is the scalar field vector for mass fractions of N species and temperature. The Favre-averaged joint pdf of the mean reaction rate can be defined using Equation 2.59.

$$\overline{\dot{\omega}} = \int_{\psi} \dot{\omega}\tilde{p}(\psi) d\psi \tag{2.59}$$

A transport equation for $\widetilde{p}(\psi)$ is used to give an exact evolution of the joint probability density function, with Dopazo and O'Brien [85] and Pope [86] deriving Equation 2.60 for the transport of $\widetilde{p}(\psi)$. For this expression, the unsteady, convection and chemical terms are closed and the turbulent flux and micro-mixing terms require closure. The inclusion of chemical source terms also allows for finite chemistry to be implemented.

$$\begin{aligned}\frac{\partial}{\partial}\left(\bar{\rho}\tilde{p}(\psi)\right) + \frac{\partial}{\partial z_i}\cdot\left(\bar{\rho}\tilde{u}\tilde{p}(\psi)\right) + \sum_{k=1}^{N}\frac{\partial}{\partial\psi_k}\left(\dot{\omega}_k\left(\bar{\rho}\tilde{p}(\psi)\right)\right) = \\ -\frac{\partial}{\partial z_i}\left(\bar{\rho}\left\langle u''\middle|\psi\right\rangle\tilde{p}(\psi)\right) + \sum_{k=1}^{N}\frac{\partial}{\partial\psi_k}\left(\left\langle\frac{\partial\, j_k|\,\psi}{\partial z_i}\right\rangle\tilde{p}(\psi)\right)\end{aligned} \tag{2.60}$$

2.4 Other Relevant Models

The CFD methods discussed in the previous sections are the most popular approaches for describing premixed turbulent combustion. As the work in this thesis focuses on the development of a predictive one-dimensional S_T model, the lesser known One-Dimensional

Turbulence (ODT) numerical approach, developed by Kerstein [87], is worth discussing. While turbulence is by nature, a three-dimensional phenomenon, the ODT model, as the name would suggest, is restricted to a single dimension where the domain is a single line of sight through the 3D domain. The model resolves all spatial and temporal scales along this line by representing turbulent advection as a postulated stochastic process rather than an evolution equation. By adopting this methodology, the ODT model is much more computationally affordable when compared to other approaches capable of fully resolving the flow, as the ODT model is restricted to flows with homogeneous turbulence in at least one direction.

The One Dimensional Turbulence model has been previously implemented as both a stand-alone approach [88, 89] and as a subgrid-scale model for LES [90, 91]. For the sake of brevity, the stand-alone version will be discussed solely from here on. When implementing the stand-alone case, the 1D domain is defined along the path perpendicular to the direction of primary gradients. For a slot-burner, like the one shown in Figure 2.4, where the streamwise direction is defined to be the x-axis and the ODT domain is defined along the y-axis. The ODT model was developed to describe two types of flows, temporal flows where the model solves for two independent variables (t, y) or spatial flows where the independent variables are (x, y).

The spatial One-Dimensional Turbulent model consists of two main components (1) governing equations written with the two independent variables (x, y) that are similar in form to Equations 2.1, 2.3 and 2.34 (mass, energy and species transport equations respectively) , and (2) a stochastic representation of "eddy events" at various points in (x, y) to represent turbulence along the 1D domain. Figure 2.5 shows the implementation of the stochastic approach known as triplet mapping which represents the effects of increased gradients due to a redistribution of the fluid elements along the ODT domain. The triplet approach works by taking a segment of a scalar profile and compressing it to $1/3$ of its original length. The compressed portion of the profile is then mapped back over one third of the original domain. This is carried out three times over the original segment length,

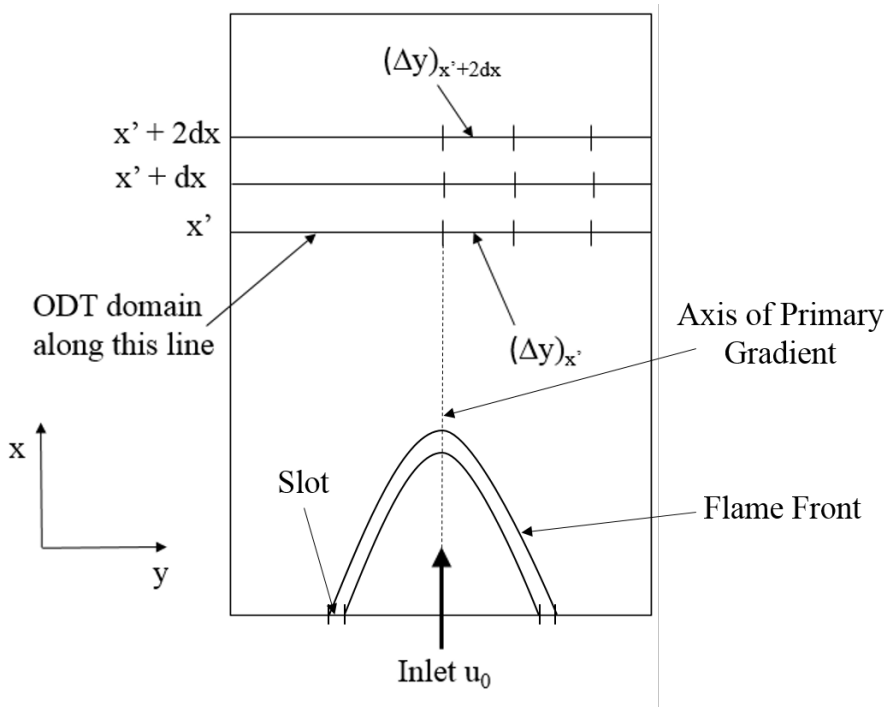

Figure 2.4: 2D representation of a slot-burner configuration where the slot is normal to the page and the ODT domain is in the y direction. Recreated from [92]

with the middle mapping being inverted. The location, length and implementation of the triplet mapping is based on the properties of the reactive flow [93]. When an eddy event is implemented the triplet mapping is applied to all of the solution variables. The triplet mapping of a function $\varphi(y)$ is $\varphi(f(y;y_0,\ell))$ and can be defined using Equation 2.61.

$$f(y;y_0,\ell) \equiv y_0 + \begin{cases} 3(y-y_0) & y_0 \leqslant y \leqslant y_0 + \frac{1}{3}\ell \\ 2\ell - 3(y-y_0) & y_0 + \frac{1}{3}\ell \leqslant y \leqslant y_0 + \frac{2}{3}\ell \\ 3(y-y_0) - 2\ell & y_0 + \frac{2}{3}\ell \leqslant y \leqslant y_0 + \ell \\ (y-y_0) & \text{otherwise} \end{cases} \tag{2.61}$$

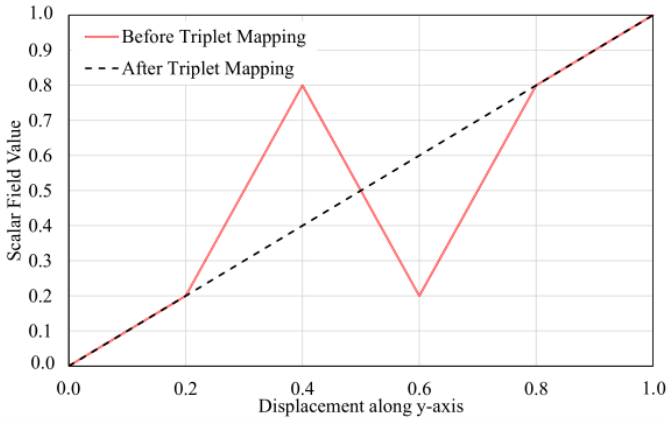

Figure 2.5: Hypothetical triplet mapping for a scalar field with a constant initial gradient, where the segment $0.2 < x < 0.8$ is compressed and mapped three times over the original segment length. Recreated from [87]

Using the above methodology the One-Dimensional Turbulence model has been implemented and show good agreement over a wide range of conditions for both reactive [94, 95] and non-reactive [88, 96] flows.

2.5 Turbulent Flame Speed

Turbulent flame speed is not only an important aid for researchers to estimate combustor reactivity when varying parameters, it is also an essential closure parameter in many turbulent premixed flame modelling approaches such as G-equations [97] and Turbulent Flame speed Closure (TFC) [98], which are commonly used in commercial CFD software. Due to its significance, S_T has been the focus of a large number of experimental, analytical and computational studies, as well as literature reviews.

In the following sections, an overview of measurement and prediction of turbulent flame speed will be reviewed. Before this, however, the definition dependency of S_T must be discussed. Unlike laminar flame speed, there is no single definition for turbulent burning velocity [39]. Some researchers define S_T to be a consumption speed which gives an indicator of the mass consumed per second and is determined by recognizing that all the reactants leaving the burner must flow through the flame brush as shown in Equation 2.62.

A progress variable iso-surface of 0.5 [39] is generally used when measuring consumption speed [99,100]. Others express S_T as a displacement speed and determine it by examining the kinematic balance between the mean flow field and the flame brush propagating speed at the leading edge of the flame brush, where $\bar{c}$ = 0.05 [101], [28], as shown in Equation 2.64.

$$\text{Global Consumption Speed: } \mathrm{S}_{T,GC} = \frac{\dot{m}_R}{\rho_R A_{\bar{c}=0.5}} \tag{2.62}$$

$$\text{Local Consumption Speed: } \mathrm{S}_{T,LC} = S_L I_0 \int_{-\infty}^{\infty} \Sigma d\eta \tag{2.63}$$

$$\text{Local Displacement Speed: } \mathrm{S}_{T,LD} = \left(V_{flame} - V_{gas}\right)_{LE} \cdot \mathbf{n}_{LE} \tag{2.64}$$

$\dot{m}_R$ is the total mass flow rate of reactants, $A_{\bar{c}=0.5}$ is the area for an iso-surface of $\bar{c}$ = 0.5, I_0 is the stretch factor, η is coordinate normal to the iso-surface of $\bar{c}$ = 0.5, V_{flame} is the velocity of the flame, V_{gas} is the velocity of the gas into which the flame front is propagating and the subscript LE refers to the leading edge in the normal direction $\mathbf{n}$. Equation 2.62 is proportional to $\dot{m}_R$ which is defined as the total mass flow provided to the burner divided by an area of an iso-surface of $\bar{c}$ = 0.5. For Equation 2.63 the integral is evaluated for a direction normal to a flame surface. $\mathrm{S}_{T,LC}$ is therefore local mass burning rate corresponding to the spatial location on the reference surface [102]. The local displacement speed is defined as the difference between V_{flame}, which is typically zero because counterflow and V-flames are stationary, and V_{gas} with both velocities being defined at the leading edge of the flame.

From this point forward S_T measured as a displacement speed ($\bar{c}$ = 0.05) and consumption speed ($\bar{c}$ = 0.5) shall be referred to as $S_{T,0.05}$ and $S_{T,0.5}$ respectively, and S_T will be used to refer to turbulent flame speed in general. While one definition of S_T is no more correct than another, it is important to use the same definition when comparing turbulent flame speed values, as S_T obtained using different definitions are not always equal. Reasons for this difference include convergence or divergence of streamlines within a

flame. As a result of this, a reactant flux in the transverse direction is introduced. This leads to different velocities at the $\bar{c}$ = 0.05 and $\bar{c}$ = 0.5 iso-surfaces and therefore different measurements of S_T [26]. For diverging flows, such as a low swirl burner, V-flames and Bunsen flames, it has been found that $S_{T,0.05}$ / $S_{T,0.5}$ has values of 4, 3 and 1.7, respectively. In contrast, for spherically expanding flames, the ratio of $S_{T,0.05}$ / $S_{T,0.5}$ has been found to be 0.45 [35]. Therefore it is important to only compare S_T values obtained using the same definitions of turbulent flame speed. Due to the multiple definitions of S_T, Bradley [35] derived a relationship, shown in Equation 2.65, to estimate turbulent flame speed at different $\bar{c}$ iso-surfaces for expanding flames only. Taking the leading edge ($\bar{c}$ = 0.05) as a reference surface, Table 2.3 shows the relationship between flame radii ($r_{\bar{c}}$) and S_T at various iso-surfaces. This method allows for the comparison of measured [103] or modelled [33] values of S_T at different $\bar{c}$ iso-surfaces. This method is highly valuable to researchers examining expanding flames. By removing the definition dependency of S_T, a much larger set of experimental data and predictive approaches can be used. The author is unaware of any such relationship for relating S_T at different $\bar{c}$ iso-surfaces for other non-expanding flame types.

$$\frac{S_{T\bar{c}_2}}{S_{T\bar{c}_1}} = \left(\frac{r_{\bar{c}_1}}{r_{\bar{c}_2}}\right)^2 \tag{2.65}$$

Table 2.3: Radii and turbulent flame speed ratios for various $\bar{c}$ iso-surfaces, taking the leading edge ($\bar{c}$ = 0.05) as a reference. Reproduced from Bradley et al. [35]

Measurement Technique	$\bar{c}$	$r_{0.05}/r_{\bar{c}_2}$	$S_{T,\bar{c}_2}$ / $S_{T_{0.05}}$
OH PLIF	0.05	1	1
Schlieren	0.1	1.11	1.23
Equal Volume Method	0.34	1.36	1.85
Equal Area Method	0.4	1.41	1.99
Mean Flame	0.5	1.49	2.22
Pressure Trace	0.6	1.56	2.42

Table 2.3 shows the variety of turbulent flame radii and speeds ratios at different values of $\bar{c}$ commonly used to measure S_T. It can be noted that, for expanding flames, as $\bar{c}$ increases so too does S_T . Whereas the opposite is true for Bunsen flames, where an in-

crease in $\bar{c}$ results in lower values of S_T. As well as converging or diverging streamlines, the standard definition of $\bar{c}$, ranging from unburnt ($\bar{c} = 0$) to burnt ($\bar{c} = 1$), has an influence on this difference. Using this definition for progress variable, Liu [103] suggested the reason for the difference in the relationship between $\bar{c}$ and S_T, for the Bunsen and expanding flame geometries, is due to the method used to define $\bar{c}$ in a flame. For Bunsen flames, unburnt gas is present in the centre of the flame, whereas for expanding flames burnt gas occupies the centre. Figure 2.6 shows a 2D example of the relationship between $\bar{c}$ and S_T for Bunsen and expanding flames. Liu proposed this as an explanation to why S_T / S_L values from Bunsen flames are found to be greater than spherical flames when measured at $\bar{c}$= 0.1 even though, under the same conditions, both measurements of flame speed should be close.

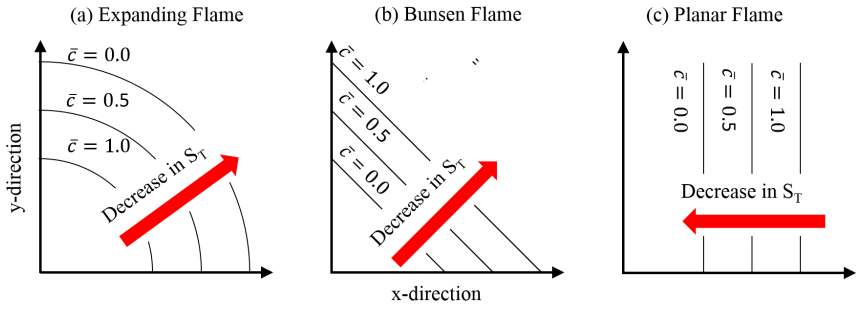

Figure 2.6: 2D representation of the relationship between $\bar{c}$ and S_T for (a) an expanding, (b) a Bunsen and (c) a planar flame with $\bar{c}$ iso-surfaces for 0, 0.5 and 1 through the flame brush

By measuring S_T at an iso-surface of $\bar{c}$ = 0.5, Liu found good agreement between Bunsen flame and expanding flame data. As a result, it was suggested that flame speeds determined at $\bar{c}$ = 0.5 may be a better representation of S_T and could help to eliminate the effect of combustor flow configuration on S_T measurements. The findings of a wide ranging correlation study [104] found that the most accurate expressions were developed to predict S_T at $\bar{c} = 0.5$, further supporting this assumption. Although $S_{T,0.5}$ may be a better representation of S_T, many existing analytical models predict $S_{T,0.05}$ and therefore both definitions are considered here. It should also be noted that the planar flame geometry, as shown in Figure 2.6, has a similar relationship between S_T and $\bar{c}$, when compared to

expanding flames. As a results good agreement can be found between planar and expanding flames for S_T, regardless of the $\bar{c}$ iso-surface used. The relationship between S_T and $\bar{c}$ for planar and Bunsen flames however is not the same. Therefore S_T recorded at $\bar{c} = 0.5$ should be considered for planar flames to remove the influence of progress variable when comparing to flame speeds measured using Bunsen flames.

2.5.1 Experimental Studies

Experimental campaigns were the first approaches used to investigate premixed turbulent flames. A large variety of experimental campaigns have been carried out to investigate the complex nature of turbulent flames. Due to the importance of premixed turbulent flame speed, a significant volume of these studies have focused on how S_T is affected under a variety of operating conditions. Many experimental studies have investigated the effect of turbulence levels within the flame and its effect on S_T. As displayed in Figure 2.7, Kobayashi [32] showed how initially as the velocity ratio increases so too does the flame speed ratio. This is caused by the local flame surface increasing in area due to turbulent eddies, after a certain point, the response of S_T to turbulence begins to decrease. This response is known as the "bending effect" and can be attributed to flamelets merging and quenching resulting in a reduction of flame area [56]. If the velocity ratio is further increased, the response of S_T/S_L to u'/S_L can become negative and eventually lead to quenching of the flame. The bending effect has been observed in many studies [105–107] and is independent of fuel and pressure conditions.

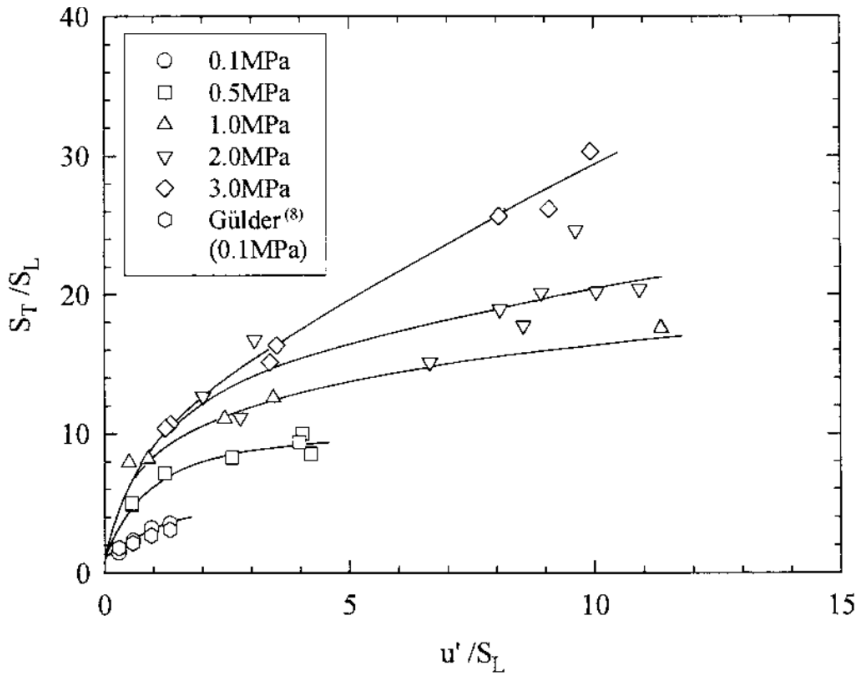

Figure 2.7: Variation of normalized turbulent flame speed with turbulent velocity ratio for a lean methane/air Bunsen flame with bending effects for higher turbulent intensities [32]

The influence of fuel composition on turbulent flames has been well documented in a review paper by Lipatnikov [40]. The influence of the fuel molecule can be a result of two phenomena, preferential diffusion and strain rate. Preferential diffusion can be characterised by the Lewis number and occurs for fuels with non-unity values. *Le* defines the relationship between species and thermal diffusion, where the species diffusion term relates to the diffusion of the deficient reactant into nitrogen. For non-unity values of Lewis numbers, turbulent flame speed changes due to a changes in the local flame surface area. Methane typically has a $Le \approx 1$ and so the effects are negligible, this is not the case for hydrogen, hydrocarbon-hydrogen mixtures and larger hydrocarbons such as ethylene or propane where preferential diffusion has a significant effect on S_T. Muppala et al. [108] showed how an increase in Lewis number from $Le \approx 1.2$ for ethylene to $Le \approx 1.62$ for propane results in a decrease in S_T/S_L over a range of u'/S_L conditions. Kido et al. [109] showed similar results for hydrogen, methane, ethane and propane flames, with Lewis numbers ranging from 0.63 to 1.88, respectively. For each fuel, the turbulent flame speed increased with a decrease in *Le*.

The strain rate also has an effect on S_T, with its influence varying depending on the fuel molecule. Within a turbulent flame, strain rate can cause stretching of the laminar mass burning velocity due to the flow field and can also influences the turbulent flame front propagation. The flame strain rate Markstein number (Ma_{sr}) is used to characterize strain rate where a decrease in Ma_{sr} is associated with an increase in S_T, with the opposite being true for an increase in Ma_{sr}. Nakahara et al. [110] aimed to show these effects by simultaneously altering ϕ and the fuel composition to ensure S_L remained constant. The results presented showed that the mixtures with high hydrogen content had a turbulent flame speed an order of magnitude larger than the propane mixtures, thus showing mixtures with the same laminar flame speed, turbulence intensity and experimental configuration can have significantly different values of S_T as a result of different strain rates.

For laminar flames, it is well known that pressure effects typically reduce the laminar flame speed. The limited number of experimental campaigns carried out at elevated pressure and the disagreement between the reported influence of pressure on turbulent flame speeds make it difficult to define the relationship between P and S_T. Early experimental studies for premixed turbulent flames showed an increase in S_T with increasing pressure [111, 112]. Although these finds may have been the result of a more rapid decay of the grid-generated turbulence [113]. Other studies where the turbulent flow characteristics were independent of pressure found that P had no influence on S_T. A more recent study by Kobayashi [114] further supports these trends showing that for a methane flame, S_T was constant for $P = 0.1 - 3.0$ MPa. While the ratio of flame speed $\frac{S_T}{S_L}$ does change, this is a result of S_L decreasing with pressure rather than any change in turbulent flame speed. Results from Bradley et al. [115], however, agree with the early predicted trends for P and S_T. For a stoichiometric iso-octane flame, the turbulent flame speed was found to increase with initial pressure in a fan stirred bomb. Vukadinovic et al. [116] found similar results of an increase in turbulent flame speed with pressure for both hydrogen and propane flames for $P = 0.1 - 0.4$ MPa. As a result of these disagreements, the effects of P on turbulent flame speed is not well defined.

In addition to providing a detailed insight into the interaction between turbulence and combustion and the influence of operating conditions on S_T in premixed flames, experimentally measured turbulent flames speed also provide validation points for analytical and computational methods. Experimental points will be used extensively to validate empirical and numerical methods developed in this work. To achieve this an experimental database has been created using results from 15 studies and comprising of $\approx$335 different turbulent flame speeds at various operating conditions. An overview of the experimental data can be seen in the modified Borghi diagram in Figure 2.8, with further details displayed in Table 2.4. The data has been taken over a range of progress variables, fuel types, pressures, turbulence levels and experimental apparatus. The majority of the data (209 points) was measured with expanding flames, including cruciform burners (CB), spherical bombs (SB), cylindrical vessels (CV), explosive vessels (EV), with the remaining flames (141 points) using Bunsen burners (BB) or (53 points) conical diffuser (CV) set-up.

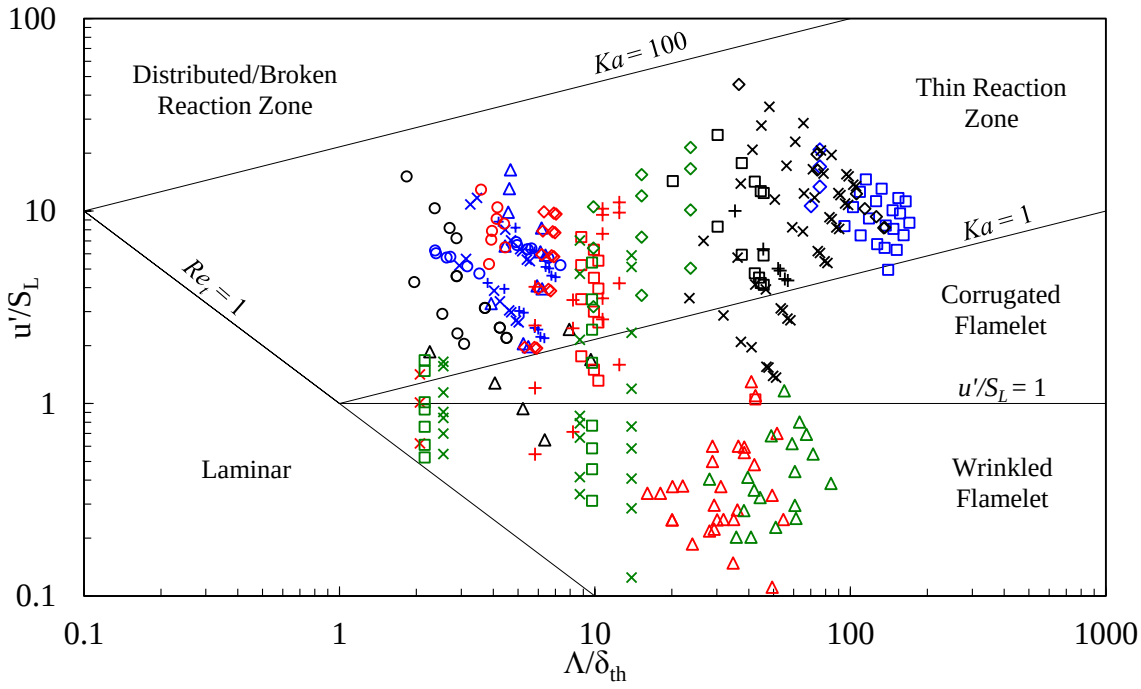

Figure 2.8: Turbulence and flame conditions for the data displayed in Table 2.4 plotted on a Borghi diagram modified by Peters [41] (For legend see Table 2.4)

Laminar properties were calculated rather than taken from the experimental studies due to variations in the reported values, which would influence the consistency of the data. Literature values of S_L are relatively consistent, however, variations in the reported values do exist. The majority of the studies used in the literate define laminar flame thickness as the diffusive flame thickness. This definition is expressed using either the thermal diffusivity α such that $\delta_{diff} = \alpha/S_L$ [101], [122], [103] or kinematic viscosity υ where $\delta_{diff} = \upsilon/S_L$ [31], [106]. It should also be noted that the numerator used for defining δ_{diff} is not always provided in the literature, and can therefore introduce further uncertainty into the exact definition of laminar flame thickness used. As previously discussed, the thermal flame thickness has been adopted for this thesis. While δ_{diff} and δ_{th} are both equally valid, only a single value of laminar flame thickness can be used to ensure consistency. As a result of δ_{diff} being up to an order of magnitude smaller than δ_{th} [68] and the difference between S_L calculated for this thesis and those reported in the literature, the turbulent velocity (u'/S_L) and length (Λ/δ_{th}) ratios may be different to those reported. This can be most notably seen in the modified Borghi plotted in Figure 2.8. Similarly,

Flame	Symbol	Apparatus	Fuel	$\bar{c}$	ϕ	P (MPa)	$\frac{u'}{S_L}$	$\frac{\Lambda}{\delta_{th}}$	$\frac{S_{T\bar{c}=0.5}}{S_L}$	Ref	Data Points
A	◇	CB	CH_4	0.1	0.8	0.1	10.6-20.8	70.1-70.6	9.4-12.6	[103]	4
B	□	CB	CH_4	0.1	0.8	0.2-1.0	5.0-14.5	3.5-170.1	5.0-15.8	[103]	20
C	◁	SB	CH_4	0.6	0.8 & 1.2	0.1	1.9-16.4	3.9-6.4	1.9-6.1	[110]	12
D	×	BB	CH_4	0.5	0.7-1.35	0.1	2.6-11.7	2.9-5.6	2.7-5.0	[101]	16
E	+	BB	C_2H_6	0.5	0.7-1.45	0.1	2.2-8.8	3.8-7.0	2.0-6.4	[101]	16
F	○	BB	C_3H_8	0.5	0.8-1.35	0.1	2.4-7.3	4.7-6.9	1.6-4.9	[101]	12
G	◇	SB	CH_4	0.1	0.6-1.3	0.5	8.2-45.5	3.7-136.1	9.4-33.6	[117]	8
H	□	SB	CH_4	0.34	0.6-1.3	0.1	2.0-15.1	1.8-4.5	1.8-4.8	[106]	13
I	◁	BB	CH_4	0.05	0.7,0.8,1.0	0.1	0.65-2.4	2.3-9.4	5.6-11.1	[118]	6
J	×	CB	CH_4	0.5	0.7-1.4	0.1	1.4-34.7	23.4-105	2.1-20.5	[31]	47
K	+	SB	CH_4	0.1	0.7-1.2	0.1	4.4-10.0	35.3-56.8	3.8-6.9	[33]	6
L	○	BB	CH_4	0.5	0.7-1.0	0.1	2.0-15.1	1.8-4.5	1.8-4.8	[101]	16
M	◇	SB	C_3H_8	0.6	0.7-1.45	0.1	1.9-9.9	5.3-7.0	2.0-8.0	[119]	15
N	□	CV	CH_4	0.6	0.8-1.25	0.1	1.3-6.3	8.1-10.0	1.9-5.1	[107]	13
O	◁	CD	CH_4	0.5	0.75 - 0.95	0.1	0.04-1.3	4.5-54.6	2.3 - 6.0	[120]	39
P	×	BB	CH_4	0.5	0.9	0.1	0.31-1.4	2.06	1.6-3.7	[32]	4
Q	+	BB	CH_4	0.5	0.9	0.5-3.0	0.55-11.1	5.83-12.5	4.8-31.8	[32]	16
R	○	BB	C_3H_8	0.5	0.8 & 1.0	0.1	1.5-12.9	3.6-4.5	4.3-11.4	[121]	9
S	◇	EV	C_3H_8	0.5	0.71	0.1-0.4	0.02-21.4	9.9-23.7	1.0-5.6	[116]	14
T	□	BB	C_3H_8	0.5	0.9	0.1-0.5	0.18-5.4	2.19-9.75	1.2-7.2	[114]	17
U	◁	CD	C_2H_4	0.5	0.6-0.75	0.1	0.5-1.2	55-71	2.7-4.3	[120]	19
V	×	BB	C_2H_4	0.5	0.9	0.1-1.0	0.04-7.0	2.6-13.9	1.2-15.5	[114]	29

Table 2.4: Experimental operating conditions, apparatus and measured $\bar{c}$ iso-surfaces for each data set used in the study. Symbols shown related to the data in the modified Borghi diagram in Figure 2.8

due to using δ_{th} rather than δ_{diff}, the dimensionless numbers Re_t, Da and Ka reported in Table 2.4, are smaller than those from the literature.

To calculate S_L and δ_{th}, the one-dimensional freely-propagating laminar flame solvers of Chemkin PRO [123] and a C_3 version of ArmacoMech 1.3 [124] are used for the CH_4 flames. Cantera 2.2.1 [42] and a C_5 version of the same mechanism are used for the C_2H_4, C_2H_6 and C_3H_8 flames. Chemkin PRO is not used for the larger molecule fuels due to memory issues caused by the larger kinetic mechanism (346 species). In addition to calculating the laminar flame properties of larger molecule fuels, Cantera is also used to calculate Lewis numbers (Equation 2.66) for each of the reactant mixtures at inlet conditions, giving average values of 0.95, 1.2, 1.4 and 1.7 for CH_4, C_2H_4, C_2H_6 and C_3H_8, respectively.

$$Le = \frac{\lambda}{\rho c_p D_{k,m}} \tag{2.66}$$

where c_p is the specific heat capacity at constant pressure and $D_{k,m}$ is the mixture-averaged molecular diffusion coefficient. To ensure the kinetic mechanism and solvers used do not introduce any uncertainty into the laminar properties, four sets of laminar properties are calculated; using two laminar flame speed solvers, Chemkin PRO and Cantera with two chemical kinetic mechanisms, AramcoMech 1.3 and USC Mech Version II [50]. Figure 2.9 shows the results for the laminar flame speed (S_L) and thickness (δ_{th}) for the two kinetic mechanisms predicted using Cantera 2.2.1 and Chemkin PRO, for a methane flame at T_i = 300 K and P_i = 0.1 MPa. The maximum difference between the predicted values of S_L for the two mechanisms is 11%, while the maximum difference for δ_{th} is 17%. The differences shown in Figure 2.9 are the largest differences between the two kinetic mechanisms. For the values predicted for the C_2H_4, C_2H_6 and C_3H_8 flames the deviation while on the same order of magnitude is smaller. Due to these small differences only a single solver and mechanism, Cantera 2.2.1 and AramcoMech 1.3, are used to calculate laminar properties in this thesis.

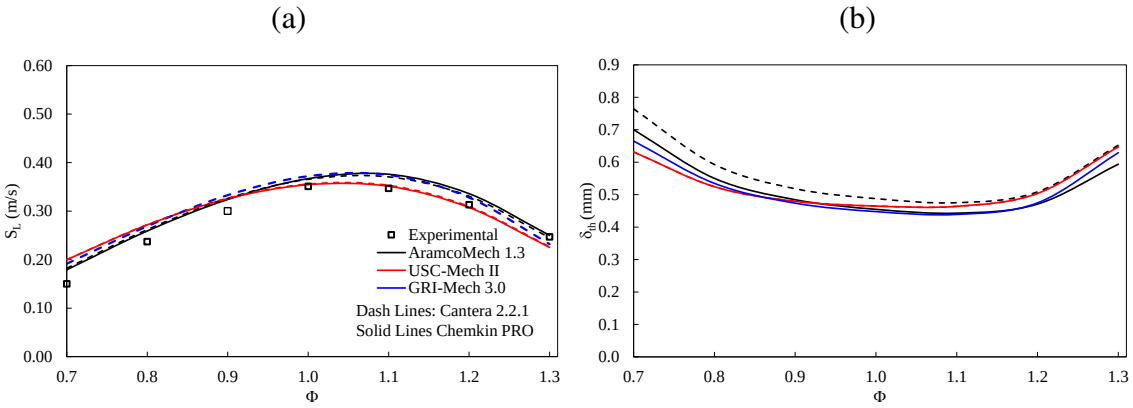

Figure 2.9: Results of 1D freely-propagating flame speed modelling of (a) laminar flame speed (S_L), and (b) flame thickness (δ_{th}) using Cantera 2.2.1 (dashed) and Chemkin PRO (solid) solvers and AramcoMech1.3 (red) and USC Mech Version II (black) mechanisms

Despite the fact that the data shown in Figure 2.8 is extensive, it does not include all of the available experimental data in the literature, as not all experimental results are applicable for the following study. As mentioned in the previous section, multiple definitions for turbulent flame speed are used within the research community. While no single definition is more correct than any other, turbulent flame speeds measured at different $\bar{c}$ surfaces cannot be compared to one another. Due to this, the experimental Bunsen flame data in this section has S_T values recorded at $\bar{c} = 0.05$ and 0.5. Studies that measured turbulent flame speeds at other values of progress variable [125] were excluded as a comparison against these values could not be made. For expanding flames, the Bradley relationship allows for S_T recorded at $\bar{c}$ other than 0.05 or 0.5 to be related back to usable values of progress variable. This allows any experimental data from an expanding flame to be used in a meaningful comparison. This is the reason why the majority of the data in Table 2.4 has been measured using expanding flames (CD, SB, CV and EV).

A variety of models for predicting $S_{T,0.5}$ and $S_{T,0.05}$ are examined in this thesis, with their accuracy being determined through a comparison against experimental data. Table 2.4 displays the entire range of data gathered for the thesis. Although the entire dataset is used in the thesis, only portions of the experimental data can be used for each purpose. The first study in Chapter 3 investigates the accuracy of sixteen turbulent flame speed cor-

relations, these expressions fall under both definitions of turbulent flame speed, S_T at $\bar{c} =$ 0.05 and 0.5. As a result experimental campaigns that measure flame speed at alternative progress variables or where the Bradley relationship is inappropriate, are omitted. The later studies in Sections 3.4.2 and 3.4.3 only examines five models with each expression predicting S_T at $\bar{c} = 0.5$, therefore the entire range of experimental data in Table 2.4 can be employed. Although the numerical model developed in Chapter 4 also predicts S_T at $\bar{c} = 0.5$ the entire range of data is not included in the validation of the computational approach due to time restrictions. As the entire range of experimental data from Table 2.4 is not used for each study, an overview of the experimental values employed for each study will be given in Chapters 3 and 4.

2.5.2 Correlation Studies

Over the past seven decades, more than forty correlations for predicting S_T have been developed. These correlations are based on laminar flame properties (S_L and δ_{th}), turbulent flow properties (Λ and u'), and dimensionless numbers (Re_t, Ka and Da). Some of these correlations are based on semi-empirical scaling laws [126, 127] and others are based on the physics of passive scalars [30]. Thanks to their simplicity and only relying on parameters readily available from experimental results, correlations are a very attractive method for quickly estimating turbulent flame speed. S_T is an essential closure parameter in many computational approaches for premixed flames, making these expressions valuable for efficient computational modelling of premixed turbulent flames. Zimont was one of the first to suggest closing the turbulent combustion equations by highlighting the importance of mean flame brush thickness (δ_t) and S_T [40]. Due to the widespread use of S_T correlations, considerable attempts to develop a universal expression have been made, however, a general expression for determining S_T does not exist. This is due to the complex nature of turbulent flames, and the influence that flame wrinkling, experimental flame configuration, bending effects and measurement techniques have on S_T. This problem is further compounded by the fact that no single definition for S_T exists, as previously discussed. Using Damköhler's physical model, the correlation shown in Equation 2.67 has

been proposed numerous times. To accurately predict S_T using this expression the adjustable parameters, C and n must be evaluated for the operating conditions of the flame under examination. C is typically on the order of unity while $n \approx 0.7$.

$$\frac{S_T}{S_L} = 1 + C\left(\frac{u'}{S_L}\right)^n \tag{2.67}$$

In addition to Damköhler's physical model, many other correlations of varying forms have been proposed. A list of these correlations and a brief description of the theory used is shown below. The author, equation, definition of S_T used and the adjustable parameters for each correlation are displayed. It should be noted that for the Zimont correlation the definition of S_T could not be determined. Though due to its extensive use and close agreement with $S_{T,0.5}$ it is assumed the expression predicts S_T at an iso-surface of $\bar{c}$ = 0.5. Only a portion of existing correlations are being examined for this thesis. Many more correlations exist [128–130], but are excluded from the current study due to difficulty in determining the iso-surface of $\bar{c}$ used to define S_T. A recently-derived correlation by Kolla et al. [28] is also excluded from the study due to the fact that the definition of $S_{T,0.05}$ did not relate well to the leading edge measurement for the expanding flames used in this study. While the correlation shows good agreement to Bunsen flame data it was not possible to achieve similar agreement with other burner set-ups, as also demonstrated by Lawes et al [131].

The variety in how the correlations are written is quite large and this is reflective of the underlying theory associated with each correlation. The following list provides a short overview of the theoretical basis and defines the expression for each of the fifteen correlations.

Zimont [98] developed the correlation for high Re_t combustion, characterised by flamelets thickened through their interaction with small scale turbulent structures. This type of regime has been defined by Zimont as intermediate steady propagation (ISP) flame, which corresponds to a flame with a Kolmogorov length scale less than δ_{diff}. Using

this theory, Zimont defined turbulent flame speed as

$$S_{T,0.5} = Cu'Da^{0.25} \tag{2.68}$$

where C = 0.52.

Klimov [132] examined how the propagating flame surface is contorted by a single-scale of turbulence for a period of time until opposite flame fronts merge due to flame propagation, defining S_T as:

$$S_{T,0.5} = Cu'Da^{0.25} \tag{2.69}$$

where C = 3.5.

Gouldin [133], under fractal theory where homogeneous turbulence is not space filling but rather has a fractal dimension, evaluated the influence of turbulent eddies on the flamelet surface area such that turbulent flame speed could be defined as:

$$\frac{S_{T,0.05}}{S_L} = C\left(\left\{1-\left(1-{A_t}^{-0.25}\,\mathrm{Re}_t^{-0.75}\right)\exp\left(-\left(\frac{A_t}{\mathrm{Re}_t}\right)^{0.25}\frac{u'}{S_L}\right)\times\right\}^{D-2}\right) \tag{2.70}$$
$$\qquad\qquad {A_t}^{0.25}\,\mathrm{Re}_t^{0.75}$$

where $D = 2.32-2.4, A_t = 0.37, C = 1$.

Duclos [53] employed the Kolmogorov-Petrovski-Piskunov (KPP) theory, which is based on the assumption that a turbulent flame propagates in a statistically one-dimensional planar domain into frozen turbulence and mixture composition. This allowed an expression for turbulent flame speed using CFM, which accounts for flame stretch using the large-scale strain, and is corrected by the function Γ_K, to be expressed as:

$$S_{T,0.5} = Cu'\left(\frac{C_\mu \Gamma_{\overline{k}}}{Sc_T}\right)^{0.5}\left[1+D_1\left(1+D_2\frac{u'}{S_L}\right)\right]^{-0.5} \tag{2.71}$$

where $C = 6, D_1 = 0.5, D_2 = 0.6, Sc_T = 0.7$ and for Γ_K see [53].

Mantel and Borghi [83] also predicted turbulent flame speed using the KPP theorem. For large turbulent Reynolds numbers, S_T is dependent on u', whereas the integral scale eddies have little effect. For smaller values of Re_t, the Kolmogorov scales have the largest influence on the turbulent flame speed.

$$S_{T,0.05} = Cu' {Re_t}^{0.25} \left[1 + \frac{D_2 {Re_t}^{0.5}}{\left(1 + D_1 \frac{S_L}{u'}\right)^{D_3}} \right]^{-0.5} \tag{2.72}$$

where $C = 0.7, D_1 = 0.8165, D_2 = 1.25$ and $D_3 = 1$.

Kerstein [134] developed the pair exchange model, which proposed that turbulent convection can be defined as a random exchange of state between fluid elements represented by pairs of cells in the direction normal to the flame and defines the displacement speed as:

$$\begin{aligned} S_{T,0.05} &= \sqrt{8D} \text{ when } D > 27.82 \\ S_{T,0.05} &= 1 + \tfrac{D}{2} \text{ when } D < 27.82 \end{aligned} \tag{2.73}$$

where $D = Cu' Re_t^{0.75}$ and $C = 0.082$.

Abdel - Gayed and Bradley [135] used the two-eddy theory to define S_T as the product of the rate of eddy decay and the amount of mixture which chemically reacts over the associated time scale of the eddy lifetime.

$$\frac{S_{T,0.05}}{S_L} = C \left\{ \begin{array}{c} {\mathrm{Re}_t}^{0.47} \frac{u'}{S_L} \left[1 - \exp\left(-3.178 {\mathrm{Re}_t}^{0.5} \frac{u'}{S_L} \right) \right] + \\ 8.13 {\mathrm{Re}_t}^{0.22} \frac{u'}{S_L} \left[1 - \exp\left(-0.391 {\mathrm{Re}_t}^{-0.25} \frac{u'}{S_L} \right) \right] \end{array} \right\}^{0.25} \tag{2.74}$$

where $C = 1.34$.

Anand and Pope [136] used a transport equation for the joint probability density function of the reaction progress variable and velocity to define turbulent flame speed through a Monte Carlo simulation.

$$\frac{S_{T,0.05}}{S_L} = C \frac{u'}{S_L} \tag{2.75}$$

where $C = 1.5$.

Gülder [126] used two distinct expressions for the turbulent flame brush thickness and a chemical lifetime expression to determine the time required for the flame to consume the mixture. Turbulent flame speed is then defined as:

$$\frac{S_{T,0.05}}{S_L} = 1 + C\left(\frac{u'}{S_L}\right)^{0.5} \mathrm{Re}_t{}^{0.25} \tag{2.76}$$

where $C = 0.62$.

Kobayashi [127] fit an expression to experimental data, measured over a range of turbulent conditions for C_1 - C_3 fuels and pressures up to 3.0 MPa [137], resulting in S_T being expressed as

$$\frac{S_{T,0.5}}{S_L} = C\left(\frac{u'}{S_L}\right)^{0.38}\left(\frac{P}{0.1\ MPa}\right)^{0.38} \tag{2.77}$$

where $C = 2.9\ \left(CH_4\ \&\ C_2H_4\right)$ and $C = 1.9\ \left(C_3H_8\right)$

Muppala [108] developed the expression based on the Zimont correlations with three additional terms, u'/S_L, Le and P/P_0. These new terms were included to better capture pressure and fuel effects as well as more accurately account for low to moderate turbulence, allowing the consumption speed to be defined as:

$$\frac{S_{T,0.5}}{S_L} = 1 + \frac{C}{Le}\mathrm{Re}_t^{0.25}\left(\frac{u'}{S_L}\right)^{0.3}\left(\frac{P}{0.1\ MPa}\right)^{0.2} \tag{2.78}$$

where $C = 0.46$.

Ronney [30] focused on flames within the distributed reaction zone correlations (DRZ). Here Damköhler argued that a flame could be distributed by a rapid increase in temperature over a large region of reactants, that are above the ignition temperature, whereas S_T is primarily influenced by increasing diffusive transport inside the flame with no effect on the rate of reaction. S_T is therefore defined as:

$$\frac{S_{T,0.5} - S_L}{u'} = C(Da)^{0.5} \tag{2.79}$$

$C = 0.12$.

Peters [97] related S_T to the flame propagation of the laminar flamelet by algebraically defining the influence of turbulence on the flame surface area ratio. The correlation was developed for the thin reaction zone where turbulent scales can penetrate and affect the thicker preheat zone. They cannot however, penetrate or influence the thinner reactions zones within the flame.

$$\frac{S_{T,0.05}}{S_L} = 1 - \frac{0.78}{2C}\frac{\Lambda}{\delta_{th}} + \left\{ \left(\frac{0.78}{2C}\frac{\Lambda}{\delta_{th}} \right)^2 + 0.78\frac{u'\Lambda}{S_L\delta_{th}} \right\}^{0.5} \tag{2.80}$$

where $C = 2.0$.

Cant [81] also used KPP theory. Cant neglected curvature effects and assumed that the Kolmogorov scales have the largest influence on creating strain rate effects within the flame. The correlation is based solely on turbulent characteristics and does not consider any chemistry effects, allowing the displacement speed to be expressed as:

$$S_{T,0.05} = Cu' \mathrm{Re}_t^{0.25} \tag{2.81}$$

where $C = 0.5$

Liu [103] expressed S_T using the same theory as Ronney [30] with different adjustable parameters.

$$\frac{S_{T,0.5} - S_L}{u'} = CDa^{0.47} \tag{2.82}$$

where $C = 0.14$

Figures 2.10 and 2.11 shows a comparison for the fifteen correlations outlined above for a variety of fuel and turbulent conditions as shown in Table 2.5.

Table 2.5: Experimental data used for comparison with literature correlations in Figures 2.10 and 2.11

Figure	Fuel	ϕ	p	T	$\frac{u'}{S_L}$	$\frac{\Lambda}{\delta_{th}}$	Ref
2.10 (a,b)	CH_4	1	0.1	300	2.0-5.4	50.0-102.5	[31]
2.10 (c,d)	CH_4	0.7-1.2	0.1	300	4.4-10.0	35.3-56.8	[33]
2.11 (a,b)	C_3H_8	1	0.1	300	1.3-5.5	9.4-10.5	[107]
2.11 (c,d)	C_3H_8	0.8-1.35	0.1	300	4.9-7.3	5.2-6.9	[101]

For the figures, the upper panels (a,b) show the impact of velocity fluctuations (u'), while the lower panels (c,d) show the impact of equivalence ratio (ϕ). The left panels (a,c) show data for $S_{T,0.05}$ and the right panels (b,d) show $S_{T,0.5}$. It can be seen that there is a large distribution in the predicted values of S_T as well as trends by each correlation. This can be attributed to the different underlying theory of each expression and the adjustable parameters not being tuned to the experimental data under examination. An in-depth investigation and discussion relating to each correlation will occur later in Chapter 3.

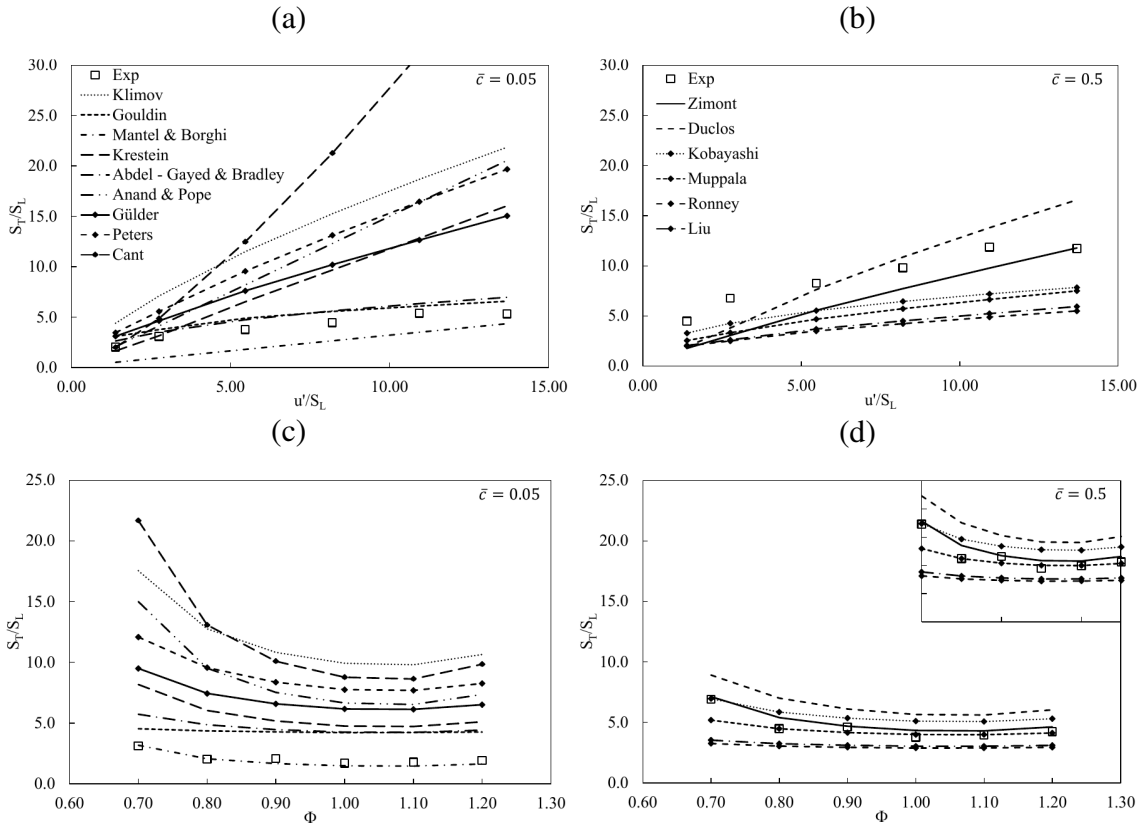

Figure 2.10: Results of a comparison between the fifteen literature corrections and experimental values shown in Table 2.5. The upper panels show the impact of velocity fluctuations (u') for correlations that predict (a) $S_{T,0.05}$, and (b) $S_{T,0.5}$, while the lower panels show the impact of equivalence ratio (ϕ) for predictions of (c) $S_{T,0.05}$, and (d) $S_{T,0.5}$

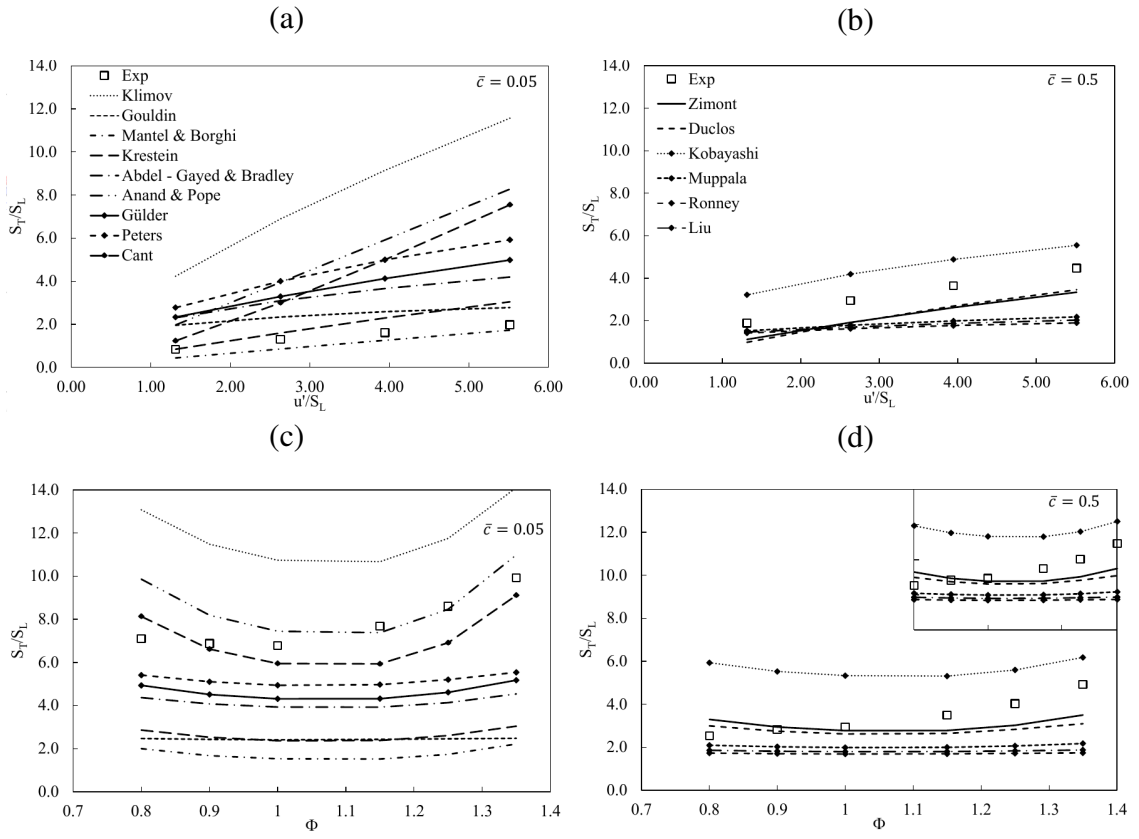

Figure 2.11: Results of a comparison between the fifteen literature corrections and experimental values shown in Table 2.5. The upper panels show the impact of velocity fluctuations (u') for correlations that predict (a) $S_{T,0.05}$, and (b) $S_{T,0.5}$, while the lower panels show the impact of equivalence ratio (ϕ) for predictions of (c) $S_{T,0.05}$, and (d) $S_{T,0.5}$

2.5.3 Numerical Studies

In the past, computational methods struggled to accurately define premixed turbulent flame speed. With improved computational power in recent years, accurate results have been produced using LES and DNS approaches. The following section will discuss the findings of some of the previous RANS studies before moving on to the more accurate models employing LES and DNS methods. While LES and DNS are more appropriate methods for predicting turbulent flame speed, the RANS approaches were a first step towards modelling S_T and so are worth discussing.

Using the CFM2-b flame surface density approach, Duclos et al. [53] predicted comparable result to the experiential results of Abdel-gayed et al. [54]. The experimental results are recorded in a highly turbulent bomb $(0.17 < u'/S_L < 45.95)$ with no mean flow for propane-air mixtures with $\phi = 0.8$ and 1.1 for a pressure and temperature of 1 atm and 328 K respectively and an integral length scales between 36 and 45 mm. The bending effects were accounted for by the fact that the merging rate is assumed proportional to the flame surface density squared. Even though the values of S_T and the bending effects, shown in the trends, are underpredicted by the FSD approach, the overall results are very comparable for a RANS approach. Similar to the above study, Choi and Huh [55] used a coherent flamelet model to show agreement between predicted and measured values of S_T. The model was compared with results measured by Bradley et al. [138] for a centrally ignited spherical flame that propagates outwards with intense isotropic turbulence $(2.5 < u'/S_L < 17.5)$. The results were grouped by the *KLe* term, where *Le* and *K* refers to Lewis number and Bradleys turbulent Karlovitz number based on the Taylor length scale (λ), respectively. For the data studied *KLe* had values of 0.070, 0.14, 0.30, 0.63. Similar to Duclos et al., the experimental and predicted values of S_T are comparable, and without bending effects the trends show satisfactory agreement. Peters [97] used the time-averaged G-equations in a RANS approach to show agreement with experimental data recorded by Abdel-gayed et al. [54], where the calculated values of S_T relate to a Re_t = 625 and the experimental data is measured for a range of Re_t 500 and 750 for a pressure and temperature of 1 atm and 328 K respectively. Peters also illustrated the importance of Λ in the G-equations for S_T over a range of integral length scales.

The Reynolds-averaged Navier-Stokes methods calculate an exact time-averaged flow field and involves closure models that require turbulent flame speed as an input are needed. As a result, RANS can struggle to accurately predict the complex nature of premixed turbulent combustion. For this reason, and the availability of high levels of computational power, LES and DNS are seen to be more appropriate approaches for calculating S_T. Lecocq et al. [139] presented a comparison between LES predicted and measured val-

ues of S_T for a laboratory flame at atmospheric conditions with methane-air mixture for equivalent ratios between 0.8 and 1.0, integral length scales between 24.3 - 50.0 mm and $0.0 < u'/S_L < 10.5$. Using an extended coherent flamelet model (ECFM), coupled with a transport equation for the flame surface density, the authors were able to show satisfactory agreement with experimental data measured by Shy et al. [31]. The simulated results illustrate bending effects for both $\phi = 0.8$ and 1.0 At higher velocity ratios however, the simulated results tend to overpredict the values of turbulent flame speed for both equivalent ratios.

Keppeler et al. [140] developed a model based on the fractal characteristics of the flame surface using the RANS closure approach proposed by Gouldin [141] and predicted turbulent flame speed for a Bunsen burner flame. Twenty five operating conditions were simulated and compared to the values measured by Kobayashi et al. [32, 114, 142] with temperature of 300 K, Λ = 1 mm and $0.13 < u'/S_L < 4.3$. The comparison was made for four operating pressures between 0.1 - 2.0 MPa for methane and propane flames. CH_4 simulations show satisfactory agreement across the entire range of turbulence for the atmospheric conditions and very slightly over predicting the bending effect for 0.5 MPa. The C_3H_8 flame also shows agreement to the values but slightly underpredicts the slope of the measured flame speed ratio for the increasing turbulent intensity.

Charlette et al. [143] presented a new model after showing that the standard dynamic model is insufficient for modelling turbulent flame wrinkling. The power-law dynamic flame wrinkling model was therefore developed to deal with the wrinkling process in premixed turbulent combustion. Unlike the work by Lecocq et al., an algebraic closure approach was used to define the flame surface density. To validate the new model, LES predicted values were compared to experimental results from Abdel-Gayed and Bradley [135] for 15 experimental points for Re_t between 540 and 3320. The comparison of the experimental and predicted results showed partial agreement. An underprediction of the turbulent flame speed can be observed for the smaller values of turbulent velocity ratio. For the larger Reynolds number cases, good representation of the bending effect was found.

For intermediate and lower Re_t bending can be seen, a lack of experimental data however, inhibits validation of the predicted values of S_T at higher velocity ratios.

Due to the high computational expense of direct numerical simulations, many DNS campaigns use simple geometries and small simulation domains in an effort to reduce CPU costs. Nivarti et al. [62] examined the bending effects in a turbulent premixed flame by simulating a statistically-planar methane/air flame using the 3D geometry, where the domain has a stream wise length of 1.5 cm. The computational campaign was carried out for stoichiometric conditions for five cases where the inlet turbulent intensity was the only parameter varied between runs and results in a range of Re_t between 39 and 737 at atmospheric temperature and pressure. Assuming single step chemistry and $Le = 1$, Navarti et al. predicted the results of turbulent global consumption flame speed exhibiting bending effects. Multi-step chemistry would introduce additional effects within the flame and experimental results would allow for validation of the simulations, bending effects have been observed in the DNS domain and can be studied in depth.

Similar to the work by Nivarti, Fru et al. [61] used a simple geometry of a cubic computational domain, with 4 cm sides, to investigate the impact of u' and ϕ on the burning rate of premixed turbulent flames using DNS. Simulations were carried out at atmospheric conditions for equivalence ratios between 0.6 and 1.0 and turbulence intensities ranging from 2.0 to 22.0 m/s. Unlike the previous DNS study discussed, Fru et al. employ a C_1 chemical kinetics mechanism consisting of 16 species and 25 reactions [144] to calculate the turbulent consumption speed of each flame (S_c). S_c is an interesting measure of the turbulent flame speed S_T, with the two being related using an iso-surface scaling area. Fru et al. was able to illustrate both the linear increase in turbulent consumption speed for low turbulence and the bending effects at higher levels of u' for five mixture equivalence ratios and a large range of Re_t.

While expensive, DNS studies examining three-dimensional laboratory simulations have been carried out. Bell et al. [145, 146] simulated the laboratory slot burner of Fi-

latyev et al. [147] and the V-flame for methane-air mixtures at atmospheric conditions. The slot burner has a computational domain of 7.5 x 5 x 10 cm and operated at stoichiometric conditions and u'/S_L = 0.69. The V-flame operated at leaner and more turbulent conditions with $\phi = 0.7$ and u'/S_L = 1.1. Both studies employed DRM19 to define detailed chemistry using 20 species and 84 reactions. This allowed Bell et al. to calculate turbulent global consumption speed of 2.45 x S_L and 3.95 x S_L for the slot burner and V-flame respectively. When compared to the experimental data, an error of 4% and 19% can be found for the two flame speeds respectively. This shows it is possible to model laboratory scale turbulent premixed flames using DNS. To achieve this level of accuracy however, detailed descriptions of the experimental inlet conditions were required and the simulation is therefore extremely computationally expensive. Furthermore, even though DRM19 is a chemical kinetics mechanism, a more detailed mechanism would better describe the combustion process.

2.6 Research Need

As previously discussed, turbulent flame speed is essential for combustion device design, as it can be used to estimate the species consumption and heat release rates and allow for the reactivity of the flame to be assessed. S_T is also a key parameter for the closure of reactive numerical models. Because of this S_T has been the focus of many studies including experimental, analytical and computational approaches. Although experimental campaigns can give exact values of turbulent flame speeds, they can be expensive, require high levels of expertise and time-consuming to initially commission. This is more apparent at gas turbine conditions, in which pressures and temperatures are high.

In comparison, analytical approaches are fast and simple to implement, however, the underlying theory and adjustable parameters are not always applicable to the flames under examination. Figure 2.11 clearly shows the large distribution in predicted values using S_T correlations. Coupling this with a lack of detailed chemical description, correlations

are not always applicable for predicting premixed turbulent flame speed. This becomes more apparent for H_2 and C_{2+} flames, in which the fuel effects begin to have a large influence on the flame and S_T. In an attempt to improve the applicability of analytical approaches, an empirical correlation with adjustable parameters optimized using a large experimental database of S_T values has been developed. A Nelder-Mead simplex direct search method [43], implemented in Matlab, and $\approx$ 335 data points, over a wide range of conditions, are employed to define seven parameters in the new model for defining S_T.

While numerical approaches allow for the inclusion of more detailed turbulence and chemistry, it is often very computationally expensive, time-consuming and requires high levels of user expertise. For DNS study of statistically-planar methane-air flames by Nivarti et al., a typical simulation used $\approx 2.5\text{x}10^4$ core-hours when running on the DARWIN (Intel Sandy Bridge E5-2670) and ARCHER (Cray XC30) supercomputers [62]. The simulations by Fru et al. required 10 days of computing time for the coarsest grid and two months for the finest using a variety of supercomputers.

In an attempt to minimize this expense, reduced chemistry is employed. As shown in the DNS approaches previously described, even the most complex finite rate chemistry methods employed very small chemical kinetic mechanisms. For RANS and LES simulations, simplifications to the chemistry are also made. The G-equations and FSD closure approaches use detailed chemistry, however, all of this chemical information is reduced into a single quantity; laminar flame speed. Therefore the complex chemistry effects are not fully being taken into account by any of these approaches. Other closure methods, such as the BML and the EBU models, take this simplification further and completely neglect chemistry effects.

In an effort to preserve chemical fidelity and minimise computational cost, a one-dimensional turbulent flame speed solver has been developed. The computional model is built on top of the existing Cantera 2.3.0 laminar freely-propagating flame speed model. The modifications to Cantera have been made to introduce turbulence and to account for

turbulent flow effects such as Reynold's fluxes, turbulent chemistry interactions and the influence of temperature fluctuations on mean reaction rate. As a result, the model will be able to account for a range of turbulent conditions as well as describing the effects of chemistry in premixed turbulent flames.

Chapter 3

Premixed Turbulent Flame Speed Correlations

3.1 Introduction

As discussed in Chapter 2, turbulent flame speed correlations are used extensively for the closure of computational premixed turbulent combustion models and as an aid in determining species consumption rate, heat release rate, and flame reactivity in gas turbine combustors at untested operating conditions. Due to the complexity of turbulent premixed flames, the large number of correlations available in the literature, and the array of underlying theories associated with each expression, the correct choice of correlation to predict S_T is not always clear. The aims of this chapter are to provide insight into the accuracy of fifteen state-of-the-art S_T correlations, as presented in Section 2.5.2, and to determine the most appropriate correlations to use under different turbulent premixed combustion conditions. A novel alternative empirical S_T correlation for use across the entire range of turbulent conditions will also be presented. It is based solely on experimental data obtained from the literature and uses a Nelder-Mead simplex direct search method [43] to fit adjustable parameters to minimise the mean absolute percentage error (MAPE) between the modelled and measured data. To assess the accuracy of the fifteen literature correlations and newly-developed expression, the following three studies are carried out and presented in this chapter:

1. A comparison of the fifteen literature correlations plus the newly-developed empirical correlation for eleven experimental studies performed at over 200 different flame conditions on the basis of S_T. This study will henceforth be referred to as Study A.

2. A further study of the four most accurate literature correlations and the newly-developed empirical correlation. Each expression will be compared to an extended data set of fifteen experimental studies comprising of 335 different flame conditions on the basis of S_T. This study will henceforth be referred to as Study B.

3. Optimisation of the five most accurate correlations from Study B, using the Nelder-Mead simplex direct search method. The optimised correlations will then be compared to the same data as Study B to investigate what, if any, improvements to values and trends of S_T can be made. This study will henceforth be referred to as Study C.

An absolute percentage error (APE) value is used to determine the difference between correlation predictions and experimentally obtained S_T values as shown in Equation 3.1. Overall correlation accuracy can then be calculated by average MAPE over the range of the data under examination, as shown in Equation 3.2.

$$APE = \left| \frac{x_{\text{exp},i} - x_{corr,i}}{x_{\text{exp},i}} \right| \times 100 \tag{3.1}$$

$$MAPE = \frac{\sum_{i=1}^{n_{points}} APE}{n_{points}} \tag{3.2}$$

where $x_{exp,i}$ is the experimental value i, $x_{corr,i}$ is the value predicted by the correlation, and n_{points} is the number of data points in the corresponding study. The MAPE provides a single error value for each correlation, making it convenient to assess accuracy for the large numbers of correlations and data. When using an extensive array of data, a correlation with a low MAPE has the ability to be applied over a wide range of turbulent conditions. This ability is of key importance for model closure within CFD. Equally as important is a correlation's ability to predict experimental trends. Accurate predictions of trends are important for combustion device design. During gas turbine development,

turbulent flame speed results obtained at atmospheric pressure are frequently extrapolated to engine conditions. This can result in the introduction of errors and/or uncertainty. To assess the correlations' ability to match trends, S_T trends predicted by each correlation in Study B and C will be compared graphically to experimental S_T trends over a range of fuel types, equivalence ratios and turbulent velocity ratios.

3.2 Experimental Results

To assess the correlations applicability to predicting turbulent flame speed, S_T measurements from a number of experimental campaigns found in the literature are used. An overview of the data gathered for this thesis can be seen in Section 2.5.1. As previously noted, the entire range of experimental S_T data is not applicable to all of the studies in this chapter. For Study A the S_T expressions selected are defined at progress variable iso-surfaces equal to either 0.05 or 0.5. To remove the influence of $\bar{c}$, predictions from each correlation are compared to experimental S_T values measured at applicable $\bar{c}$ iso-surfaces only. This is achieved with Bunsen flames comparing S_T measurements at the same operating conditions recorded at surfaces of $\bar{c}$ = 0.05 and $\bar{c}$ = 0.5. As a result, the experimental measurements from Bunsen flames are restricted to studies that measured S_T at both values of progress variable. Although S_T was measured at various values of $\bar{c}$ for spherically-expanding flames the relationship developed by Bradley [35] is used to determine S_T at $\bar{c}$ = 0.05 and $\bar{c}$ = 0.5, making the data applicable for all of the literature correlations. Equation 2.65 shows how the relationship, which defines the ratio of S_T at different surface radii, is used to relate S_T back to values associated with $\bar{c}$ = 0.05 and $\bar{c}$ = 0.5. Due to these restrictions, only 200 of the available 335 data points can be used for this study. The remaining 135 data points either (i) did not measure S_T at $\bar{c}$ = 0.05 and $\bar{c}$ = 0.5 or, (ii) were performed using apparatus in which the Bradley relationship is not applicable. An overview of the 200 experimental points can be seen in modified Borghi diagram shown in Figure 3.1. The points in colour denote the 200 experimental points that can be used and the greyscale points refer to the remaining 135 data points. More details for the 200 points are displayed in Table 3.1.

Table 3.1: Experimental operating conditions, apparatus and measured $\bar{c}$ iso-surfaces for each data set used in the study. Symbols shown relate to the data in the modified Borghi diagram in Figure 3.1

Flame	Apparatus	Fuel	$\bar{c}$	ϕ	P (MPa)	$\frac{u'}{S_L}$	$\frac{\Lambda}{\delta_{th}}$	$\frac{S_{T\bar{c}=0.5}}{S_L}$
A ◇	CB	CH_4	0.1	0.8	0.1	10.6-20.8	70.1-70.6	9.4-12.6
B □	CB	CH_4	0.1	0.8	0.2-1.0	5.0-14.5	3.5-170.1	5.0-15.8
C △	SB	CH_4	0.6	0.8 & 1.2	0.1	1.9-16.4	3.9-6.4	1.9-6.1
D ×	BB	CH_4	0.5	0.7-1.35	0.1	2.6-11.7	2.9-5.6	2.7-5.0
E +	BB	C_2H_6	0.5	0.7-1.45	0.1	2.2-8.8	3.8-7.0	2.0-6.4
F ○	BB	C_3H_8	0.5	0.8-1.35	0.1	2.4-7.3	4.7-6.9	1.6-4.9
G ◇	SB	CH_4	0.1	0.6-1.3	0.5	8.2-45.5	3.7-136.1	9.4-33.6
H □	SB	CH_4	0.34	0.6-1.3	0.1	2.0-15.1	1.8-4.5	1.8-4.8
I △	BB	CH_4	0.05	0.7,0.8,1.0	0.1	0.65-2.4	2.3-9.4	5.6-11.1
J ×	CB	CH_4	0.5	0.7-1.4	0.1	1.4-34.7	23.4-105	2.1-20.5
K +	SB	CH_4	0.1	0.6-1.2	0.1	4.4-10.0	35.3-56.8	3.8-6.9
L ○	BB	CH_4	0.5	0.7-1.0	0.1	2.0-15.1	1.8-4.5	1.8-4.8
M ◇	SB	C_3H_8	0.6	0.7-1.45	0.1	1.9-9.9	5.3-7.0	2.0-8.0
N □	CV	CH_4	0.6	0.8-1.25	0.1	1.3-6.3	8.1-10.0	1.9-5.1

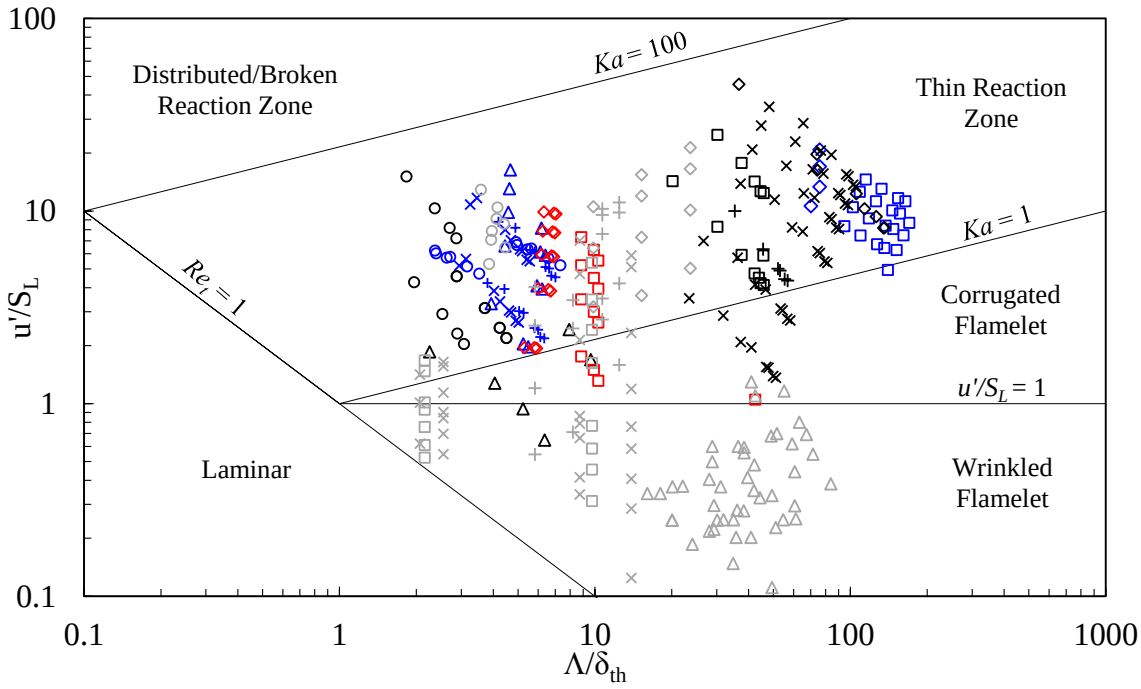

Figure 3.1: Turbulence and flame conditions for the data displayed in Table 3.1 plotted on a Borghi diagram modified by Peters [41]

The expressions examined in Study B are the most accurate correlations from Study A. Each of the correlations in Study B predict the turbulent flame speed at a progress variable iso-surface of $\bar{c} = 0.5$. This allows the entire range of experimental data in Section 2.5.1 to be employed when testing the accuracy of the five correlations as there is no need to have turbulent flame measurements at both progress variables. A detailed description of the data can be seen in Table 2.4, with the greyscale symbols in Figure 3.1 providing a visual overview of the turbulent properties of this data. When compared to the coloured points in the diagram, it can be seen that the additional 135 data points fill the gap between the two groups of data in the thin reactions zone and corrugated flamelet regimes. The results from Savarianandam et al. [120] also provides a substantial volume of experimental measurements in the wrinkled flamelet regime. With these additional experimental points the correlations can be examined in much greater detail compared to Study A. Another contribution of the new data is the addition of flames involving large fuel molecules, increasing the number of experimental points of C_2+ flames from 55 to 119. Comparing the

correlations to these operating conditions is important as natural gas is mainly comprised of methane but can contatin larger hydrocarbons (e.g. ethane, propane, butane) as high as 50% by volume.

Due to the large volume and variety of conditions in the experimental studies used in this chapter the data has been divided into data groups of more manageable size. Four data groups are defined based on the various flame operating conditions, this allows for a deeper examination of the large data set. The correlations are first compared to methane flame data over the entire range of experimental test conditions (Data Group 1). Correlations are then compared, again for CH_4, at elevated pressure conditions only (0.2-1.0 MPa) (Data Group 2). A third comparison for CH_4 takes place for conditions at elevated-pressure (0.2-1.0 MPa) and high turbulence $(u'/S_L > 10)$, which are of relevance to industrial combustion systems (Data Group 3). Finally, fuel effects are examined through the comparison of the correlations for ethane and propane flames (Data Group 4).

3.3 Methodology

The extensive volume of data discussed in Section 3.2 requires a straightforward method to represent the accuracy of each correlation is essential. The mean absolute percentage error was selected over other forms of defining error as (1) it gives the same weight to predicted values regardless of whether the correlated flame speed is above or below the measured value of S_T, and (2) the size of the MAPE depends on both the absolute deviation $(x_{exp,i} - x_{corr,i})$ and the experimental value $(x_{exp,i})$, therefore, the deviation from a large number gives a smaller error compared to the same deviation from a smaller number. Examples of these characteristics can be seen in Table 3.2. Other statistical methods see these traits are seen as limitations however for this work they are desirable. This is because (1) an over/under-prediction of S_T is treated the same because both predictions have the same deviation from the target value, this is shown in Table 3.2 where the ± 5 predictions around the experimental value of 10 have the same error. The second characteristic means that similar deviations from different predicted values are not treated the

same as the deviation is further from the target value as displayed in the Table 3.2 for characteristic (2).

Table 3.2: Examples of the mean absolute percentage error characteristics

Characteristic	(1)		(2)	
Predicted	5	15	10	10
Experimental	10	10	15	5
Absolute Deviation	5	5	5	5
MAPE (%)	50.0	50.0	33.3	100.0

A detailed discussion regarding the literature correlations took place Section 2.5.2, therefore Table 3.3 and 3.4 give a brief recap of the turbulent flame speed expressions. Table 3.3 presents the author and correlation equation, while Table 3.4 displays the original authors' adjustable parameters used for each correlation. The definition of S_T used by each author either $S_{T_{0.05}}$ or $S_{T_{0.5}}$ is also shown. It should again be noted that for the Zimont correlation the definition of S_T could not be determined. However due to its extensive use and close agreement with $S_{T_{0.5}}$ it is assumed the expression predicts S_T at an iso-surface of $\bar{c} = 0.5$. Additionally Table 3.4 shows that the correlation developed by Ronney and Liu are essentially the same format but with different adjustable parameters. As two separate authors have proposed these correlations each expression is examined individually. Although a large number of correlations are being examined, only a portion of the total number of correlations available in the literature are examined for this study. Many more correlations exist [128–130], but are excluded due to difficulty in determining the definition of S_T used by these expressions. A recently-derived correlation by Kolla [28] is also excluded from the study because the definition of $S_{T_{0.5}}$ did not relate well to the leading edge measurement for expanding flames used in this study. While the correlation shows good agreement with Bunsen flame data, it is not possible to achieve similar agreement with other burner set-ups, as also demonstrated by Lawes et al [131].

Table 3.3: Turbulent premixed flame correlations by various authors and their reported parameters

#	Author	Correlation
C1	Zimont	$S_{T_{0.5}} = au'Da^b$
C2	Klimov	$S_{T_{0.05}} = au'^b {S_L}^c$
C3	Gouldin	$\frac{S_{T_{0.05}}}{S_L} = a\left\{\left[1-\left(1-{A_t}^{-b}{Re_t}^{-c}\right)\cdot \exp\left(-\left(\frac{A_t}{Re_t}\right)^b \frac{u'}{S_L}\right)\right]{A_t}^b {Re_t}^c\right\}^{D-2}$
C4	Duclos	$S_{T_{0.05}} = au'\left(\frac{C_\mu \Gamma_{\bar{k}}}{Sc_t}\right)^b \left[1+D_1\left(1+D_2\frac{u'}{S_L}\right)\right]^{-b}$
C5	Mantel & Borghi	$S_{T_{0.05}} = au'{Re_t}^b \left[1+\frac{D_2 {Re_t}^b}{\left(1+D_1\frac{S_L}{u'}\right)^{D_3}}\right]^{-c}$
C6	Kerstein	$S_{T_{0.05}} = \begin{cases}\sqrt{8D} \text{ when } D > 27.82 \\ 1+\frac{D}{2} \text{ when } D < 27.82\end{cases}$ where $D = au'Re_t^b$
C7	Abdel-Gayed & Bradley	$\frac{S_{T_{0.05}}}{S_L} = a\left\{\begin{array}{c}{\mathrm{Re}_t}^b \frac{u'}{S_L}\left[1-\exp\left(-3.178{\mathrm{Re}_t}^c\frac{u'}{S_L}\right)\right]+ \\ 8.13{\mathrm{Re}_t}^d\frac{u'}{S_L}\left[1-\exp\left(-0.391{\mathrm{Re}_t}^{-e}\frac{u'}{S_L}\right)\right]\end{array}\right\}^e$
C8	Anand & Pope	$\frac{S_{T_{0.05}}}{S_L} = a\frac{u'}{S_L}$
C9	Gülder	$\frac{S_{T_{0.05}}}{S_L} = 1+a\left(\frac{u'}{S_L}\right)^b {\mathrm{Re}_t}^c$
C10	Kobayashi	$\frac{S_{T_{0.5}}}{S_L} = a\left(\frac{u'}{S_L}\right)^b \left(\frac{P}{0.1\ MPa}\right)^c$
C11	Muppala	$\frac{S_{T_{0.5}}}{S_L} = 1+\frac{a}{Le}{\mathrm{Re}_\mathrm{t}}^b \left(\frac{u'}{S_L}\right)^c \left(\frac{P}{0.1\ MPa}\right)^d$
C12	Ronney	$\frac{S_{T_{0.5}}-S_L}{u'} = aDa^b$
C13	Peters	$\frac{S_{T_{0.05}}}{S_L} = 1-\frac{0.78}{2a}\frac{\Lambda}{\delta_{th}}+\left\{\left(\frac{0.78}{2a}\frac{\Lambda}{\delta_{th}}\right)^b+0.78\frac{u'\Lambda}{S_L\delta_{th}}\right\}^c$
C14	Cant	$S_{T_{0.05}} = au'\,\mathrm{Re}_t^b$
C15	Liu	$\frac{S_{T_{0.5}}-S_L}{u'} = aDa^b$

Table 3.4: Original adjustable parameters defined by the authors for the correlations presented in Table 3.3

#	Adjustable Parameters
C1	a = 0.52, b = 0.25
C2	a = 3.5, $b = 0.7, c = 0.3$
C3	D = 2.32-2.4, A_t = 0.37, a = 1, $b = 0.25, c = 0.75$
C4	a = 6, D_1 = 0.5, D_2 = 0.6, Sc_t = 0.7, $\Gamma_{\tilde{k}}$ See [53] , b = 0.5
C5	a = 0.7, D_1 = 0.8165, D_2 = 1.25, D_3 = 1, $b = 0.25, c = 0.5$
C6	a = 0.082, b = 0.75
C7	a = 1.34, $b = 0.47, c = 0.5, d = 0.22, e = 0.25$
C8	a = 1.5
C9	a = 0.62, $b = 0.5, c = 0.25$
C10	a = 2.9 (CH_4 & C_2H_4), b = 0.38, $c = 0.38$ a =1.9 (C_3H_8), $b = 0.38, c = 0.38$
C11	$a = 0.46, b = 0.25, c = 0.3, d = 0.2$
C12	a = 0.12,$b = 0.5$
C13	a = 2.0, $b = 2, c = 0.5$
C14	a = 0.5,$b = 0.25$
C15	a = 1.5, $b = 0.47$

The newly-developed empirical correlations, based on the entire range of data in Table 2.4, has been optimised using the Nelder-Mead simplex direct search method. The new expression takes the form shown in Equation 3.3 with constants a-g being defined to ensure a minimum overall average MAPE. Similar to many literature expressions the correlation uses the power law to define the relationship between turbulent flame speed and a variety of combustion properties. The power law allows for a relative change in the combustion properties to result in a propertional change in S_T, independent of the initial size of the combustion properties.

$$\frac{S_{T_{0.5}}}{S_L} = a + b\left(\frac{\Lambda}{\delta_{th}}\right)^c \left(\frac{u'}{S_L}\right)^d \phi^e Le^f \left(\frac{P}{P_{ref}}\right)^g \tag{3.3}$$

While the expression in Equation 3.3 is empirical in nature, the variables were selected in an attempt to best represent the chemical/flow properties and the interaction between turbulence and chemistry within premixed turbulent combustion. Although Re_t, Da, and

Ka are not explicitly included in the expression, the $\frac{\Lambda}{\delta_L}\frac{u'}{S_L}$ term can be considered a combination of the three dimensionless numbers and therefore is representative of the effect of the combined parameters. The combination of the three terms can be seen in Equation 3.4. The equivalence ratio and Lewis number are used to represent the composition of the air-fuel mixture and preferential diffusion effect within the flame receptively. The pressure effects are defined in a manner similar to that employed by Kobayashi and Muppala, in which a reference pressure of 0.1 MPa is used to normalize the operating pressure of the flame under examination. Finally, the correlation is normalised using the laminar flame speed, as is common practise for S_T correlations.

$$\begin{aligned} Re_t^x \cdot Da^y \cdot Ka^z &= \left(\left(\frac{u'}{S_L}\right)\left(\frac{\Lambda}{\delta_{th}}\right)\right)^x \left(\left(\frac{u'}{S_L}\right)^{-1}\left(\frac{\Lambda}{\delta_{th}}\right)\right)^y \left(\left(\frac{u'}{S_L}\right)^{\frac{3}{2}}\left(\frac{\Lambda}{\delta_{th}}\right)\right)^z \\ &= \left(\left(\frac{u'}{S_L}\right)^x \left(\frac{u'}{S_L}\right)^{-y} \left(\frac{u'}{S_L}\right)^{\frac{3}{2}z}\right)\left(\left(\frac{\Lambda}{\delta_{th}}\right)^x \left(\frac{\Lambda}{\delta_{th}}\right)^y \left(\frac{\Lambda}{\delta_{th}}\right)^z\right) \\ &= \left(\frac{u'}{S_L}\right)^{x-y+\frac{3}{2}z} \left(\frac{\Lambda}{\delta_{th}}\right)^{x+y+z} \Rightarrow c = x-y+\frac{3}{2}z \quad \& \quad d = x+y+z \end{aligned} \tag{3.4}$$

The algorithm for determining the constants a-g is implemented using the *fminsearch* function within Matlab which uses the Nelder-Mead direct simplex search method of Lagarias et al. [148]. *fminsearch* aims to reduce the error between the experimental and predicted values of S_T by minimising the function displayed in Equation 3.5 through optimisation of a-g. It can be seen that Equation 3.5 corresponds to the MAPE equation. More details on the the Nelder-Mead direct simplex search method are provided in Appendix A

$$f(a,\ldots,g) = \frac{x_{\text{exp}} - \left(a + b\left(\frac{\Lambda}{\delta_L}\right)^c \left(\frac{u'}{S_L}\right)^d \phi^e Le^f \left(\frac{P}{P_{ref}}\right)^g\right)}{x_{\text{exp}}} \tag{3.5}$$

Using this approach and tight convergence criteria of 1×10^{-10} two sets of parameters were determined for Equation 3.3. These parameters can be seen in Table 3.5, where the

first set is defined to predict values of S_T at atmospheric pressure conditions. At high pressure the yse of a single set of parameters, optimized over the entire range of experimental data, resulted in an unacceptably high MAPE for the elevated pressure flames. For this reason a second set of parameters have been developed for $P > 0.1$ MPa. These are shown in the bottom row of the table.

Table 3.5: Optimised parameters for each correlation to be used at atmospheric and elevated pressure conditions.

Conditions	a	b	c	d	e	f	g
$P = 0.1$ MPa	2.244	0.132	0.61	0.516	-0.35	-1.215	-2.96
$P > 0.1$ MPa	-0.242	5.611	-0.244	0.35	0.193	-1.323	0.381

3.4 Results and Discussion

The following section is divided into three subsections with each section presenting the results and a discussion of the three studies described in the introduction to this chapter. The large data set has been divided into data groups of more manageable sizes in order to better facilitate a more in depth investigation of the results. Allowing for a deeper examination of the large data set. The first section will display results for the comparison between the fifteen literature correlations, the newly-developed empirical expression, and two hundred experimental data points. This will be followed by a comparison between the five most accurate literature correlations, the new expression, and the entire range of gather experimental data. Finally, the difference between the original and newly-obtained adjustable parameters for the literature correlations are examined again for the full range of experimental data. The first study only includes a MAPE analysis for the sixteen correlations and the remaining studies comprise of a MAPE and experimental trend investigation.

3.4.1 Study A

Figure 3.2 shows the MAPE of each of the correlations using the parameters given in Table 3.4 for the four data groups. Due to the high MAPE values in the bar chart, Figure

3.3 shows the results for correlations with the lowest MAPEs to provide more resolution.

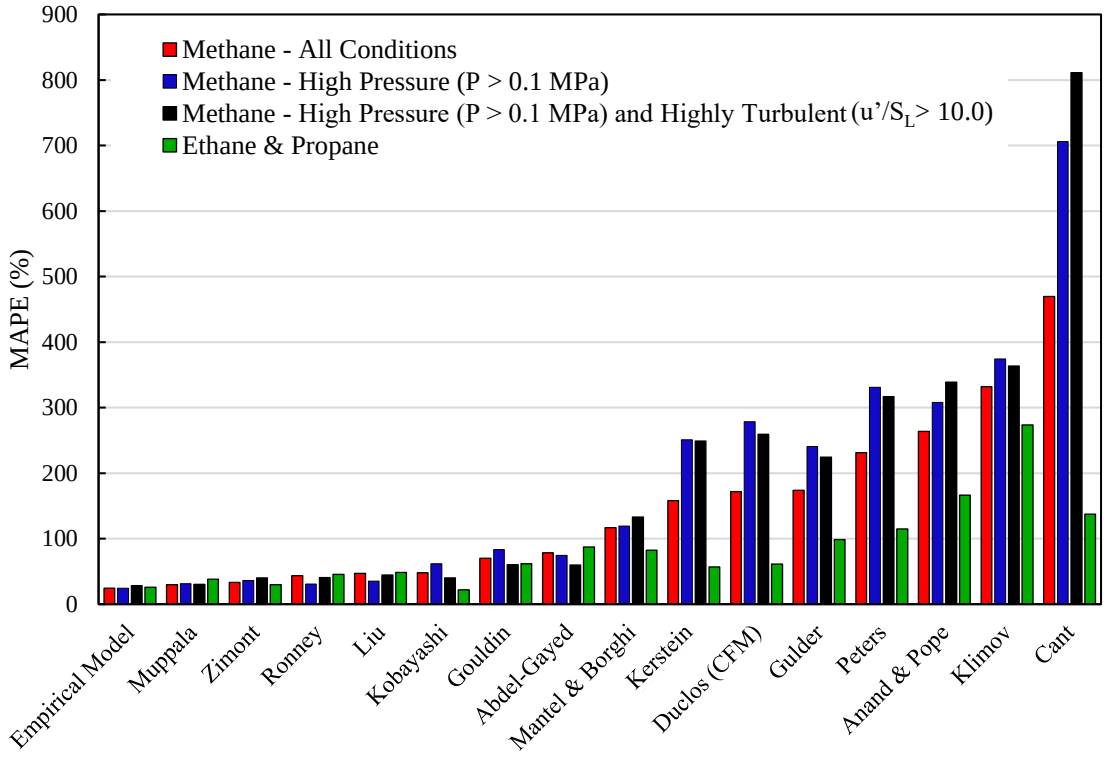

Figure 3.2: MAPE for the newly-developed empirical correlation and 15 correlations from the literature for Data Groups 1-4 using 200 data points

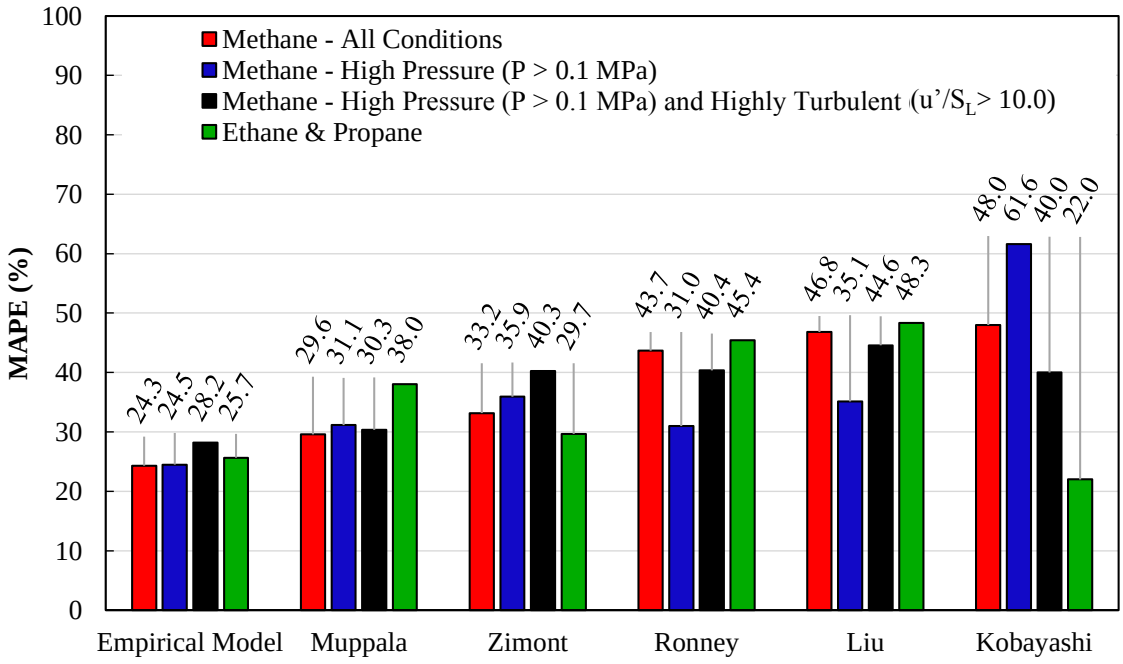

Figure 3.3: MAPE for the newly-developed empirical correlation and 5 most accurate correlations from the literature for Data Groups 1-4 using 200 data points

It can be seen in Figure 3.2 that there are significant errors for some correlations. This is because (1) the correlations are being employed over ranges of conditions for which they were not previously calibrated, and (2) the underlying theories on which these correlations are based are not applicable for the entire range of data used in the study. The bending effect, as discussed in the previous chapter, is a well-known phenomenon, where at high turbulent intensities the relationship between S_T and u' becomes non-linear and in some cases may even invert. It is possibly caused by flamelets merging due to the inability of the flame surface area to grow due to the increased turbulence within the flame [147]. Many correlations, Klimov, Mantel & Borghi, Abdel-Gayed & Bradley, Anand & Pope, and Cant do not capture this trend and so tend to over-predict S_T in moderate to intense turbulence $(u/S_L < 10)$, therefore leading to the higher error.

Other correlations, Gülder and Kobayashi, were curve-fitted to a large arrays of experimental data. The quality of the data used during the fitting process is therefore important. A large portion of the data used to derive Gülder did not consider flame stretch, which

therefore affected its accuracy [149]. Kobayashi was fitted to experimental data over a wide range operating conditions and as a result, has one of the lowest MAPEs in the study, however, the empirical nature of the expression will always lead to a certain level of error. The correlations by Ronney and Liu are the same expression however separate authors have proposed different adjustable parameters and so these correlations are examined individually. They are based on the distributed reaction zone (DRZ), first defined by Damköhler who argued that a flame may be distributed by a rapid increase in temperature over a large region of reactants that are above the ignition temperature, however S_T is primarily influenced by increasing diffusive transport inside the flame with no influence on the reaction rate. The DRZ model is applicable when $1.2 < Da < 6.0$ (assuming that $\delta_{th} = 0.1\delta_{diff}$) but under-predicts S_T at higher values of Da [31]. Although a large portion of the data sets examined lie within this distributed reaction zone, not all do. Therefore outside the DRZ, the underlying theory no longer holds true and these correlations become less applicable, resulting in higher MAPEs. Similar trends are seen for; Zimont, Kerstein and Gouldin, correlations which are accurate for certain ranges of turbulent conditions only. Zimont is based on intermediate steady propagation (ISP) flames defined by $Re_t \gg 1$ and $Da \gg 1$. Kerstein follows a similar trend and is only applicable when $\delta_{th} \gg \Lambda$ and $u'/S_L > 1$. The values of S_T predicted by Gouldin are highly dependent on the stretch term (Γ_k). The definition of this term is only valid when $S_L \frac{\delta_L}{\nu} \simeq 1$ and becomes less applicable when this criterion is not satisfied. Muppala has been shown to be the most accurate literature correlation using the original authors adjustable parameter. This is due to the fact that the Muppala correlation is based on the Zimont correlation, with the addition of three terms: (1) an additional velocity ratio (u'/S_L), (2) pressure ratio (P/P_0), and (3) Lewis number (Le) [108]. These additions result in the correlation being more applicable at both low and high levels of turbulence.

The MAPE of the newly-developed empirical correlation is the smallest for the entire range of expressions examined for all of the methane data at all conditions, Data Group 1. Compared to the next most accurate correlation, developed by Muppala, the empirical correlation's MAPE decreases by $\approx 5\%$ going from 29.6% to 24.3%. This trend is also seen

for the breakdown of the methane data groups, Data Group 2 and 3, where the empirical correlation again has the lowest MAPE. For the larger fuel molecule data group (DG4) the correlation by Kobayashi is capable of achieving a smaller MAPE as a significant portion of the larger fuel molecule data comes from experimental campaigns carried out by Kobayashi and so the correlation is specifically optimized towards this data. Nevertheless the empirical correlation still performs well for these conditions. The newly-developed correlation achieves the lowest overall MAPE of 24.7% across all data groups. The Muppala correlation is the next most accurate correlation predicts S_T such that a MAPE of 31.9% is achieved for the entire 200 operating conditions. In summary, Study A saw the development of an optimised S_T correlation that can be used to model S_T with an error lower than any published correlation across a wide range of data.

3.4.2 Study B

Figure 3.4 shows the comparison between the four most accurate correlations from the literature (Zimont, Muppala, Kobayashi, and Ronney) using the original author's parameters and the correlation developed in this work for the extended set of 335 data points. Although the correlation by Liu is more accurate than the Kobayashi expression, it is based on the same theory as the equation developed by Ronney but with different adjustable parameters. The MAPE predicted by the Ronney correlation is smaller than that of Liu expression therefore it is omitted from future sections. The MAPE results are again presented for the four groups using the same characteristics to define each data group.

To assess the ability of correlations to match S_T trends predicted values are compared to individual S_T data points. The selected data covers three regimes of turbulence (thin reaction zone $(Ka > 1)$, corrugated flamelet zone $(Ka < 1)$ and wrinkled flamelet $(u' < S_L)$) and a wide range of Da (0.29 - 31.2), for varying values of ϕ. This allows for an extensive study of each correlation over a broad range of turbulent combustion conditions. Figure 3.5 show trends for CH_4 and C_3H_8 flames at atmospheric pressure with varying values of turbulent velocity ratio and equivalence ratio. A similar evaluation of each correlation is

then carried out for the experimental data, with similar turbulent and chemistry properties, at elevated pressures. These predictions can be seen in Figures 3.6 where u'/S_L and ϕ vary for CH_4, C_2H_6 and C_3H_8 flames.

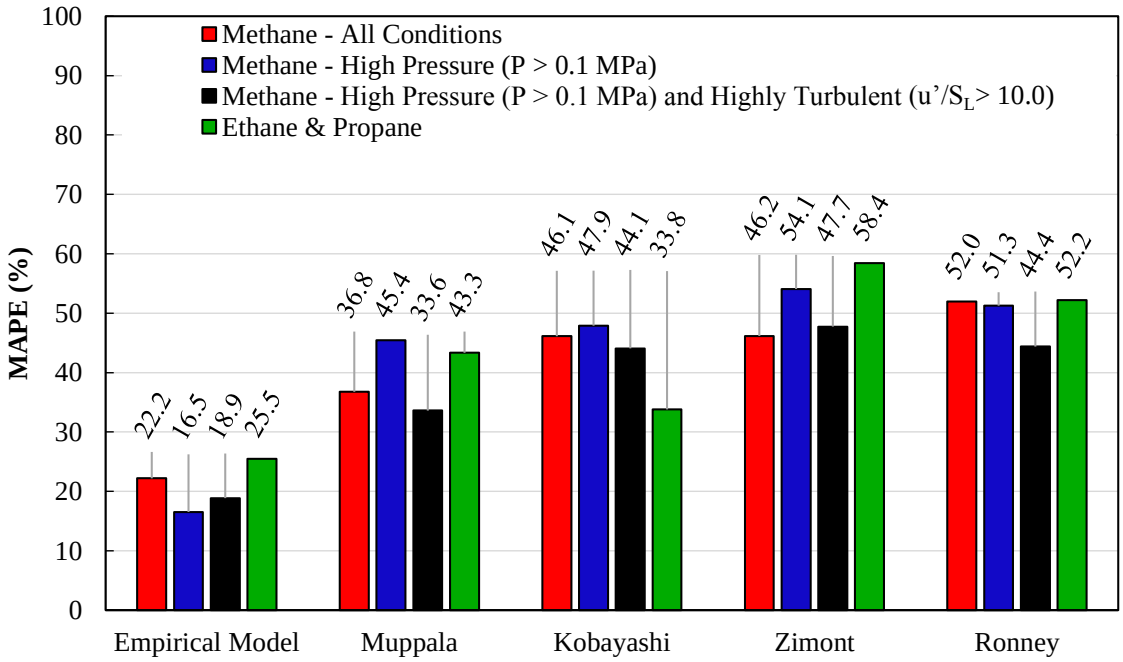

Figure 3.4: MAPE for the newly-developed empirical correlation and 5 most accurate correlations from the literature for Data Groups 1-4 using 335 data points

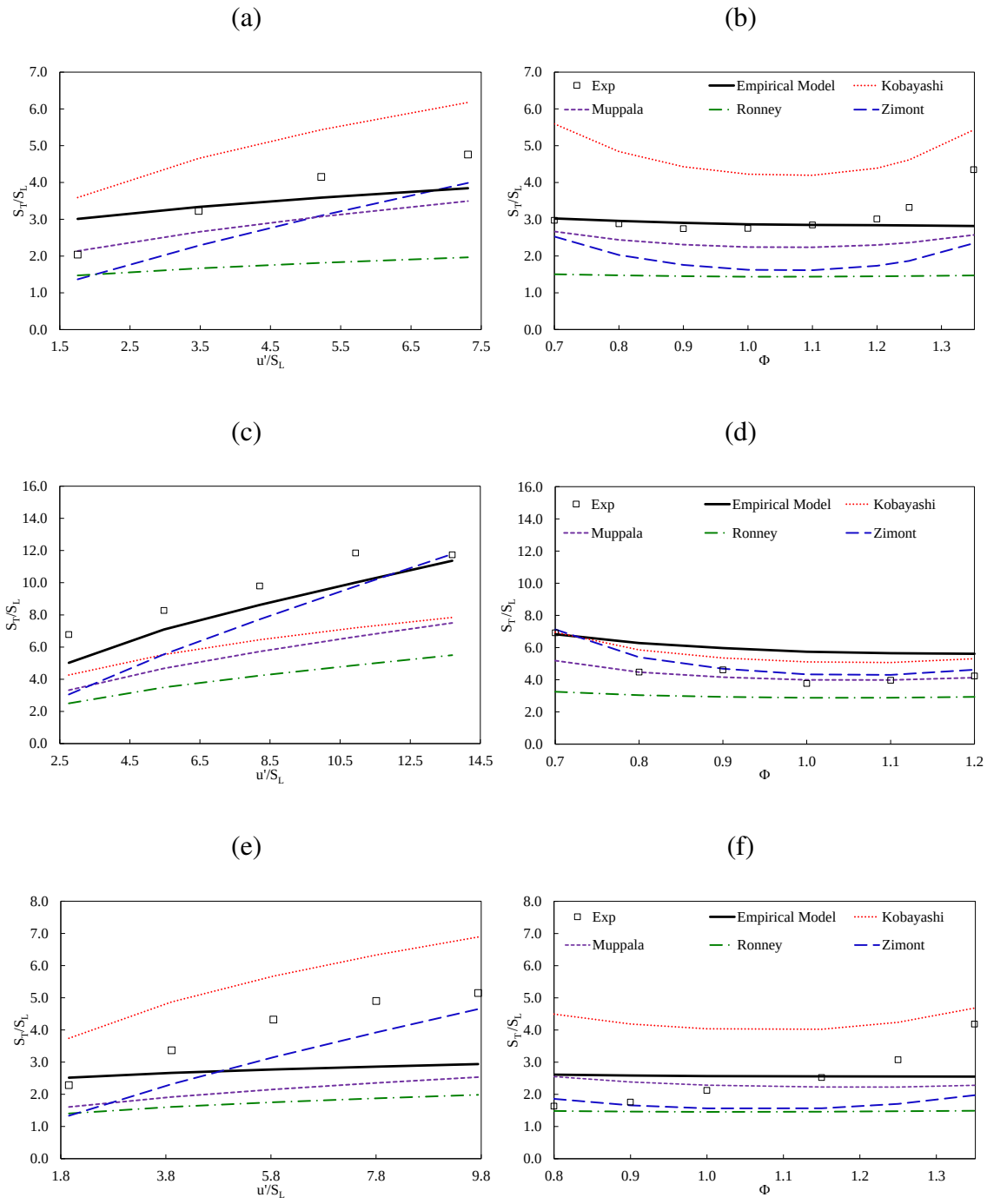

Figure 3.5: Predicted trends for (a) Flame C (CH_4) for ϕ= 0.8, (b) Flame D (CH_4) with u'= 0.91, (c) Flame J (CH_4) where ϕ= 1.0, (d) Flame K (CH_4) for u'= 1.5, (e) Flame R (C_3H_8) at ϕ= 1.0, (f) Flame F (C_3H_8) with u'= 0.91, using the original authors adjustable parameters at inlet pressures and temperatures of 0.1 MPa and 300 K respectively

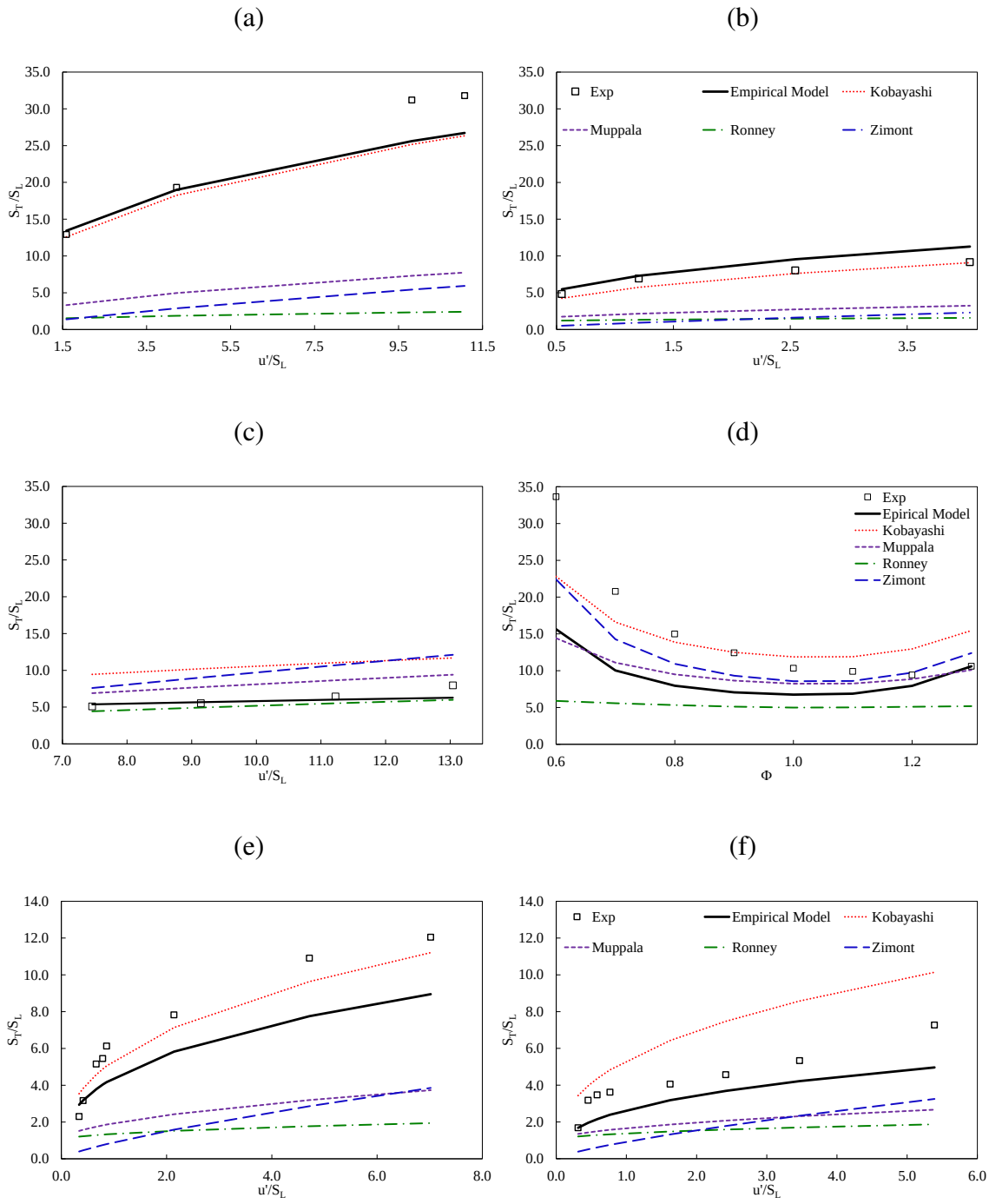

Figure 3.6: Predicted trends for (a) Flame Q (CH_4, T = 300 K, P = 3.0 MPa) at ϕ= 0.9, (b) Flame Q (CH_4, T = 300 K, P = 0.5 MPa) where ϕ= 0.9, (c) Flame B (CH_4, T = 300 K, P = 0.5 MPa) with ϕ= 0.8, (d) Flame G (CH_4, T = 360 K, P = 0.5 MPa) for u'= 2.0, (e) Flame T (C_2H_4, T = 300 K, P = 0.5 MPa) at ϕ= 0.7, and (f) Flame T (C_3H_8 where T = 300 K, P = 0.5 MPa) for ϕ= 0.9, using the original authors adjustable parameters

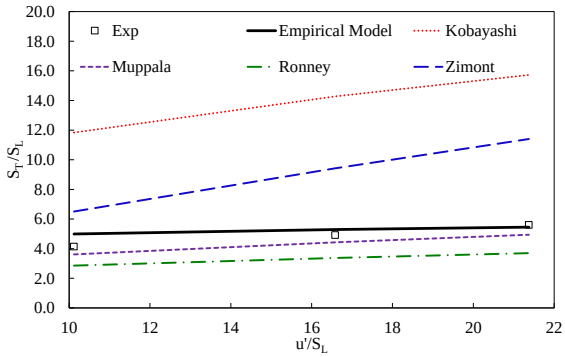

Figure 3.7: Predicted trends for Flame S (C_3H_8, T = 300 K, P = 0.4 MPa) where ϕ= 0.71 using the original authors' adjustable parameters

Study A found that the most accurate literature correlations were those by Zimont, Kobayashi, Ronney, Muppala and the newly-developed empirical correlation. Study B aims to provide further insight into the five most accurate state-of-the-art turbulent flame speed correlations from the previous study. This is achieved by: (1) comparing a larger set of experiential data consisting of 335 points, and (2) examining the correlations ability to match trends. The same Data Groups used in Study A are also in Study B. For the newly-developed empirical correlation although the range of experimental data has increased, the MAPE for each of the data groups has dropped. This is due to the expression being optimized over the full 335 points rather than the 200 used in Study A. If the correlation had been optimised over the smaller data set, a lower MAPE could be achieved for the 200 points. However, a set of adjustable parameters applicable to a wider range of conditions can be defined when the larger data set is employed. The MAPE associated with each of the literature correlations increases with the additional data points. The order of most accurate correlation also changes where the expressions by Zimont and Ronney are overtaken by that of Kobayashi.

An additional 135 data points at low turbulence levels are used in Study B and as a result the correlations are tested against weak turbulent flames, which did not occur in Study A. The correlation developed by Zimont was intended to be used for flames within the Intermediate steady propagation (ISP) zone characterised by $\eta < \delta_{diff}$. For turbulent

flames in this zone small scale turbulence serves to increase the area of the flame, however as the time scale for small scale turbulence is low equilibrium between increase in flamelet area and area consumption due to flamelet self-propagation will be rapidly reached. When this $\eta < \delta_{diff}$ is not satisfied, the Zimont correlation struggles to accurately predict flame speed. This is particularly evident when comparing results of Data Groups 2 and 3, the error is much larger for Data Group 2 which includes S_T at weak turbulence. The average MAPE for Data Groups 1, 2 and 4 show $\lesssim 13\%$ increase in MAPE over the corresponding data groups in Study A. The MAPE fo for Data Group 3 which contains high turbulent flames, shows a $\approx 7\%$ increase in the MAPE when compare to the corresponding group in Study A. The Ronney correlation was similarly developed for a specific regime of turbulence known as the DRZ, defined by $1.2 < Da < 6.0$ (assuming that $\delta_{th} = 0.1\delta_{diff}$). The correlation performs better within this regime, outside it the expression developed by Ronney still performs adequately but with higher errors. It does however account for the increase in MAPE between the two data sets. Similar to the Zimont correlation there is a large increase in MAPE for Data Groups 1, 2 and 4 when compared to the change in Data Group 3 between Study B and Study A.The increase in the error between the two studies is greater for the Zimont correlation, going from 32.2% to 50.5% compared to an increase of 47.2% to 52.1% for the Ronney expression. This is due to a larger portion of the data being in the DRZ when compare to the number of points within the ISP zone. Therefore Ronney is more applicable to the new data, resulting in a smaller increase in error.

The Muppala correlation, a modified version of the Zimont expression, is again the most accurate of the correlations from the literature. The additional terms in the Muppala correlation enables the expression to better account for lower turbulence and elevated pressure flames, as can be seen in Figure 3.4. Although the MAPE increases by the same margins as the Ronney expression, the Muppala equation still remains 10% more accurate for methane at all conditions than the next most accurate correlation. While the difference in the overall MAPE between the Muppala and the Kobayashi correlations is much smaller ($\approx 3\%$), due to Kobayashi better representing the larger fuel molecule data rather than Muppala failing to replicate the trends of the additional ethane/propane data. The

Kobayashi correlation is empirically-based and so depends solely on the data for which it was developed. With more than 40% of the additional data coming from studies carried out by Kobayashi or his group, the correlation is better optimized towards these data points and can be seen in the substantial improvement in overall MAPE between the first and current study. This is especially true for the high pressure methane data group and the ethane/propane data group.

In terms of trends, the main interest is the correlations' ability to match the shape of the data. However, predicting the individual values of S_T is also important. The plots displayed in Figures 3.5 to 3.7 are examples that best represent the range of data in each group. The discussion of the results displayed in each plot can also be applied to the corresponding Data Group as a whole. Figure 3.5(a) and (b) show turbulent flame speeds from low pressure and low turbulence methane flames. For the constant ϕ experimental points, the expression by Zimont and Kobayashi both capture the trend well. Due to the low turbulence level within the flame, however, the Zimont correlation underestimates the values of S_T whereas the empirical nature of the Kobayashi expression leads to an over-prediction of the turbulent flame speed. The newly-developed empirical correlation has the lowest MAPE out of all of the expression for the data set in Figure 3.5(a) however, the slope of the trend is under-predicted. Ronney predicts a similar trend to the new correlation but due to weak turbulence predicts the lowest values of S_T of all the expressions under investigation. The Zimont correlation also under-predicts the turbulent flame speed due to the low levels of turbulence present however it is the best expression at capturing the experimental trends. Although the Muppala correlation is based on the Zimont expression, it is unable to predict the experimental trends as well as the Zimont equation, however, the additional terms employed by Muppala still result in good trend agreement and the lowest MAPE of all the literature correlations tested.

The constant turbulent intensity results are shown in Figure 3.5(b). None of the expressions are capable of capturing the entire experimental trend shown. The newly-developed empirical correlation and the Muppala correlation best match the lean - $\phi < 1.2$ data, but,

struggle at the very rich conditions. Due to the lack of experimental data at $\phi > 1.2$, the newly-developed correlation is unable to predict these values, and the theory of the Muppala expression struggles to account for the chemistry present in the highly rich flame. The Ronney correlation, similar to the other two correlations, predicts the trend well for $\phi < 1.2$. Again the low turbulence level present in the flame causes the expression to highly under-predict the flame speed values. The trends predicted by the Zimont and Kobayashi correlations show the opposite characteristics, predicting turbulent flame speed trends for $\phi > 1.0$ well, but over-predicting for lean flames.

Figures 3.5(c) and (d) show the turbulence within the flame is much higher than the previous figures. The slope of the trends with constant equivalence ratio are very similar for all of the correlations with the except of the Zimont correlation. The Zimont correlation predictions can be explained in either of two ways: (1) the initial linear trend is captured well, however the points at high u'/S_L experience bending effects therefore the linear relation between u' and S_T disappear and the Zimont expression cannot account for this, or, (2) there is no bending effect and the relationship between u' and S_T is linear over the entire range of u'/S_L and the Zimont correlation predicts a steeper slope than is present in the experimental data. The Zimont correlations generally predicts trends well for these conditions, therefore it is much more likely that bending effects are present in the flame at the high turbulent intensities and Zimont is does not account for this phenomenon. Without additional experimental data it is difficult to make a definitive decision on the trend predicted by Zimont. For the remaining correlations, the predicted slopes represent the data in Figure 3.5(c) well over all velocity ratios. The empirical correlation achieves the lowest MAPE by a large margin. The under-predicted value of the literature correlations is most likely due to the use of adjustable parameters not calibrated for the conditions investigation.

The trends shown in Figure 3.5(d) display the opposite characteristics to the low pressure flame displayed in Figure 3.5(b). The turbulent flame speed at $\phi = 0.7$ for the low pressure, high turbulence methane flame is much larger than the remaining equivalence

ratios. As a result, the correlation by Zimont and the Kobayashi, which struggled to predict the trends in Figure 3.5(b), both capture the trend in Figure 3.5(d) well. The newly-developed correlation and the Muppala correlation predict similar trends to each other. The Muppala correlation very accurately determines S_T for $\phi > 0.7$ but the empirical correlation overestimates turbulent flame speed over the same range of conditions. The theory used by the Zimont and Muppala correlations are well suited to these conditions and this can be seen in the accurate prediction of the turbulent flame speed values. Although the expression by Ronney shows similar trends to Muppala and Kobayashi, the flame speeds are highly under-predicted again due to the inappropriate adjustable parameters.

Figures 3.5(e) and (f) examines low pressure and turbulent C_{2+} flames. All of the correlations fail to predict either the trend or the majority of the values of S_T. Unlike methane flames, large hydrocarbon flames exhibit preferential diffusion effects. Preferential diffusion occurs in flames when the major species have different diffusive velocities $(v_{i,diff})$. While $v_{CH_4,diff} \approx v_{O_2,diff}$, $v_{C_{2+},diff} < v_{O_2,diff}$ and $v_{H_2,diff} > v_{O_2,diff}$, which contributes to the variation in maximum turbulent flame speed with respect to equivalence ratio. This effect can be seen for propane flames in Figure 3.5(f) where u'/S_L is constant and S_T increases from a minimum at the leanest conditions to a maximum at the richest conditions. The correlations from this work and by Muppala have *Le* terms, which helps to account for fuel effects. Nevertheless, none of the correlations have the ability to account for differences in the major species diffusive velocities. The constant equivalence ratio flames are shown in Figure 3.5(e). Similar to the methane flame, the correlations by Zimont and Kobayashi best match the trends but under and over-predict turbulent flame speed values respectively. The remaining correlations show very little sensitivity to the variations of u'/S_L in the experimental data with the newly-developed, Muppala and Ronney correlations progressively under-predicting S_T. For the constant u'/S_L flame shown in Figure 3.5(f), none of the correlations can predict the trend due to the larger influence preferential diffusion has on non-stoichiometric conditions. This can most notably be seen with the Zimont correlation that predicts a trend more closely related to a methane flame.

The data in Figure 3.6 includes flames with similar properties to those shown in Figure 3.5, however, these flames are operating at pressures greater than 0.1 MPa. The data in Figures 3.6(a) and 3.6(b) are elevated pressure, low turbulence methane flames. At these conditions for both the constant ϕ and u'/S_L trends the newly-developed and the Kobayashi correlation show good agreement due to their empirical nature matching the conditions. The Muppala correlation does not predict these trends. This is most likely due to the adjustable parameters being unoptimised for the data under examination, as the Muppala correlation was not developed for $P > 0.5$ MPa [108]. For the Ronney and Zimont correlations the predicted results were as expected, similar to the low turbulence CH_4 flames the expressions under-predict the values and slopes of the experimental data in both the constant ϕ and u'/S_L trends due to the low turbulence in the flame.

Figures 3.6(c) and 3.6(d) show a significant spread in the predicted turbulent flame speed for the high pressure, high turbulence methane flames. Figure 3.6(c) show constant u'/S_L plots, all of the expressions predict the slope of the trend well as all the correlations were developed for the same regimes of turbulence. The spread of values of turbulent flame speed is associated with the various adjustable parameters implemented in each correlation. Figure 3.6(d) shows that similar observations regarding the constant ϕ data. The majority of the S_T correlations predict the shape of the experimental data for $\phi > 0.7$ but fail to account for the fast flame speed at the leanest conditions due to the exceptionally high turbulence present at $\phi = 0.7$.

Figure 3.6(e) and 3.6(f) show experimental data for propane and ethane flames operating with high pressure and low turbulence. At these conditions, the correlations exhibit many of similar trends that were observed in the methane data. The Muppala correlation under-predicts both the slope and values of the experimental data due the adjustable parameters being unoptimised for the data under examination. The expressions from Zimont and Ronney also struggle due to the low level of turbulence present resulting in under-predicted turbulent flame speeds. The Kobayashi and newly-developed expressions best match the trend, however, unlike the CH_4 data, the correlations struggle to predict the

values of S_T. Only a small portion of data is available for the final set of C_{2+} flames at high pressure and turbulence levels. Nevertheless, a constant ϕ trend can still be examined.

This trend, unlike the other flames at high turbulence levels, is best matched by the correlation from this work and by Muppala and Kobayashi, while those by Ronney and Zimont predict a trend that more closer matches trends from the previous data groups. The reason for this is the high levels of u'/S_L, which results in bending effects, causing the flatter slope of the trend.

3.4.3 Study C

The results of Study A and Study B show that the most accurate literature correlations are those developed by Zimont, Kobayashi, Ronney and Muppala. The original authors adjustable parameters for each correlations were defined to best match a range of experimental data available to the authors at the time of the correlation development. Study C significantly expands the volume of data when compared to the data sets used by the original authors, this allows the expressions to be optimised over a much wider range of conditions. The Nelder-Mead simplex direct search method, as described in Section 3.3, was employed for the optimization process and enabled the adjustable parameters shown in Table 3.6 to be obtained. During the optimization process it was found that when compared with other variables such as fuel type, Re_t, Da, Le, ϕ pressure had the largest influence on MAPE. Therefore two sets of parameters are required to obtain acceptable MAPE values for flames at various pressures, this is also the case for the newly-developed correlation. The first set is for atmospheric pressure flames ($P = 0.1$ MPa) and the second set is for flames at elevated pressures ($P > 0.1$ MPa). Henceforth the parameters optimised for atmospheric pressure data and high pressure will be defined as the atmospheric pressure form and high pressure form of the parameters, respectively.

Table 3.6: Optimised parameters for the literature correlation to be used at atmospheric and elevated pressure conditions. Elevated pressure parameters are in brackets

Author/Parameter	P (MPa)	a	b	c	d
Zimont	0.1	0.532	0.326		
	> 0.1	0.302	0.325		
Kobayashi	0.1	2.972	0.077	0.844	
	> 0.1	1.201	0.291	0.694	
Muppala	0.1	0.941	0.317	-0.047	-1.378
	> 0.1	3.340	-0.246	0.642	0.500
Ronney	0.1	0.311	0.522		
	> 0.1	0.215	0.389		

The same experimental data used in Section 3.4.2 was examined again and S_T is predicted using a combination of optimised parameters as shown in Table 3.6. The selection of the optimised parameter was solely dependent on the operating pressure of the flame for both the MAPE and trend analysis.

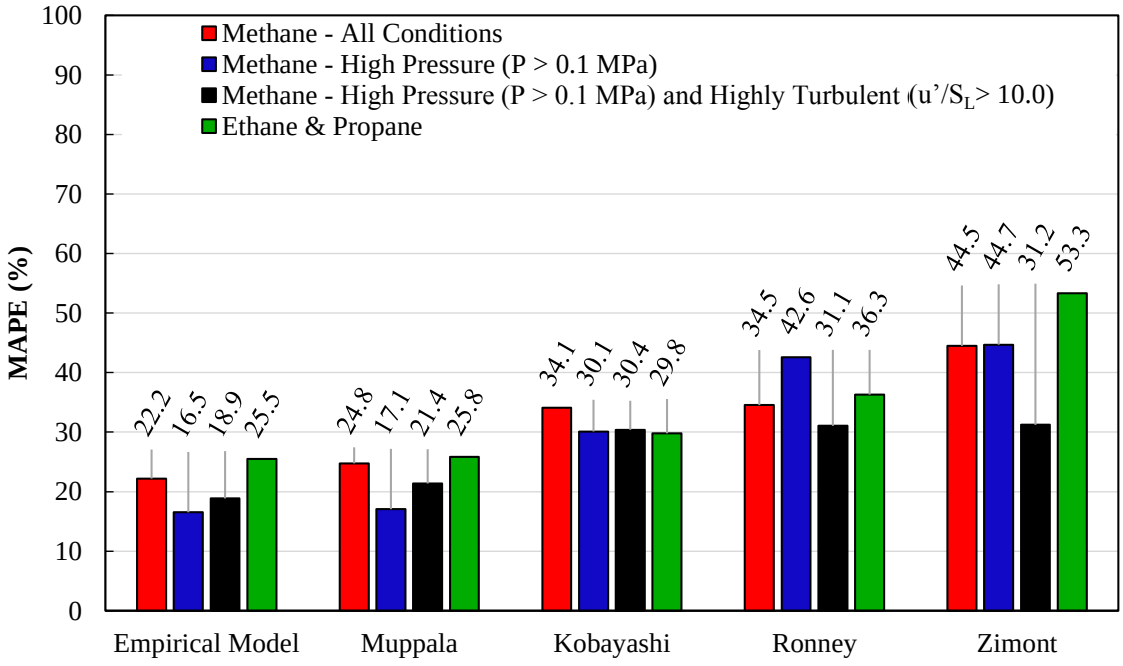

Figure 3.8: MAPE for the newly-developed empirical correlation and the five most accurate correlations from the literature, with optimised adjustable parameters, for Data Groups 1-4 using 335 data points

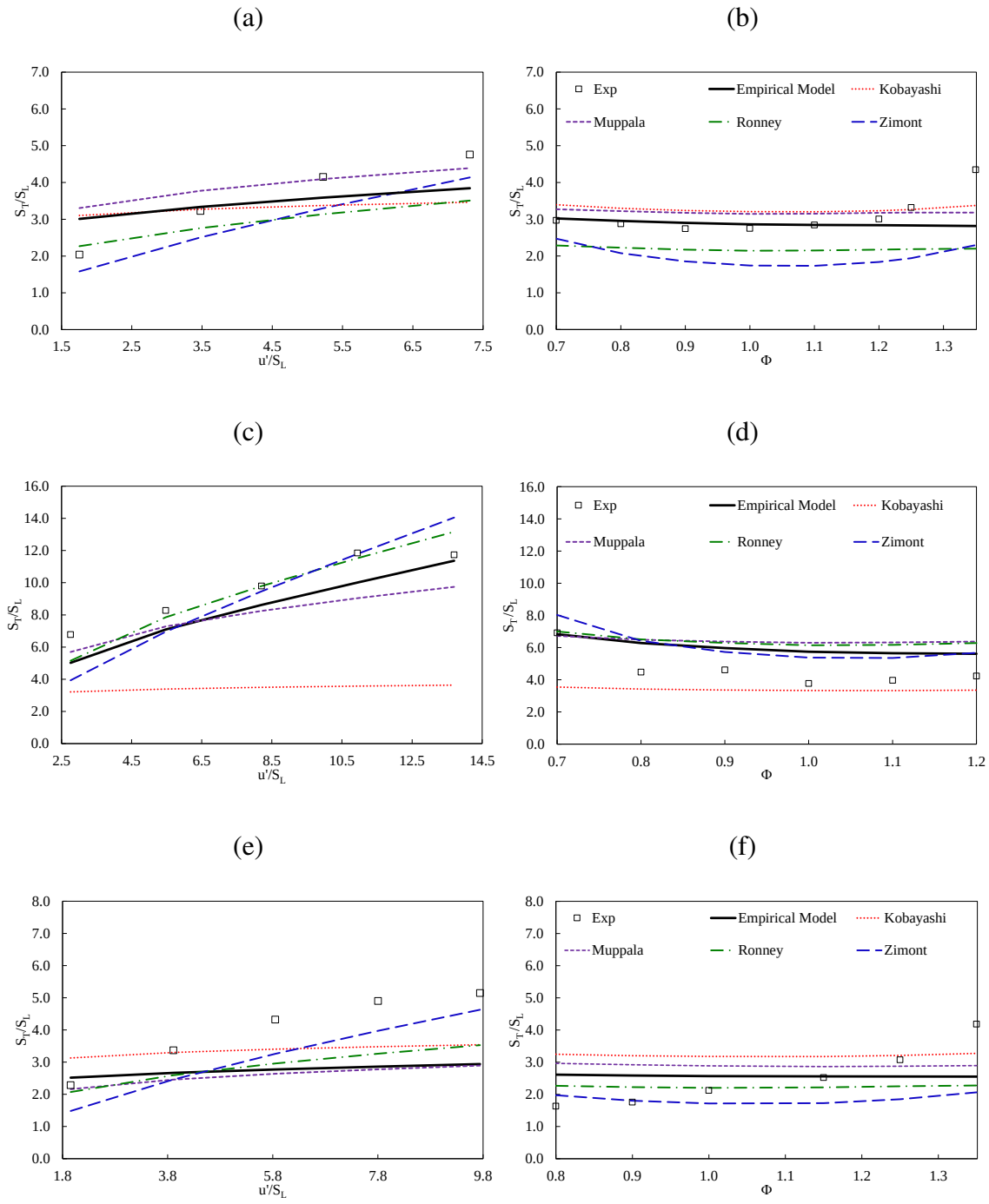

Figure 3.9: Predicted trends for (a) Flame C (CH_4) at ϕ= 0.8, (b) Flame D (CH_4) where u'= 0.91, (c) Flame J (CH_4) with ϕ= 1.0, (d) Flame K (CH_4) for u'= 1.5, (e) Flame R (C_3H_8) where ϕ= 1.0, (f) Flame F (C_3H_8) at u'= 0.91, using atmospheric pressure adjustable parameters with each flame having an inlet pressure and temperature of 0.1 MPa and 300 K respectively

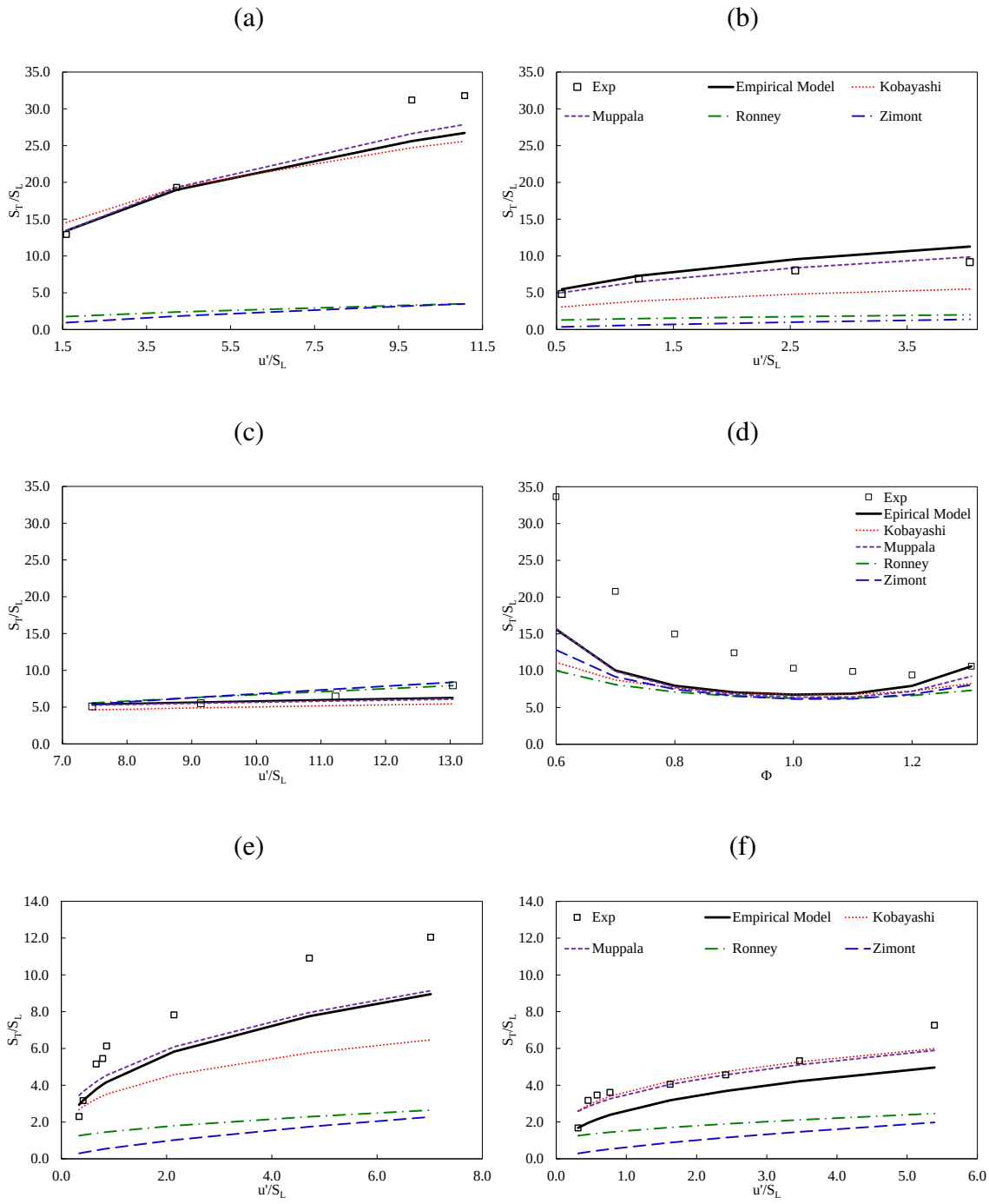

Figure 3.10: Predicted trends for (a) Flame Q (CH_4, T = 300 K, P = 3.0 MPa) where ϕ= 0.9, (b) Flame Q (CH_4, T = 300 K, P = 0.5 MPa) for ϕ= 0.9, (c) Flame B (CH_4, T = 300 K, P = 0.5 MPa) at ϕ= 0.8, (d) Flame G (CH_4, T = 360 K, P = 0.5 MPa) with u'= 2.0, (e) Flame T (C_2H_4, T = 300 K, P = 0.5 MPa), at ϕ= 0.7, and (f) Flame T (C_3H_8, T = 300 K, P = 0.5 MPa) where ϕ= 0.9, using high pressure adjustable parameters

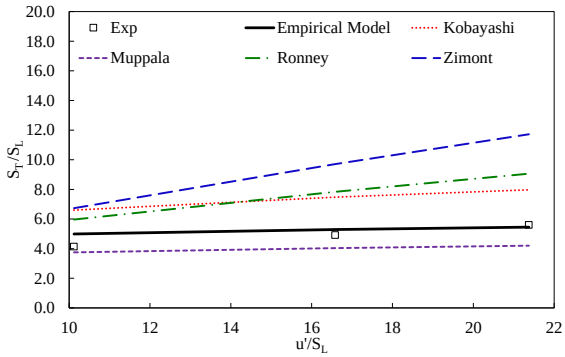

Figure 3.11: Predicted trends for Flame S (C_3H_8, $T = 300$ K, $P = 0.4$ MPa) where $\phi = 0.71$ using high pressure adjustable parameters

Study B demonstrated that the correlations can often match the shape of the trends but struggle to predict the values of the turbulent flame speed, an example of this is shown Figure 3.5(c). The goal of Study C was to determine how much of an improvement can be achieved if the Nelder-Mead simplex direct search method is implemented to optimise the literature correlations. The MAPE displayed in Figure 3.8 shows the large improvement when the parameters for each correlation are optimised. Reductions in the MAPE of 14.0%, 8.9% 2.9% and 16.9% were achieved for Muppala, Kobayashi, Zimont and Ronney respectively. Although these improvements are significant, the issue with the underlying theory of each correlation not being applicable to the turbulent conditions of certain flames still exists, resulting in MAPEs up to $\approx 50\%$. It should be noted that the newly optimised parameters are based on δ_{th} rather than δ_{diff}. For this reason, when using the optimised parameters, δ_{th} should be used as the laminar flame thickness.

The optimization process also had a significant impact on the trends predicted by each of the correlations. One of the major results of the process is the consolidation of the turbulent flame speed predictions, which can be seen for each expression. Comparisons clearly illustrate each predicted trend moving closer to the experimental data, and in some cases trends from different authors overlapped. This to occurs when the influence of the optimization process is different for each correlation, and these influences were independent of the data under examination.

The following general observations can therefore be made for each correlation:

- *Zimont*: The changes to the Zimont adjustable parameters were small. As a result, the slope of the correlation does not appear to have been altered by the process. Instead, the trend moves closer to the experimental values of S_T as indicated by the reduction in the MAPE between Study B and Study C.

- *Kobayashi*: The optimization process had the largest impact on the Kobayashi correlation. In the previous trend study, it can be seen that the expression tended to over-predict the values of S_T and showed a high degree of sensitivity to the varying operating conditions of the trend. The new adjustable parameters corrected the over-prediction, but in doing so have also reduced the sensitivity of the expression to ϕ and u'/S_L, resulting in a flatter slope across all the trends.

- *Muppala*: For the low pressure data, the optimization process appears to have little influence on the trends of any of the fuels. A major improvement was observed at high pressure flames, predicted values of S_T increased and better matched the experimental data much more closely.

- *Ronney*: Optimization of the adjustable parameters had a major beneficial impact on the ability of the Ronney correlation to predict both the values and the slope of the turbulent flame speed. In the previous trend study, the correlation showed very little sensitivity to any of the varying operating conditions and generally under-predicted most values of S_T. After the optimization process, the expression predicted S_T closer to experimental measurement and more accurately matched the experimental trend slopes.

- *Newly-developed Empirical Correlation*: The parameters for this correlation did not changed between Study B and Study C, so there is no change in the predicted trends.

3.5 Conclusion

The aim of this chapter is to provide insight into fifteen state-of-the-art premixed turbulent flame speed correlations and to determine the most appropriate correlation to employ under different combustion conditions. A newly-developed empirical correlation is also introduced in this chapter and assessed alongside the literature correlations. The assessment of each correlation is carried out using three studies, with each study comparing a set of correlations against a range of experimental data. A mean absolute percentage error was employed to determine the accuracy of each of the fifteen expression. Additional visual trend studies were used to further examine the best performing expressions .

Study A employed MAPE values to assess the accuracy of the fifteen literature correlations and the newly-developed correlation for 200 laboratory flame data points over a variety of experimental conditions. Overall it is found that the errors can be high for parameters reported by the original authors of each correlation, this is due to the fact that these parameters were originally derived for smaller data sets than were used in this study. In addition, each correlation was based on a model that describes a single regime of turbulence. This means that each correlation is only applicable to certain turbulent and inlet conditions. Outside these conditions the theories on which certain correlations are based may no longer be valid. It is commonly accepted that no single correlation is applicable over the complete range of turbulence encountered in turbulent premixed combustion. However it was found that the newly-developed empirical correlation provided the closest overall agreement to the range of data examined with a MAPE of 24.7% compared to the most accurate literature correlation by Muppala with a MAPE of 31.9%. Although proving to be the most applicable correlations for the data studied, it cannot be defined as a general correlation. This is particularly evident for larger hydrocarbon molecules.

Study A showed that no correlation can be defined as a general expression for predicting premixed turbulent flame speed and some correlations are more accurate than others. To better understand the most accurate correlations an extended experimental data set, ob-

tained from the literature was employed to further investigate the expressions by Zimont, Kobayashi, Muppala, Ronney and the newly-developed correlation. In addition to the MAPE analysis performed in Study A, the accuracy of each correlation was also assessed by visually comparing the predicted trends to the corresponding experimental trends in Study B.

From the MAPE analysis, an increase in the error for each of the literature correlations can be seen for the overall data set and the individual Data Groups. This is a result of the increase in the number of data points and the larger range of operating conditions that it encompasses. The error decreases for the newly-developed correlation, this appears to be counter-intuitive but is a result of the optimisation of the expression for conditions in Study B and so having the lower MAPE for this data set. The second major observation between the MAPE analysis from Study A and the Study B is the change in the order of the most accurate correlations. The new experimental data contains a significant number of flames operating with low turbulent intensities. The Zimont and the Ronney correlations struggle to predict S_T at these conditions and therefore are less accurate overall than the Kobayashi correlation.

For the trend study, it was found that the newly-developed correlation was best suited for the range of cases studied, predicting both the values and trends well and would be recommended to be used for predicting premixed turbulent flame speed at any conditions. The Zimont and the Kobayashi correlations also performed well for predicting trends but struggled in predicting the values of S_T especially at low turbulent intensities. In both Study A and Study B the Muppala correlation had the lowest MAPE of all the literature correlation. However at elevated pressures it was found that the expression was unable to predict the values of S_T because the adjustable parameters employed were not calibrated for the data under examination. The correlation by Ronney under-predicted both the values and slope of the turbulent flame speed due to unsuitable parameters employed by the expression.

Many of the adjustable parameters used by the literature correlations were unsuitable for the operating conditions examined. As a result the goal of Study C was to determine what improvements could be made to the accuracy of the correlations if the original authors' adjustable parameters were optimized for the current set of data. To ensure the overall MAPE was minimised for each correlation the adjustable parameters, for both the new empirical and the literature correlations, were optimised using a Nelder-Mead simplex direct search method. The optimisation was carried out using 335 data points from sixteen experimental studies consisting of a variety of turbulent conditions, fuel types, and pressures. Once optimized the correlations were compared to the same set of extended experimental data from Study B.

Optimizing the adjustable parameters over a much larger data set allowed each correlation's MAPE in Study C to be significantly reduced when compared to the errors in Study B. The new parameters improved each correlations' accuracy however the errors cannot be eliminated entirely. The errors of the newly-developed correlation and the expression developed by Kobayashi, were the result of the empirical nature of the correlations and the large data set used in the Study C. The three remaining correlations MAPEs are due to the fact that portions of the experimental data were outside of the single regimes of turbulence that were used to develop each of the correlations. It should also be noted that the newly optimised parameters will be different than the authors' original parameters because a different definition of laminar flame thickness has been used in the current study.

The correlations by Zimont and Ronney were the most accurate at capturing the shape of the experimental data for atmospheric flames. However for $Re_t < 150$ it was common to see these correlations under-predicting the values of flame speed. The remain three correlations performed better at capturing the values of S_T, even at low turbulence levels, but did not capture the trends as well. When moving to the elevated pressure flames, the correlation from this work and that by Muppala performed the best in capturing both the trends and values of S_T. The expression derived by Kobayashi also performs well but tends to underestimate values of flame speed more so than the previous two equations.

The correlations by Zimont and Ronney predict good trends when $Re_t > 150$, however, fail to calculate the values or trends for low turbulence levels. From these findings, the Zimont correlation would be recommended for predicting trends for atmospheric flames, as long as care is taken to note the turbulence levels because the correlation tends to under-predict S_T for low turbulence. For low turbulent or high pressure flames, the correlations from this work or by Muppala are recommended for these conditions.

Each of the three studies aimed to provide the reader with insight into various turbulent flame speed correlations. The combined findings of these studies show that the correlations under investigation are applicable to the data under examinations. However the fact that a minimum of two correlations and two sets of adjustable parameters from Study C are required to accurately account for the entire range of data shows that there is currently no general turbulent flame speed correlation. While correlations are still required for closing Favre-averaged $\bar{c}$ equations, the author believes that an alternative approach is needed for predicting S_T for the assessment of combustor reactivity. Therefore the author has developed a modified version of Cantera's 1D freely propagating laminar flame speed model, which is capable of predicting S_T. The following chapter will describe the modifications made to Cantera to enable the prediction of premixed turbulent flame speed using detailed chemistry and will present the results of a comparison between the model, experimental data and the correlations used in Study C.

Chapter 4

Predictive One-Dimensional Turbulent Flame Speed Model

4.1 Introduction

Chapter 2 showed that DNS or LES approaches require large computational expense and extensive expertise to solve premixed turbulent combustion, this is further compounded with the inclusion of detailed chemistry. Turbulent flame speed correlations are therefore regularly employed to predict S_T due to these limitations. However, as Chapter 3 has shown these expressions also have drawbacks. A general expression for predicting S_T does not exists, because of this the selection of the correct correlation is not always straightforward. While the newly-developed correlation from Chapter 3 has show good results it is entirely empirical and based on known experimental data set. Outside of these data sets where little experimental data exists, for example gas turbine conditions, an alternative method of predicting turbulent flame speed is needed. In an effort to improve on these drawbacks a predictive one-dimensional freely-propagating planar turbulent flame speed model, implemented in Cantera, has been developed. Cantera [42], written in C++, is a collection of open source object-oriented software tools for solving 0D and quasi-1D chemically reacting flows, with current versions of Cantera focusing on laminar combustion. In comparison to laminar flow, turbulent flow is more complex, characterised by (1) temporal fluctuations in properties, (2) increased rates of mixing and diffusion of species,

momentum and heat, and (3) spatially non-uniform and locally-enhanced chemical reaction rates.

Models for these phenomena exist and are briefly described here with more detailed treatment given in Section 4.3.1. Three well known numerical methods are used to account for temporal fluctuations terms present in the transport equations for reactive turbulent flows. These are (a) time-resolved, (b) filtered time-resolved, and (c) time-averaged methods. These methods can be found in DNS, LES, and Reynolds-averaged Navier-Stokes (RANS) models respectively. The widely used k-ε model, which is described in Section 4.3.3, has been selected to define the level of turbulence within the flame in the Cantera S_T model for modelling the temporal fluctuations. The Reynolds fluxes, described in Section 4.3.3.1, in the flame are defined using turbulent species diffusion (D_t) and thermal conductivity (λ_t) terms. The turbulence-chemistry interaction (TCI) in the flame is handled using the Eddy Dissipation Concept [44]. TCI causes spatial non-uniformity and is described in 4.3.3.3. In addition to TCI, temperature fluctuations (T') present in the turbulent flames enhances the mean chemical reaction rate of species i $(\dot{\omega}_i)$, and is modelled using a Taylor series expansion of $\dot{\omega}$ around the time-averaged temperature $(\bar{T})$ as described in 4.3.3.2.

To validate the new S_T predictive model an experimental data set consisting of 116 experimental points for methane flames over a range of turbulence and pressures was used, further details regarding the experimental data are provided in Section 4.2. The chemical kinetics within the flame were accounted for by employing the GRI3.0 mechanism and transport is handled using a mixture-average diffusion approach as described in Section 4.3.2.2. To benchmark the predictive model against current methods for predicting S_T, flame speeds from the model are compared to values determined by the correlations from Study B in Chapter 3. To investigate the new predictive model as thoroughly as possible the analysis was be carried out using the same MAPE and trend study approach implemented in the Chapter 3 .

This chapter is divided into four main sub-sections, Section 4.2 provides a short explanation on the experiential data used in the validation of the predictive model. Section 4.3 describes the numerical and theoretical background of the existing freely-propagating 1D flame speed model. This is followed by an in-depth discussion of the modifications that were made to the existing version of Cantera. With the addition of the turbulent modifications the robustness of the original solver has suffered, therefore the best practice for implementation of the S_T is described. A validation of the new predictive model through a comparison of predicted results to a set of experimental data as well as the five correlations from Chapter 3 is presented in Section 4.4. The chapter closes with a discussion of the results and key findings related to the development of the model.

4.2 Experimental Data

The experimental data used to validate the S_T predictive model was obtained from nine experimental campaigns and contains a wide range of operating conditions. An overview of the entire range of data gathered for this thesis is shown in Section 2.5.1, however due to time restrictions only a portion of the data has currently be modelled. Table 4.1 shows the experimental results selected for validation of the predictive model. Figure 4.1 graphically summarises the turbulent conditions of each flame in the form of a modified Borghi Diagram. A total of 116 flames were used, the main body of the experimental data consisted of expanding flames (76 points), with Bunsen burner (28 points) and conical diffuser flames (12 points) making up the remainder. The selected data was chosen as it comprises of a wide range of turbulent conditions, occupying three turbulent combustion regimes (see Figure 4.1), and covers both atmospheric and elevated pressures. The large diversity in the measured data allows the new predictive model to be validated over a wide range of conditions.

Table 4.1: Experimental operating conditions, apparatus and measured $\bar{c}$ iso-surfaces for each data set used to validate the newly developed predictive model. Symbols shown relate to the data in the modified Borghi diagram in Figure 4.1

Flame	Apparatus	Fuel	$\bar{c}$	ϕ	P (MPa)	$\frac{u'}{S_L}$	$\frac{\Lambda}{\delta_{th}}$	$\frac{S_{T\bar{c}=0.5}}{S_L}$
A ◇	CB	CH_4	0.1	0.8	0.1	10.6-20.8	70.1-70.6	9.4-12.6
B □	CB	CH_4	0.1	0.8	0.2-1.0	4.9-14.6	94.8-170.1	5.0-10.0
F ○	BB	CH_4	0.5	0.7-1.2	0.1	5.5-11.7	3.5-5.6	3.2-3.9
G ◇	SB	CH_4	0.1	0.6-1.3	0.5	2.0-9.9	5.3-6.3	2.7-8.0
H □	SB	CH_4	0.34	0.6-1.3	0.1	4.1-14.3	20.2-45.8	2.5-6.4
I △	BB	CH_4	0.05	0.7,0.8,1.0	0.1	0.65-2.4	2.3-9.4	5.6-11.1
J ×	CB	CH_4	0.5	0.7-1.3	0.1	1.4-15.7	31.8-95.3	2.1-13.0
K +	SB	CH_4	0.1	0.7-1.2	0.1	4.4-10.0	35.3-56.8	3.8-6.9
N □	CV	CH_4	0.6	0.8-1.25	0.1	1.3-7.3	8.9-10.3	1.9-4.1
O △	CD	CH_4	0.5	0.95	0.1	0.2-1.3	16.0-51.6	3.1-6.0
Q +	BB	CH_4	0.5	0.9	0.5-3.0	0.5-11.1	5.8-12.5	4.8-31.8

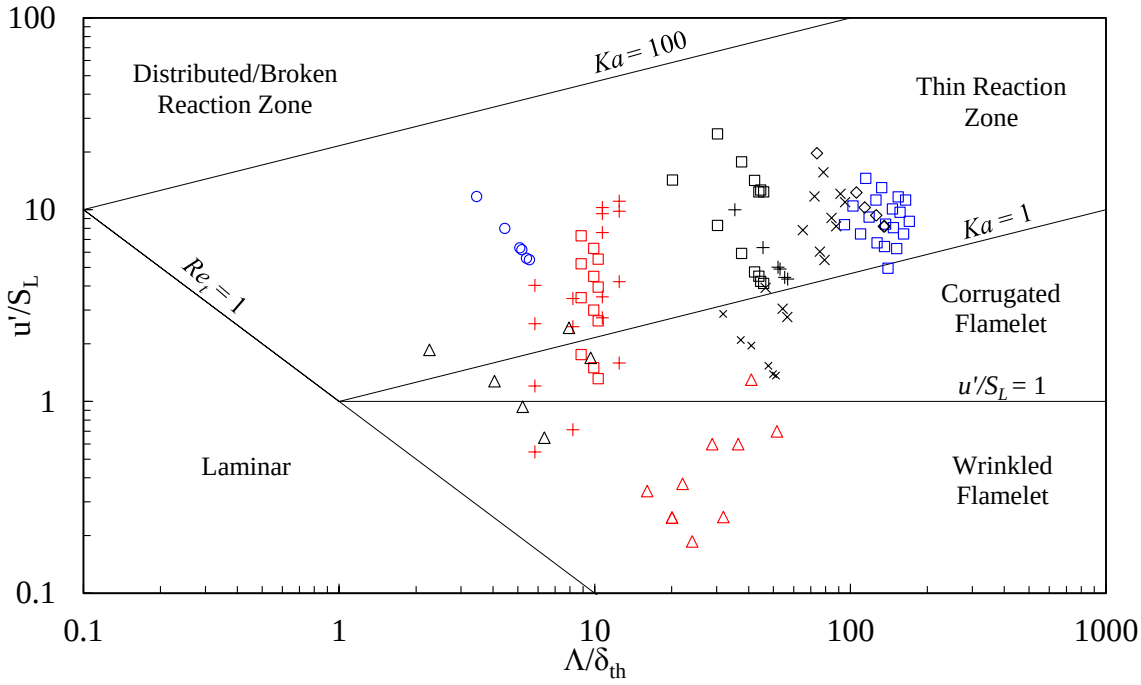

Figure 4.1: Flame conditions for the predictive model validation data displayed in Table 4.1 plotted on a modified Borghi diagram

The entire range of experimental data used in this chapter has been recorded at, or can be related back to a flame surface with a reaction progress variable, $\bar{c}$, of 0.5. As previously shown in Section 3.4, the most accurate turbulent flame speed correlations

were developed to predict S_T at a progress variable of 0.5 ($S_{T_{0.5}}$). Liu [103] proposed that $\bar{c}$ = 0.5 is the most accurate measurement surface due to the experimental apparatus used to measure S_T. Figure 4.2 shows that as $\bar{c}$ increases for a expanding flame so too does S_T, while the opposite is true for the Bunsen burner flame where S_T decreases with an increase in $\bar{c}$. These discrepancies in the values of S_T when measured with Bunsen burners and expanding flames can be reduced by measuring turbulent flame speed in the centre of the flame brush. For planar flame, like the ones predicted by the model, the relationship between $\bar{c}$ and S_T is the same form as the expanding flame relationship as shown in Figure 4.2. Therefore $\bar{c} = 0.5$ is selected for both the experimental and model values of S_T.

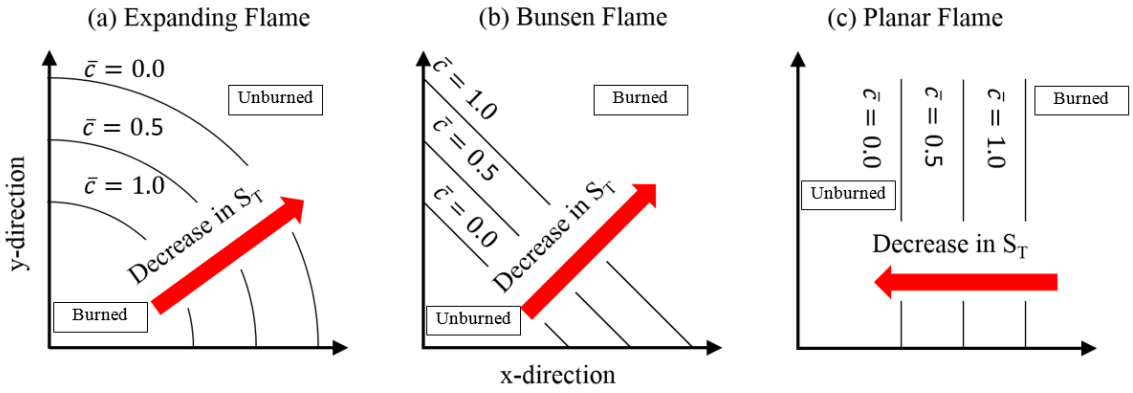

Figure 4.2: 2D representation of the relationship between $\bar{c}$ and S_T for (a) an expanding flame, (b) a Bunsen burner flame and (c) a planar flame with $\bar{c}$ iso-surfaces for 0, 0.5 and 1.0 through the flame brush

4.3 Methodology

In 1985 one-dimensional laminar flame speed model were first developed by Kee et al. [150] in the form of Sandia's *Premix* code written in Fortran [151]. Since then, other laminar flame speed model have been developed such as Chemkin II , Chemkin PRO, DARS [152], Ember [153] and Cantera. Cantera was selected for this project because of its good agreement with experimental data, as shown by the CERFACS group through their mechanism validation [154], large, active and supportive user community, and its

free and open source nature. Cantera is built using objects that represent components for gas/liquid mixtures, interfaces between the phases of matter, equations of state, ODE solvers, reactors and flames. Figure 4.3 provides a graphical overview of the Cantera structure. Although most of the source code is in C++, the user has a number of options on how to interface with the solver, including Fortran 90/95, Python [155], and MATLAB [156].

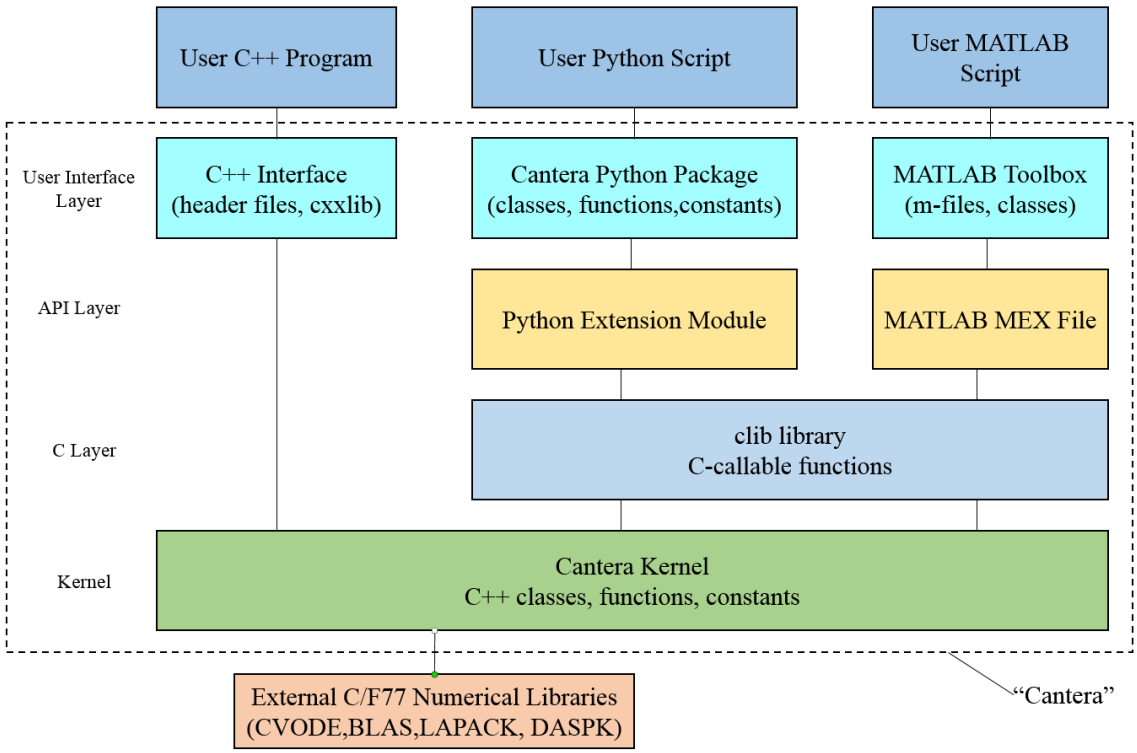

Figure 4.3: Overview of Cantera Interface and Wrapper Classes. Reproduced from [157]

When selecting the language to interface with Cantera a good approach to use is: Python or MATLAB if possible; C++ or Fortran if necessary [42]. While Matlab and Python are preferable interfaces when compared to C++ and Fortran, the Python interface has several advantages over Matlab. Python provides more functionality than Matlab, with most of the features of the C++ core being available in a flexible environment. An example of this is that the freely-propagating S_L model is accessible through the Python interface but not the Matlab version. The ability to solve a freely-propagating, premixed flame that allows for the calculation of the unstretched laminar flame speed is essential for

this work. Due to these advantages, Python is currently the most commonly used interface for Cantera.

The interfaces between the C++ source code and the interface languages are built using wrapper classes. These classes provide bindings between the interface language (i.e. Python) and the underlying C++ code. These wrapper classes include the User Interface, API and C layers, as shown in Figure 4.3. Also displayed is the C++ source code known as the Kernel Layer. This layer is the core of Cantera and has been developed to have a modular structure so that it can be configured with only the user desired features. When introducing the turbulent properties into the Cantera's source code, the Kernal Layer is the location in which these modifications are made. In addition to the core Cantera packages, external programmes, such as Sundials [158] and BLAS [159]/LAPACK [160], are required to successfully run the solver. These packages are used to solve the non-linear and differential/algebraic equations while the software libraries of Boost are used to account for the linear algebra (i.e. equations). All these equations need to be solved numerically to calculate the properties of the flame.

To define chemical kinetics, thermodynamic and transport properties Cantera uses a single input file (.cti). Existing Chemkin PRO files can be converted into the .cti format using the ck2cti.py script. Figure 4.4 shows a comparison of Cantera and Chemkin PRO predicted freely-propagating laminar flame speeds using two chemical mechanism, Zhao [161] and AramcoMech1.3 [124], and two sets of experimental data from Yu et al. [162] and Lowry et al. [163]. To ensure a valid comparison the same numerical settings and grid refinement criteria, as shown in Table 4.2, were used in each solver. As a result, both solvers give very similar predictions using the Zhao and AramcoMech1.3 mechanisms.

Table 4.2: Numerical settings and grid refinement criteria used in Cantera and Chemkin PRO to predict the S_L values shown in Figure 4.4

Parameter	Value	Parameter	Value
Gas Energy Equation	On	Absolute Timestepping Tolerance	1.0E-09
Transport	Multi & Soret	Absolute Tolerance	1.0E-09
Grid Control (Curvature)	0.12	Minimum Pseudo Time Step (sec)	1.0E-10
Grid Control (Gradient)	0.06	Maximum Pseudo Time Step (sec)	1.0E-02
Initial Number of Grid Points	12	Time Steps Before Increasing	25
Maximum Grid Points	1000	Maximum Pseudo Time Stepping	100
Ending Axial Position (cm)	30	Iterations before Updating Jacobian	20
Starting Axial Position (cm)	-5	Relative Timestepping Tolerance	1.0E-4
		Relative Tolerance	1.0E-4

Figure 4.4: Laminar flame speed comparison between the Cantera and Chemkin PRO freely-propagating laminar flame speed solvers for CH_4-air using AramcoMech1.3 and Zhao mechanisms , P_i=0.1 MPa T_i=303 K)

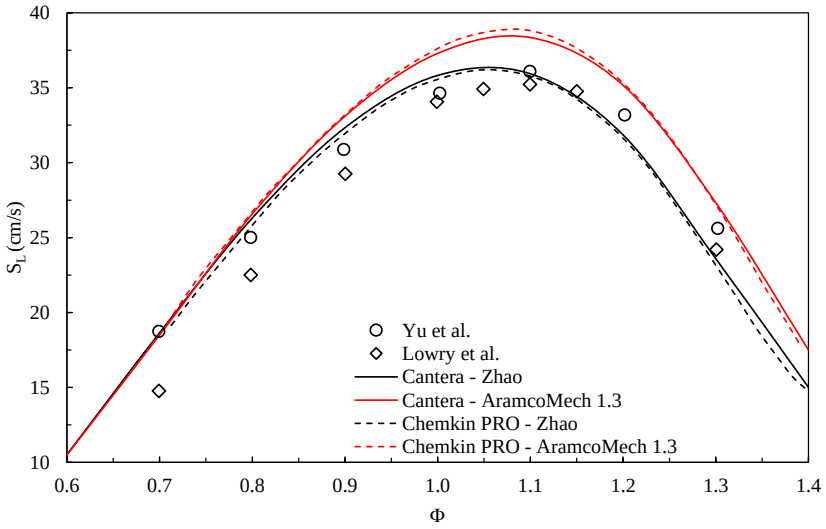

4.3.1 One Dimensional Numerical Methods

To predict S_L, the laminar model calculates the 1D steady-state solutions for the continuity, energy and species conservation equations of a reactive gaseous mixture over a user-specified domain that has been discretised into a computational grid. The governing equations follow those derived in [63] for continuity, energy and species. Cantera does not need to solve the momentum equation because dp/dz would be the only result which does

not occur outside the axial momentum equation. As a result the solution of the momentum equation provides no useful information and so is not solved. The following section focuses on the numerics of the solver and a detailed description of both the laminar and turbulent versions of these equations will take place in Section 4.3.2 and 4.3.3 respectively. Cantera uses a finite difference approach with the governing equations to form a system of nonlinear algebraic equations. A first-order upwinded differences approach is employed for the convective terms and second-order centred differences for the diffusive terms.

Once discretised the equations become a system of non-linear expressions that are solved using a damped Newton-Raphson method. This approach is employed to iteratively resolve continuity, energy and species values until equation errors reach user specified solution tolerances. By taking the difference between the true solution and the values predicted $(\varphi_{n,j})$, for the n^{th} equation at the j^{th} point, by Newtons approach, a residual vector $(F(\varphi))$ can be defined. Newton's method is too expensive and lacks robustness to be practically implemented, because the first guess $(\varphi^{(0)})$ has to be close to the true solution and the Jacobian matrices $(\frac{\partial F}{\partial \varphi})$ is time consuming to resolve.

Cantera employs the usual numerical approaches to improve on these shortcomings in the form of a damped Newton method. Rather than solving the Jacobian matrix at every iteration, the matrix is inherited from the previous iteration of the algorithm. In addition to this, the step from one solution sequence to the next, $\varphi^{(n)}$ - $\varphi^{(n+1)}$, may be interrupted using a damping parameter $(\lambda^{(n)})$, where $0 < \lambda^{(n)} < 1$. As a result, the iterative process becomes the expression shown in Equation 4.1. The selection of $\lambda^{(n)}$ and $J^{(n)}$ are controlled by a look-ahead procedure, which puts certain restrictions on the behaviour of the algorithm.

$$\varphi^{(n+1)} = \varphi^{(n)} - \lambda^{(n)} \left(J^{(n)}\right)^{-1}_{\varphi^{(n)}} F\left(\varphi^{(n)}\right) \tag{4.1}$$

This approach continues until $\Delta\varphi$ is reduced within user-specified relative tolerance (R) and absolute tolerance (A). The relative tolerance specifies the number of significant

digits the convergence values should contain, typically of the range of 10^{-3} to 10^{-4}. The absolute tolerance excludes solution components smaller than A from the relative tolerance assessment and should be greater than the smallest mass fraction (Y) of all species of interest. Other solution components are not considered as Y is typically the smallest solution component in the solution array.

If convergence cannot be reached with a damped Newtons method, a new Jacobian is computed, based on the most up to date solution variables, and the above process is repeated. If convergence is still is not reached, a pseudo-transient approach is used to estimate a new solution. While this is more expensive, the time integration process has a larger likelihood of reaching convergence. The time step and the number of steps to be taken are both user defined, usually having values of 10^{-6} seconds and 80 steps, respectively. The time derivatives of the temperature and mass fraction equations are added to obtain the transient T and Y_k transport equations. This results in the system becoming a set of partial differential equations, rather than ordinary differential equations. The backward Euler method is employed to solve the finite difference approximations of the time derivatives as shown in Equation 4.2.

$$\rho A \frac{\partial \varphi}{\partial t} = \rho_j^{n+1} A_j \frac{\varphi_j^{n+1} - \varphi_j^n}{h} \tag{4.2}$$

where h represents the size of the time step. The system is solved for each time step, using the same damped Newton method employed for the steady-state equations. With a sufficiently small time step it is likely the transient approach will reach convergence. The switch back to the steady state approach takes place once the number of user-defined time steps has been reached. The solution from the transient approach is then used as a new starting point for the steady state Newton algorithm. This gives the Newton algorithm a higher probability of solving than before the pseudo-transient step because the pseudo-transient solution is closer to the converged result. If convergence is still not reached another set of time steps are taken.

Reaching convergence also relies heavily on an initial first guess. Each point is initialised assuming a linear approach, where inlet conditions are defined at the start of the domain and equilibrium conditions at the outlet as illustrated in Figure 4.5.

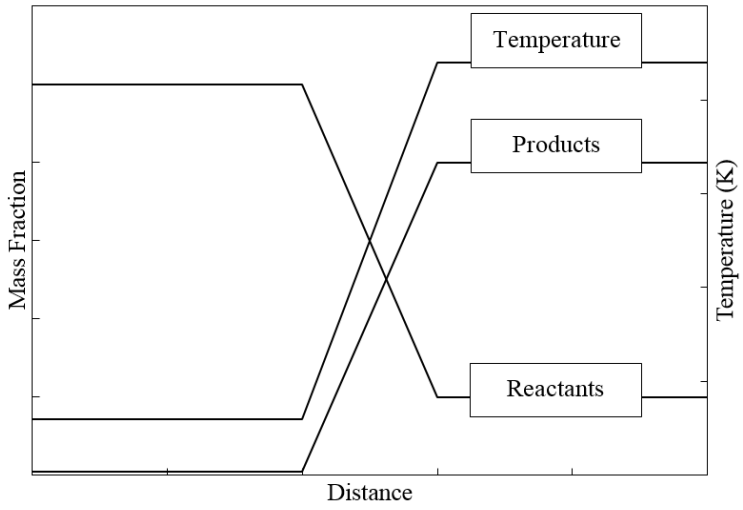

Figure 4.5: General form of the first guess taken by Cantera using the equilibrium calculation

The initial guess is usually defined on a small equidistant grid ($\approx$ 10 points). Once the Newton iteration obtains a converged solution for this grid, more grid points are added based on grid refinement value thresholds. The refinement criteria are user-defined and assess the slope, curvature and ratio of all the solution components (temperature, velocity, species mass fraction) within the flame. If these criteria are not satisfied, new grid points are added and Cantera attempts to find a converged solution on the new grid. This process is repeated until no new points are needed and a final converged solution is obtained. Even though the solution meets the required level of grid refinement, a grid independent solution may not have been reached therefore it is important to ensure the flame domain is sufficiently discretised to avoid the number of points in the domain affecting Cantera's converged predictions.

The boundary conditions are implemented within the flow domain. The specified cold (inlet) boundary condition for the species mass fractions $(Y_{k,0})$ and temperature (T_0) at the

inlet point, z_0, are determined using Equation 4.3. For the outlet boundary, the gradients for temperature and species mass fluxes are kept at zero as shown in Equation 4.4.

$$T(z_0) = T_0 \qquad \dot{m}_0 Y_{k,0} - j_k(z_0) - \rho(z_0) u(z_0) Y_k(z_0) = 0 \tag{4.3}$$

$$\left.\frac{\partial T}{\partial z}\right|_{z_0} = 0 \qquad \left.\frac{\partial Y_k}{\partial z}\right|_{z_0} = 0 \tag{4.4}$$

4.3.2 The Global Laminar Theory

The previous section gave an overview of the numerical approach used by Cantera to solve for S_L. The following section presents the physics employed to describe the reacting flow. The S_T predictive model is built on top of the existing one-dimensional freely-propagating laminar flame speed model within Cantera 2.3a. Cantera computes the laminar flame speed by solving the steady-state solution for the transport equations for a reactive gaseous mixture. The equations for continuity, species conservation and energy conservation are reduced and solved in a single dimension.

4.3.2.1 Mass Conservation

Regardless of flow type or device configuration, a bulk-fluid mass conservation equation is essential. For Cantera this takes the form:

$$\frac{\partial \rho u}{\partial z} = 0 \tag{4.5}$$

where u is velocity.

4.3.2.2 Species Conservation

For species conservation, the mass fraction transport equation as show in Equation 4.6 is used. The expression takes into account the relationship between mass fluxes and species concentration fields:

$$\rho u \frac{\partial Y_k}{\partial z} = -\frac{\partial j_k}{\partial z} + W_k \dot{\omega}_k \tag{4.6}$$

where j_k is the diffusive mass flux, W_k is the molecular weight and $\dot{\omega}_k$ is the molar production rate of species k. With the presence of species in the flow, molecular diffusion transports species from regions of high concentrations to regions of low concentration. Fick's law describes this transport using a diffusive mass flux, j_k. The diffusion coefficient can be defined using either mixture-averaged or multi-competent approach with thermal diffusion due to a temperature gradient determined using Soret diffusion coefficient. For turbulent flow, j_k is dominated by the turbulent diffusion coefficient and as a result, the differences in values between the mixture-averaged and multi-competent approach are negligible. Therefore, the mixture-averaged approach for defining the diffusion coefficient $(D_{k,m})$ was selected. Under laminar conditions this approach takes the form:

$$j_k^* = \rho \frac{W_k}{\bar{W}} D_{k,m} \frac{\partial X_k}{\partial z} \tag{4.7}$$

where j_k^* is the ordinary diffusion flux, X_k is the mole fraction for species k and the mixture-averaged diffusion coefficient is defined using the matrix of binary diffusion coefficients (D_{jk}):

$$D_{k,m} = \frac{1 - Y_k}{\sum_{j \neq k}^{K} X_j / D_{jk}} \tag{4.8}$$

The mixture-averaged formulation does not guarantee that the sum of the diffusion fluxes vanish and so Equation 4.9 ensures that the sum of the mass fluxes is zero.

$$j_k = j_k^* - Y_k \sum_k j_k^* \tag{4.9}$$

$\dot{\omega}_k$ can be defined in compact notation for a multi-step mechanism as:

$$\dot{\omega}_k = \sum_{r=1}^{L} \upsilon_{kr} q_r \qquad where \qquad \upsilon_{kr} = (\upsilon_{kr}^{''} - \upsilon_{kr}^{'}) \tag{4.10}$$

$\upsilon_{kr}^{'}$ and $\upsilon_{kr}^{''}$ are the stoichiometric coefficients on the reactants and products side of the

chemical reactions r and the rate-of-progress variable q_r is defined as

$$q_r = k_{f,k} \prod_{k=1}^{N} [X_k]^{\upsilon'_{ji}} - k_{b,k} \prod_{k=1}^{N} [X_k]^{\upsilon''_{ji}} \tag{4.11}$$

Cantera is capable of supporting a number of reaction types including Pressure Independent, Three-Body, Falloff, Pressure Dependent Arrhenius Rate Expressions (P-Log) and Chebyshev reactions. Each reaction type requires a different approach for defining the rate coefficients.

Pressure-Independent Reactions [164]

The increase in the rate of chemical reaction with respect to temperature is well established [11]. For reactions independent of pressure, this relationship is described using the modified Arrhenius equation:

$$k_f(T) = AT^{\beta} exp(-E_a/RT) \tag{4.12}$$

where $k_f(T)$ is the forward rate constant and R is the universal gas constant. The A, β and E_a terms are the Arrhenius parameters and are user supplied using chemical kinetic mechanisms. To determine the reverse rate constant (k_b), equilibrium constants $(K_{c,k})$ are used to define a relationship between the forward rate and reverse rate constants:

$$k_b(T) = \frac{k_f(T)}{K_{c,k}} \tag{4.13}$$

Three-Body Reactions [164]

A three-body reaction takes the form $\mathrm{A} + \mathrm{B} + \mathrm{M} \rightleftharpoons \mathrm{AB} + \mathrm{M}$ where M is a collision partner that is required to carry away excess energy for the forward reaction to stabilize the AB molecule or supply the energy in the reverse direction to break the AB bond. The effectiveness of a collision partner depends on the species M represents. The effects of M on the reaction rate can be described using a modified rate-of-progress variable by adding an additional term as shown in Equation 4.14.

$$q_r = \left(\sum_{k=1}^{N} (a_{kr}) [X_k] \right) \left(k_{f,k} \prod_{k=1}^{N} [X_k]^{\upsilon'_{ji}} - k_{b,k} \prod_{k=1}^{N} [X_k]^{\upsilon''_{ji}} \right) \tag{4.14}$$

If the contribution from each species in the mixture is equal the collision efficiency $(a_{k,r})$ is unity for all k. This is rarely the case and so $a_{k,r}$ differs for each species and must be defined by chemical kinetics mechanisms.

Falloff Reactions [164]

For a reaction with the high-pressure limit, the reaction can be described using the Arrhenius rate, Equation 4.12, and for the low-pressure limit a third body reaction coefficient can be used. However, for a pressure and temperature where the reaction is between the limits, neither of these approaches can be used. This kind of reaction is said to be in the "fall-off" region. The simplest expression for defining the rate coefficient in the fall-off region is the Linderman form [63]:

$$k_f(T, [\mathrm{M}]) = \frac{k_0[\mathrm{M}]}{1 + \frac{k_0[\mathrm{M}]}{k_\infty}} \tag{4.15}$$

For the low-pressure limit Equation 4.15 approaches $k_0[M]$, whereas for the high-pressure limit the expression approaches k_∞. The rate coefficient at any pressure can then be defined with a reduced pressure term (P_r) such that

$$k_f(T, P_r) = k_\infty \left(\frac{P_r}{1 + P_r} \right) \tag{4.16}$$

where $P_r = \frac{k_0[\mathrm{M}]}{k_\infty}$. To more accurately model the rate coefficient in the falloff region requires a more complex form for the dependence on reduced pressure. This can be achieved with the inclusion of a falloff function $F(T, P_r)$ in Equation 4.16. Cantera defines this function using the TROE or SRI falloff functions which take the forms shown in Equation 4.17 and 4.18 respectively.

TROE:

$$\log_{10} F(T, P_r) = \frac{\log_{10} F_{cent}(T)}{1 + f_1^2}$$

$$F_{cent}(T) = (1-A)\exp(-T/T_3) + A\exp(-T/T_1) + \exp(-T_2/T)$$

$$f_1 = (\log_{10} P_r + C)/(N - 0.14(\log_{10} P_r + C))$$

$$C = -0.4 - 0.67 \log_{10} F_{cent}$$

$$N = 0.75 - 1.27 \log_{10} F_{cent} \tag{4.17}$$

with the first three parameters (A, T_3, T_1) requiring specifying by the user, while the fourth parameter is optional.

SRI:

$$F(T, P_r) = d\left[a\exp(-b/T) + \exp(-T/c)\right]^{1/(1+\log_{10}^2 P_r)} T^e \tag{4.18}$$

similar to the TROE function the parameters $(a, b, c, d$ and $e)$ are required user inputs.

P-LOG Reactions [164]

Rates are determined for the Pressure-Dependent Arrhenius Rate Expressions using logarithmic interpolation between Arrhenius rate expressions for different pressures. At two given pressure, P_1 and P_2 the related rate coefficient being defined as:

$$P_1 : k_1(T) = A_1 T^{\beta_1} exp(-E_{a1}/RT) \qquad P_2 : k_2(T) = A_2 T^{\beta_2} exp(-E_{a2}/RT) \tag{4.19}$$

The rate coefficient at the desired pressure, where $P_1 < P < P_2$, can be expressed as

$$\log k(T, P) = \log k_1(T) + \left(\log k_2(T) - \log k_1(T)\right) \frac{\log P - \log P_1}{\log P_2 - \log P_1} \tag{4.20}$$

The P-Log approach for defining the rate coefficient is a straightforward approach that allows for the inclusion of data from more than one pressure regime.

Chebyshev Reaction Rate [164]

For these reactions $k(T,P)$ is expressed in terms of a bivariate Chebyshev polynomial and can be written as:

$$\log k(T,P) = \sum_{t=1}^{N_T} \sum_{p=1}^{N_P} \alpha_{tp} \phi_t(\tilde{T}) \phi_p(\tilde{P}) \tag{4.21}$$

where α_{tp} are the constants defining the rate, $\phi_n(\tilde{x})$ is the Chebyshev polynomial of the first kind of degree n evaluated at x, and

$$\tilde{P} \equiv \frac{2\log P - \log P_{\min} - \log P_{\max}}{\log P_{\max} - \log P_{\min}} \tag{4.22}$$

$$\tilde{T} \equiv \frac{2T^{-1} - T_{\min}^{-1} - T_{\max}^{-1}}{T_{\max}^{-1} - T_{\min}^{-1}} \tag{4.23}$$

4.3.2.3 Energy Conservation

As illustrated above, temperature is used extensively to define reaction rate. To describe the conservation of energy, Cantera uses a temperature transport equation derived from the one-dimensional enthalpy transport equation, as shown below, under the perfect gas assumption.

$$\sum \dot{m}_k'' \frac{dh_k}{dz} + \sum h_k \dot{m}_k''' = \frac{d}{dx}\left(\lambda \frac{dT}{dx}\right) \tag{4.24}$$

where the mass flux can be defined as $\dot{m}_k'' = (\rho Y_k u + j_k)$ and $\dot{m}_k''' = \frac{d\dot{m}_k''}{dz}$. Under the perfect gas assumption the specific heat (c_p) can be defined as:

$$c_{p,k} = \left(\frac{\partial h_k}{\partial T}\right)_p \Rightarrow dh_k = c_{p,k} dT \tag{4.25}$$

and substituted into Equation 4.24 such that the following equation can be written

$$(\rho Y_k u + j_k) c_{p,k} \frac{dT}{dz} + \sum h_k \dot{m}_k''' = \frac{d}{dx}\left(\lambda \frac{dT}{dx}\right) \tag{4.26}$$

Expanding Equation 4.26 and recognising that $\dot{m}_k'''$ is the net rate of mass production of species k, the temperature transport equation can be written as:

$$\sum_k \rho c_p u \frac{\partial T}{\partial z} = \frac{\partial}{\partial z}\left(\lambda \frac{\partial T}{\partial z}\right) - \sum_k j_k c_{p,k} \frac{\partial T}{\partial z} - \sum_k h_k W_k \dot{\omega}_k \tag{4.27}$$

Note that the heat source due to chemical-reaction is not really a source term per se. Chemical reaction breaks and forms chemical bonds, causing the temperature to increase or fall. However, the total energy in the system is not altered by the reaction. Rather chemical energy is converted to thermal energy, which manifests as changes in temperature and species composition. Thus the temperature form of the energy equation has a chemical-reaction term, whereas the enthalpy (or internal energy) form does not.

4.3.3 The Global Turbulent Theory

This section describes the modifications made to laminar flame modelling theory to allow for the predictions of S_T. Before additions to the model accounting for the influence of turbulence on the flame can be made, a method to introduce turbulence is needed. The well-known k-ε model [165] was selected due to the relative simplicity of two-equation models and the significant level of information available for the model in the literature. The turbulent kinetic energy (k) and energy dissipation (ε) are defined in the z-direction as:

$$\frac{\partial}{\partial t}(\rho k) + \frac{d}{dz}(\rho k u) = \frac{d}{dz}\left(\mu + \frac{\mu_t}{\sigma_k}\frac{dk}{dz}\right) - \rho \overline{u_i' u_j'} \frac{\partial u_j}{\partial z} - \rho \varepsilon \tag{4.28}$$

$$\frac{\partial}{\partial t}(\rho \varepsilon) + \frac{d}{dz}(\rho \varepsilon u) = \frac{d}{dz}\left(\mu + \frac{\mu_t}{\sigma_\varepsilon}\frac{d\varepsilon}{dz}\right) + C_{1\varepsilon}\frac{\varepsilon}{k}\rho \overline{u_i' u_j'} \frac{\partial u_j}{\partial z} - C_{2\varepsilon}\rho \frac{\varepsilon^2}{k} \tag{4.29}$$

$$\mu_t = C_\mu \rho \frac{k^2}{\varepsilon} \tag{4.30}$$

where the model constants are defined as $C_{1\varepsilon} = 1.44,\ C_{2\varepsilon} = 1.92,\ C_\mu = 0.09,\ \sigma_k = 1.0,\ \sigma_\varepsilon$

= 1.3 and μ_t is the turbulent viscosity. Unfortunately, due to the flame being in a single dimension and the 3D nature of turbulent eddies, a transport equation for the turbulent terms cannot be implemented within the Cantera domain. Although a 1D transport equation can be written, similar to the u and T expressions above, the Reynolds stress tensor $(\rho\overline{u_i'u_j'}\frac{\partial u_j}{\partial z})$ cannot be accounted for with a unidirectional flow as there is no radial velocity (u_j). Attempts where made to define $\rho\overline{u_i'u_j'}\frac{\partial u_j}{\partial z}$ using the Boussinesq approach with axial velocity as shown in Equation B.4 in Appendix B. It was found that this approach was unable to accurately predict $k-\varepsilon$ profiles within the flame for a range of turbulent inlet conditions. This was due to the under prediction of the rates of production of k and ε as the values of $\frac{du_i}{dz}$ were too small to use in the Boussinesq approach when compared to $\frac{du_j}{dz}$. The approach used in the new predictive model is to define turbulent conditions at the inlet and hold them constant throughout the flame domain. The inlet conditions are defined using k-ε theory, as shown in Equation 4.31, with the fluctuating velocity (u') and integral length scale (Λ) taken from experimental results as input values and $C_\mu = 0.09$. Turbulent viscosity is also defined using k-ε theory and can be seen in Equation 4.30.

$$k = \frac{1}{2}u'^2 \qquad \varepsilon = C_\mu^{\frac{3}{4}}\frac{k^{1.5}}{\Lambda} \tag{4.31}$$

To solve for premixed turbulent flame speed significant additions to the existing Cantera model were made. These modification were made to model the effects of: (1) the enhanced transport of the species and temperature due to the respective fluctuating terms, (2) an increase in the reactivity of the flame as the result of temperature fluctuation and the exponential nature of the Arrhenius rate, and (3) a decrease in the flames reaction rate caused by the influence of the turbulent-chemistry interactions. The new predictive model accounts for each of these phenomena by implementing (1) the gradient transport model for the temperature and species transport equations, (2) a Taylor series expansion of the reaction rate around the mean temperature, and (3) the eddy dissipation concept model with finite rate chemistry.

4.3.3.1 Addition of fluctuating terms in transport equations

One of the major differences between laminar and turbulent reactive flow is the temporal fluctuating terms for species, temperature and velocity. In the governing equations these are represented by Reynolds stresses $(\widetilde{u_i'' u_j''})$, species Reynold fluxes $(\widetilde{u_i'' Y_k''})$ and enthalpy Reynold fluxes $(\widetilde{u_i'' h_k''})$. These terms physically correspond to the transport of each property due to the turbulent fluctuations. The Reynolds stresses are implemented in the momentum equation in standard CFD models, however, Cantera does not solve for momentum because dp/dz would be the only result from this equation and this does not occur outside the axial momentum equation. As a result, the momentum equation and therefore $\widetilde{u_i'' u_j''}$ is not included in the predictive model. For the scalar fluxes $(\widetilde{u_i'' \varphi''})$, it is general practice in turbulent combustion to use a gradient transport model, first introduced by Daly [51], for both non-reactive and reactive scalars. The scalar fluxes can, therefore, be defined using a turbulent diffusive term as shown in Equation 4.32. For $\widetilde{u_i'' Y_k''}$, the diffusion term is defined using μ_T and a turbulent Schmidt number (Sc_t) with a value of 0.7 [166]. The new term can then be combined with $D_{k,m}$ (defined in Equation 4.8) to form an effective diffusive flux as shown in Equation 4.33 and replaces the existing diffusive flux term in Equation 4.6. A similar approach is used for the energy transport equation where a turbulent thermal conductivity term can be derived from $\widetilde{u_i'' h_k''}$ to construct a turbulent heat flux, using an effective thermal conductivity as shown in Equation 4.34 employing a Prandtl (Pr_t) number of 0.85.

$$\widetilde{u_i'' \varphi''} = -D_T \nabla \varphi \tag{4.32}$$

$$j_{k,eff} = -\rho D_{k,eff} \nabla Y_k - D_{t,k} \frac{\nabla \bar{T}}{\bar{T}} \tag{4.33}$$

$$\textit{where} \quad D_{k,eff} = D_{k,m} + \frac{\mu_T}{\rho Sc_t}$$

$$\lambda_{eff} = \lambda_{lam} + \frac{C_p \mu_T}{\mathrm{Pr}_t} \tag{4.34}$$

Substituting these new effective (*eff*) terms into the laminar transport equations allows for turbulent species and temperature transport equations to be defined as shown below.

$$\rho u \frac{\partial Y_k}{\partial z} = -\frac{\partial j_{k,eff}}{\partial z} + W_k \dot{\omega}_k \tag{4.35}$$

$$\rho c_p u \frac{\partial T}{\partial z} = \frac{\partial}{\partial z}\left(\lambda_{eff} \frac{\partial T}{\partial z}\right) - \sum_k j_k c_{p,k} \frac{\partial T}{\partial z} - \sum_k h_k W_k \dot{\omega}_k \tag{4.36}$$

The expressions in Equations 4.33 and 4.34 relate to the gradient transport model [167]. While countergradient transport often takes place in turbulent premixed flames, the predictive model uses gradient transport. Countergradient transport occurs when the pressure decreases from the unburned to the burned side of the flame and as a result the pressure gradient causes a stronger acceleration of the lower density product gases towards the high density reactants. The countergradient transport is a pressure-driven effect [167] and because pressure remains constant throughout the domain in Cantera, the gradient transport model was selected.

4.3.3.2 Influence of temperature fluctuations on reaction rate

As shown in the previous section, Cantera is capable of solving complex gas phase chemical kinetics problems. For laminar flames, the reaction coefficients are calculated as functions of mean temperature $(\bar{T})$ and composition, for turbulent flames because of the nonlinear relationship between reactivity and temperature (see Equation 4.12 for example) the mean temperature cannot be used. In a turbulent flame, the average temperature is much smaller when compared to the temperature required to calculate the true reaction rate present in the flame, defined as the equivalent kinetic temperature $(\bar{T}_k)$ [168]. This is due to the significant effect time-dependent temperature fluctuations $(T'(t))$, as defined in Equation 4.37, have on average values of k. Figure 4.6 shows the time-dependent temperature fluctuations and the mean temperature typically encountered in a turbulent flame, as well as the equivalent kinetic temperature.

$$T(t) = \bar{T} + T'(t) \tag{4.37}$$

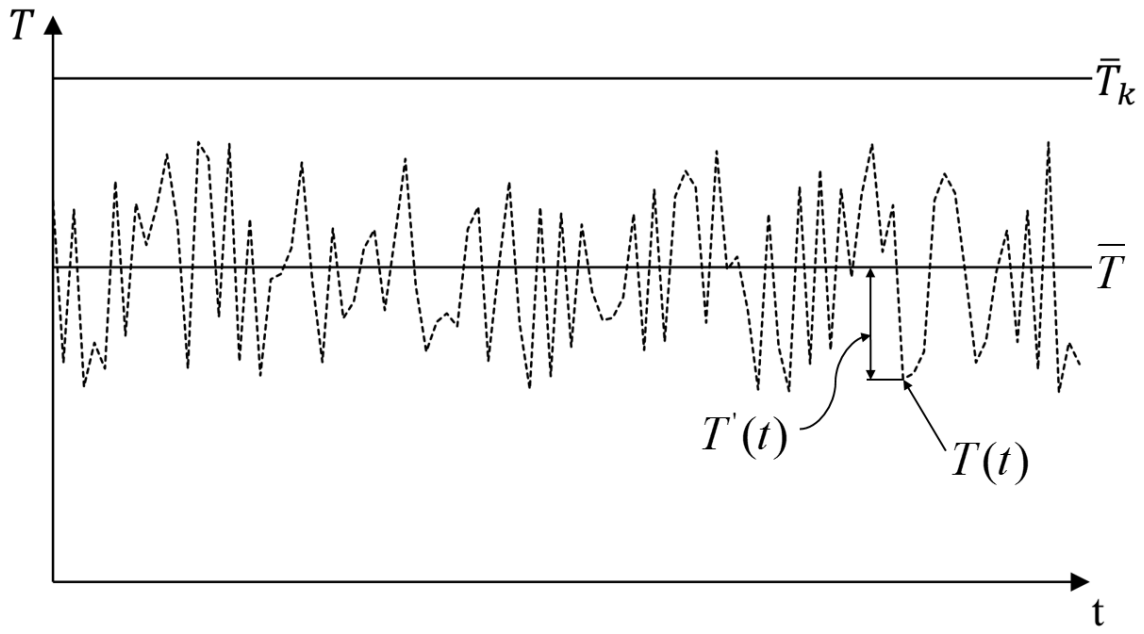

Figure 4.6: Temporal temperature profile of the mean and fluctuating temperature

Due to the exponential nature of the reaction coefficient, temperature fluctuations above the mean have a greater influence on reactivity than those below the mean. Equation 4.38 illustrates how the reaction rate based on the time-dependent temperature cannot equal $k(\bar{T})$, and how this effect increases with larger temperature fluctuations.

$$\bar{k} = \frac{\int_0^\tau k(T(t))\,dt}{\tau} = k(\bar{T}_k) \neq k(\bar{T}) \tag{4.38}$$

To account for this phenomenon, with a minimum of computational effort, a Taylor series expansion of k around the mean temperature is used to define a correction coefficient (Cc) [168,169] as shown in Equation 4.39. A Taylor series expansion of this equation can be seen in Equation 4.40. At a given temperature fluctuation intensity $(T'/\bar{T})$ the series expansion is slowest to converge when the activation temperature (Ta_f) is great than $\bar{T}$.

$$\bar{k} = k(\bar{T}) \times Cc = k(\bar{T}) + \sum_{n=2}^{\infty} \frac{1}{n!} \frac{\partial^n k}{\partial T^n}\bigg|_{\bar{T}} \cdot T'^n \tag{4.39}$$

$$\bar{k} = k(\bar{T}) \times Cc = k(\bar{T}) \cdot \left(\begin{array}{c} 1 + \frac{\beta^2 R^2 - \beta R^2 + 2E_a R\bar{T}^{-1}(\beta-1) + E_a^2 \bar{T}^{-2}}{4R^2} \mathrm{x} \left(\frac{T'}{\bar{T}}\right)^2 + \\ \frac{R^3\beta(\beta-1)(\beta-2) + 3E_a R^2(\beta-1)(\beta-2)\overline{T}^{-1} + 3E_a^2 R(\beta-2)\overline{T}^{-2} + E_a^3 \overline{T}^{-3}}{6R^3} \cdot \left(\frac{T'}{\overline{T}}\right)^3 + \ldots \end{array} \right) \tag{4.40}$$

Cc is dependent on the temperature, activation energy (Ea) and temperature exponent (β), and because of this, the Cantera source code was modified so that a Cc value is calculated for each reaction, reaction type and temperature at each grid point within the flame by the model.

Three-body reactions are modelled with the modified Arrhenius term and the additional Cc term to describe the influence of T'. To account for the falloff and pressure dependent reactions, the Arrhenius portion of each of these reaction coefficients is modified to reflect the form shown in Equation 4.40. For falloff reactions, the Cc is included in the lower (k_0) and higher limits (k_∞) of the reaction coefficients such that Equation 4.16 becomes:

$$k_f(T, P_r) = (k_\infty \times Cc) \left(\frac{P_r}{1 + P_r} \right) \tag{4.41}$$

where $P_r = \frac{k_0[\mathrm{M}] \times Cc}{k_\infty \times Cc}$. The falloff function can be calculated in a number of ways, one of the most common approaches is the Troe and SRI methods, with both temperature and pressure required for these approaches. The Chebyshev expressions have remained unmodified as there is no Arrhenius form for the rate coefficient to correct for these types of reactions.

The correction coefficient increases with temperature when activation energy is kept constant, similarly Cc also increase with β when temperature is held constant. For reverse reactions, Cc is calculated using the same approach but using the parameters of the reverse reactions. When compared to the computationally more expensive β-pdf model [170], the approach described above has shown good agreement [168]. To achieve this agreement a significant number of terms are recommended for the series expansion. To improve

convergence time, a simple truncation of the series after the first few terms is attractive. However, at high temperature fluctuation intensity $(T'/\bar{T})$ and/or Ta_f up to the eighth term in the expansion is required [168, 169]. The influence of each additional term on the overall Cc, with n equal to the number of the terms in the expansion, can be seen in Figure 4.7 for a reaction with E_a = 30,000 cal/mol, β = 0.0 and $\bar{T}$ = 1500 K. To put some perspective on the meaning of the Cc, for $T'/\bar{T}$ = 0.5, a mean temperature 1500 K corresponds to equivalent average kinetic temperature 2030 K. These larger kinetic temperatures have a significant effect on k and as a result the overall reaction rate.

(a)

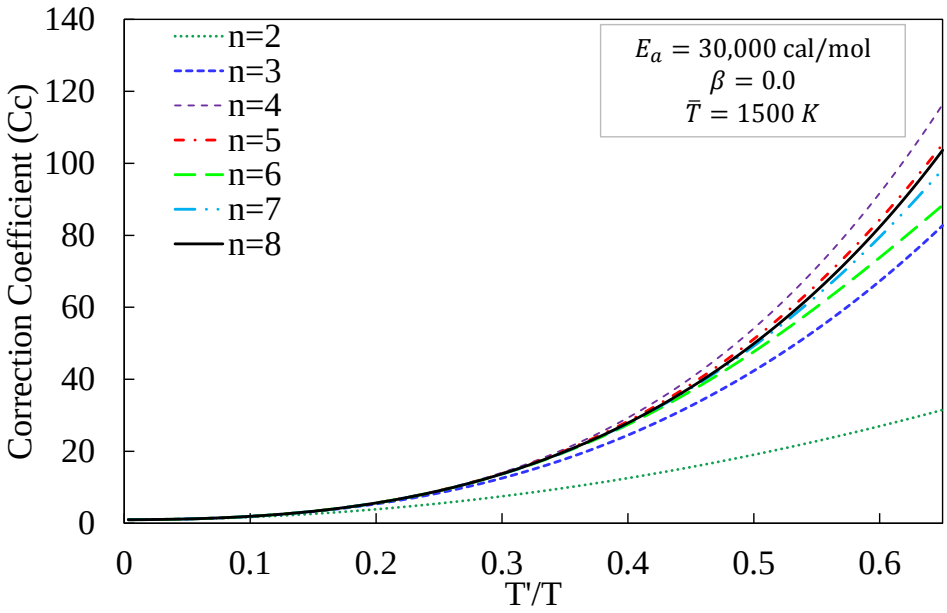

(b)

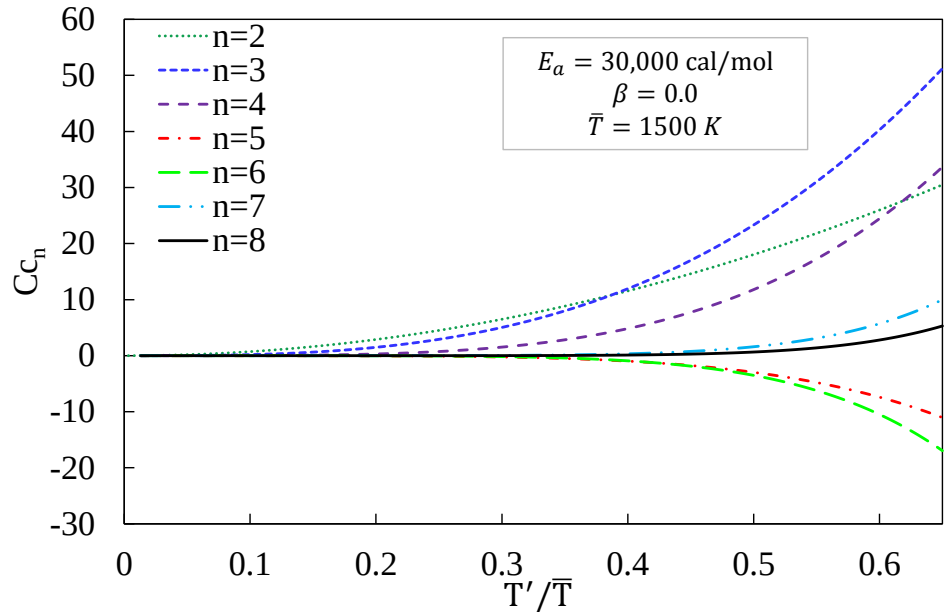

Figure 4.7: Breakdown of the correction coefficient Taylor series showing (a) the influence of each term in the series, and (b) the individual values of each term for a series of eight terms for a reaction with Ea = 30,000 cal/mol, β = 0.0 and $\bar{T}$ = 1500 K

The fluctuating temperature term (T') in Equation 4.40 can be described by solving a transport equation for the temperature variance T'^2 [171, 172], where $T' = \sqrt{T'^2}$ or using an algebraic approach [173]. The transport equation can be derived from the energy equation such that

$$\underbrace{\rho\frac{d\bar{T'^2}}{dt}}_{A_{T'}} + \underbrace{\rho u\frac{d\bar{T'^2}}{dz}}_{C_{T'}} = \underbrace{-\frac{d}{dz}\left(u\bar{T'^2} + \lambda\frac{d\bar{T'^2}}{dz}\right)}_{D_{T'}} \underbrace{-2\rho u\bar{T'}\frac{d\bar{T}}{dz}}_{P_{T'}} - 2\rho\varepsilon_{T'} \tag{4.42}$$

where $A_{T'}$ is the accumulation term, $C_{T'}$ is the convective term, $D_{T'}$ is the diffusive term, $P_{T'}$ is the production term and $\varepsilon_{T'}$ is the dissipation term. The three terms on the right hand side of the transport equation require closure. It can be seen from the production term that $u\bar{T'}$ is the heat flux term and so can be closed using the gradient diffusion hypothesis. Similarly the same approach can be applied to the $u\bar{T'^2}$ parameter in the diffusive term, which leads to:

$$u\bar{T'} = \frac{\mu_t}{\sigma_t}\frac{d\bar{T}}{dz} \qquad\qquad u\bar{T'^2} = \frac{\mu_t}{\sigma_t}\frac{d\bar{T'^2}}{dz} \tag{4.43}$$

The dissipation of the temperature variance can be described using an additional transport equation for $\varepsilon_{T'}$, however the expression is very difficult to close due to the large number of free parameters present. An alternative approach is to adopt a constant temperature fluctuations (τ_θ) and turbulence (τ_m) decay time scale ratio (R) [172] defined as:

$$R = \frac{\tau_\theta}{\tau_m} \tag{4.44}$$

where $\tau_\theta = \frac{T'^2}{2\varepsilon_{T'}}$ and $\tau_m = \frac{k}{\varepsilon}$. Assuming R = 0.5 [174, 175], the dissipation rate can be defined as shown in Equation 4.45. It should be noted that taking $R = 0.5$ results in the dissipation term matching the definition used within the Fluent CFD package [166]

$$\varepsilon_{T'} = 2\frac{\varepsilon}{k}T'^2 \tag{4.45}$$

Substituting these closed terms back into Equation 4.42 allows for the temperature variance transport equation used in the new predictive model to be defined as:

$$\rho u \frac{dT'^2}{dz} = \frac{d}{dz}\left(\mu + \frac{\mu_T}{\sigma_T}\frac{dT'^2}{dz}\right) + C_g \mu_T \left(\frac{d\bar{T}}{dz}\right)^2 - C_d \rho \frac{\varepsilon}{k} T'^2 \tag{4.46}$$

The new transport equation is added to the Cantera source code and solved in the same manner as the existing transport equations using Cantera's existing numerical solver, Sundials. It also worth noting that T'^2 is also included in the solution array and so influences the grid refinement process. Similar to the other transport equations, the diffusive term is calculated using the gradient transport model with $\sigma_T = 0.85$ [166]. For the boundary conditions, T'^2 is treated using the same approach employed for $\bar{T}$. For the inlet, the user-specified conditions are held constant, for a boundary located at a point z_0 where there is an inflow, $T'^2(z_0) = T_0'^2$ is computed, where $T_0'^2$ is user-specified. For the outlet boundary conditions, the gradient of the temperature fluctuations is held constant, for a boundary located at a point z_0 where there is an outflow, $\left.\frac{\partial T'^2}{\partial z}\right|_{z_0} = 0$ is solved.

The algebraic model, shown in Equation 4.47, attempts to represent some of the physical properties of the temperature variance transport equation. It was found that, as the source, convection and diffusion terms were neglected, the algebraic approach was inadequate for defining the temperature fluctuations in the new model. For this reason the transport equation was employed.

$$T'^2 = \frac{\mu_T}{\rho}\frac{k}{\varepsilon}\frac{C_g}{C_d}(\nabla \bar{T})^2 \tag{4.47}$$

where C_g and C_d are constants with values of 2.86, and 2.0, respectively.

4.3.3.3 Turbulent Chemistry Interaction

Many approaches to account for turbulent chemistry interaction have been discussed in Chapter 2. Because detailed chemistry is a highly desired attribute of the predictive

model, the Eddy Dissipation Concept (EDC) approach has been selected to account for TCI in the predictive model. The EDC model is based on the eddy break-up model and has been developed over the past few decades. It was first described by Magnussen et al. [176] in 1977 and further expanded a decade later [177]. The model has the capability to define an empirical expression for the mean reaction rate for premixed, partially premixed and nonpremixed combustion. The EDC model assumes that chemical reactions only take place in regions where there is sufficient dissipation of turbulent energy into thermal energy and adequate molecular mixing. According to the turbulent energy cascade theory [178], the dissipation of turbulent kinetic energy into heat takes place where the smallest eddies are dissipated due to viscous forces. This process occurs as the mechanical energy of the mean flow is transferred from bigger to smaller turbulent structures as shown in Figure 4.8. Each step in the cascade is represented by a certain strain rate (ω') interval.

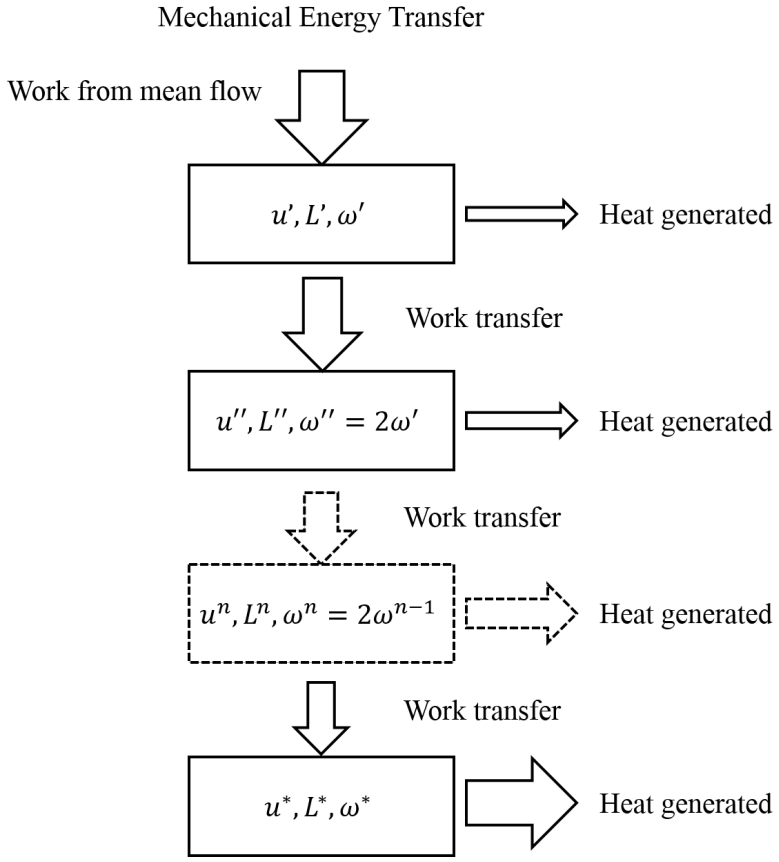

Figure 4.8: A model representing the cascade of energy from mechanical energy, within the mean flow, being transferred from larger to smaller turbulent structures and finally dissipated as heat. Reproduced from Magnussen [177]

The first level in the above figure represents the whole spectrum of turbulence and is typically modelled using a turbulent velocity (u'), length scale (L') and vorticity or characteristic strain-rate $(\omega' = u'/L')$. Similarly the next level is characterized by velocity (u''), length scale (L'') and vorticity or characteristic strain-rate (ω'') where $\omega'' = 2\omega'$. The transfer of energy (w') and the proportion dissipated into heat (q') between these levels are defined as:

$$w' = \zeta^2 12 \frac{u'}{L'} \left(u'''\right)^2 \tag{4.48}$$

$$q' = \zeta^2 15 \upsilon \left(\frac{u'}{L'}\right)^2 \tag{4.49}$$

where $\zeta = 0.18$. For each subsequent level, more energy is dissipated into heat, with this sequence continuing down to a level where all the energy transferred from the level above is dissipated as heat. The EDC model defines the final level, where all of the kinetic energy is dissipated as heat, as fine structures and are on the order of the Kolmogorov scale in two directions, but not the third. The fine structures are characterised by velocity (u^*), length scale (L^*) and strain-rate (ω^*) with the mechanical energy transferred to the fine structure being expressed as:

$$w^* = \zeta^2 6 \frac{u^*}{L^*} (u^*)^2 \tag{4.50}$$

and the heat dissipation by:

$$q^* = \zeta^2 15 \upsilon \left(\frac{u^*}{L^*} \right)^2 \tag{4.51}$$

It can be shown that $\approx 75\%$ of the total dissipation of turbulent kinetic energy to heat occurs in these fine structures [179]. The model assumes that the fluid state within the flame is determined by three distinct volumes of fluid. These volumes are defined as (1) fine structure, (2) the remaining portions of the flame, known as the surrounding fluid, and (3) the fraction of the fine structure that is reacting. The model uses superscripts to differentiate between the fine structure $(^*)$ and surrounding fluid $(^\circ)$ properties.

Figure 4.9 shows a 2D illustration of the various portions of a flame defined by EDC theory. The overall mass is represented by the large black circle, and within this mass exists a fine-structure (black region) where, it is assumed, all of the turbulent kinetic energy is dissipated into heat. The fraction of the flow occupied by such a region is expressed using γ. The definition of γ can be seen in Equation 4.52 and is limited to values between 0 and 1.

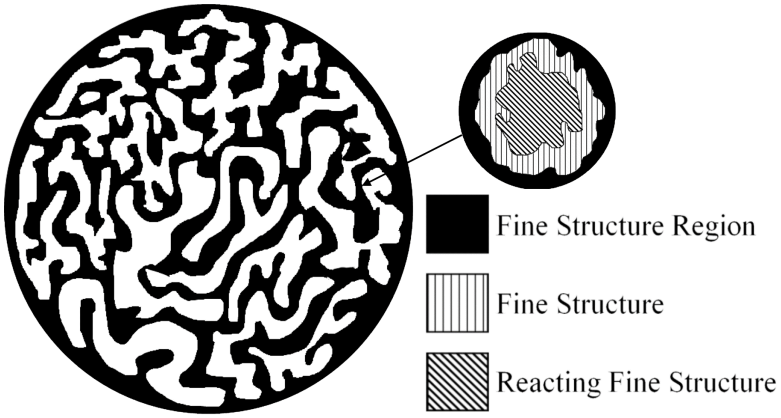

Figure 4.9: 2D breakdown of the EDC regions within a turbulent flame showing the fine structure region and the reacting and non-reacting fine structure within an insert

$$\gamma = \left(\frac{3C_{D2}}{4C_{D1}^2}\right)^{0.25}\left(\frac{\upsilon\varepsilon}{k^2}\right)^{0.25} \text{ where } C_{D1} = 0.134 \text{ and } C_{D2} = 0.5 \tag{4.52}$$

Contained in these fine structure regions, is the fine structure (vertically hatched area shown in the smaller inserted circle). The ratio of mass in the fine structure to the total mass is expressed as γ^3. The fine structure can be further broken down into a reacting and non-reacting portion. Portion within the fine structure where there is insufficient energy dissipation, a lack of reactants or a combination of both can result in an inert mixture, and are defined as non-reacting portion. The reacting portion of the fine structures have suitable condition for reactivity to occur. The ratio of reacting and non-reacting mass is determined by χ. While it is possible to determine χ using detailed chemistry, the current approach assumes fast chemistry, therefore, the definition of χ below is used with the model.

$$\chi = \chi_1 \cdot \chi_2 \cdot \chi_3 \tag{4.53a}$$

$$\chi_1 = \frac{\left(\tilde{Y}_{\min} + \tilde{Y}_{pr}/(1+r)\right)^2}{\left(\tilde{Y}_{fu} + \tilde{Y}_{pr}/(1+r)\right)\left(\tilde{Y}_{ox} + \tilde{Y}_{pr}/(1+r)\right)} \tag{4.53b}$$

$$\chi_2 = \min\left\{\frac{1}{\gamma}\frac{\tilde{Y}_{pr}/(1+r)}{\tilde{Y}_{\min} + \tilde{Y}_{pr}/(1+r)}, 1\right\} \tag{4.53c}$$

$$\chi_3 = \min\left\{\frac{\gamma\left(\tilde{Y}_{\min} + \tilde{Y}_{pr}/(1+r)\right)}{\tilde{Y}_{\min}}, 1\right\} \tag{4.53d}$$

$$where \quad \tilde{Y}_{\min} = \min\left\{\tilde{Y}_{fu}, \tilde{Y}_{ox}/r\right\}$$

r is the number of moles of oxidiser per mole of fuel and the subscripts *fu, ox* and *pr* relate to fuel, oxidiser and product respectively. The EDC model can be used with a fast chemistry or detailed chemical kinetics. Fast chemistry assumes that there is sufficient time for equilibrium to be reached in the fine structures. This allows for the reaction to be represented by a single one-step infinite-rate irreversible reaction. By using the fast chemistry approach the EDC method is greatly simplified however assuming there is sufficient time to reach equilibrium is not always valid and does not allow for detailed chemistry to be used. For this reason the detailed chemical kinetics was selected over fast chemistry. To account for finite rate chemistry within the predictive model using the EDC model, the reacting portion of the fine structures are treated as constant pressure perfectly stirred reactors (PSRs). As radiation is neglected, an adiabatic assumption is made and the governing equations are defined using Equations 4.54 to 4.56. The rate of mixing within the reactor is expressed using the mass transfer per unit of mass of the fine structure region ($\dot{m}^*$), and can be considered as an inverse of residence time (τ^*) as shown in Equation 4.57.

$$\frac{dh}{dt} = 0 \tag{4.54}$$

$$\frac{dp}{dt} = 0 \tag{4.55}$$

$$\frac{dY_k}{dt} = \omega_k^* + \dot{m}^*\left(Y_k^0 - Y_k^*\right) \tag{4.56}$$

$$\dot{m}^* = \frac{1}{\tau^*} = \left(\frac{C_{D2}}{3}\right)^{0.5}\left(\frac{\upsilon}{\varepsilon}\right)^{0.25} \tag{4.57}$$

Using Equations 4.52, 4.53a and 4.57, a PSR is created at each grid point, as shown in Figure 4.10, and the existing Cantera PSR solver is used to solve the reactors transport equations within the 1D flame model. The configuration of the reactors and grid points results in the grid points becoming the surrounding fluid and the reactors being connected to a single grid point. As a result, the only mass transfer that occurs for a PSR is to and from its associated grid point. As the Arrhenius rate is used to calculate ω_k^* for each of the

PSRs, the correction coefficient defined in Equation 4.40 is used in each reactor. Equation 4.58 is then used to express the new reaction rate for the temperature and species transport equations shown in Equations 4.36 and 4.35. The old reaction rate, in the surround fluid (i.e. in the 1D model), is discarded, essentially shifts kinetic modelling out of the 1D flame and into the 0D reactor.

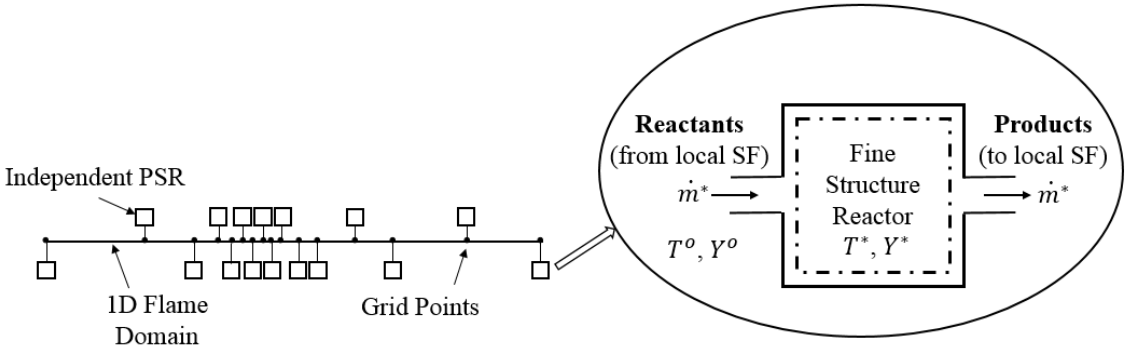

Figure 4.10: Graphical representation of the predictive models 1D domain with each grid point and its associated PSR. The inset image shows the flow from the surrounding fluid (SF)/grid point into the reacting fine structure (PSR).

$$\dot{\omega}_k = \rho \dot{m}^* \gamma^2 \chi \left(Y_k^* - Y_k^o\right) \tag{4.58}$$

When solving the PSR with each iteration of the flame governing equations (Equations 4.5-4.6) the predictive model was very computationally expensive, to the point of being impractical. To improve the computational time the reactors were only solved after each grid refinement and $\dot{\omega}_k$ was held constant between each refinement. An approach where the PSRs were refreshed after a set number of iterations was also tested. However it was found that recalculating the PSRs properties after each grid refinement proved to be a more robust approach. A combination of the two approaches was also tested, however the grid refinement only approach remained the most efficient option.

4.3.3.4 Numerical Implementation

Unfortunately, the inclusion of EDC in Cantera's source code adversely affected the robustness of the model, making it difficult to reach convergence. By limiting the refresh rate of the PSR solutions, the solver is more likely to diverge. While the refresh rate can be increased this leads to unacceptable computational time. Because of this, the solution approach used within the Python interface has a large influence on whether the predictive model reaches convergence or not. Parameters such as initial grid size, domain size and refinement criteria were found to have the largest influence on robustness. The best method to ensure convergence is an iterative approach involving the following steps:

1. Starting on an equidistant coarse grid (5-15 points), the predictive model solves for loose grid refinement criteria, slope and curve values $\approx$ 0.75-0.99, with all turbulent additions active apart from the influence of EDC. Instead a scaled version of the laminar reaction rate $(\dot{\omega}_{k,lam})$ is used as shown in Equation 4.59 where $\dot{\omega}_{EDC,k} < \dot{\omega}_{k,lam}$.

$$\dot{\omega}_{EDC,k} = (\gamma)^2 \chi \dot{\omega}_{k,lam} \tag{4.59}$$

2. When step one has reached convergence the solution is used as a first guess with full EDC switched on. The grid refinement criteria are reduced by a user-defined grid reduction value (rv), generally ranging between 0.65 and 0.85. Equation 4.60 shows how the gradient ratio $(Grad)$ is calculated using the new grid refinement criterion.

$$Grad_{new} = Grad_{current} \times rv \tag{4.60}$$

3. Taking the solution from the step two as a first guess, the predictive model iterates, adding new grid points, until the grid refinement criteria are satisfied. This process is repeated until a user-defined slope and curve target value is reached, typically equal to 0.08.

An example of this approach can be seen in Table 4.3, with a grid reduction value of 0.75 and a grid refinement slope and curve target value of 0.08. It should be noted that the conditions shown in the table are only an example and different grid reduction values can influence the solver performance and robustness. At conditions in which convergence was difficult to reach, small adjustments to the predictive model parameters had a large influence, with the initial grid size and grid reduction value being the most important parameters.

Table 4.3: Adaptive grid settings used in turbulent burning velocity computations with a grid reduction value of 0.75 and a grid refinement slope and curve target value of 0.08

Calculation Number	Slope	Curvature	Reaction Rate
1	0.80	0.80	Scaled $\dot{\omega}_k$ (Eqn 4.59)
2	0.60	0.60	Fully Enabled (Eqn 4.58)
3	0.45	0.45	Fully Enabled (Eqn 4.58)
4	0.34	0.34	Fully Enabled (Eqn 4.58)
5	0.25	0.25	Fully Enabled (Eqn 4.58)
6	0.19	0.19	Fully Enabled (Eqn 4.58)
7	0.14	0.14	Fully Enabled (Eqn 4.58)
8	0.11	0.11	Fully Enabled (Eqn 4.58)
9	0.08	0.08	Fully Enabled (Eqn 4.58)

A good initial guess is essential for reaching a converged solution for the laminar model, and this also holds true for the turbulent predictive model. A second numerical approach was used, in Python, to provide a better first guess for conditions that cannot be solved using the above approach alone. This method involved using a previous solution as the first guess for the current conditions under investigation. This was achieved by using the approach shown in Table 4.3 to solve conditions which are known to converge (Conditions A), then using this solution as an improved first guess for the conditions of interest (Conditions B). If the change in parameters between the two set of conditions is too large or convergence is particularly difficult to reach, a number of iterations between the first and final set of conditions may be required. An example of this is to start at $\phi = 0.8$ with a target condition of 1.0. To ensure convergence a solution at $\phi = 0.9$ may be needed as it would provide a better first guess for the stoichiometric case.

When using this approach, a fully converged grid of the previous solution for Conditions A cannot be used as an initial guess. This is because the change in the values in the solution array is too small for each iteration, therefore the predictive model stops iterating as the small changes are still within convergence criteria. However, the results will not reflect the operating conditions desired by the user (Conditions B), but more closely related to the conditions used to provide the initial guess (Conditions A). This issue is overcome by coarsening the initial guess solution to a less refined grid (i.e. changing the number of grid points from 500 to $\approx$ 100) before using the initial guess as a starting point. By keeping the original slope and curve target value, the predictive model will iterate and refine the grid using the method described above, and in doing so move towards the converged solution with the desired operating conditions. An example of the solution approach described above can be seen in the Python code in Appendix C and a flow chart of the process used to solve for turbulent flame speed is shown in Appendix D.

4.4 Results

The following section is dividedintofour subsections which examines the effects of the modifications to Cantera, assess the accuracy of the new model using a MAPE and trend studies and finally examines the the influnence of chemical kinetic mechanisms on turbulent flame speed. Due to the extensive number of data points examined and wide array of domain size, grid reduction value, initial and final gird size, which do not remain constant, are not described.

4.4.1 Impact of individual turbulence modifications

The sequential modification to Cantera's laminar freely-propagating flame model have different influences on the predicted values of premixed turbulent flame speed. The addition of enhanced transport and correction coefficient both increase S_T values, while the inclusion of the EDC model reduces flame speeds. The new predictive model was developed to allow the user to independently switch on/off the effects of each turbulent

phenomena. This allows for better control of the solution process in an attempt to improve the robustness of the model. An example of this is switching to full EDC chemistry after a number of iterations, since starting with full EDC can result in a divergent solution. This also allows a user to examine the effects of individual turbulence modifications on turbulent flame speed as shown in Figure 4.11.

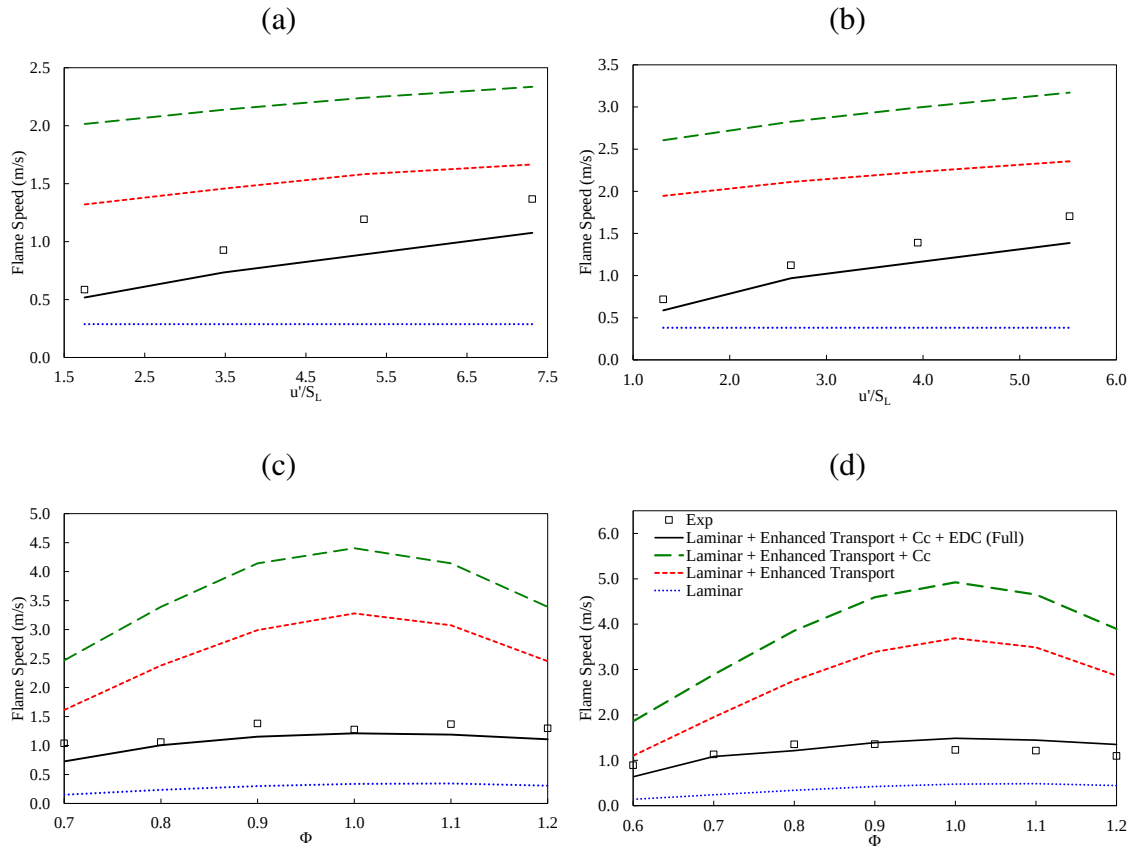

Figure 4.11: The cumulative influence of each modification for (a) Flame N at ϕ= 0.8 (b) Flame N with ϕ= 1.0, (c) Flame K for u'/S_L= 1.5, and (d) Flame H where u'/S_L= 2.0 for CH_4 at an inlet pressure and temperature of 0.1 MPa and 300 K respectively

The importance of each modification can clearly be seen in the above plots. The addition of the enhanced transport increased the level of thermal conductivity and species diffusion thus extending the reaction zone. The correction coefficient accounts for the effect of $T^{'}$ on the Arrhenius rates which increases the rate of reaction within the flame. Both modifications considerably increased the flame speed predicted by the model. The inclusion of EDC theory reduced the volume of the reaction zone, resulting in a decreased

rate of reaction in the flame and therefore a lower predicted flame speed. Figure 4.11 shows how the results of the combined modifications show good agreement with the experimental data. The addition of EDC is also particular important for matching experimental trends for varying ϕ. As shown in Figure 4.11(c) and 4.11(d), the new predictive model displays an overly large sensitivity to equivalence ratio when EDC is excluded.

4.4.2 MAPE Study

Figure 4.12 shows the comparison between the four state-of-the-art correlations from the literature (Zimont, Muppala, Kobayashi, and Ronney) using the original author's parameters, the newly developed empirical correlation and the Cantera flame speed predictive model using GRI3.0. The mean absolute percentage error was calculated using Equation 3.1 from Chapter 3. A data set of 116 flame speed predictions were used for the MAPE analysis. The results are presented for weak turbulence ($Re_t < 150$) and moderate turbulence ($Re_t > 150$). The selected data covers three regimes of turbulence (thin reaction zone $(Ka > 1)$, corrugated flamelet zone $(Ka < 1)$ and wrinkled flamelet $(u' < S_L)$) and a wide range of Da (0.30 - 129.2), for varying values of ϕ and pressures. This allows for an extensive study of each correlation over a broad range of turbulent combustion conditions.

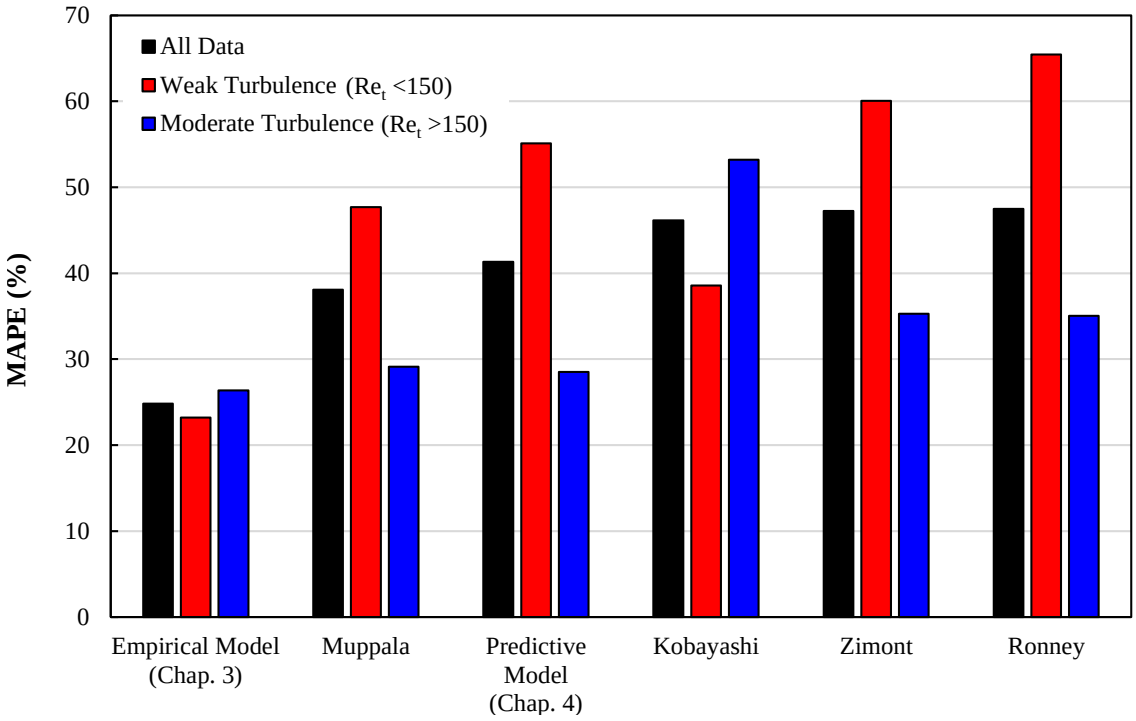

Figure 4.12: Accuracy of the state-of-the-art correlations and the predictive model using GRI3.0, determined through the use of MAPE for reported parameters

For the above MAPE study, which contains the entire range of the experimental data, the predictive model shows satisfactory agreement with $< 3.5\%$ difference between the model and the most accurate literature correlation. The breakdown of the data, based on Re_t, gives more insight into the errors. Figure 4.12 shows the low turbulence flames $(Re_t < 150)$ has a larger contribution towards this error than the high turbulence flames at $(Re_t > 150)$, with a MAPE of 55.1% and of 28.5% respectively. It should also be noted that at $Re_t > 150$ the predictive model is more accurate than the entire range of literature correlations included in the validation.

A small number of ethane flames (5 data points) in the wrinkled flamelet and thin reaction zone regimes have also been modelled using a high temperature C3 version of the AramcoMech2.0 mechanism (89 species and 668 reactions) [180]. While only a small volume of results were predicted, an average MAPE of 37% was achieved over the range of data examined. Although the predictive model was not the most accurate when compared

to the literature correlations, it was found to have $< 4\%$ difference in MAPE between the model and the most accurate literature correlation of Muppala.

4.4.3 Trend Studies

Figures 4.13 to 4.16 shows the comparison between the five correlations and the predictive model for a series of experimental trends. To assess the ability of predictive model to match S_T trends, predicted values are compared to individual S_T data points and the trends of five correlations. The selected data covers three regimes of turbulence (thin reaction zone ($Ka > 1$), corrugated flamelet zone ($Ka < 1$) and wrinkled flamelet ($u' < S_L$)), a wide range of Da (1.1 - 127.6), for varying values of ϕ and pressures up to 3.0 MPa. This allows for an extensive study of each correlation over a broad range of turbulent combustion conditions. The trend studies also provide some insight into why the MAPE is higher for low turbulence flames ($Re_t < 150$) when compared to the error associated with high turbulent flames ($Re_t > 150$).

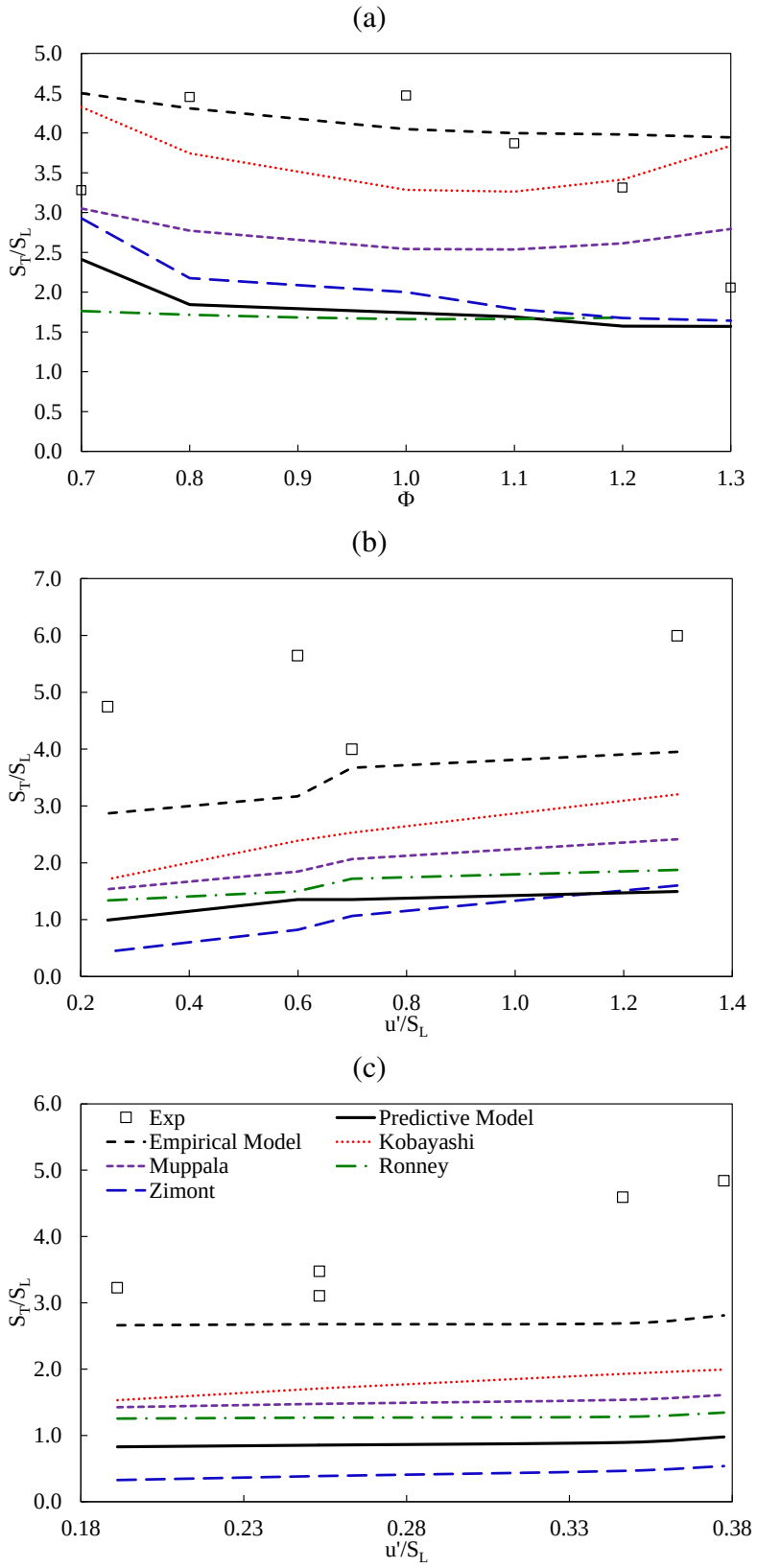

Figure 4.13: Predicted trends for (a) Flame J for u'= 0.47 m/s, (b) Flame O at ϕ= 0.75, and (c) Flame O with ϕ= 0.95 for CH_4 at an inlet pressure and temperature of 0.1 MPa and 300 K respectively

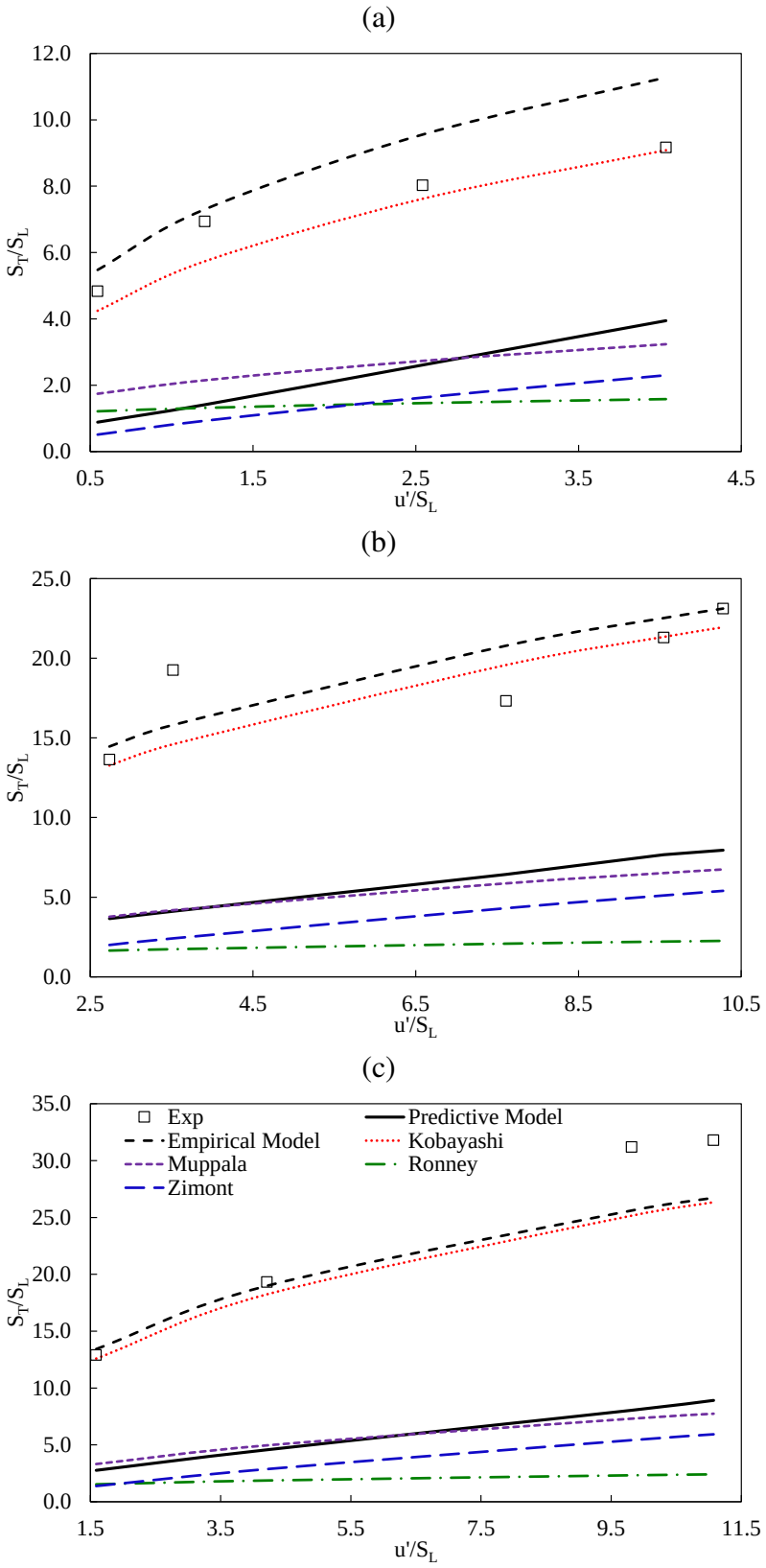

Figure 4.14: Predicted trends for (a) Flame Q (CH_4, T = 300 K, P = 0.5 MPa) at ϕ= 0.9, (b) Flame Q (CH_4, T = 300 K, P = 2.0 MPa) where ϕ= 0.9, (c) Flame B (CH_4, T = 300 K, P = 3.0 MPa) for ϕ= 0.8

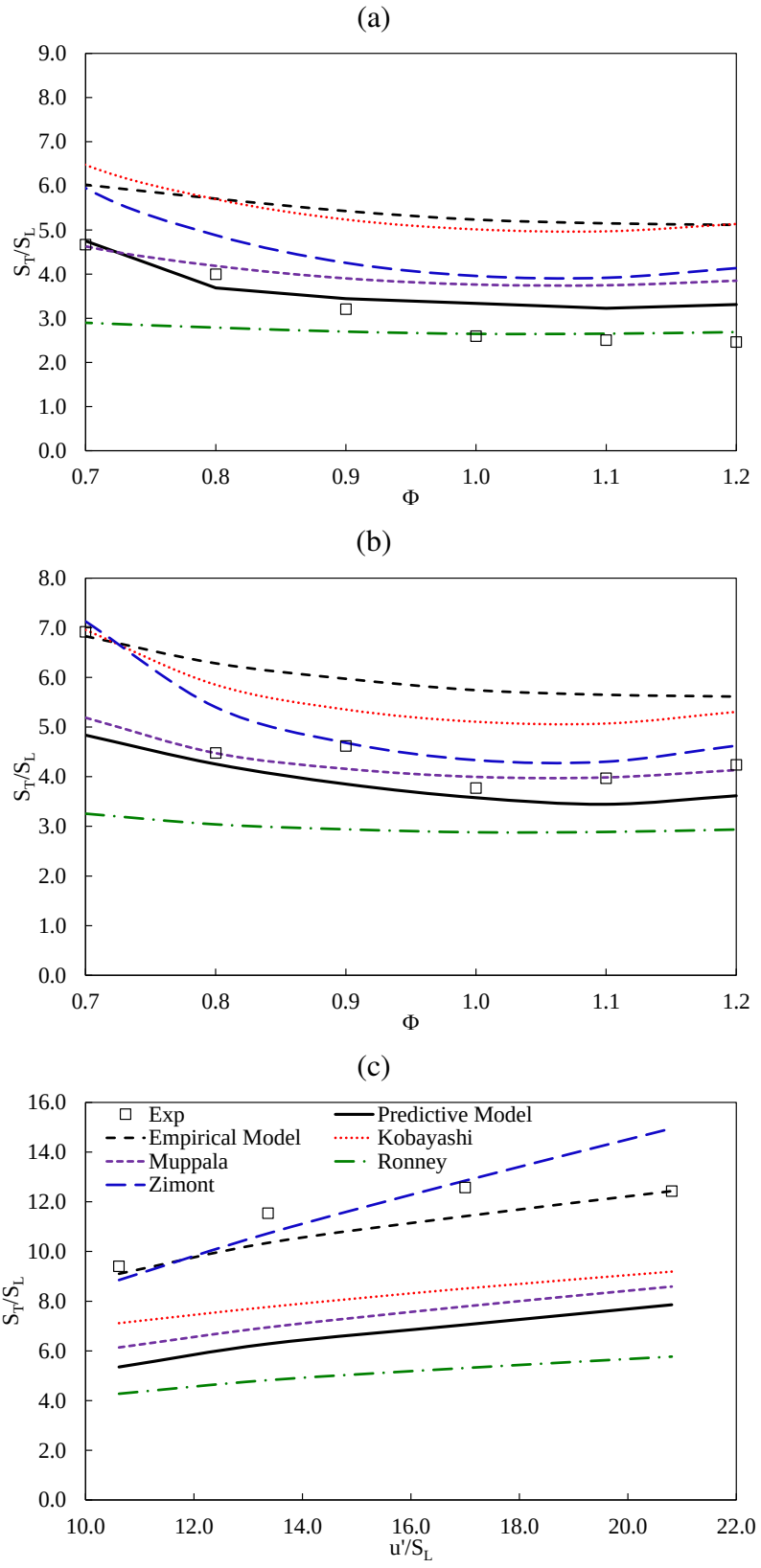

Figure 4.15: Predicted trends for (a) Flame K for u'= 1.5 and T = 300 K, (b) Flame Q with u'= 2.0 m/s and T = 360 K, (c) Flame A at ϕ= 0.8 and T = 300 K, for CH_4 at an inlet pressure 0.1 MPa

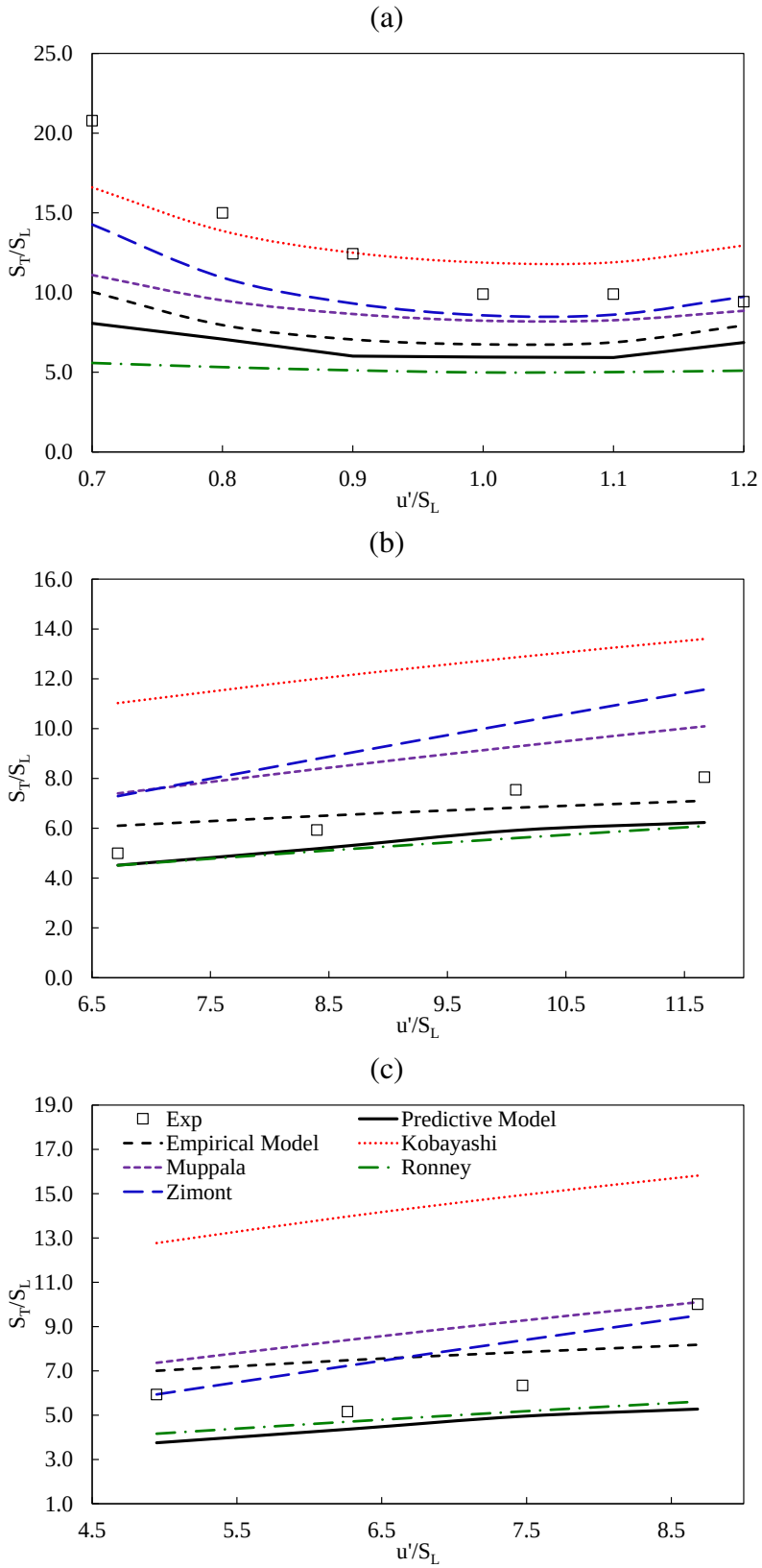

Figure 4.16: Predicted trends for (a) Flame Q (CH_4, T = 300 K, P = 3.0 MPa) where ϕ= 0.9, (b) Flame Q (CH_4, T = 300 K, P = 0.5 MPa) with ϕ= 0.9, (c) Flame B (CH_4, T = 300 K, P = 0.5 MPa) at ϕ= 0.8

For flames in the corrugated and wrinkled flamelet regimes, the predictive model struggles to predict turbulent flame speeds due to the model inability to accurately determine k and ε within the flame. Hydrodynamic (Landau-Darrieus) instabilities [40] have also been found to result in an under prediction for low turbulent flames, where $u' < S_L$, with these instabilities having a significantly larger effect at elevated pressures as shown in Figure 4.14. For values of $u' > S_L$ the role of the instabilities and the necessity to accurately predict k and ε play a reduced role. Therefore better agreement is seen between the predicted and experimental values of S_T. For flames in the thin reaction zone, an accurate prediction of $k-\varepsilon$ in the flame and the Landau-Darrieus instabilities have less of an impact, however the stretching of the flame geometry begins to have an effect on turbulent flame speed. Figures 4.15 (a) & (b) and Figures 4.16 (b) & (c) show that at moderate stretch effects, the predictive model is still capable of accurately predicting S_T. Figure 4.15 (c) and Figure 4.16 (a) show that at intense stretching turbulent flame speed is under predicted.

4.4.4 Kinetic Mechanism Analysis

GRI3.0 was used for the main analysis and validation of the new freely-propagating turbulent flame speed model. The DRM19 mechanism was also employed to predict values of S_T to investigate the influence of chemical kinetics mechanism on predictions. Figure 4.17 shows the comparison between the two mechanisms for atmospheric pressure methane flames. It should be noted that the laminar flame speeds used to normalise turbulent flame speed in Figure 4.17 are the same for both mechanisms. Therefore any difference presented in the plots are soley differences in S_T. Figure 4.17(a) and 4.17(b) show predicted results for $Re_t < 150$ and Figure 4.17(c) and 4.17(d) show flame speeds for $Re_t > 150$.

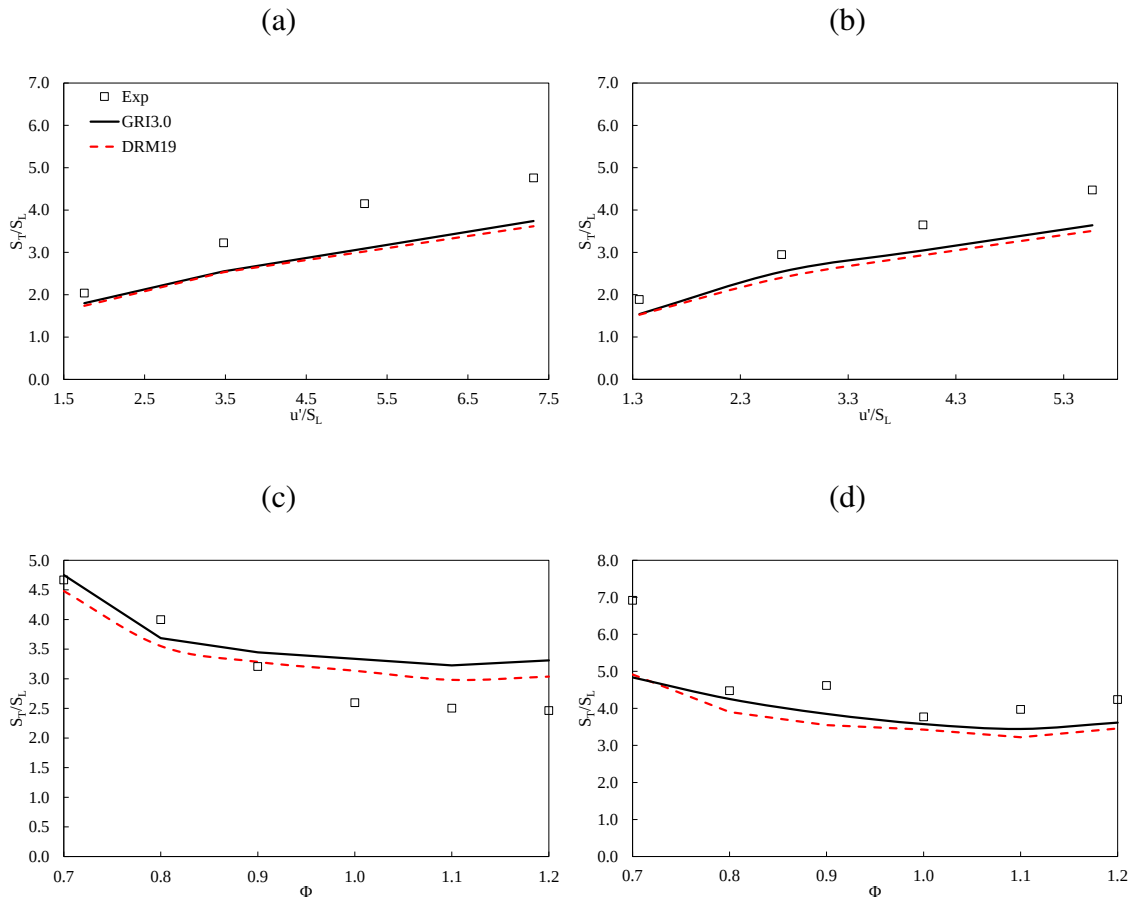

Figure 4.17: Predicted trends using DRM19 and GRI3.0 for (a) Flame N at ϕ= 0.8 (b) Flame N at ϕ= 1.0, (c) Flame K with u'/S_L= 1.5, and (d) Flame H with u'/S_L= 2.0 for CH_4 at an inlet pressure and temperature of 0.1 MPa and 300 K respectively

The comparison shows there is little difference in turbulent flame speed between the two mechanisms for the conditions examined. The largest variation in S_T is seen for flames with varying equivalence ratio where the importance of chemistry is more significant. However these variations are still small because the mechanisms are based on similar chemistry.

4.4.5 Summary

From the results displayed above the following observations can be made:

1. Figure 4.11 shows the importance of including all of the modifications, discussed in Section 4.3.3, within the new predictive model in order to accurately predict turbulent flame speed. The inclusion of the eddy dissipation concept theory is particularly important for matching experimental trends for varying ϕ. As shown in Figure 4.11(c) and 4.11(b), the new predictive model displays an overly large sensitivity to equivalence ratio when EDC theory is excluded.

2. The MAPE analysis shows satisfactory agreement between the predicted and experimental values of S_T over the entire range of 116 data points with $< 3.5\%$ difference between the model and the most accurate literature correlation. As shown in Figure 4.12, the low turbulence flames $(Re_t < 150)$ had a larger contribution towards this error than the high turbulence flames $(Re_t > 150)$. The trends displayed in Section 4.4.3 give insight into the reasons behind the different contributions.

   - For flames with a $Ka < 1$ the prediction of an accurate turbulent kinetic energy and its dissipation is essential for the prediction of S_T. The constant values of k and ε predicted by the model result in an under prediction of flame speeds for flames with $Ka < 1$ as shown in Figure 4.13. For flames in the thin reaction zone, there is less variation in k and ε, and as a result the model better predicts S_T as shown in Figure 4.15.

   - The lack of hydrodynamic (Landau-Darrieus) instabilities [40] within the model have also been found to result in an under-prediction of S_T for low turbulent flames where $u' < S_L$. These instabilities having a significantly larger effect at elevated pressures as shown in Figure 4.14. For values of $u' > S_L$ the role of the instabilities play a reduced role and as a result better agreement is seen between the predicted and experimental values of S_T for $u'/S_L > 1$.

   - While an accurate prediction of $k - \varepsilon$ in the flame and the Landau-Darrieus instabilities have less of an impact at higher turbulence levels, the stretching

of the flame geometry begins to have an effect on turbulent flame speed. At moderate stretch effects, the predictive model is still capable of predicting S_T, as shown in Figure 4.15 (a) and (b), while at intense stretching turbulent flame speed is under predicted, as can be seen in 4.15 (c).

3. From the comparison of the results predicted by DRM19 and GRI3.0 it was shown that there is very little difference in the values of S_T predicted by the two chemical mechanisms for the data examined. The largest variation in S_T occurs for the flames where ϕ is not constant resulting in a variation in chemical kinetics within the flame.

4.5 Discussion

Turbulent flame speed is a important property of premixed turbulent combustion. Current methods for predicting S_T include computational approaches such as LES or DNS or single line equations that correlate operating conditions to flame speed. The drawbacks associated with these methods requires a new approach for predicting premixed turbulent flame speed that can account for turbulence, chemistry and the interactions between them. A modified version of Cantera's freely-propagating laminar flame speed solver has been developed to meet this requirement. The aim of this chapter is to provide insight into (1) the numerics of the standard version of Cantera, (2) the theory behind the modifications made to account for the influence of turbulence within the flame, and (3) the validation of a new predictive model through comparison with experimental data and values predicted by five state-of-the-art correlations. The numerical solution method used by Cantera has not been modified and is discussed in detail elsewhere [151], therefore the following discussion will be limited to the modifications and validation of the predictive model.

4.5.1 Model Modifications

The first addition to Cantera's laminar flame speed model was a method for defining turbulence within the flame. The $k-\varepsilon$ model was selected due to it's widespread use, ease of implementation and low computational expense. The first attempt to implement

the $k-\varepsilon$ was made by adding the turbulent kinetic energy and energy dissipation transport equations shown in Equation 4.28 and 4.29, and solving them in the same manner as the existing transport equations. As the flame domain exists in one dimension, the Reynolds Stresses were solved using the Boussinesq approach [181] where the velocity gradients were set equal to the gradient along the 1D domain ($\frac{du}{dz}$). It was found that this approach was unable to accurately predict $k-\varepsilon$ profiles within the flame for a range of turbulent inlet conditions. This was due to the under prediction of the rates of production of k and ε as the values of $\frac{du}{dz}$ were too small to use in the Boussinesq approach when compared to $\frac{du_j}{dz}$. While the spatial version of the One-Dimensional Turbulence model [87] is capable of solving the Reynolds stresses, this technique requires two dimensions to fully resolve the velocity field. The additional dimension required to solve the $k-\varepsilon$ transport equations would result in an larger computational expense. To keep computational time low, a decision to define turbulence at the inlet, based on experimental values, and hold it constant throughout the domain was made. Although variations in $k-\varepsilon$ within the flame occur, it is not expected to change significantly from the inlet conditions. This is particularly the case with flames in the thin reaction zones regime [182, 183].

Once turbulence was introduced, its influence on the transport of species and temperature was accounted for using the gradient transport model [178]. Similar to the $k-\varepsilon$ model, the gradient transport model is employed due to its widespread use in the literature. Although countergradient transport often takes place in turbulent premixed flames it is not implemented in the new predictive model. Countergradient transport occurs when the pressure decreases from the unburned to the burned side of the flame and as a result the pressure gradient causes a stronger acceleration of the lower density product gases towards the high density reactants. The countergradient transport is a pressure-driven effect and because pressure remains constant throughout the domain in Cantera, the gradient transport model was selected. The constant Schmidt and Prandtl numbers used in the model for the species and temperature diffusion were based on the values employed in the commercial CFD program Fluent [166]. Values of $Pr_t = 0.85$ and $Sc_t = 0.7$ are used by the predictive model however the Schmidt number can vary from 0.4 to 0.9, while the

Prandtl number can have a value between 0.5 and 0.91 [184]. Ideally these values would be optimised to better account for reactive turbulent flow within the predictive model, and potentially vary based on the properties at each grid point, however, this is beyond the scope of this thesis.

In addition to accounting for the increased effective thermal conductivity and species diffusivity, the increased reactivity as the result of the temperature fluctuations also needed to be considered. The correction coefficient [168, 169] was selected over an assumed Gaussian probability density function (PDF) or β PDF [170] as these approaches have been found to be more computational expensive while predicting similar results [168]. To determine the temperature fluctuation intensity required for the correction coefficient expression, in Equation 4.39, a complete transport equation was implemented. While slightly more challenging to implement when compared to an algebraic model, the results were found to be much more realistic, as shown in Figure 4.18, while having no significant effect on computational expense. Although the range of data measuring T' is sparse, the complete transport equation satisfied the temperature ratio limit, $\frac{T'}{T} > 1.0$ [169], with values typically of $\frac{T'}{T} > 0.7$. While the algebraic model neglects the source, convection and diffusion terms, $\frac{T'}{T}$ is often predicted with values greater than unity, which results in the divergence of the Taylor series used to calculate Cc [169].

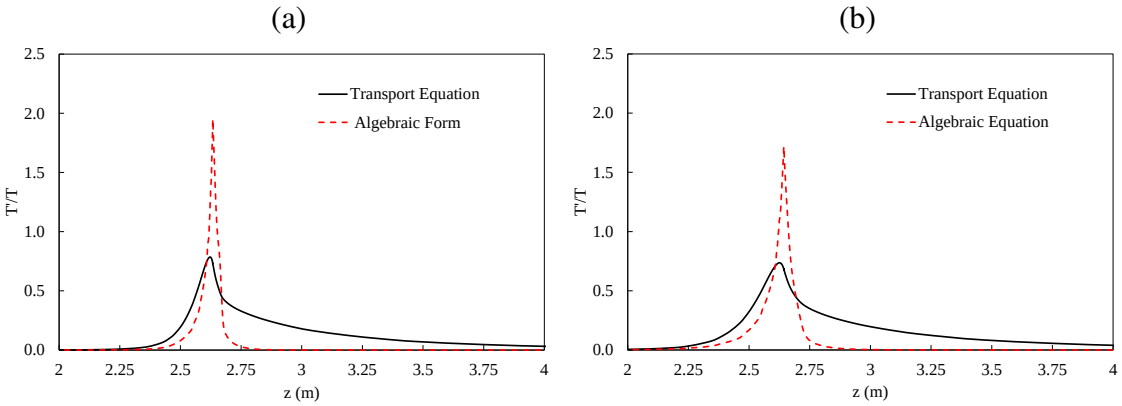

Figure 4.18: Comparison of calculation approaches for temperature fluctuation intensity for flames at ϕ= 1.0 and (a) u'/S_L= 1.4, and (b) for u'/S_L= 2.7 for CH_4 at an inlet pressure and temperature of 0.1 MPa and 300 K respectively

To account for turbulent chemistry interaction within the predictive model, the eddy dissipation concept model was also included in the modifications. When compared to the other combustion models discussed in Section 2.3.3, the EDC model was selected as (1) it has a high level of theory, and (2) uses Arrhenius rates to account for detailed chemistry which accurately account for the reactivity in the flame. Where as the FSD model and Level Set approaches, as discussed in Section 2.3.3, employ laminar flame speed to incorporate finite rate chemistry. While the transported PDF combustion model which has no theoretical basis. Although one of the most widely used combustion models [185], EDC also has its drawbacks. When compared to the rest of the modifications made to Cantera, the addition of EDC results in a significant increase in solution time and a negative effect on the solver's robustness. While further investigation is required to determine the reasons behind the loss in robustness, the increase in solution time is due to the addition of a PSR at each grid point. Limiting the rate at which the reactor solution is updated to after each grid refinement aided in reducing the solution time. A similar approach is used by Gran [186]. However while improved, the solution time still remains large $(\approx 10\times)$ when compared to the laminar solver. Despite these shortcomings, the modified model has been rigorously tested using both DRM19 and GRI3.0 mechanisms, over a range conditions for methane flames. It can be seen from Figure 4.17 that there is very little difference between the values predicted by the two mechanisms for the constant ϕ flames and a maximum of

a 12% difference at constant u'/S_L. For laminar flames under the same conditions a maximum difference of 8.6% is observed. The larger difference for the turbulent flames shows how the new turbulent model is more sensitive to chemistry than the laminar model. Further testing is also required for larger mechanisms. A small number of ethane flames in the wrinkled flamelet and thin reaction zone regimes have been modelled using a high temperature C3 version of the AramcoMech2.0 mechanism (89 species and 668 reactions) [180]. However, only a small volume of results (5 data points) were predicted. While an average MAPE of 37% was achieved over the range of data examined, additional investigation is required to determine the applicably of the model for larger hydrocarbon fuels.

Each addition to the new model was implemented so that it can be switched on/off from the Python interface. Figure 4.11 shows the influence of each modification on the turbulent flame speed. The enhanced transport increases the mixing of species and effective conduction of heat resulting in an extended reaction zone due to the increased level of transport. This leads to higher values of S_T. The correction coefficient serves to increase the reactivity of the flame due to the effect of temperature fluctuation on the Arrhenius rates. As a result the burning rate, and therefore the flame speed, is increased. Finally, the EDC model significantly reduces the reaction rate through a reduction in the reaction volume which has the opposite effect as the previous additions, reducing S_T. It should also be noted that the addition of EDC does not result in a uniform reduction of the reaction rate. Figure 4.11(c) and 4.11(b) show how EDC has a larger effect on S_T at stoichiometric conditions when compared to the lean and rich conditions, as a result, the predictive model shows better agreement to the constant ϕ trends when EDC is included.

4.5.2 Validation

To validate the newly developed predictive model the same approaches (MAPE and trend studies) employed to assess the accuracy of the correlations in Chapter 3, are also used in this chapter. In addition to comparing the numerically predicted values of S_T to experimental results, comparisons to the most accurate correlations from Chapter 3 are also

included. This allows the predictive model to be assessed against both measured values of S_T and values predicted by the current state-of-the-art approaches. The MAPE results in Figure 4.12 show that while the new predictive model is not as accurate as the empirical correlation developed in Chapter 3, the predictive model has a MAPE only slightly higher ($< 3.5\%$) than the most accurate literature correlation for the entire range of data examined. The breakdown of the MAPE displayed in Figure 4.12 shows that the results predicted for flames with $Re_t < 150$ have a larger contribution to the error than the higher turbulent flames with MAPEs of 55.1% and 28.5% respectively. It should also be noted that the MAPE for flames with $Re_t > 150$ is lower than that of the correlation developed by Muppala, making the model more accurate than the existing literature approaches for predicting S_T at gas turbine relevant conditions.

Although these results are promising, errors still exist as the modifications do not account for the entire range of physics encountered within a premixed turbulent flame. Three of the most important phenomena found in turbulent flames that are not accounted for in the model are (1) generation and dissipation of turbulent kinetic energy throughout the flame [182, 187], (2) hydrodynamic (Landau-Darrieus) instabilities, and (3) the effects of flame geometry [39]. The influence of these phenomena on turbulent flame speed vary depending on the level of turbulence present in the flame. For flames with weak turbulence $(Re_t < 150)$, the effects of phenomena (1) and (2) are large. In contrast, for moderate turbulence the influence of (1) and (2) weaken, and (3) becomes prominent.

4.5.2.1 Re_t <150 Flames

As previously discussed, the k and ε terms are kept constant and uniform at the initially calculated values throughout the flame domain. This is not the case in reality. In addition to turbulent kinetic energy being transferred through the flow via the energy cascade [178], flame generated turbulence can augment turbulent kinetic energy and its dissipation rate [188]. For the corrugated flamelets regime, this effect can be significant [182, 183]. This effect is due to the mean pressure gradient, mean velocity gradient, pressure dilatation and viscous dissipation terms, which all contribute to the transport of k. The mean pressure

gradient term and the pressure dilatation term counteract the decay of the turbulent kinetic energy by viscous dissipation, resulting in the profiles of k and ε for Case A (corrugated flamelets regime) in Figure 4.19. It can be seen that there is a large variation in the profiles of k and ε throughout the flame domain for Case A. The predictive model is unable to account for this and so under predicts S_T at these conditions.

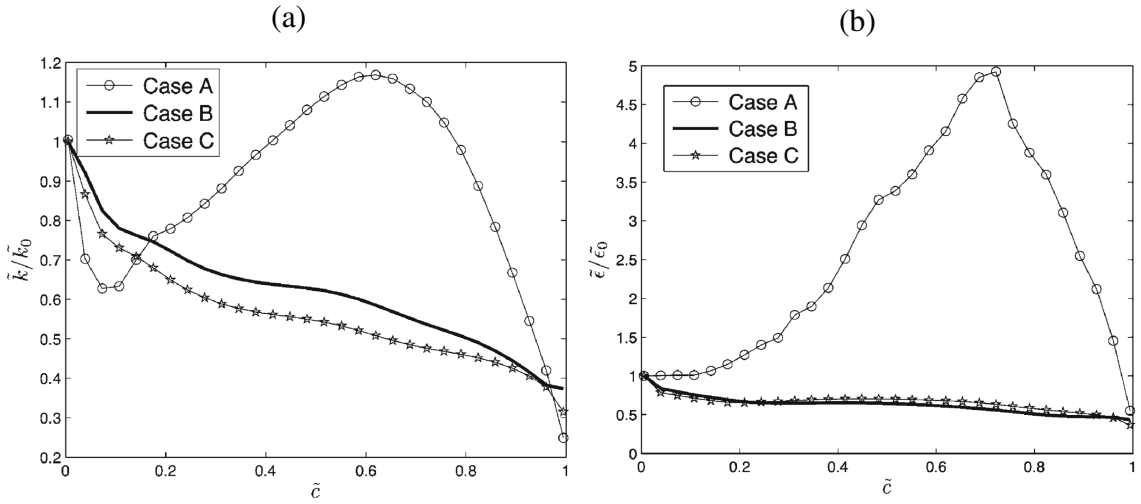

Figure 4.19: Variations of (a) k and (b) ε normalised by the values at the leading edge of the flame ($\bar{c} = 0.005$) across the flame brush for three flames. Case A relates to a flame in the corrugated flamelets regime, while Case B and C relate to flames in the thin reaction zones regime. [182]

The second phenomena not modelled is the geometry of the flame. According to the flamelet assumption, turbulent flames locally retain the structure of laminar flames and are influenced by the turbulent eddies present in the flow [41]. The geometry of a premixed turbulent flame is important as S_T depends on the flamelet wrinkling process. This process increases the surface area of the flame and, in turn, increases the turbulent flame speed [39]. The extent to which the turbulent eddies affect the flame depends on the ratio between the Kolmogorov length scale and the laminar flame thickness. The Karlovitz number ($Ka = (\delta_L/\eta)^2$) is often used to define the different influences turbulence has on the structure of the flame. Flames with weak turbulence are typically characterised by a $Ka < 1$, which is used to define the wrinkled flamelet regime in which the turbulent eddies are too large to affect the structure of the flame. Instead these eddies only

wrinkle the surface and have very little influence on S_T. However at $u' \approx S_L$ hydrodynamic instabilities can lead to a large increase in turbulent flame speed for small increases in u'/S_L [32]. These instabilities have an even larger influence at elevated pressures, at which the stabilising diffusive effects weaken with increasing P [40] and S_T can be effected by Landau-Darrieus instabilities at conditions where $u'/S_L > 1$.

For $Re_t < 150$, displayed in Figure 4.12, the errors between the predicted and experimental values for the atmospheric pressure flames can be attributed to the lack of $k-\varepsilon$ transport equation. These are required to accurately represent flames in the corrugated regime, as shown by the data for Case A in Figure 4.19. For the values measured at elevated pressure, where hydrodynamic instabilities have a considerable influence [32], the MAPE is significantly higher for the predictive model (72%) compared to the overall MAPE for the model (41.3%). These errors are however similar to the Muppala correlation (71%). Due to a lack of information on the budget of turbulent kinetic energy and its dissipation at elevated pressure, it is difficult to determine the effect of the constant $k-\varepsilon$ assumption at these conditions. However with the instabilities present in the flame, the error may remain high unless both phenomena are accounted for.

Figures 4.13 and 4.14 show the trends for a variety of conditions in the flamelet regime ($Ka < 1$) for a range of operating conditions. Figure 4.13 shows S_T measured in flames with very weak turbulence in which $u'/S_L \approx 1$. At these conditions, both the predictive model and the correlations struggle to match the values of flame speed and the trends. As previously discussed, with $u' \approx S_L$,/ Landau-Darrieus instabilities have a large effect on the turbulent flame speed which results in an under prediction of the trends by all of the correlations. Coupling this with the inability to accurately predict the $k-\varepsilon$ budget, the predictive model significantly under predicts the turbulent flame speed. For the elevated pressure flames shown in Figure 4.14 the level of turbulence with these flames is higher, with an average $Re_t \approx 57$ and $Ka \approx 4.4$, when compared to Figure 4.13. However as Kobayashi et al. [32] stated, elevated pressure results in larger hydrodynamic instabilities even at higher values of u'. For this reason, many of the correlations and the

predictive model, while matching the trends, significantly under predicts the values of turbulent flame speed. It should be noted that the correlations that show good agreement at these conditions are empirically based and have been optimized for the data measured by Kobayashi et al. [32]. While the remaining correlations are theoretical based and have not be optimised for the data in these graphs. It can be seen from Figure 4.14 that of the four theory based models, the predictive model best represents the trend in each of the plots.

4.5.2.2 Re_t >150 Flames

For flames with $Ka > 1$ the smallest turbulent eddies can penetrate and thicken the preheating zone of the flamelets and as a result, the turbulent flame speeds are substantially increased by u'. These flames are said to be in the thin reaction zone regime. The accurate prediction of the $k-\varepsilon$ budget has been found to be less relevant in thin reaction zones regime where k and ε monotonically decay across the flame domain. For Ka larger than unity, the molecular diffusion and viscous dissipation, which act as a sink of k, become dominant over the mean pressure gradient and pressure dilatation contributions [182,187]. This leads to the profiles of k and ε in Figure 4.19 for Case B and C. When compared to the results of Case A, the assumption of constant $k-\varepsilon$ in the model has less of an influence on turbulent flame speed predictions for flames in the thin reaction zone.

For the markedly higher values of fluctuating velocity associated with $Ka > 1$, the influence of the hydrodynamic instabilities on S_T weakens, even at elevated pressures. At $Ka > 1$ the instabilities are dampened by local flamelets strain rate produced by the large scale eddies [40]. For these conditions flame geometry plays a more significant role. The extensive review by Driscoll [39] concluded that the dependency of turbulent flame speed on the flame geometry can only be accounted for through the solution of a transport equation for the flame surface area. The one-dimensional nature of the newly developed predictive model makes the implementation of such an equation practically impossible. While the current version does not account for the effect of turbulent eddies on the flame structure, future work may examine alternative methods for accounting for the wrinkling process within the predictive model.

The MAPE for the flames with $Re_t > 150$ is considerably smaller for the predictive model as can be seen in in Figure 4.12. The predictive model is unable to account for the decay of k and ε and the wrinkling of the flame geometry, however it has been found that at moderate values of the Karlovitz number $(1.5 < Ka < 4.5)$ it is capable of predicting values of S_T that show good agreement with experimental data. This is most likely due to the constant values of turbulent kinetic energy and its dissipation predicted by the model, which over estimates the $k-\varepsilon$ budget, compensating for the lack of stretch effects. For the larger values of Ka, where stretch effects are stronger, the predictive model under predicts the values of S_T as the constant $k-\varepsilon$ budget cannot compensate for the effects of the wrinkling process on the flame geometry. For the case with elevated pressure and $Re_t > 150$ the Landau-Darrieus instabilities have a vastly reduced effect when compared to the $Re_t < 150$ cases. Therefore the same theory for the high turbulence atmospheric flames can be applied to the predictions made at elevated pressures where higher values $k-\varepsilon$ compensate for the stretch effects at moderate Ka values, but cannot overcome them at higher Karlovitz numbers.

The trends for flames with the larger Re_t are shown in Figure 4.15 and 4.16. It was found that pressure had little influence on the MAPE for the predictive model for flames with Reynolds numbers great than 150. Instead the level of flame stretch became more dominant in influencing the error between the predicted and experimental values. For moderate values of Karlovitz number, where stretch is also moderate, the predictive model shows good agreement to the experimental data for both the values and the trends because the $k-\varepsilon$ budget is overestimated by the predictive model therefore compensating for lack of stretch effects. In addition to showing good agreement with the experimental data, the predictive model also, on average, outperforms each of the correlations when predicting both the values and trends of turbulent flame speed under conditions with moderate Karlovitz numbers and $Re_t > 150$. The cases of moderate Ka can be seen in Figures 4.15 (a) & (b) and Figures 4.16 (b) & (c). Values of Ka are much larger in Figure 4.15 (c) and Figure 4.16 (a) and so have a larger stretch effects, therefore the trend is under predicted

by the predictive model.

4.6 Conclusion

The aim of this chapter is to provide insight into the numerics and theory used by the existing laminar flame speed model within Cantera, and to discuss and validate the new turbulent flame speed predictive model. In order to solve for premixed turbulent flame speed, significant addition to the existing model had to be made. These modification were made to model the effects of: (1) the enhanced transport of the species and temperature due to the respective fluctuating terms, (2) an increase in the reactivity of the flame as the result of temperature fluctuation and the exponential nature of the Arrhenius rate, and (3) a decrease in the flames reaction rate caused by the influence of the turbulent-chemistry interactions. The new predictive model accounts for each of these phenomena by implementing (1) the gradient transport model for the temperature and species transport equations, (2) a Taylor series expansion of the reaction rate around the mean temperature, and (3) the eddy dissipation concept model with finite rate chemistry.

With the addition of these modifications it became apparent that both the robustness and the solution times of the solver had been negatively affected mainly due to the inclusion of the EDC model. To overcome these drawbacks an alternative solution approach, within Python, had to be developed in an effort to reduce the solution time and improve robustness. After considerable testing, the solution approaches discussed in Section 4.3.3.4 were determined to be the best numerical method and were used to validate the predictive model for 116 experimental points of turbulent flame speed over a wide range of turbulent and operating conditions.

The predictive model was also compared against five state-of-the-art premixed turbulent flame speed correlations to assess the models accuracy against current literature approaches. The comparison for the entire range of data found only small difference exists between the MAPE of the most accurate correlation, developed by Muppala, (38.1%)

and the error associated with the predictive model (41.3 %). A significant portion of this MAPE comes from flames with weak turbulence ($Ka < 1.5$ and $Re_t < 150$) where the predictive model struggled with the large variations in the $k-\varepsilon$ budget and the Landau-Darrieus instabilities. These became even more influential at weak turbulence and elevated pressure. For moderate turbulence where flame stretch effects are also moderate ($1.5 < Ka < 4.5$ and $Re_t > 150$) the model performs significantly better capturing both the values and the trends well. Even more importantly, at these conditions and elevated pressures, which are relevant to gas turbines, the model outperforms all of the literature correlations making it a valuable tool for gas turbine designers. Although additional modifications are required to further improve the accuracy of the model, the current version has shown to be as accurate as existing empirical approaches and more accurate for gas turbine relevant conditions.

Chapter 5

Discussion and Conclusion

This chapter summarises and discusses the findings of the work carried out during this research. A summary of the outcomes of the work presented in this thesis is given in Section 5.1. Ideas for future studies related to this work are provided in Section 5.2. Finally, overall conclusions are given in Section 5.3.

5.1 Discussion of Thesis

In order to further improve gas turbine combustor technologies, a better understanding of the combustion process is required. Premixed turbulent flame speed is an key parameter in turbulent combustion, and is influenced by chemistry, flow properties and laminar and turbulent transport. As a result it can be used to indicate the level of reactivity of the flame within the gas turbine combustor. Due to the importance of premixed turbulent combustion, a significant amount of research has taken place with particular focus on turbulent flame speed. Current approaches for defining S_T include experimental campaigns, empirical correlations and computational methods. Key contributions from this thesis include (i) assembly of a large database of experimental data from a wide range of sources, (ii) comprehensive review of the extensive range of empirical correlations, (iii) optimization of the five most accurate correlations over a large volume of experimental data, (iv) development and testing of a new empirical correlation, and (v) development and validation of a 1D turbulent flame speed predictive model using detailed chemistry.

The long list of literature correlations, shown in Section 2.5.2, the complexity of turbulent premixed flames, and large variety of theory used to develop each expression can make choosing the correct correlation to predict S_T difficult. To provide a better understanding of the current empirical S_T predictive methods available in the literature, an extensive study of fifteen turbulent flame speed correlations was carried out in Chapter 3. In addition to the literature correlations, a newly developed empirical correlation is also purposed and tested along side the literature correlations. The first comparison (Study A) involved all of the correlations and a portion of the total experimental data available. Only a portion of the data could be used for Study A due the requirement of having S_T measure at progress variables of 0.05 and 0.5. From this comparison, using 200 data points for a variety of turbulent conditions, the expressions by Zimont, Kobayashi, Muppala, Ronney and the newly-developed correlation were found to be the most accurate. These correlations were therefore selected for further investigation with a larger data set of 335 experimental data points. Two studies were carried out for this data set. The first (Study B) used the authors original adjustable parameters. While the second comparison (Study C) used parameters optimized using a Nelder-Mead simplex direct search method and the large experimental data set.

It was found in both studies that the newly-developed correlation had the smallest MAPE, followed in order of decreasing accuracy by expressions developed by Muppala, Kobayashi, Zimont and Ronney. For the trend studies it was found again that the newly developed correlation was best suited to match experimental trends for the data examined. The literature correlations were less suited and tended to struggle depending on the conditions under investigation. Many of these areas can be associated with inappropriate adjustable parameters. The optimization of the adjustable parameters of the literature correlations reduced the MAPE for each correlation by an average of $\approx 13\%$ and improved each correlations ability to match trends. While correlations are still required for closing Favre-averaged $\bar{c}$ equations, the author believes that an alternative approach is needed for predicting S_T for the assessment of combustor reactivity as the study showed no general

correlation exists for predicting turbulent flame speed.

For this reason, the author developed a modified version of Cantera's 1D freely propagating laminar flame speed model, which is capable of predicting S_T. Chapter 4 describes the underlying theory used by the laminar version of Cantera before going on to discuss the development of the new turbulent flame speed predictive model. The modifications to Cantera include:

- The gradient transport model to handle the increased transport of species, temperature variance and energy due to the respective fluctuations within the flow.
- A Taylor series expansion of the reaction rate around the time-averaged temperature to account for the influence of temperature fluctuations on the reaction rate.
- The eddy dissipation concept model to account for the interactions between the turbulent flow and detailed chemistry.

As shown in Section 4.4 each of these additions are essential for the accurate prediction of S_T. As expected the increased transport and enhanced reaction rate drastically increased the turbulent flame speed. The EDC theory on the other hand results in a reduction in reactivity and therefore S_T due to the interaction between turbulence and chemistry. A negative outcome of these modifications was (1) the increase in solution time due to the need to solve the PSRs, and (2) the decrease in the robustness of the solver due to the refresh rate of the PSR solution which is a trade off between stability and solution time. A new solution approach, within Python, was developed in order to resolve these issues. Using this approach, the predictive model was validated against 116 data points over a wide range of turbulence and operating conditions. From the validation the following observations were made:

- For flames with weak turbulence, in which $Ka < 1$, the constant $k-\varepsilon$ assumption results in under prediction of the turbulent flame speed. This assumption was made as $k-\varepsilon$ transport equations can not be implemented in a 1D domain.

- Landau-Darrieus instabilities are not accounted for by the above modifications, therefore for flames with hydrodynamic instabilities present, the model tends to under predict S_T.

- At moderate turbulence ($1.5 < Ka < 4.5$ and $Re_t > 150$) the instabilities and variation in the $k-\varepsilon$ budget have less of an influence on the turbulent flame speed, resulting in good agreement between the model and experimental data.

- For flames with high levels of stretching, S_T tends to be under predicted by the predictive model as the model does not account for geometry effects on S_T.

Overall both the new empirical correlation and the predictive model were found to be more accurate than the existing state-of-the-art empirical approaches available in the literature for gas turbine relevant conditions.

5.2 Recommendations for Future Work

The work presented here provides a significant investigation into methods for the prediction of turbulent flame speeds using both correlations and numerical approaches. Over the course of this work, several areas for additional study were identified. These areas would aim to further improve the accuracy of the empirical and predictive methods. This section provides details on a number of potential areas that could be investigated as a direct follow on from this research.

5.2.1 Correlations

The empirical correlation has been optimised over a wide range of experimental conditions and shown a high level of accuracy for the data investigated. For future work it would be valuable to investigate the accuracy of the empirical model against experimental conditions beyond the ranges of data examined in Chapter 3 in order to test the applicability of the correlation at conditions outside the optimization range. Such conditions would include flame speeds at elevated pressure with moderate to intense turbulence. It

was interesting to note that the MAPE was larger in Study A when compare to Study B even though the size of the data set in Study A was a smaller subset of that used in Study B. This is due to the correlation being optimised for the entire range of data in Study B rather than the subset of data in Study A. Therefore studying the correlations outside of the optimization range would give further insight into the empirical correlations. Such an investigation would be valueable for (1) gas turbine conditions, and (2) hydrogen and hydrogen/hydrocarbon blends, to determine the applicability of transferring the adjustable parameters defined in Chapter 3 to these conditions.

5.2.2 Predictive Model

Significant modifications have been made to Cantera's source code to allow for the accurate prediction of turbulent flame speed. While the validation of the model shows satisfactory agreement with experimental data, future work would aim to further improve the model by:

- Optimizing the turbulent Prandtl and Schmidt numbers within the model: As discussed in Section 4.5.1, values of $Pr_t = 0.85$ and $Sc_t = 0.7$ are used by the predictive model and were selected based as their default values in the commercial CFD program Fluent. These values can however vary significantly depending on the flame conditions [184]. For this reason optimizing Pr_t and Sc_t for the flame conditions under investigation, could lead to reduced MAPE values and improve the predictive models ability to match trends.

- Modification to include flame stretch effects: As shown in Chapter 4, for flame with $Re_t > 150$ and intense flame stretch, the predictive model tended to under predict the turbulent flame speed. A major contribution to this was the inability of the model to account for the dependency of S_T on the flame geometry. According to Driscoll [39] the dependency of turbulent flame speed on the flame geometry can only be accounted for through the solution of a transport equation for the flame surface area. However the single dimensional nature of the predictive model makes a transport equation for the flame surface area impossible to implement. Therefore

future work would aim to use an alternative method similar to that proposed by Zimont [189] and used in Ansys Fluent [166]. This approach includes a stretch factor (G) in the source term of the progress variable transport equation to account for the effect of stretching on the turbulent heat release intensity. While this exact method is not applicable for the predictive model, as there is no c transport equation, future work would aim to implement a similar approach of modifying a transport equation to represent the increase in reactivity associated with the increase of flame surface area due to turbulent stretching of the flame front.

- Further testing kinetic mechanisms: While GRI3.0 and DRM19 have been used over a wide range of experimental data, a large number of alternative mechanisms are available in the literature. Some of these mechanisms, DLW99 [190], have been found to predict results similar to GRI3.0, while others, San Diego mechanism [191], have found to show better agreement with experimental data [192]. This is due to mechanisms having different Arrhenius parameters for describing chemistry and therefore predict different results rather than the mechanisms being larger in size and therefore more accurate [192]. It should also be noted that GRI3.0 has not been optimised for pressures greater than 2.0 MPa [193] or pure fuel hydrocarbons (such as ethane, propane, methanol, ethylene and acetylene) [194]. For these reasons future work would investigate the influence of alternative chemical kinetic mechanisms on both MAPE and trend predictions.

- Modelling larger fuels: Following on from the previous point, larger mechanisms would allow for modelling of larger fuels. As natural gas is not composed of pure methane, but rather a mixture of various hydrocarbons, validating the predictive model for fuels molecules larger than CH_4 as well as mixtures similar to natural gas would be highly valuable. Although large chemical mechanism would be required, resulting in longer computational times, a validated turbulent flame speed model for gas turbine relevant conditions and fuels would be a significant asset for designers.

- Improve solver solution time and robustness: One of the major draw back as a result of the modifications is the increase in solution time and loss of robustness. These

two phenomena are interlinked, therefore improving solution time will allow for the refresh rate of the PSR to be increased and therefore improve robustness. There are a number of approaches that can be taken to achieve this such as (1) decreasing the refresh rate of the reactors where reactivity is low (i.e. close to the inlet/outlet), and (2) solving a number of the PSRs simultaneous rather than individually as is currently done.

5.3 Conclusion

This work has resulted in numerous useful observations relating the determining premixed turbulent flame speed using empirical and predictive methods. A number of the key finding found during this research are summarised below:

- A large number of S_T correlations existing in the literature and are based on a variety of turbulent combustion theory. However even after seventy years of research examining S_T correlations a general expression remains elusive. Chapter 3 provides a detailed study of the existing correlations and presents a newly developed empirical correlation. Using an extensive data set of 335 experiential flame speed values, it was found that the newly developed correlation was overall the most accurate expression for both MAPE and trend studies, while the equation developed by Muppala was the best preforming literature correlation. However the study also showed that a minimum of two correlations and two sets pf adjustable parameters are need to achieve these findings.

- In an attempt to overcome these drawbacks a turbulent flame speed predictive model has been developed which incorporates turbulence and detailed chemistry in a one dimensional model. The additions made to Cantera included: (1) the gradient transport model for the temperature and species transport equations to account for increase transport, (2) a Taylor series expansion of the reaction rate around the mean temperature to model the effects of temperature fluctuation on the Arrhenius rate, and (3) the eddy dissipation concept model with finite rate chemistry to define the

influence of the turbulent-chemistry interactions. From the validation of the model it was found that each of the modifications made to Cantera were essential for the accurate prediction of S_T.

The results from the model showed a very small difference between the MAPE of the most accurate correlation of Muppala, (38.1%) and the predictive model (41.3 %). For gas turbine relevant conditions it was found that the model improved on existing empirical approaches, providing a smaller error. This is due to the new model being more accurate for flames with moderate turbulence and stretch effects and at these conditions the model out performed the most accurate literature empirical correlations. While accurate at moderate conditions, the model tends to under predict turbulent flame speeds where the influence of flame geometry plays a significant role. Further work will seek to include this phenomenon, thereby expanding the applicability of the model.

Bibliography

[1] International Energy Agency (IEA). World Energy Outlook 2016. *Secure Sustainable Together*, page 684, 2016.

[2] BP. BP Statistical Review of World Energy 2017. Technical report, 2017.

[3] Dieter Helm. The future of fossil fuels - is it the end? *Oxford Review of Economic Policy*, 32(2):191–205, 2016.

[4] V. Bex Stocker, T.F., D. Qin, G.-K. Plattner, M. Tignor, S.K. Allen, J. Boschung, A. Nauels, Y. Xia and P.M. Midgley (eds.). *IPCC, 2013: Climate Change 2013: The Physical Science Basis. Contribution of Working Group I to the Fifth Assessment Report of the Intergovernmental Panel on Climate Change*. Number Annex I. Cambridge University Press, Cambridge, United Kingdom and New York, NY, USA, 2013.

[5] R.J. Andres T.A. Boden, G. Marland. Global, Regional, and National Fossil-Fuel CO2 Emissions. Carbon Dioxide Information Analysis Center. *Oak Ridge National Laboratory, U.S. Department of Energy*, 2010.

[6] United Nations Framework Convention on Climate Change (UNFCCC). The Paris Agreement, in 21st Conference of the Parties, 2015.

[7] Christophe McGlade and Paul Ekins. The geographical distribution of fossil fuels unused when limiting global warming to 2 C. *Nature*, 517:187, jan 2015.

[8] A H Lefebvre and D R Ballal. *Gas Turbine Combustion: Alternative Fuels and Emissions, Third Edition*. Taylor & Francis, third edition, 2010.

[9] T. Lieuwen and V. Yang. *Gas Turbine Emissions*. Cambridge Aerospace Series. Cambridge University Press, 2013.

[10] R J Reed. *North American Combustion Handbook*. North American Mfg. Company, Cleveland, third edit edition, 1986.

[11] S R Turns. *An Introduction to Combustion: Concepts and Applications*. McGraw-Hill, New York, thrid edit edition, 2012.

[12] P. Capros, De Vita A., Tasios N., Siskos P., Kannavou M., Petropoulos A., Evangelopoulou S., Zampara M., Papadopoulos D., and C. Nakos et Al. *EU reference scenario 2016. Energy, transport and GHG emissions: trends to 2050*. Luxembourg: Publications Office, 2016.

[13] Gerneral Electric. 9HA.01 SETS EFFICIENCY WORLD RECORD, 2016.

[14] Siemans. Siemens sets new performance and efficiency world record at Düsseldorf power plant, 2016.

[15] L Berkley Davis. Dry Low NOx Combustion Systems for GE Heavy-Duty Gas Turbines, 1996.

[16] S Johnson, B Pepperman, M Koenig, and K Abou-Jaoude. Ultra Low Nox Combustion Technology, 2008.

[17] Meherwan Boyce. *Gas Turbine Engineering Handbook*. Gulf Professional Publishing, Boston, MA, third edition, 2006.

[18] Krishna Venkataraman, Skigh E Lewis, Jayaprakash Natarajan, Stephen R Thomas, and Joseph V Citeno. F-Class DLN Technology Advancements: DLN2.6+. *ASME. Turbo Expo: Power for Land, Sea, and Air*, 3(54631):587–594, 2011.

[19] Tim Lieuwen, Vince McDonell, Eric Petersen, and Domenic Santavicca. Fuel flexibility influences on premixed combustor blowout, flashback, autoignition, and stability. *Journal of engineering for gas turbines and power*, 130(1):11506, 2008.

[20] T M Muruganandam, S Nair, D Scarborough, Y Neumeier, J Jagoda, T Lieuwen, J Seitzman, and B Zinn. Active Control of Lean Blowout for Turbine Engine Combustors. *Journal of Propulsion and Power*, 21(5):807–814, sep 2005.

[21] Achintya Mukhopadhyay, Rajendra R Chaudhari, Tanoy Paul, Swarnendu Sen, and Asok Ray. Lean Blow-Out Prediction in Gas Turbine Combustors Using Symbolic Time Series Analysis. *Journal of Propulsion and Power*, 29(4):950–960, 2013.

[22] M P Boyce. *Gas Turbine Engineering Handbook*. Elsevier Science, 2017.

[23] GE Power. Dry Low NOx 2.6+ Combustion System 9FA/9FB Gas Turbines, 2016.

[24] Stanka Kokanovic, Gianfranco Guidati, Stephan Torchalla, and Bruno Schuermans. Active Combustion Control System for Reduction of NOx and Pulsation Levels in Gas Turbines. *Turbo Expo: Power for Land, Sea, and Air*, 1(42363):673–682, 2006.

[25] Roointon Pavri and Gerald D Moore. Gas turbine emissions and control. *General Electric Report No. GER-4211*, 2001.

[26] H. Kolla, J. W. Rogerson, and N. Swaminathan. Validation of a Turbulent Flame Speed Model across Combustion Regimes. *Combustion Science and Technology*, 182(3):284–308, 2010.

[27] Prabhakar Venkateswaran. Measurements and modeling of turbulent consumption speeds of syngas fuel blends. (May):273, 2013.

[28] H. Kolla, J. W. Rogerson, N. Chakraborty, and N. Swaminathan. Scalar Dissipation Rate Modeling and its Validation. *Combustion Science and Technology*, 181(3):518–535, 2009.

[29] Alan R Kerstein. Pair-exchange model of turbulent premixed flame propagation. *Symposium (International) on Combustion*, 21(1):1281–1289, 1988.

[30] P. D. Ronney. Some Open Issues in Premixed Turbulent Combustion. *Modeling in Combustion Science, Lecture Notes in Physics*, 449, 1995.

[31] S. S. Shy, W. J. Lin, and J. C. Wei. An experimental correlation of turbulent burning velocities for premixed turbulent methane-air combustion. *Proceedings of the Royal Society A: Mathematical, Physical and Engineering Sciences*, 456(2000):1997–2019, 2000.

[32] Hideaki Kobayashi, Takashi Tamura, Kaoru Maruta, Takashi Niioka, and Forman a. Williams. Burning velocity of turbulent premixed flames in a high-pressure environment. *Symposium (International) on Combustion*, 26(1):389–396, 1996.

[33] Sankaranarayanan Ravi, Anibal Morones, and Eric Petersen. Evaluation of Numerical Turbulent Combustion Models Using Flame Speed Measurements from a Recently Developed Fan- Stirred Explosion Vessel. *8 th U. S. National Combustion Meeting*, 2013.

[34] R. G. Abdel-Gayed, D. Bradley, and M. Lawes. Turbulent Burning Velocities: A General Correlation in Terms of Straining Rates. *Proceedings of the Royal Society A: Mathematical, Physical and Engineering Sciences*, 414(1847):389–413, 1987.

[35] D. Bradley, M. Lawes, and M.S. Mansour. Correlation of turbulent burning velocities of ethanolair, measured in a fan-stirred bomb up to 1.2MPa. *Combustion and Flame*, 158(1):123–138, 2011.

[36] P. Venkateswaran Prabhakar, Andrew Marshall, Dong Hyuk Shin, David Noble, Jerry Seitzman, and Tim Lieuwen. Measurements and analysis of turbulent consumption speeds of H2/CO mixtures. *Combustion and Flame*, 158(8):1602–1614, 2011.

[37] Piotr Siewert, Peter Griebel, and Peter Jansohn. Influence of pressure on flame front corrugation and turbulent flame speed: fractal analysis of lean premixed methane/air flames. *Third European Combustion Meeting*, pages 1–6, 2007.

[38] S.P.R Muppala. A Comparative study of the different reaction models for turbulent methane/hydrogen/air. *Journal of Thermal Engineering*, 1(1):367–380, 2015.

[39] James F. Driscoll. Turbulent premixed combustion: Flamelet structure and its effect on turbulent burning velocities. *Progress in Energy and Combustion Science*, 34(1):91–134, 2008.

[40] N. Lipatnikov and J. Chomiak. Turbulent flame speed and thickness: Phenomenology, evaluation, and application in multi-dimensional simulations. *Progress in Energy and Combustion Science*, 28:1–74, 2002.

[41] Norbert Peters. *Turbulent combustion*. Cambridge University Press, 2000.

[42] David G. Goodwin and Harry K. Moffat and Raymond L. Speth. Cantera: An Object-oriented Software Toolkit for Chemical Kinetics, Thermodynamics, and Transport Processes, 2014.

[43] R. Mead Nelder J. A. A Simplex Method for Function Minimization. *The Computer Journal*, 7(4):308–313, 1965.

[44] B Magnussen. On the structure of turbulence and a generalized eddy dissipation concept for chemical reaction in turbulent flow. In *19th Aerospace Sciences Meeting*, Aerospace Sciences Meetings. American Institute of Aeronautics and Astronautics, 1981.

[45] J Warnatz, U Maas, and R W Dibble. *Combustion: Physical and Chemical Fundamentals, Modeling and Simulation, Experiments, Pollutant Formation*. Springer Berlin Heidelberg, 2013.

[46] Osborne Reynolds. On the Dynamical Theory of Incompressible Viscous Fluids and the Determination of the Criterion. *Philosophical Transactions of the Royal Society of London A: Mathematical, Physical and Engineering Sciences*, 186:123–164, 1895.

[47] B Baldwin and H Lomax. Thin-layer approximation and algebraic model for separated turbulentflows. In *16th Aerospace Sciences Meeting*, Aerospace Sciences Meetings. American Institute of Aeronautics and Astronautics, 1978.

[48] P Spalart and S Allmaras. A one-equation turbulence model for aerodynamic flows. In *30th Aerospace Sciences Meeting and Exhibit*, Aerospace Sciences Meetings. American Institute of Aeronautics and Astronautics, jan 1992.

[49] B. E. Launder and B. I. Sharma. Application of the energy-dissipation model of turbulence to the calculation of flow near a spinning disc. *Letters in Heat and Mass Transfer*, 1(2):131–137, nov 1974.

[50] François G Schmitt. About Boussinesq's turbulent viscosity hypothesis: historical remarks and a direct evaluation of its validity. *Comptes Rendus Mécanique*, 335(9):617–627, 2007.

[51] Bart J. Daly. Transport Equations in Turbulence. *Physics of Fluids*, 13(11):2634, 1970.

[52] B Eisfeld. *Differential Reynolds Stress Modeling for Separating Flows in Industrial Aerodynamics*. Springer Tracts in Mechanical Engineering. Springer International Publishing, 2015.

[53] J M Duclos, D Veynante, and T Poinsot. A comparison of flamelet models for premixed turbulent combustion. *Combustion and Flame*, 95(12):101–117, 1993.

[54] R. G. Abdel-Gayed, K J Al-Khishali, and D Bradley. Turbulent Burning Velocities and Flame Straining in Explosions. *Proceedings of the Royal Society of London A: Mathematical, Physical and Engineering Sciences*, 391(1801):393–414, 1984.

[55] Chang R Choi and Kang Y Huh. Development of a Coherent Flamelet Model for a Spark-Ignited Turbulent Premixed Flame in a Closed Vessel. *Combustion and Flame*, 114(3):336–348, 1998.

[56] T Poinsot and D Veynante. *Theoretical and Numerical Combustion*. R.T. Edwards, 2nd edition, 2005.

[57] J Janicka and A Sadiki. Large eddy simulation of turbulent combustion systems. *Proceedings of the Combustion Institute*, 30(1):537–547, 2005.

[58] J. Smagorinsky. General Circulation Experiments With the Primitive Equations. *Monthly Weather Review*, 91(3):99–164, 1963.

[59] J Bardina, J Ferziger, and W Reynolds. Improved subgrid-scale models for large-eddy simulation. In *13th Fluid and PlasmaDynamics Conference*, Fluid Dynamics and Co-located Conferences. American Institute of Aeronautics and Astronautics, 1980.

[60] Massimo Germano, Ugo Piomelli, Parviz Moin, and William H Cabot. A dynamic subgridscale eddy viscosity model. *Physics of Fluids A: Fluid Dynamics*, 3(7):1760–1765, 1991.

[61] Gordon Fru, Dominique Thévenin, and Gábor Janiga. Impact of turbulence intensity and equivalence ratio on the burning rate of premixed methane-air flames. *Energies*, 4(6):878–893, 2011.

[62] Girish Nivarti and Stewart Cant. Direct Numerical Simulation of the bending effect in turbulent premixed flames. *Proceedings of the Combustion Institute*, 36(2):1903–1910, 2017.

[63] R J Kee, M E Coltrin, and P Glarborg. *Chemically Reacting Flow: Theory and Practice*. Wiley-Interscience, 2003.

[64] E. Ranzi, A. Frassoldati, R. Grana, A. Cuoci, T. Faravelli, A. P. Kelley, and C. K. Law. Hierarchical and comparative kinetic modeling of laminar flame speeds of hydrocarbon and oxygenated fuels. *Progress in Energy and Combustion Science*, 38(4):468–501, 2012.

[65] E Mallard and H.L Le Chatelier. Thermal model for flame propagation. *Annales Des Mines*, 4:379–568, 1883.

[66] A Kazakov and M Frenklach. Reduced Reaction Sets based on GRIMech 1.2, 1995.

[67] Z. Qin G.P. Smith, D.M. Golden, M. Frenklach, N.W. Moriarty, B. Eiteneer, M. Goldenberg, C.T. Bowman, R.K. Hanson, S. Song. W.C. Gardiner, V.V Lissianski. GRI-Mech.

[68] N Peters. Length scales in laminar and turbulent flames. *Numerical Approaches to Combustion Modeling*, 135:155–182, 1991.

[69] Gerhard Damkoehler. The Effect of Turbulence on the Flame Velocity in Gas Mixtures. *Zeitschrift fuer Elektrochemie und Angewandte Physikalische Chemiw*, 46(11):601–626, apr 1947.

[70] R Borghi. On the Structure and Morphology of Turbulent Premixed Flames. In Corrado Casci and Claudio Bruno, editors, *Recent Advances in the Aerospace Sciences: In Honor of Luigi Crocco on His Seventy-fifth Birthday*, pages 117–138. Springer US, Boston, MA, 1985.

[71] D. B. Spalding. Mixing and chemical reaction in steady confined turbulent flames. *Symposium (International) on Combustion*, 13(1):649–657, jan 1971.

[72] K. N. C. Bray, Paul A. Libby, and J. B. Moss. Unified modeling approach for premixed turbulent combustion part I: general formulation. *Combustion and Flame*, 61(1):87–102, jul 1985.

[73] F.A. Williams. Turbulent Combustion. In John D. Buckmaster, editor, *The Mathematics of Combustion*, pages 97–131. SIAM, Menlo Park, CA., 2nd edition, 1985.

[74] F. E. Marble and J. E. Broadwell. The Coherent Flame Model for Turbulent Chemical Reactions. *Project Squid ,*, (January), 1977.

[75] I R. Gran and B. F. Magnussen. A Numerical Study of a Bluff-Body Stabilized Diffusion Flame. Part 2. Influence of Combustion Modeling And Finite-Rate Chemistry. *Combustion Science and Technology*, 119(1-6):191–217, 1996.

[76] K N C Bray, Michel Champion, and Paul A Libby. Premixed flames in stagnating turbulence: Part I. The general formulation for counterflowing streams and gradient models for turbulent transport. *Combustion and Flame*, 84(3):391–410, 1991.

[77] M. Dekena and N. Peters. Combustion modeling with the G-equation. *Oil and Gas Science and Technology*, 54(2):265–270, 1999.

[78] K.N.C. Bray and Nedunchezhian Swaminathan. Scalar dissipation and flame surface density in premixed turbulent combustion. *Comptes Rendus - Mecanique*, 334(8-9):466–473, aug 2006.

[79] K N C Bray, M Champion, and Paul A Libby. The Interaction Between Turbulence and Chemistry in Premixed Turbulent Flames. In R Borghi and S N B Murthy, editors, *Turbulent Reactive Flows*, pages 541–563. Springer US, New York, NY, 1989.

[80] S. B. Pope. The evolution of surfaces in turbulence. *International Journal of Engineering Science*, 26(5):445–469, jan 1988.

[81] R. S. Cant, S. B. Pope, and K. N C Bray. Modelling of flamelet surface-to-volume ratio in turbulent premixed combustion. *Symposium (International) on Combustion*, 23(1):809–815, 1991.

[82] D. Veynante, J. Piana, J. M. Duclos, and C. Martel. Experimental analysis of flame surface density models for premixed turbulent combustion. *Symposium (International) on Combustion*, 26(1):413–420, jan 1996.

[83] T. Mantel and R. Borghi. A new model of premixed wrinkled flame propagation based on a scalar dissipation equation. *Combustion and Flame*, 96(4):443–457, 1994.

[84] Wai K Cheng and Joachim A Diringer. Numerical Modelling of SI Engine Combustion with a Flame Sheet Model. In *SAE Technical Paper*. SAE International, 1991.

[85] C Dopazo and E. E. O'Brien. An approach to the autoignition of a turbulent mixture. *Acta Astronautica*, 1(9-10):1239–1266, sep 1974.

[86] S. B. Pope. The probability approach to the modelling of turbulent reacting flows. *Combustion and Flame*, 27(C):299–312, aug 1976.

[87] A R. Kerstein. One-dimensional turbulence: model formulation and application to homogeneous turbulence, shear flows, and buoyant stratified flows. *Journal of Fluid Mechanics*, 392(1999):277–334, 1999.

[88] Wm T. Ashurst and Alan R. Kerstein. One-dimensional turbulence: Variable-density formulation and application to mixing layers. *Physics of Fluids*, 17(2):1–26, 2005.

[89] Esteban D. Gonzalez-Juez, Alan R. Kerstein, and Lucinda H. Shih. Vertical mixing in homogeneous sheared stratified turbulence: A one-dimensional-turbulence study. *Physics of Fluids*, 23(5), 2011.

[90] Randall J. McDermott, Alan R. Kerstein, Rodney C. Schmidt, and Philip J. Smith. The ensemble mean limit of the one-dimensional turbulence model and application to residual stress closure in finite volume large-eddy simulation. *Journal of Turbulence*, 6(December 2014):1–33, 2005.

[91] Esteban D. Gonzalez-Juez, Rodney C. Schmidt, and Alan R. Kerstein. ODTLES simulations of wall-bounded flows. *Physics of Fluids*, 23(12), 2011.

[92] Allen J Ricks, John C Hewson, Alan R Kerstein, Jay P Gore, Sheldon R Tieszen, and William T Ashurst. A spatially developing one-dimensional turbulence (ODT) study of soot and enthalpy evolution in meter-scale buoyant turbulent flames. *Combustion Science and Technology*, 182(1):60–101, 2010.

[93] Naveen Punati, Evatt Hawkes, and James C Sutherland. ODT vs DNS: Non-premixed flames at different Re with extinction and reignition charateristics. *International journal of research in physical chemistry and chemical physics*, 231(10):1709–1735, 2017.

[94] Naveen Punati, James C Sutherland, Evatt Hawkes, Alan R Kerstein, and Jacqueline H Chen. A Comparison of Direct Numerical Simulations with the One-Dimensional Turbulence Model for a Syngas Jet Flame. In *Fall Technical Meeting of the Western States Section of the Combustion Institute*, pages 2–26, Irvine, 2009.

[95] J C Hewson and A R Kerstein. Stochastic simulation of transport and chemical kinetics in turbulent CO/H2/N2 flames. *Combustion Theory and Modelling*, 5(4):669–697, 2001.

[96] Esteban D Gonzalez-Juez, Alan R Kerstein, and Lucinda H Shih. Vertical mixing in homogeneous sheared stratified turbulence: A one-dimensional-turbulence study. *Physics of Fluids*, 23(5):55106, 2011.

[97] N. Peters. The turbulent burning velocity for large-scale and small-scale turbulence. *Journal of Fluid Mechanics*, 384:107–132, 1999.

[98] V. L. Zimont. Gas premixed combustion at high turbulence. Turbulent flame closure combustion model. *Experimental Thermal and Fluid Science*, 21(1-3):179–186, 2000.

[99] A Bagdanavicius, P J Bowen, N Syred, P Kay, and A Crayford. Burning Velocities of Alternative Gaseous Fuels at Elevated Temperature and Pressure. 48(2), 2010.

[100] A Y Poludnenko and E S Oran. The interaction of high-speed turbulence with flames: Global properties and internal flame structure. *Combustion and Flame*, 157(5):995–1011, may 2010.

[101] Parsa Tamadonfar and Ömer L Gülder. Effects of mixture composition and turbulence intensity on flame front structure and burning velocities of premixed turbulent hydrocarbon/air Bunsen flames. *Combustion and Flame*, 162(12):4417–4441, 2015.

[102] Santosh Hemchandra and Tim Lieuwen. Local consumption speed of turbulent premixed flames An analysis of memory effects. *Combustion and Flame*, 157(5):955–965, 2010.

[103] Chien Chia Liu, Shenqyang Steven Shy, Ming Wei Peng, Chien Wen Chiu, and Yi Chih Dong. High-pressure burning velocities measurements for centrally-ignited premixed methane/air flames interacting with intense near-isotropic turbulence at constant Reynolds numbers. *Combustion and Flame*, 159(8):2608–2619, 2012.

[104] Eoin M Burke, Felix Güthe, and Rory F D Monaghan. A Comparison of Turbulent Flame Speed Correlations for Hydrocarbon Fuels at Elevated Pressures. *ASME. Turbo Expo: Power for Land, Sea, and Air*, Volume 4B, 2016.

[105] Hiroyuki Kido, Kimitoshi Tanoue, Masaya Nakahara, Hideki Kido, and Takayoshi Inoue. Experimental study of the turbulent combustion mechanism of non-stoichiometric mixtures. *JSAE Review*, 17(4):361–367, 1996.

[106] M. Fairweather, M. P. Ormsby, C. G W Sheppard, and R. Woolley. Turbulent burning rates of methane and methane-hydrogen mixtures. *Combustion and Flame*, 156(4):780–790, 2009.

[107] T Brutscher, N Zarzalis, and H Bockhorn. An experimentally based approach for the space-averaged laminar burning velocity used for modeling premixed turbulent combustion. *Proceedings of the Combustion Institute*, 29(2):1825–1832, 2002.

[108] S.P.R Muppala, Naresh K Aluri, Friedrich Dinkelacker, and Alfred Leipertz. Development of an algebraic reaction rate closure for the numerical calculation of turbulent premixed methane, ethylene, and propane/air flames for pressures up to 1.0 MPa. *Combustion and Flame*, 140(4):257–266, 2005.

[109] Hiroyuki Kido, Toshiaki Kitagawa, Kenshiro Nakashima, and Katsutoshi Kato. An improved model of turbulent mass burning velocity. *Kyushu University, Faculty of Engineering, Memoirs*, 49:229–247, 1989.

[110] Masaya Nakahara and Hiroyuki Kido. Study on the Turbulent Burning Velocity of Hydrogen Mixtures Including Hydrocarbons. *AIAA Journal*, 46(7):1569–1575, 2008.

[111] V A Khramtsov. Seventh Symposium (International) on Combustion. *Butterworh's Scientific Publications, London*, 7:609, 1959.

[112] S. A. Goldenberg and V. S. Pelevin. Influence of pressure on rate of flame propagation in turbulent flow. In *Symposium (International) on Combustion*, volume 7, pages 590–594. Elsevier, jan 1958.

[113] V P Karpov and A S Sokolik. The effect of pressure on the rate of laminar and turbulent combustion, Institute of Chemical Physics Academy of Sciences, USSR Translated from Dokl. *Akad. Nauk. SSSR*, 132:1341–1343, 1960.

[114] Hideaki Kobayashi, Yasuharu Kawabata, and Kaoru Maruta. Experimental study on general correlation of turbulent burning velocity at high pressure. *Symposium (International) on Combustion*, 27:941–948, 1998.

[115] D Bradley, M Lawes, C G W Sheppard, and R Woolley. Study of turbulence and combustion interaction: measurement and prediction of the rate of turbulent burning. Technical report, 1994.

[116] Vlade Vukadinovic, Peter Habisreuther, Rainer Suntz, and Nikolaos Zarzalis. Gt2013-94307 Influence of Pressure on Markstein Number Effect in Turbulent. *Proceedings of ASME Turbo Expo 2013*, pages 1–10, 2013.

[117] C. Mandilas, M. P. Ormsby, C. G W Sheppard, and R. Woolley. Effects of hydrogen addition on laminar and turbulent premixed methane and iso-octane-air flames. *Proceedings of the Combustion Institute*, 31 I:1443–1450, 2007.

[118] G Smallwood. Characterization of flame front surfaces in turbulent premixed methane/Air combustion. *Combustion and Flame*, 101(94):461–470, 1995.

[119] Masaya Nakahara, Hiroyuki Kido, and Kenshiro Nakashima. A Study on the Local Flame Displacement Velocity of Premixed Turbulent Flames. *JSME International Journal Series B*, 48(1):164–171, 2005.

[120] Vivek R. Savarianandam and C. J. Lawn. Burning velocity of premixed turbulent flames in the weakly wrinkled regime. *Combustion and Flame*, 146(1-2):1–18, 2006.

[121] Esen Cintosun, Gregory J. Smallwood, and Ömer L. Gülder. Flame Surface Fractal Characteristics in Premixed Turbulent Combustion at High Turbulence Intensities. *AIAA Journal*, 45(11):2785–2789, 2007.

[122] Parsa Tamadonfar and Ömer L. Gülder. Flame brush characteristics and burning velocities of premixed turbulent methane/air Bunsen flames. *Combustion and Flame*, 161(12):3154–3165, 2014.

[123] Reaction Design. CHEMKIN-PRO.

[124] Wayne K Metcalfe, Sinéad M Burke, Syed S Ahmed, and Henry J Curran. A Hierarchical and Comparative Kinetic Modeling Study of C1 C2 Hydrocarbon and Oxygenated Fuels. *International Journal of Chemical Kinetics*, 45(10):638–675, 2013.

[125] Hideaki Kobayashi, Katsuhiro Seyama, Hirokazu Hagiwara, Yasuhiro Ogami, and Ralph Aldredge. Burning velocity correlation of methane/air turbulent premixed flames at high pressure and high temperature. *Proceedings of the Combustion Institute*, 30 I(1):827–834, 2005.

[126] Ömer L. Gülder. Turbulent premixed flame propagation models for different combustion regimes. *Symposium (International) on Combustion*, 23(1):743–750, 1991.

[127] H Kobayashi. Experimental study of high-pressure turbulent premixed flames. *Experimental Thermal and Fluid Science*, 26(2-4):375–387, 2002.

[128] H G Weller, S Uslu, D Gosman, R R Maly, R Herweg, and B Heel. Prediction of Combustion in Homogeneous-Charge Spark-Ignition Engines. In *International Symposium COMODIA 94*, pages 163–169, 1994.

[129] Hans-Peter Schmid, Peter Habisreuther, and Wolfgang Leuckel. A Model for Calculating Heat Release in Premixed Turbulent Flames. *Combustion and Flame*, 113(1-2):79–91, 1998.

[130] P. Clavin and F. a. Williams. Effects of molecular diffusion and of thermal expansion on the structure and dynamics of premixed flames in turbulent flows of large scale and low intensity. *Journal of Fluid Mechanics*, 116:251–282, 1982.

[131] Malcolm Lawes, Matthew P Ormsby, Chris G W Sheppard, and Robert Woolley. The turbulent burning velocity of iso-octane/air mixtures. *Combustion and Flame*, 159(5):1949–1959, may 2012.

[132] A M Klimov. Premixed turbulent flames-interplay of hydrodynamic and chemical phenomena. *Flames, lasers, and reactive systems*, 1:133–146, 1983.

[133] F.C. Gouldin. An application of fractals to modeling premixed turbulent flames. *Combustion and Flame*, 68(3):249–266, 1987.

[134] Alan R Kerstein. Pair-exchange model of turbulent premixed flame propagation. *Symposium (International) on Combustion*, 21(1):1281–1289, 1988.

[135] R. G. Abdel-Gayed and D Bradley. A two-eddy theory of premixed turbulent flame propagation. *Philosophical Transactions of the Royal Society of London. Series A, Mathematical and Physical Sciences*, 301(1457):1–25, 1981.

[136] M.S. Anand and S.B. Pope. Calculations of premixed turbulent flames by PDF methods. *Combustion and Flame*, 67(2):127–142, 1987.

[137] S.P.R Muppala and F. Dinkelacker. Numerical modelling of the pressure dependent reaction source term for premixed turbulent methane/air flames. *Progress in Computational Fluid Dynamics, an International Journal*, 4(6):328–336, 2004.

[138] Derek Bradley. How fast can we burn? *Symposium (International) on Combustion*, 24(1):247–262, 1992.

[139] Guillaume Lecocq, Stéphane Richard, Olivier Colin, and Luc Vervisch. Hybrid presumed pdf and flame surface density approaches for Large-Eddy Simulation of premixed turbulent combustion. Part 1: Formalism and simulation of a quasi-steady burner. *Combustion and Flame*, 158(6):1201–1214, jun 2011.

[140] Roman Keppeler, Eike Tangermann, Usman Allaudin, and Michael Pfitzner. LES of Low to High Turbulent Combustion in an Elevated Pressure Environment. *Flow, Turbulence and Combustion*, 92(3):767–802, mar 2014.

[141] F. C. Gouldin, K. N.C. Bray, and J. Y. Chen. Chemical closure model for fractal flamelets. *Combustion and Flame*, 77(3-4):241–259, sep 1989.

[142] Hideaki Kobayashi, Teppei Nakashima, Takashi Tamura, Kaoru Maruta, and Takashi Niioka. Turbulence measurements and observations of turbulent premixed flames at elevated pressures up to 3.0 MPa. *Combustion and Flame*, 108(1-2):104–117, 1997.

[143] F Charlette, D Veynante, and C Meneveau. A power-law wrinkling model for {LES} of premixed turbulent combustion: Part {I} - non-dynamic formulation and initial tests. *Combustion and Flame*, 131:159–180, 2002.

[144] Mitchell D Smoke and Vincent Giovangigli. Formulation of the premixed and non-premixed test problems. In Mitchell D Smooke, editor, *Reduced Kinetic Mechanisms and Asymptotic Approximations for Methane-Air Flames: A Topical Volume*, pages 1–28. Springer Berlin Heidelberg, Berlin, Heidelberg, 1991.

[145] J B Bell, M S Day, I G Shepherd, M R Johnson, R K Cheng, J F Grcar, V E Beckner, and M J Lijewski. Numerical simulation of a laboratory-scale turbulent V-flame. *Proceedings of the National Academy of Sciences*, 102(29):10006–10011, 2005.

[146] John B. Bell, Marcus S. Day, Joseph F. Grcar, Michael J. Lijewski, James F. Driscoll, and Sergei A. Filatyev. Numerical simulation of a laboratory-scale turbulent slot flame. *Proceedings of the Combustion Institute*, 31 I:1299–1307, 2007.

[147] Sergei A. Filatyev, James F. Driscoll, Campbell D. Carter, and Jeffrey M. Donbar. Measured properties of turbulent premixed flames for model assessment, including burning velocities, stretch rates, and surface densities. *Combustion and Flame*, 141(1-2):1–21, 2005.

[148] Jeffrey C Lagarias, James A Reeds, Margaret H Wright, and Paul E Wright. Convergence properties of the Nelder–Mead simplex method in low dimensions. *SIAM Journal on optimization*, 9(1):112–147, 1998.

[149] Toshiaki Kitagawa, Takashi Nakahara, Kosuke Maruyama, Kunihiro Kado, Akihiro Hayakawa, and Shoichi Kobayashi. Turbulent burning velocity of hydrogen-air premixed propagating flames at elevated pressures. *International Journal of Hydrogen Energy*, 33(20):5842–5849, 2008.

[150] R J Kee, F M Rupley, and J A Miller. CHEMKIN-II: A FORTRAN Chemical Kinetics Package for the Analysis of Gas-Phase Chemical Kinetics. Technical report, 1989.

[151] Rj Kee, Jf Grcar, M Smooke, Ja Miller, and E Meeks. PREMIX : A FORTRAN Program for Modeling Steady Laminar One-Dimensional. *SANDIA National Laboratories*, (April):1–87, 1985.

[152] CD-Adapco. Digital Analysis of Reaction Systems (DARS), 2015.

[153] Raymond L. Speth. Ember: A Quasi-One-Dimensional, Unsteady Flame Solver, oct 2017.

[154] A Felden. Cantera User's Guide, 2015.

[155] Python Software Foundation. Python, 2016.

[156] The MathWorks Inc. MATLAB 2013b.

[157] David G Goodwin. Cantera Workshop - Introduction to Cantera, 2004.

[158] Alan C Hindmarsh, Peter N Brown, Keith E Grant, Steven L Lee, Radu Serban, Dan E Shumaker, and Carol S Woodward. SUNDIALS: Suite of Nonlinear and Differential/Algebraic Equation Solvers. *ACM Trans. Math. Softw.*, 31(3):363–396, sep 2005.

[159] C L Lawson, R J Hanson, D R Kincaid, and F T Krogh. Basic Linear Algebra Subprograms for Fortran Usage. *ACM Trans. Math. Softw.*, 5(3):308–323, sep 1979.

[160] E Anderson, Z Bai, C Bischof, L S Blackford, J Demmel, Jack J Dongarra, J Du Croz, S Hammarling, A Greenbaum, A McKenney, and D Sorensen. *LA-*

PACK Users' Guide (Third Ed.). Society for Industrial and Applied Mathematics, Philadelphia, PA, USA, 1999.

[161] Zhenwei Zhao, Marcos Chaos, Andrei Kazakov, and Frederick L Dryer. Thermal decomposition reaction and a comprehensive kinetic model of dimethyl ether. *International Journal of Chemical Kinetics*, 40(1):1–18, 2008.

[162] Huibin Yu, Erjiang Hu, Yu Cheng, Xinyi Zhang, and Zuohua Huang. Experimental and numerical study of laminar premixed dimethyl ether / methane air flame. 136:37–45, 2014.

[163] W. B. Lowry, Z. Serinyel, M. C. Krejci, H. J. Curran, G. Bourque, and E. L. Petersen. Effect of methane-dimethyl ether fuel blends on flame stability, laminar flame speed, and Markstein length. *Proceedings of the Combustion Institute*, 33(1):929–937, 2011.

[164] Inc. Reaction Design. CHEMKIN Theory Manual. (July):1–402, 2013.

[165] W P Jones and B E Launder. The prediction of laminarization with a two-equation model of turbulence. *International Journal of Heat and Mass Transfer*, 15(2):301–314, 1972.

[166] Ansys Inc. ANSYS FLUENT Theory Guide 12.0 Theory Guide. (November), 2011.

[167] Tarek Echekki and Epaminondas Mastorakos. *Turbulent combustion modeling: Advances, new trends and perspectives*, volume 95. 1st edition, jan 2011.

[168] A. Cuoci, A. Frassoldati, G. Buzzi Ferraris, T. Faravelli, and E. Ranzi. The ignition, combustion and flame structure of carbon monoxide/hydrogen mixtures. Note 2: Fluid dynamics and kinetic aspects of syngas combustion. *International Journal of Hydrogen Energy*, 32(15):3486–3500, oct 2007.

[169] R. L. Gaffney, J. A. White, S. S. Girimaji, and J. P. Drummond. Modeling temperature and species fluctuations in turbulent, reacting flow. *Computing Systems in Engineering*, 5(2):117–133, 1994.

[170] Rodney O Fox. *Computational Models for Turbulent Reacting Flows*. Cambridge University Press, Cambridge, 2003.

[171] I. Otic, G. Grotzbach, and M. Worner. Analysis and modelling of the temperature variance equation in turbulent natural convection for low-Prandtl-number fluids. *Journal of Fluid Mechanics*, 525:237–261, 2005.

[172] A. Shams, F. Roelofs, E. Baglietto, Sylvain Lardeau, and S. Kenjeres. Assessment and calibration of an algebraic turbulent heat flux model for low-Prandtl fluids. *International Journal of Heat and Mass Transfer*, 79:589–601, 2014.

[173] A. Beretta, N. Mancini, F. Podenzani, and L. Vigevano. The Influence of the Temperature Fluctuations Variance on NO Predictions for a Gas Flame. *Combustion Science and Technology*, 121(1-6):193–216, 1996.

[174] Yannick Lecocq. *Contribution to the analysis and the modelling of turbulent flows in mixed convection regime - Application to radioactive waste management*. Theses, Université de Poitiers, dec 2008.

[175] Gunarjo Suryanto Budi. *Contribution to Advanced Modelling of Turbulent Natural and Mixed Convection*. PhD thesis, Delft University of Technology, 2003.

[176] B.F. Magnussen and B.H. Hjertager. On mathematical modeling of turbulent combustion with special emphasis on soot formation and combustion. *Symposium (International) on Combustion*, 16(1):719–729, jan 1977.

[177] Bjorn f. Magnussen. Modeling of Pollutant Formation in Gas Turbine Combustors Based on The Eddy Dissipation Concep. In *International flame research foundation first topic oriented technical meeting*, pages 719–729, 1989.

[178] Stephen B. Pope. *Turbulent Flows*. Cambridge University Press, 2000.

[179] S. Byggstoyl and B.F. Magnussen. A Model for Flame Extinction in Turbulent Flow. In *Fourth Symposium on Turbulent Shear Flows*, pages 381–395, Germany, 1985. Springer, Berlin, Heidelberg.

[180] Yang Li, Chong-Wen Zhou, Kieran P Somers, Kuiwen Zhang, and Henry J Curran. The oxidation of 2-butene: A high pressure ignition delay, kinetic modeling study and reactivity comparison with isobutene and 1-butene. *Proceedings of the Combustion Institute*, 36(1):403–411, 2017.

[181] J O Hinze. *Turbulence*. McGraw-Hill classic textbook reissue series. McGraw-Hill, 1975.

[182] Nilanjan Chakraborty, Mohit Katragadda, and R. Stewart Cant. *Statistics and modelling of turbulent kinetic energy transport in different regimes of premixed combustion*, volume 87. 2011.

[183] Songwei Zhang and Christopher J. Rutland. Premixed flame effects on turbulence and pressure-related terms. *Combustion and Flame*, 102(4):447–461, 1995.

[184] Konrad Koeltzsch. The height dependence of the turbulent Schmidt number within the boundary layer. *Atmospheric Environment*, 34(7):1147–1151, 2000.

[185] Bjorn F Magnussen. The Eddy Dissipation Concept- A Bridge Between Science and Technology. *ECCOMAS thematic conference on computational combustion*, pages 21–24, 2005.

[186] I.R. Gran. *Mathematical modeling and numerical simulation of chemical kinetics in turbulent combustion*. Doctoral thesis, Norwegian Institute of Technology, Trondheim, Norway, 1994.

[187] Zhiyan Wang and John Abraham. Effects of Karlovitz number on turbulent kinetic energy transport in turbulent lean premixed methane/air flames. *Physics of Fluids*, 29(8):85102, aug 2017.

[188] B Karlovitz, D W Denniston, D H Knapschaefer, and F E Wells. Studies on Turbulent flames: A. Flame Propagation Across velocity gradients B. turbulence Measurement in flames. *Symposium (International) on Combustion*, 4(1):613–620, 1953.

[189] V. Zimont, W. Polifke, M. Bettelini, and W. Weisenstein. An Efficient Computational Model for Premixed Turbulent Combustion at High Reynolds Numbers Based on a Turbulent Flame Speed Closure. *J. of Gas Turbines Power*, 120:526–532, 1998.

[190] S G Davis, C K Law, and H Wang. Propene pyrolysis and oxidation kinetics in a flow reactor and laminar flames. *Combustion and Flame*, 119(4):375–399, 1999.

[191] University of California at San Diego. San Diego Mechanism web page, Mechanical and Aerospace Engineering (Combustion Research). Chemical-kinetic mechanisms for combustion applications, 2016.

[192] Jeffrey M Bergthorson and Paul E Dimotakis. Premixed laminar C1C2 stagnation flames: Experiments and simulations with detailed thermochemistry models. *Proceedings of the Combustion Institute*, 31(1):1139–1147, 2007.

[193] John M Simmie. Detailed chemical kinetic models for the combustion of hydrocarbon fuels. *Progress in Energy and Combustion Science*, 29(6):599–634, 2003.

[194] H.J. Curran. Detailed chemical kinetic modeling; is there life after GRI-MECH 3.0? *Spring Technical Meeting American Chemical Society*, 2004.

[195] J H Mathews and K D Fink. *Numerical methods using MATLAB*. Pearson Prentice Hall, fourth edition, 2003.

Appendix A

Nelder-Mead Direct Simplex Search Method

The solution approach implemented by the algorithm can be easily visualised. An initial first guess is defined by the user, with the number of variables k in the guess being one greater than the spatial domain (3 points for a 2D domain, 4 points for a 3D domain, etc.). By having the number of points one greater than the dimensions of the domain, a simplex S can be defined where a two-dimensional simplex would take the form of a triangle. The initial simplex is defined by generating vertices $x_0, ..., x_k$ where $x \in \mathbb{R}^k$. The algorithm evaluates the function at each point within the simplex, seeking a better estimate using a variety of approaches, described below, through an iterative process.

Assuming a function $f(x)$ with 3 variables such that the simplex is a triangle, to simplify the description, the following steps are taken with each iteration.

1. Ordering: The order of the best to worst (resulting in the smallest to largest functions/MAPE) vertices of S is determined such that the below equality is satisfied.

$$f(x_0) \leq f(x_1) \leq f(x_2)$$

2. Calculation of the Centroid: The centroid (c) of the best side of the simplex is determined using the following equation.

$$c := \frac{1}{k} \sum_{j \neq h} x_j \tag{A.1}$$

3. Transformation: In order to minimize the function $f(x)$, a new working simplex is calculated from the current one. This is achieved by replacing only the worst vertex (x_2) with a better point using reflection, expansion or contraction methods with respect to the best side. If this succeeds, the new point is used to define the working simplex and the iteration returns to step 1. If these approaches fails, the simplex is shrunk towards the best vertex, x_0, where all points are replaced except (x_0). The transformations of S are controlled by four parameters: α for reflection, β for contraction, γ for expansion and δ for shrinkage and typically have values of:

$$\alpha = 1, \quad \beta = \frac{1}{2}, \quad \gamma = 2, \quad \delta = \frac{1}{2}$$

   – Reflect: The worst vertex, x_2, is reflected through the centroid c to calculate the new vertex x_r. This can be seen in Figure A.1 where $x_r = c + \alpha(c - x_2)$. If $f(x_0) \leq (x_r) < f(x_1)$ is satisfied, x_r is accepted as a new vertex and the current iteration is terminated.

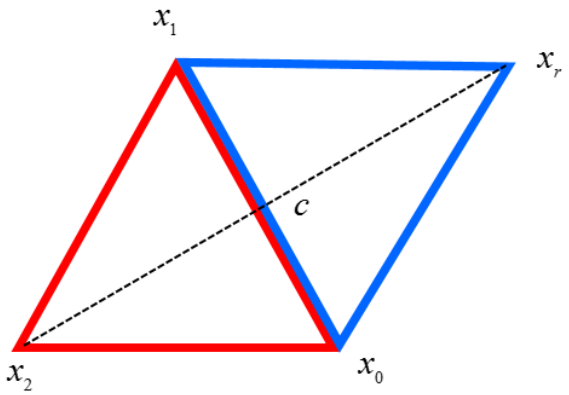

Figure A.1: Reflection of the worst vertex, x_2, through the centroid. The red triangle represents the initial simplex and the blue represents the newly calculated simplex

– Expand: If $f(x_r) < f(x_0)$, the expansion point x_e is computed such that $x_e = c + \gamma(x_r - c)$ as shown in Figure A.2. If $f(x_e) < f(x_r)$ is satisfied, x_e is accepted as the new vertex and terminate the iteration. Otherwise, if $f(x_e) \geq f(x_r)$, accept x_r and the iteration is terminated.

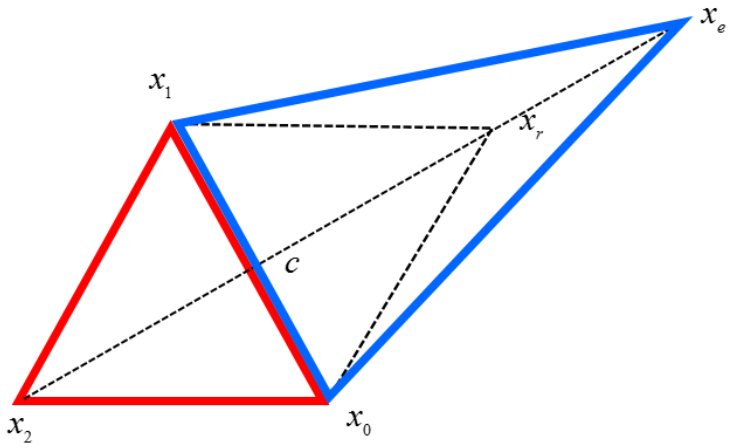

Figure A.2: Expansion of the reflected point x_r away from the centroid

– Contract: If $f(x_r) \geq f(x_1)$, the contraction point x_c is calculated using the better of the two points x_2 or x_r.

  – Outside: If $f(x_1) \leq f(x_r) < f(x_2)$, the new vertex is computed outside the initial simplex such that $x_c = c + \beta(x_r - c)$ as shown in Figure A.3(a). If $f(x_c) \leq f(x_r)$ is satisfied, x_c is accepted as the new vertex and the iteration is terminated, otherwise the shrink transformation is performed.

  – Inside: If $f(x_r) \geq f(x_2)$, the new vertex is computed inside the initial simplex such that $x_c := c + \beta(x_2 - c)$ as shown in Figure A.3(b). If $f(x_c) \leq f(x_2)$ is satisfied, x_c is accepted as the new vertex and the iteration is terminated, otherwise the shrink transformation is performed.

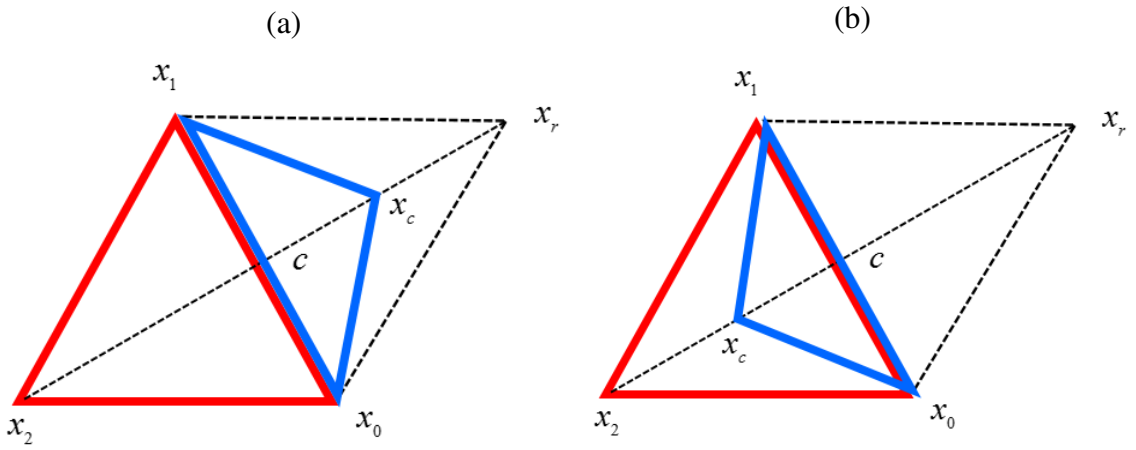

Figure A.3: Contraction of the reflected point away from x_r to the (a) outside and (b) inside of the initial simplex

– Shrink: The simplex is shrunk by computing k-1 new vertices, where the best vertex remains unchanged. The new points are calculated as $x_j := x_l + \delta(x_j - x_l)$, for $j = 0...k-1$, with $j \neq l$

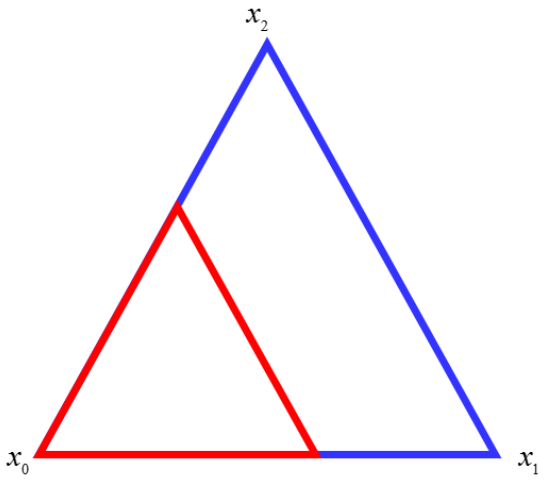

Figure A.4: Shrink of the worst points in the simplex towards the best vertex

Figure A.5 show this process for ten steps of the simplex search method in a 2D domain converging to the point (3, 2).

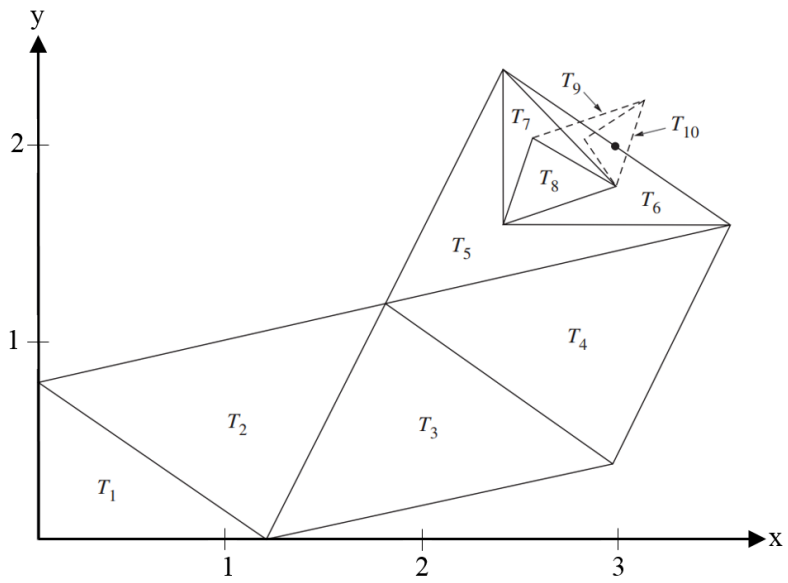

Figure A.5: Ten iterations of the Nelder-Mead simplex direct search method for a 2D problem [195]

To determine when convergence is reached, the algorithm uses three parameters (1) the number of iterations taken, (2) the size of the current simplex, and (3) the current solution values of the function. The user can assign values for each of these parameters and when one of the convergence parameters is satisfied, the algorithm will return the values of the function. For the simplex size convergence parameters, this is satisfied when the working simplex is sufficiently small such that a user limit is reached for some or all vertices of the simplex. Although the Matlab version of the Nelder-Mead simplex direct search method is highly robust, the initial guess has an influence on both the solution time and the final results of the algorithm. An initial guess closer to the correct solution will result in fast computational times, a better final result and therefore lower MAPEs. This is especially true for functions with a large number of variables such as the newly-developed empirical correlation in Equation 3.3 and less so for a function like the Zimont correlation which only contains two variables.

Termination tolerance between the current and previous values, for both the function and the input values x, are user defined and must both be satisfied before the algorithm terminates.

Appendix B

Unidirectional Turbulence Model

The following appendix describes an attempt to close turbulent transport equations in a one-dimensional (1D) domain. The Transport equations (shown in 1D) for turbulent kinetic energy (k) and energy dissipation (ε) define turbulence as shown in Equation B.1 and B.2

$$\frac{\partial}{\partial t}(\rho k) + \frac{d}{dz}(\rho k u) = \frac{d}{dz}\left(\mu + \frac{\mu_t}{\sigma_k}\frac{dk}{dz}\right) - P_k - \rho\varepsilon \tag{B.1}$$

$$\frac{\partial}{\partial t}(\rho \varepsilon) + \frac{d}{dz}(\rho \varepsilon u) = \frac{d}{dz}\left(\mu + \frac{\mu_t}{\sigma_\varepsilon}\frac{d\varepsilon}{dz}\right) + C_{1\varepsilon}\frac{\varepsilon}{k}P_k - C_{2\varepsilon}\rho\frac{\varepsilon^2}{k} \tag{B.2}$$

where eddy viscosity and production of k are defined as

$$\mu_t = C_\mu \rho \frac{k^2}{\varepsilon} \; P_k = -\rho\overline{u_z' u_y'}\frac{\partial u_j}{\partial z} \tag{B.3}$$

with model constants of $C_{1\varepsilon} = 1.44$, $C_{2\varepsilon} = 1.92$, $C_\mu = 0.09$, $\sigma_k = 1.0$, $\sigma_\varepsilon = 1.3$. An attempt to define the Reynolds stresses $(\rho\overline{u_i' u_j'}\frac{\partial u_j}{\partial x_i})$ in the source term P_k in the above equations was made using a 1D Boussinesq Approach [181], as shown in Equation B.4, where the velocity gradients are in a single direction.

$$\rho\overline{u_i' u_j'} = \mu_t\left(\frac{\partial u_i}{\partial z} + \frac{\partial u_i}{\partial z} - \frac{2}{3}\delta_{ij}\frac{\partial u_i}{\partial z}\right) + \frac{2}{3}\rho k \tag{B.4}$$

where δ_{ij} is the Kronecjer symbol. Using Equation B.4 resulted in very large values of

ε which were slow dissipate and therefore required extreme large domains (15 metres) to negate loss of k and ε, through diffusion, to the outlet. For this reason the appraoch disscussed in Section 4.3.3 is used in the predictive solver.

Appendix C

Python Interface Code

```
"""
A Freely-Propagating Turbulent Flame Speed Solver
Created by Eoin M. Burke and Rory F.D. Monaghan
National University of Ireland, Galway
20/09/2017
Please Contact Eoin Burke or Rory F.D. Monaghan for any
    queries
e.buke18@nuigalway.ie
rory.monaghan@nuigalway.ie
"""

import os
import cantera as ct
import numpy as np
import csv
import os
from datetime import datetime
from datetime import timedelta
import time
print ct.__file__
import matplotlib.pyplot as plt
startTime = datetime.now()
#################### Pre-Processing ####################
mech = "gri30 - No NOx"
mech = "drm19_mech"
mech = "gri30 - No NOx"

mech_out = mech
mech_turb = mech + " - turb"
```

```
mech_turb = mech + "-turb" + ".cti"
mech = mech + ".cti"
gas = ct.Solution(mech_turb)
#################### Reactor Physical Properties
    ####################
gas.transport_model = 'Mix' #Transport Mechanism
tburner = 300
pressure = 1e5
t_prime_burner = 1

Equi = [1.2]
u_rms = [3.701]
LT = [4.65E-02]
inc = 1.0

start_point  = 0
end_point = 2.0
initial_size = 6
ratio = 3

target_ref = 0.08
curve = target_ref
step = 0.875
while curve<0.9999:
  curve = curve/step
curve = curve*step
slope = curve
curve_cors = target_ref

while curve_cors<0.75:
  curve_cors = curve_cors/step
curve_cors = curve_cors*step
slope_cors = curve_cors
slope_int  = slope
curve_int = curve

prune = curve_cors-0.1

TKE = 0.5*(u_rms[0]*u_rms[0]) #Turbulent Kinetic Energy
ED = (0.09**0.75)*((TKE**1.5)/LT[0]) #Energy Dissap
energy_eqn = True
mdot = 0.4

loglevel= 1
step_size = 1e-5
```

```
n_steps = [2, 5, 10, 20, 40, 80]
ss_age = 10
ts_age = 10
major_it = 1
minor_it = 1

tol_ss = [1.0e-5, 1.0e-13]  # [rtol atol] for steady-state
    problem
tol_ts = [1.0e-4, 1.0e-9]  # [rtol atol] for time stepping

#################### Grid Properties ####################
initial_grid = np.linspace(start_point, end_point,
    initial_size) #Grd istart and end points (m) and number
    of grid points
fuel_species = 'CH4' #Fuel defintion
air_N2_O2_ratio = 3.76
io2 = gas.species_index('O2'); #Index of O2 in mix
in2 = gas.species_index('N2'); #Index of N2 in mix
ich4 = gas.species_index(fuel_species); #Index of fuel 2 in
     mix
c = (gas.n_atoms(fuel_species,'C') + 0.25*gas.n_atoms(
    fuel_species,'H'))

comp = [0]*gas.n_species;# Composition Array
comp[ich4] = Equi[0]
comp[io2] = c #Adding O2
comp[in2] = air_N2_O2_ratio*c

gas.TPX = tburner,  pressure, comp #Creating Gas and set
    initial conditions

# Flame object
f = ct.FreeFlame(gas, initial_grid) #Creating Domain
f.flame.set_steady_tolerances(default=tol_ss) #Setting
    Tolerance
f.flame.set_transient_tolerances(default=tol_ts) #Setting
    Tolerance
f.set_refine_criteria(ratio=ratio, slope=slope, curve=curve
    ) #Setting refinment

f.set_max_jac_age(ss_age, ts_age)
f.set_time_step(step_size, n_steps)
f.max_time_step_count = 1000
#Inlet Properties
f.inlet.T = tburner
```

```
f.inlet.T_Prime = t_prime_burner

f.inlet.TKE = TKE
f.inlet.ED = ED
f.inlet.mdot = mdot*gas.density
f.inlet.X = comp

f.flame.TurbDiff_enable = True
f.flame.TurbTcon_enable = True
f.flame.EDC_enable = False
f.energy_enabled = energy_eqn
f.flame.alpha = 0.99
f.flame.beta = 1.0
f.flame.gamma = 1.0

print("\n
    ----------------------------------------------------------------------------")

print("ER = %.2f; P = %.2f MPa; T = %.f K; u' = %.3f m/s;
    LT = %.1f mm"% (Equi[0], (gas.P/1e6),f.inlet.T,u_rms
    [0],(LT[0]*1000)))
print("Curve = %.2f; Slope = %.2f; Alpha = %.3f; Beta = %.3
    f; Gamma = %.3f"% (curve, slope,f.flame.alpha,f.flame.
    beta,f.flame.gamma))
print
    ("----------------------------------------------------------------------------

f.show_solution()
f.set_refine_criteria(ratio=ratio, slope=slope, curve=curve
    ) #Setting refinment

f.solve(loglevel=loglevel, refine_grid=True)
print("\n
    ----------------------------------------------------------------------------")

print("ER = %.2f; P = %.2f MPa; T = %.f K; u' = %.3f m/s;
    LT = %.1f mm"% (Equi[0], (gas.P/1e6),f.inlet.T,u_rms
    [0],(LT[0]*1000)))
print("Curve = %.2f; Slope = %.2f; Alpha = %.3f; Beta = %.3
    f; Gamma = %.3f"% (curve, slope,f.flame.alpha,f.flame.
    beta,f.flame.gamma))
print
    ("----------------------------------------------------------------------------

f.flame.EDC_enable = True
```

```
f.solve(loglevel=loglevel, refine_grid=True)
try:
        while curve >= (target_ref+1e-10):
                curve = curve * step
                slope = slope * step

                f.set_refine_criteria(ratio=ratio, slope=
                    slope, curve=curve) #Setting refinment
                print("Attempting with Curve = %.2f; Slope
                    = %.2f"% (curve, slope))
                print("f.inlet.Y[ich4] = %.10f"% (f.inlet.Y
                    [ich4]))
                print
                    ("-----------------------------------------------------------------


                f.solve(loglevel=loglevel, refine_grid=True
                    )
                print
                    ("-----------------------------------------------------------------

                print("Solved with Curve = %.2f; Slope =
                    %.2f"% (curve, slope))

        print("\n
            ---------------------------------------------------------------------

        print("\n
            ---------------------------------------------------------------------


        print("%.100s; Curve = %.2f; Slope = %.2f; "% (
            mech_out, curve, slope))
        print("Grid = %.f to %.f; "% ( start_point,
            end_point))
        print("ER = %.2f; u' = %.3f m/s; LT = %.1f mm"% (
            Equi[0], u_rms[0],(LT[0]*1000)))
        print("slope_int = %.2f; curve_int = %.2f; step =
            %.3f"% (slope_int, curve_int,step))
        print("target_ref = %.3f; grid points = %.f"% (
            target_ref, (f.flame.n_points - 2)))
        print("f.inlet.Y[ich4] = %.10f"% (f.inlet.Y[ich4]))
        print("f.Y[ich4,0] = %.10f"% (f.Y[ich4,0]))

        print(datetime.now()-startTime)#Print Simulation
            time
```

```
            domain_size = f.flame.n_points-1
            ProgVar=[None]*f.flame.n_points #Flame Thickness
                Array
            target = 0.5
            for x in range(0,domain_size):
                    ProgVar[x]= (f.T[x] - f.T[0])/(f.T[
                        domain_size]-f.T[0])
            for x in range(0,domain_size):
                    if ProgVar[x]>=target:
                        pos = x-1
                        break

            FS_05 = f.u[pos-1]+(target-ProgVar[pos-1])*((f.u[
                pos]-f.u[pos-1])/(ProgVar[pos] - ProgVar[pos-1])
                )

            print("ST_0.5 = %.5f;"% (FS_05))
            name = str(time.time()) + ".xml"
            f.save(filename=name)

    except Exception:
            print ("FAIL FAIL FAIL FAIL FAIL FAIL FAIL FAIL")
            print("%.100s; Curve = %.2f; Slope = %.2f; "% (
                mech_out, curve, slope))
            print("Grid = %.f to %.f; "% ( start_point,
                end_point))
            print("ER = %.2f; u' = %.3f m/s; LT = %.1f mm"% (
                Equi[0], u_rms[0],(LT[0]*1000)))
            print("slope_int = %.2f; curve_int = %.2f; step =
                %.3f"% (slope_int, curve_int,step))
            print("target_ref = %.3f; grid points = %.f"% (
                target_ref, (f.flame.n_points - 2)))
            print("f.inlet.Y[ich4] = %.10f"% (f.inlet.Y[ich4]))

            print(datetime.now()-startTime)#Print Simulation
                time
            print ("FAIL FAIL FAIL FAIL FAIL FAIL FAIL FAIL")

    while major_it < len(u_rms):
        while minor_it < inc+1:

            f.set_refine_criteria(ratio=ratio, slope=slope_cors
                , curve=curve_cors,prune = prune) #Setting
                refinment
```

```
f.solve(loglevel=loglevel, refine_grid=True)

u_rms_current = u_rms[major_it-1] + ((u_rms[
    major_it]-u_rms[major_it-1])/inc)*minor_it
LT_current = LT[major_it-1] + ((LT[major_it]-LT[
    major_it-1])/inc)*minor_it
Equi_current = Equi[major_it-1] + ((Equi[major_it]-
    Equi[major_it-1])/inc)*minor_it

TKE = 0.5*(u_rms_current*u_rms_current) #Turbulent
    Kinetic Energy
ED = (0.09**0.75)*((TKE**1.5)/LT_current) #Energy
    Dissap
comp[ich4] = Equi_current
comp[io2] = c #Adding O2
comp[in2] = air_N2_O2_ratio*c

f.inlet.TKE = TKE
f.inlet.ED = ED
f.inlet.X = comp

slope=slope_cors
curve=curve_cors

print("\n
    ------------------------------------------------------------

print("ER = %.2f; P = %.2f MPa; T = %.f K; u' = %.3
    f m/s; LT = %.1f mm"% (Equi_current, (gas.P/1e6)
    ,f.inlet.T,u_rms_current,(LT_current*1000)))
print("Curve = %.2f; Slope = %.2f; step = %.3f;
    grid points = %.3f; target_ref = %.3f"% (curve,
    slope,step,(f.flame.n_points - 2),target_ref))
print("f.inlet.Y[ich4] = %.10f"% (f.inlet.Y[ich4]))
print
    ("------------------------------------------------------------


try:
        while curve >= (target_ref+1e-10):
                curve = curve * step
                slope = slope * step

                f.set_refine_criteria(ratio=ratio,
                    slope=slope, curve=curve) #
```

```
            Setting refinment
        print("Attempting with Curve = %.2f
            ; Slope = %.2f"% (curve, slope))
        print
            ("-----------------------------------------------------------------


        f.solve(loglevel=loglevel,
            refine_grid=True)
        print
            ("-----------------------------------------------------------------

        print("Solved with Curve = %.2f;
            Slope = %.2f"% (curve, slope))

print("\n
    ------------------------------------------------------------------------

print("\n
    ------------------------------------------------------------------------

print("%.100s; Curve = %.2f; Slope = %.2f;
    "% (mech_out, curve, slope))
print("Grid = %.f to %.f; "% ( start_point,
     end_point))
print("ER = %.2f; P = %.2f MPa; T = %.f K;
    u' = %.3f m/s; LT = %.1f mm"% (
    Equi_current, (gas.P/1e6),f.inlet.T,
    u_rms_current,(LT_current*1000)))
print("slope_int = %.2f; curve_int = %.2f;
    step = %.3f"% (slope_int, curve_int,step
    ))
print("target = %.3f; grid points = %.f"% (
    target, (f.flame.n_points - 2)))
print("f.inlet.Y[ich4] = %.10f"% (f.inlet.Y
    [ich4]))
print(datetime.now()-startTime)#Print
    Simulation time

domain_size = f.flame.n_points-1
ProgVar=[None]*f.flame.n_points #Flame
    Thickness Array
target = 0.5
for x in range(0,domain_size):
        ProgVar[x]= (f.T[x] - f.T[0])/(f.T[
```

```
                    domain_size]-f.T[0])
            for x in range(0,domain_size):
                if ProgVar[x]>=target:
                    pos = x-1
                    break

            FS_05 = f.u[pos-1]+(target-ProgVar[pos-1])
                *((f.u[pos]-f.u[pos-1])/(ProgVar[pos] -
                ProgVar[pos-1]))

            print("ST_0.5 = %.5f;"% (FS_05))
            name = str(time.time()) + ".xml"
            f.save(filename=name)

        except Exception:
            print ("FAIL FAIL FAIL FAIL FAIL FAIL FAIL
                FAIL")
            print("%.100s; Curve = %.2f; Slope = %.2f;
                "% (mech_out, curve, slope))
            print("Grid = %.f to %.f; "% ( start_point,
                 end_point))
            print("ER = %.2f; P = %.2f MPa; T = %.f K;
                u' = %.3f m/s; LT = %.1f mm"% (
                Equi_current, (gas.P/1e6),f.inlet.T,
                u_rms_current,(LT_current*1000)))
            print("slope_int = %.2f; curve_int = %.2f;
                step = %.3f"% (slope_int, curve_int,step
                ))
            print("target = %.3f; grid points = %.f"% (
                target, (f.flame.n_points - 2)))
            print("f.inlet.Y[ich4] = %.10f"% (f.inlet.Y
                [ich4]))
            print(datetime.now()-startTime)#Print
                Simulation time
            print ("FAIL FAIL FAIL FAIL FAIL FAIL FAIL
                FAIL")
            f.restore(filename=name)

    minor_it = minor_it + 1
major_it = major_it + 1
minor_it = 0
```

Appendix D

Computational Process for Predicting S_T

The following appendix describes the solution process defined within the C++ source code used to solve for turbulent flame speed starting at the user defined inputs taken from the interface code (Python) right to the return of the converge solution. It can be seen in Figure D.1that for no grid refinement, the EDC terms and reaction rate are not update instead the values from the previous refinement are used. Figure D.1 also shows the iterative process when solution convergence has not been reached and the process for when additional grid points have been added.

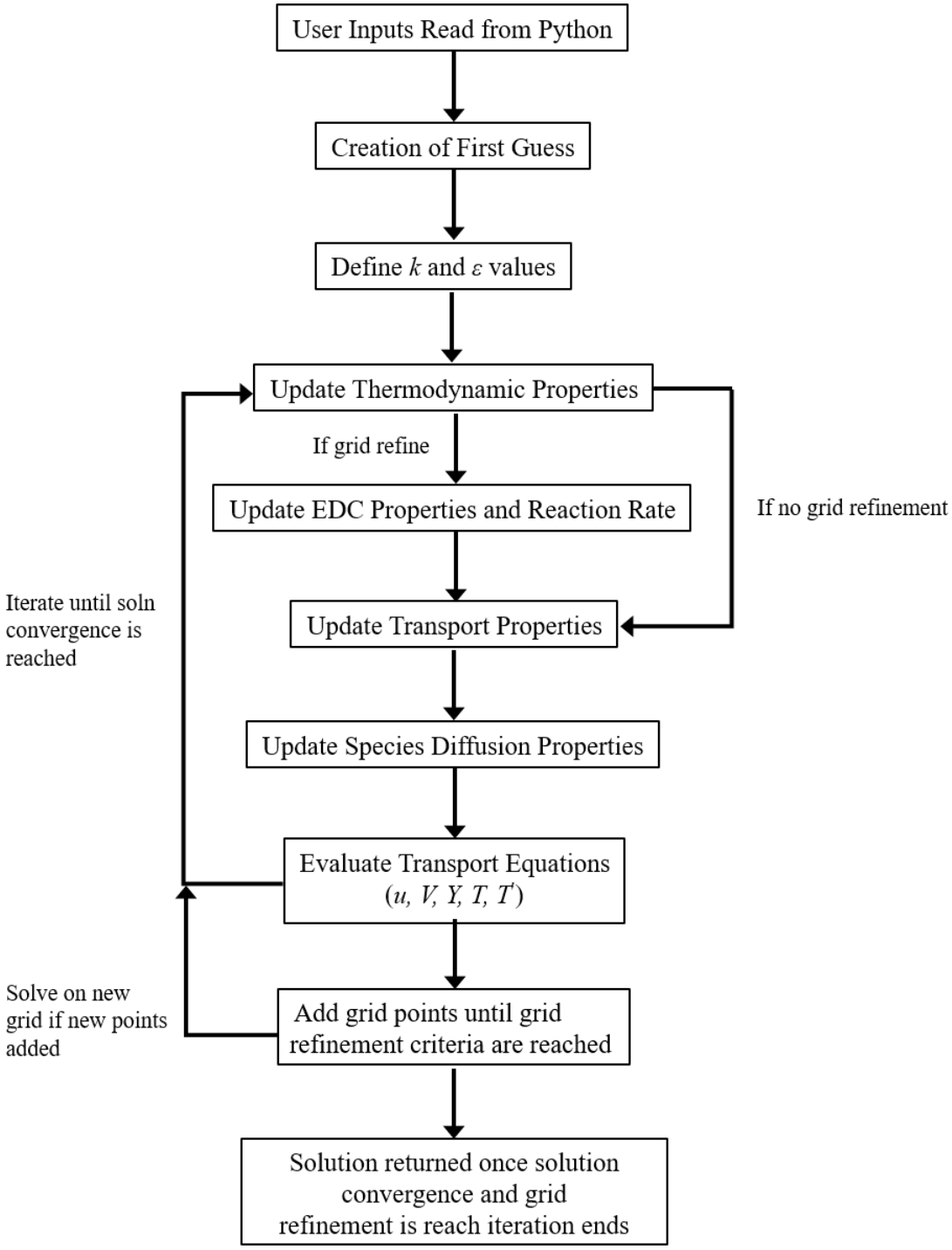

Figure D.1: Computational Process for Predicting S_T